DETACHED EDDY SIMULATION OF SUBCHANNEL FLOW PULSATIONS

INVESTIGATION OF SUBCHANNEL FLOW PULSATIONS USING HYBRID URANS/LES APPROACH – DETACHED EDDY SIMULATION

BY

DEEPAYAN HOME, B.E, M.A.Sc.

A Thesis

Submitted to the school of Graduate Studies

In Partial Fulfillment of the Requirements

For the Degree

Doctor of Philosophy

McMaster University

DOCTOR OF PHILOSOPHY (2010) McMaster University

(Mechanical Engineering) Hamilton, Ontario

TITLE: Investigation of Subchannel Flow Pulsations Using Hybrid URANS/LES Approach – Detached Eddy Simulation

AUTHOR: Deepayan Home, M.A.Sc. (McMaster University)

SUPERVISOR: Professor Dr. Marilyn F. Lightstone

NUMBER OF PAGES: xxix, 243

ABSTRACT

The work presented in this thesis focused on using the hybrid Unsteady Reynolds-Averaged Navier-Stokes (URANS)/Large Eddy Simulation (LES) methodology to investigate the flow pulsation phenomenon in compound rectangular channels for isothermal flows. The specific form of the hybrid URANS/LES approach that was used is the Strelets (2001) version of the Detached Eddy Simulation (DES). It is of fundamental interest to study the problem of flow pulsations, as it is one of the most important mechanisms that directly affect the heat transfer occurring in sub-channel geometries such as those in nuclear fuel bundles. The predictions associated with the heat transfer and fluid flow in sub-channel geometry can be used to develop simplified physical models for sub-channel mixing for use in broader safety analysis codes. The primary goal of the current research work was to determine the applicability of the DES approach to predict the flow pulsations in sub-channel geometries. It was of interest to see how accurately the dynamics associated with the flow pulsations can be resolved from a spatial-temporal perspective using the specific DES model. The research work carried out for this thesis was divided into two stages.

In the first stage of the research work, effort was concentrated to primarily understand the field of sub-channel flow pulsations and its implications from both an experimental and numerical point of view. It was noted that unsteady turbulence modeling approaches have great potential in providing insights into the fundamentals of sub-channel flow pulsations. It was proposed that for this thesis work, the Shear Stress Transport (SST) based DES model be used to understand the dynamics associated with

sub-channel flow pulsations. To the author's knowledge the DES-SST based turbulence model has never been used for resolving the effects of sub-channel flow pulsations. Next, the hybrid URANS/LES turbulence modeling technique was reviewed in great detail to understand the philosophy of the hybrid URANS/LES technique and its ability to resolve fundamental flows of interest. Effort was directed to understand the switching mechanism (which blends the URANS region with the LES region) in the DES-SST model for fully wall bounded turbulent flows without boundary layer separation. To the author's knowledge, the DES-SST model has never been used on a fully wall bounded turbulent flow problem without boundary layer separation. Thus, the DES-SST model was first completely validated for a fully developed turbulent channel flow problem without boundary layer separation.

In the second stage of the research work, the DES-SST model was used to study the flow pulsation phenomena on two rectangular sub-channels connected by a gap, on which extensive experiments were conducted by Meyer and Rehme (1994). It was found that the DES-SST model was successful in resolving significant portion of the flow field in the vicinity of the gap region. The span-wise velocity contours, velocity vector plots, and time traces of the velocity components showed the expected cross flow mixing between the sub-channels through the gap. The predicted turbulent kinetic energy showed two clear peaks at the edges of the gap. The dynamics of the flow pulsations were quantitatively described through temporal auto-correlations, spatial cross-correlations and power spectral functions. The numerical predictions were in general agreement with the experiments in terms of the quantitative aspects. From an instantaneous time scale point of view, the DES-SST model was able to identify different flow mixing patterns. The pulsating flow is basically an effect of the variation of the pressure field which is a response to the instability causing the fluid flow pulsations. Coherent structures were identified in the flow field to be comprised of eddies, shear zones and streams. Eddy structures with high vorticity and low pressure cores were found to exist near the vicinity of the gap edge region. A three dimensional vorticity field was identified and found to exist near the gap edge region. The instability mechanism and the probable cause behind the quasi-periodic fluid flow pulsations was identified and related to the inflectional stream-wise velocity profile. Simulations were also performed with two different channel lengths in comparison to the reference channel length. Different channel length studies showed similar statistical description of the flow field. However, frequency independent results were not obtained. In general, simulations performed using the DES-SST model were successful in capturing the effects of the fluid flow pulsations. This modeling technique has great potential to be used for actual rod bundle configurations.

ACKNOWLEDGMENTS

I would like to thank my supervisor Dr. Marilyn F. Lightstone for her invaluable support, guidance and motivation throughout the course of my research work. Having known her for the past five years, I have great respect and admiration for her. I have thoroughly enjoyed every moment of my research work under her guidance. Thank you very much for everything and I will always remember you wherever I am.

I would like to thank Dr. Stephen Tullis for his valuable suggestions during the course of the research work. I have enjoyed many fruitful discussions that I have had with him, specifically those that were related to turbulence modeling in general.

I would like to thank Dr. John C. Luxat for his suggestions on interpreting the physics of the problem and allowing our research group to use his computer cluster. The usage of the cluster saved the computational times considerably.

Financial support from University Network of Excellence in Nuclear Engineering (UNENE) is greatly appreciated. Special thanks to Joe Verhaege for his help related to licensing issues of the software usage.

My lab mates Cathy, Salam, George, Di, Danish and Charles had my days in the CFD lab very enjoyable and eventful.

Without the never ending support, love, inspiration and sacrifice of my mother this academic journey of mine would never have been possible. I have heartfelt gratitude for my wife Sanjukta for her love, patience, support and encouragement.

DEDICATED TO THE LOVING MEMORY OF MY DEAR FATHER

TABLE OF CONTENTS

LIST OF FIGURES

LIST OF TABLES

NOMENCLATURE

a	height of the rectangular sub-channel, mm
a_1	constant of the SST model
A	constant present in the numerical blending function of the DES-SST model
b	distance between the centre of the sub-channels
b_1	width of the sub-channel, mm
b_2	width of the sub-channel, mm
B	parameter used in the formulation of the numerical blending function of the DES-SST model
C_{DES}	constant of the DES-SST model
C_f	skin friction coefficient
C_{H1}	constant in the numerical blending function of the DES-SST model
C_{H2}	constant in the numerical blending function of the DES-SST model
C_{H3}	constant in the numerical blending function of the DES-SST model
d	gap width, mm
D_h	hydraulic diameter, m
D^k_{RANS}	dissipative term in the turbulent kinetic energy transport equation of the SST model, kg/m^2s^3
D^k_{DES}	dissipative term in the turbulent kinetic energy transport equation of the DES model, kg/m^2s^3
f	frequency, Hz
$f_{v,SGS}$	damping function of the LES model

g gap height, mm

F_1 first blending function of the SST model

F_2 second blending function of the SST model

F_{DES} switching function of the DES-SST model

h half channel height, m

k turbulence kinetic energy, m^2/s^2

k_t normalized turbulence kinetic energy ($= k/u_\tau^2$)

$\overrightarrow{k_m}$ wave number, 1/m

L length of the rectangular duct in a particular direction, m

L_t turbulent length scale, m

m parameter used in the formulation of the numerical blending function of the DES-SST model

N number of grid points in a particular direction

N_{seq} average number of alternate sequence of span-wise velocity structures

Nu_g Nusselt number based on gap spacing

$\bar{p}$ Reynolds averaged/filtered pressure variable, N/m^2

Pr Prandtl number of fluid

P_k production term in the transport equation of turbulence kinetic energy

P_ω production term in the transport equation of turbulence eddy frequency

q_{ij} heat transfer through the gap per unit length, W/s

Q second invariant of velocity gradient tensor, $1/s^2$

Re_g Reynolds number based on gap spacing

R_{uu} stream-wise temporal auto-correlation function

R_{ww} span-wise temporal auto-correlation function

R_{uw} temporal auto-correlation function for the cross velocity components

R_{u1u2} temporal correlation function for spatially separated stream-wise velocity components

R_{w1w2} temporal correlation function for spatially separated span-wise velocity Components

R_{ux} spatial cross-correlation function in the axial direction for stream-wise velocity component

R_{wx} spatial cross-correlation function in the axial direction for span-wise velocity component

Re_τ Reynolds number based on the time averaged wall friction velocity and half channel height/half gap height

$\overline{S_{ij}}$ Reynolds strain rate/ SGS strain rate tensor, 1/s

Str Strouhal number

St_g gap Stanton number

t time, s

T_i bulk temperature of a specific sub-channel, K

u instantaneous velocity in the stream-wise direction, m/s

$\overline{u_i}$ tensorial representation of Reynolds averaged/ filtered velocity variable in the Navier-Stokes equation, m/s

u_τ wall shear velocity, m/s

u^+ normalized time averaged stream-wise velocity ($= u/u_\tau$)

u' fluctuating component of the instantaneous stream-wise velocity, m/s

u" normalized turbulence intensity in the stream-wise direction ($= u'_{RMS}/u_\tau$)

U time averaged axial velocity, m/s

U_b channel bulk velocity, m/s

$U_{b,gap}$ time averaged bulk velocity in the gap, m/s

v instantaneous velocity in the wall-normal direction, m/s

v' fluctuating component of the instantaneous wall-normal velocity, m/s

v" normalized turbulence intensity in the wall-normal direction ($= v'_{RMS}/u_\tau$)

w instantaneous velocity in the span-wise direction, m/s

w' fluctuating component of the instantaneous span-wise velocity, m/s

w" normalized turbulence intensity in the span-wise direction ($= w'_{RMS}/u_\tau$)

w_{eff} effective mixing velocity, m/s

w'_{ij} mixing rate, kg/ms

x Cartesian coordinate in the stream-wise direction, mm

x_i tensorial representation of direction

Δx grid cell size in the stream-wise direction, mm

Δx^+ normalized grid cell size in the stream-wise direction ($= \Delta x u_\tau/\nu$)

y Cartesian coordinate in the normal direction, mm

y^+ normalized y coordinate ($= yu_\tau / \nu$)

Δy grid cell size in the wall-normal direction, mm

Δy_c^+ normalized grid cell size at the center of the channel in the y direction

($= \Delta y_c u_\tau / \nu$)

Δy_w^+ normalized distance of the first grid point from the wall in the y direction

($= \Delta y_w u_\tau / \nu$)

Y mixing factor

z Cartesian coordinate in the span-wise direction, mm

Δz grid cell size in the span-wise direction, mm

Δz^+ normalized grid cell size in the span-wise direction ($= \Delta z u_\tau / \nu$)

Δz_w^+ normalized distance of the first grid point from the wall in the z direction

($= \Delta z_w u_\tau / \nu$)

z_{ij} effective mixing distance, m

Greek Symbols

β constant of the SST model

β^* constant of the original k-ω and transformed k-ε model

γ constant of the SST model

Δ filter width, m

δ_{ij} Kronecker delta

ε turbulence eddy dissipation, m^2/s^3

κ Von-Karman constant

λ wavelength of the flow pulsations, mm

μ dynamic viscosity of the fluid, Pa-s

μ_t dynamic turbulence eddy viscosity, Pa-s

ν kinematic viscosity of the fluid, m^2/s

ν_t kinematic turbulence eddy viscosity, m^2/s

ρ density of fluid, Kg/m^3

σ numerical blending function of the DES-SST model

σ_k constant of the SST model

σ_ω constant of the SST model

$\sigma_{\omega 2}$ constant of the transformed k-ε model

τ_w wall shear stress, kg/ms^2

τ_{ij} Reynolds stress/ SGS stress tensor, m^2/s^2

Ω vorticity, 1/s

ψ_{ip} transported variable value at the integration point

ω turbulence eddy frequency/vorticity modulus, 1/s

CHAPTER 1

INTRODUCTION

1.1 Synopsis

Mathematical modeling of turbulent mixing in a fuel rod bundle of a nuclear reactor core is of direct relevance to nuclear reactor safety analysis. In the reactor core, the heat generation within the fuel rods is removed by the coolant which flows axially past the rods. Under loss-of-coolant accident conditions, single-phase vapor or two-phase conditions can occur depending on the magnitude of the break in the heat transport system. An understanding of the behavior of the fluid flow under normal or abnormal conditions is very important in order to accurately predict the fuel rod temperatures and ultimately improve reactor design.

The CANDU reactor core contains cylindrical rod bundle geometries, which consists of parallel matrix of solid rods (separated by small gap regions), containing a fissile material and arranged in a pressure tube. As the coolant flows axially past the rods, mass, momentum and heat are exchanged due to interchange mixing through the gaps between the rods. The current research is focused on the mathematical modeling of single-phase turbulent interchange mixing perpendicular to the main flow. The cross flow across the gaps aids in fluid mixing and in homogenizing the fluid temperature across the rod bundle cluster, thus playing an important role in determining the heat transfer rates from the fuel rods.

An understanding of the physics of this turbulent mixing process is necessary for development of constitutive models for use in nuclear safety analysis codes. Over the last four decades, extensive experimental research (Rowe et al., 1974; Hooper and Rehme, 1984; Moller, 1991; Guellouz and Tavoularis, 2000) has shed light into the important mechanisms that contribute to the natural turbulent mixing process in rod bundle geometry arrangements. The general consensus is that large-scale macroscopic pulsations with quasi-periodic characteristics are responsible for the majority of the mixing in rod bundle geometries. The flow pulsations cause enhanced mixing in these geometries. Previous computational fluid dynamics (CFD) studies based using standard steady Reynolds Averaged Navier-Stokes (RANS) turbulence models have been grossly inadequate in predicting the cross flow mixing, since the effect of the flow pulsation phenomena is not captured. Recent studies (Chang and Tavoularis, 2005; Merzari et al., 2008; Home et al., 2009) have suggested that unsteady turbulence modeling approaches are required for the accurate prediction of the dynamics of the flow pulsations.

1.2 Purpose of research

The goal of the current research is to determine the applicability of higher order turbulence models to predict the flow pulsation phenomena in sub-channel geometries. If the dynamics of the flow pulsations are accurately captured then the heat transfer can be better predicted. The predictions associated with the heat transfer and fluid flow in a sub-channel geometry will be used to develop simplified physical models for sub-channel mixing for use in broader safety analysis codes. The specific objectives of this thesis work are provided in the next section.

In order to assess the safety of nuclear reactors and to mitigate potential consequences of accidents, numerical simulations of the large reactor systems are performed. These simulations are multi-disciplinary and often include simulation of the primary side and secondary side heat transport systems, reactor physics, fuel channels, moderator flows, containment, and atmospheric dispersion. The analyses involved are of a large-scale nature and long transients occur, therefore, integrated models are used. For example, thermalhydraulics behavior is modeled using one-dimensional two-fluid codes which are able to predict the important phenomenon, but require accurate correlations and empirical models since the fine details of the flows (such as the details of the boundary layers and the turbulence) are not solved for directly.

In the Canadian nuclear industry, the fuel temperatures at the reactor cores are obtained from computer codes such as CATHENA, TUF, ASSERT-PV among others. Rather than solving for the detailed description of the fluid flow and heat transfer in fuel rod bundles, these codes average over a large region where the size of this region is dependent on the code used and the level of detail desired. Thus, constitutive relations that provide the information that was lost during the averaging process are required. This can include pressure-drop or friction factor correlations, k-factors due to obstructions such as bearing pads or spacers, heat transfer correlations, etc.

In contrast to the aforementioned numerical codes, CFD based codes solve the conservation equations for mass, momentum and energy on much finer grids and can give detailed representations of the velocity and temperature fields inside a reactor fuel bundle. Previous attempts to model inter sub-channel thermal mixing using standard turbulence models have had mixed success (Rock and Lightstone, 2001; Suh and Lightstone, 2004). Steady state predictions significantly underpredict the mixing since the flow pulsation phenomena is not captured. While accurate modeling of the two-phase flow in the fuel channel is an important objective for nuclear safety analysis, the current research is focused on single-phase flows as a first step in attaining this goal.

Numerical studies on sub-channel flows have clearly shown that unsteady turbulence modeling approaches are required for accurate prediction of the dynamics of the flow pulsations (Suh and Lightstone, 2004; Merzari et al., 2008). Two important criterion that the numerical modeling approach should satisfy for the sub-channel geometry problem are: computational cost and the ability of the turbulence model to resolve the effects of the large-scale quasi-periodic structures, responsible for the flow pulsations. In this regard, the hybrid URANS-LES methodology which has the ingredients of both URANS (computationally cost effective) and LES (important scales of motion can be captured), combined into one approach, could be a suitable choice (Home et al., 2009). For sub-channel flows, the region of interest are the gaps where large-scale coherent vortical structures are formed, which induce the flow pulsations. The hybrid URANS-LES approach can be made to work in a way such that the LES characteristics are used in the gap region to resolve the effects of the large-scale structures, while in the near-wall region a URANS model is applied (Home et al., 2009). This approach thus resolves the problem of high computational cost associated with applying LES to a near-wall region. To the author's knowledge, the hybrid URANS-LES approach has never been used to investigate flows in sub-channel geometries. Thus, it was proposed that for this thesis work, the applicability of the hybrid URANS-LES approach be fully tested for sub-channel flows. The DES-SST model (Strelets, 2001) based on the hybrid URANS-LES framework was examined for sub-channel flows.

The flow pulsations observed in sub-channel geometries is a "cold flow phenomena", which means that heat transfer is not responsible and does not affect the macroscopic flow pulsations. Thus, a major goal for this research was to examine the applicability of the DES-SST model for isothermal flow in a sub-channel geometry. Experimental and numerical investigations have shown that quasi-periodic large-scale coherent structures exist in any longitudinal slot or groove in a wall or a connecting gap between two flow channels, provided that the gap's depth is more than approximately twice its width (Meyer and Rehme, 1994; Merzari et al., 2008). It has been shown that the flow pulsation phenomena which occurs in flows in geometries forming rod bundle arrangements (such as nuclear fuel bundles) also occur in compound rectangular channels (Meyer and Rehme, 1994). It was thus decided to validate the DES-SST model which is a hybrid URANS-LES approach on the twin rectangular sub-channel geometry for which extensive experiments were conducted by Meyer and Rehme (1994). The goal of the broader numerical research work is to continue investigating the flow pulsation phenomena problem by gradually adding to it more physical and geometrical parameters, to eventually be able to predict non-isothermal turbulent flows in sub-channel bundle geometries. The long term goal is to develop a simplified physical model for inter sub-channel thermal mixing for use in the broader safety analysis codes.

1.3 Thesis objectives

Based on the overall research framework, the central objective of this thesis work is to assess the applicability of the DES-SST model in predicting the dynamics associated with the flow pulsation phenomena for an isothermal turbulent flow in a compound rectangular channel geometry. The research work for this thesis was divided into two phases. The specific objectives of the thesis work in relation to the two phases are as follows:

Phase 1:

1. Completely understand the philosophy behind hybrid URANS-LES modeling approach and specifically the working of the Strelets (2001) based DES model. This would primarily include understanding the switching mechanism (which blends the URANS region with the LES region) in the DES-SST model for fully wall bounded turbulent flows without boundary layer separation. A thorough understanding of the switching mechanism will help to design the appropriate grid, to control the region(s) where the model would switch.

2. To the author's knowledge, the DES-SST model has never been used on a fully wall bounded turbulent flow problem without boundary layer separation. Thus, it is imperative to first validate the DES-SST model for the benchmark problem, and then systematically progress towards modeling the flow pulsation phenomena in sub-channel geometries. The validation of the DES-SST model is thus performed for the fully developed turbulent

channel flow problem. The results from the DES-SST model are compared to the DNS data of Moser et al. (1999).

Phase 2: It was shown by Meyer and Rehme (1994) that a pulsating flow occurs in any longitudinal slot or groove in a wall or a connecting gap between two flow channels. The second phase of this thesis work will simulate the experimental investigation of Meyer and Rehme (1994) on the large-scale turbulence phenomena in compound rectangular channels. Meyer and Rehme (1994) have experimentally examined this geometry for turbulent flow of air at different Reynolds number and gap sizes. It is of interest to see the capability of the DES-SST model to shed light into the important physics of the flow pulsation phenomena. The main objectives of this phase of the thesis work are:

1. Resolving the effects of the large-scale pulsating flow.
2. Identifying the qualitative and quantitative aspects of the flow pulsation phenomena, and the effect of the quasi-periodic flow pulsations on the structure of turbulence.
3. Providing a detailed description of the flow field and the dynamics associated with the flow pulsations.
4. Identification of the coherent structures in the domain using an appropriate structure identification technique.
5. Understanding the origin and cause behind the instability mechanism, which leads to quasi-periodic fluid flow pulsations in a sub-channel geometry.

1.4 Thesis outline

This thesis consists of seven chapters, including the introduction chapter. Chapter 2 provides a detailed literature review on sub-channel flows in different geometries. Historical development of this field is traced. Both experimental and numerical methodologies that have been used in the past for examining sub-channel flows are presented. Major conclusions are drawn from the literature review and a relatively new turbulence modeling approach is proposed for investigating sub-channel flow in a specific geometry. Chapter 3 presents a review of Detached Eddy Simulation modeling from a hybrid URANS-LES perspective. Emphasis on the hybrid URANS-LES approach for modeling fully wall bounded turbulent flows is laid down. The use of the DES-SST model to investigate sub-channel flow is proposed. The mathematical model and numerical methodology for the DES-SST model is provided in Chapter 4. The issues related to spatial and temporal discretization, and boundary conditions for the problems studied, using the DES-SST model are discussed. Chapter 5 presents the validation study of the DES-SST model for a fully developed turbulent channel flow problem. Chapter 6 provides detailed results from the CFD analysis of the DES-SST model on the twin rectangular sub-channel geometry. Finally, the major conclusions from this thesis work and recommendations for the future work are provided in Chapter 7.

CHAPTER 2

LITERATURE REVIEW: SUB-CHANNEL FLOWS

2.1 Introduction

Mathematical modeling of turbulent mixing in a fuel rod bundle of a nuclear reactor core is of direct relevance to nuclear reactor safety analysis. A nuclear reactor fuel assembly such as that in the CANDU reactor consists of a parallel matrix of solid rods, containing a fissile material and arranged in a pressure tube. Coolant flows along the rods to remove the heat generated by nuclear fission. A Reynolds number of about 500,000 is typical of the flow conditions in CANDU-PHW (pressurized heavy water) reactors (Renksizbulut and Hadaller, 1986). The rod bundle contains a number of parallel sub-channels that are defined as small geometrical regions surrounded by rod surfaces and separated by hypothetical lines connecting the centroids of fuel rods. Sub-channels are bounded by either the fuel rod walls, pressure tube walls, or the region between the sub-channels referred to as gaps. A schematic of a typical cross section of a CANDU 37-element fuel bundle is shown in Figure 2.1, which illustrates the various types of sub-channels. In Figure 2.1, for example, sub-channels 40 and 42 denote triangular and square sub-channel respectively, whereas regions numbered from 43 to 60 represent wall sub-channels. Mass, momentum, and heat transfer between adjacent sub-channels occur mainly by turbulent transport, referred to as inter sub-channel mixing.

The maximum thermal power produced by the reactor is controlled to ensure

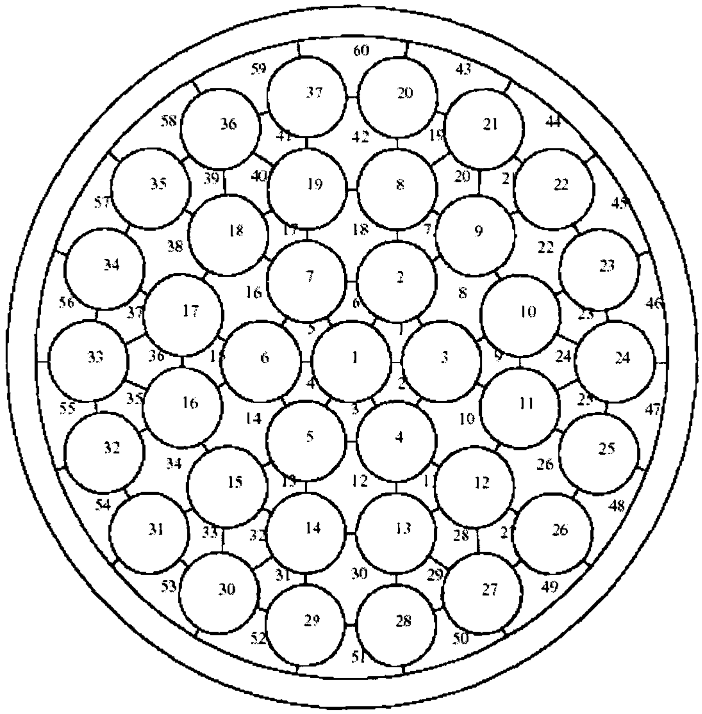

Figure 2.1 Sub-channel layout for CANDU 37 - element fuel bundle (Eiff and Lightstone, 1997).

integrity of the sheath, taking into consideration the critical heat flux (CHF), the maximum allowable rod sheath temperature and the maximum allowable circumferential variation of this temperature. Accurate prediction of detailed temperature distributions in rod bundles both under normal operating conditions and under scenarios of accidents such as loss-of-coolant accident (LOCA) is essential for their safe design and reliable operation. A highly accurate prediction requires a detailed knowledge of the three dimensional velocity field in the rod bundle which captures the physics of the mixing process between interconnected sub-channels. The rod bundle thermal-hydraulics analysis is performed by solving the conservation equations for mass, momentum and energy. In the nuclear industry, the fuel temperatures at the reactor cores are obtained using computer codes such as ASSERT – PV and COBRA, which are based on sub-channel analysis (Tóth and Aszódi, 2007). The basic limitation of the sub-channel method is that it invokes a lumped parameter approach, where many empirical correlations are used to represent the complex exchange mechanisms between the sub-channels and thus does not calculate the fine structures of the velocity and temperature distributions within the control volumes (sub-channels). Averaged mass flow rates and temperatures are computed within the individual control volumes. The interaction between the sub-channels is considered by means of mixing coefficients. In contrast to the sub-channel analysis methods, CFD codes solve the governing equations on much finer grids and can give a detailed representation of the velocity and temperature field inside a reactor fuel bundle. CFD approaches have gained popularity in the nuclear industry over the last decade and can aid in designing safe and reliable reactors (Tóth and Aszódi, 2007; Caraghiaur and Anglart, 2007; Merzari et al., 2008).

For tightly packed rod bundle arrangements (common to nuclear fuel bundles) or related sub-channel geometries, extensive experimental investigations have been carried out over a period of four decades with the aim to understand the nature of the turbulent flow field structure in narrow gap regions. With the advent of powerful computational resources, numerical approaches have gained popularity and have shed more light on the complex nature of flow in sub-channel geometries with small gap regions (Merzari et al., 2008). From both experimental and numerical investigations on sub-channel geometries, it has been shown that, for single-phase conditions, three different mechanisms contribute to the overall mixing process, namely, turbulent diffusion, convection by secondary flows, and large-scale eddy motion in the form of macroscopic flow pulsations.

In this chapter, a review of the experimental investigations on sub-channel geometries is presented in a chronological order, with the idea of providing a historical perspective on sub-channel mixing. This is followed by a discussion on the structure of turbulence in rod bundle geometries. Major conclusions are drawn from the past investigations, specifically highlighting the most important contributor to sub-channel mixing and its implication to flows in rod bundle geometries. Empirical modeling followed by numerical approaches based on the CFD methodology, for sub-channel flows are then presented. The impact of turbulence modeling approaches on prediction of sub-channel mixing will be emphasized. At the end of this chapter, a very specific turbulence modeling methodology will be proposed to understand the dynamics and its applicability for sub-channel flows.

2.2 Experimental investigations

One of the earliest investigations on sub-channel mixing was studied experimentally on a 6 rod cluster by Skinner et al. (1969) using mass-transfer theory, with nitrous oxide as tracer in air as an analogy for heat. It was found that, the measured mixing rates were high enough to be modeled by turbulent diffusion theory alone. The high diffusivity across the gaps within the sub-channels of the bundle was attributed to secondary flows. Ingesson and Kjellstrom (1970) said that the high mixing rates could also be obtained by considering only turbulent diffusion with a much smaller effective mixing length than the distance between the centroids of the sub-channels. Van der Ros and Boggardt (1970) performed single-phase liquid energy-exchange experiments with two square channels connected by a symmetric/asymmetric gap. Visual observations and fast thermocouple signals indicated that the transport through the gap could not be explained by eddy diffusivity alone. This is perhaps the first time that the presence of large-scale turbulence structure was reported. Castellena et al. (1974) deduced a correlation for mixing coefficient from single-phase sub-channel mixing data for a 25 rod square array by precisely measuring sub-channel exit temperatures over a range of test conditions. The mixing coefficient was found to have a very weak dependence on Reynolds number.

Rowe et al. (1974) performed an experimental study to investigate the effect of flow channel geometry on fully developed turbulent flow in rod bundles arranged in a square array. The experiments were performed in water with a Reynolds number range from 50,000 to 200,000 and with pitch-to-diameter ratios of 1.125 and 1.25 respectively (pitch is the centre-to-centre distance between two fuel rod elements). The experimental results showed that the rod gap spacing is the most significant geometric parameter affecting the flow structure. Decreasing the rod gap spacing increased the turbulent intensity and the dominant frequency of turbulence. The laser Doppler measurements revealed the presence of large scale turbulent structures in the form of macroscopic flow processes near the gap regions. The presence of macroscopic flow pulsations explained the fact that the inter sub-channel mixing rate in rod bundles has a weak dependence on rod gap spacing (for the range studied) which cannot be explained by a simple isotropic turbulent diffusion theory.

Trupp and Azad (1975) investigated the structure of turbulent flow using hot wire anemometry, pitot and Preston tubes in triangular array rod bundles with three pitch-to-diameter ratios (1.20, 1.35 and 1.50). The measurements included friction factor, local wall shear stress, distribution of mean axial velocity, Reynolds stresses and eddy diffusivities. The radial distribution of the three normal Reynolds stresses was similar to axisymmetric developed pipe flow. The presence of secondary flows were inferred from the distribution of wall shear stresses and turbulent kinetic energy, and also from the bulges found in the isovelocity distribution. The approximate magnitude of the secondary flows was around 0.5% of the bulk average axial velocity. Carajilescov and Todreas (1976) considered axial turbulent flows in an interior sub-channel of a triangular rod array with pitch-to-diameter ratio of 1.123. Laser Doppler measurements for the secondary flow field were inconclusive. The magnitude of secondary flows was found to be less than 0.67% of the bulk axial velocity. Aly et al. (1978) showed the presence of secondary flows in an equilateral triangular duct. The tests were conducted over a Reynolds number range of 53,000 to 107,000. The counter-rotating secondary flow cells in each duct corner were similar to secondary flow patterns found in square ducts (Brundrett and Baines, 1964). The maximum level of the mean secondary flow was found to be approximately 1.5% of the bulk axial velocity.

Seale (1979) investigated mixing between the parallel sub-channels of ducts simulating smooth rod bundles. The geometry investigated is shown in Figure 2.2, which

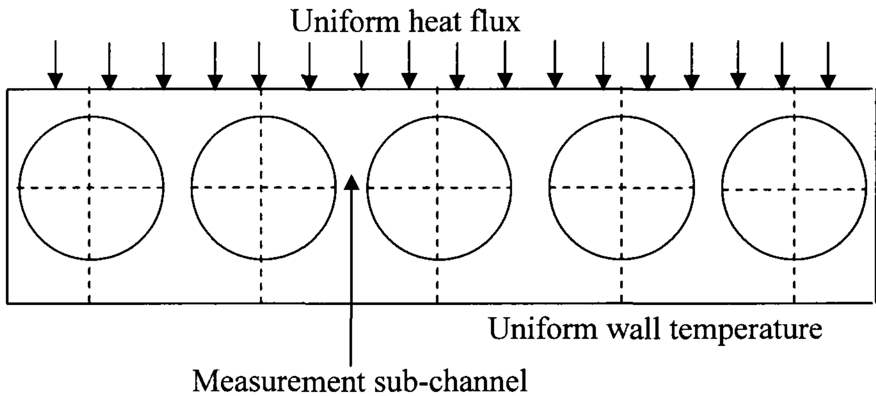

Figure 2.2 Cross section of the investigated rod bundle geometry (Seale, 1979).

comprised of regularly spaced, single row of rods enclosed by a long horizontally mounted rectangular duct. Detailed measurements were made over a range of Reynolds numbers and in three configurations simulating pitch-to-diameter ratios of 1.1, 1.375 and 1.833. The results of the experimental study showed that the effective diffusivities through the gap are strongly anisotropic. The degree of anisotropy increases as the gap width is reduced. The maximum anisotropy factor was found to be around 28 which is higher by almost a factor of 15 when compared to the anisotropy factor of a pipe or rectangular duct flow. This suggests that the flow structure in rod bundle geometry for small pitch-to-diameter ratios is very different from standard pipe or rectangular duct flows. Seale (1981) looked into the effect of sub-channel shape on heat transfer in rod bundles and found that the strong influence of sub-channel shape is a direct consequence of anisotropic effective diffusivities. Seale (1982) provided detailed measurements of the mean axial-velocity distribution and Reynolds stresses using hot wire technique on a duct simulating two sub-channels of a rod array at a pitch-to-diameter ratio of 1.20. The maximum secondary flow velocities, attained by the cells circulating in the square corners of the duct, were 1.5% of the bulk axial velocity.

The group that worked in Germany with Rehme and Meyer on sub-channel flows have looked extensively into the structure of turbulent flow through rod bundles. Rehme (1978) investigated turbulent flow in a duct for a wall sub-channel consisting of a single row of four rods between two flat walls. The pitch-to-diameter ratio of rods equaled the wall-to-diameter ratio and was 1.07, with the Reynolds number of investigation as 87,000. The rotated hot wire technique was used to measure the Reynolds stresses. The radial eddy diffusivity was found to be almost independent of the circumferential position and had higher values compared to the circular tube data. The circumferential eddy viscosity was found to depend strongly on the position in the cross section and reached very high values in the gaps. The circumferential eddy viscosity was higher by a factor of 260 compared with the maximum value of the radial eddy viscosity in a circular tube. Thus, it was concluded that the momentum transport in rod bundles is highly anisotropic which confirmed the previous findings. The anisotropy factors showed a strong dependence on the local position both in the direction normal and parallel to the wall. With the same geometry as mentioned above, Rehme (1980) investigated the flow structure for a corner sub-channel and found similar results to the wall sub-channel. A series of investigations (Rehme, 1982; Rehme 1989; Wu and Rehme, 1990) were carried out to study the influence of geometrical asymmetry on the structure of turbulence in wall sub-channels of rod bundles. The flow structure in rod bundles was found to be quite different from axisymmetric pipe flow. The axial and azimuthal intensities were found to have large values in the gap region between the rods, and the rod and channel wall. For small pitch-to-diameter and wall-to-diameter ratios, the turbulence intensities were found to increase from the wall to gap region and were much larger compared to pipe flow data. This implies a source that is not associated with the normal wall generation mechanism. From the distribution of the axial and azimuthal turbulence intensities, it was concluded that a relatively stronger transport of momentum through the gaps between the rods exists for an asymmetrical geometry compared to symmetrical one. The increased levels of turbulence, both for the axial and azimuthal intensities, only depend on the relative gap size and the flow Reynolds number.

Hooper and Rehme (1984), and Rehme (1987) carried out structural analysis of turbulent flow to understand the flow mechanism responsible for the generation of increasingly high turbulence intensities in the open rod gap, as the rod spacing or wall distance is reduced. Two different array geometries were considered: one was a rectangular cross-section duct containing four parallel rods which was used by Rehme in the past investigations, and second was a test section containing six rods set in a regular square-pitch array to represent the interior flow region of a large array (Hooper, 1980). Using the single point auto and cross-correlation, and two point spatial cross-correlation measurements the presence of an energetic large-scale and almost periodic momentum exchange process through the gaps between the rods was confirmed. The axial and transverse (directed through the gap) turbulent velocity components were found to be significantly correlated for a considerable distance from the rod gap. An energetic and almost periodic azimuthal turbulent velocity directed through the gap governs the transport processes. The cyclic momentum exchange process by a pulsating flow is the reason for increased levels of axial and azimuthal turbulence intensities in the open gap areas of rod bundle flow. Similar structural analysis of turbulent flow through closely spaced rod bundle geometries have been investigated by Moller (1991), Moller (1992), Rehme (1992), Wu and Trupp (1993), Wu and Trupp (1994), Wu (1995). The general conclusion from these investigations is that turbulent transport through the gap regions is dominated by non-gradient type macroscopic flow process which is responsible for enhanced thermal mixing between adjacent sub-channels.

Meyer (1994) investigated fully developed turbulent air flow in a heated 37 rod bundle arranged in triangular array in a hexagonal symmetric channel. The pitch-to-diameter ratio in this study was 1.12. Measurements were taken for the turbulent velocity and temperature fields in a central channel next to the central rod in two sub-channels under isothermal and non-isothermal conditions. These measurements of turbulence in heated rod bundles were performed for the very first time. The differences in the measured turbulent quantities between the unheated case and the heated case were negligible. Continuing with the work of Meyer (1994), Krauss and Meyer (1996) investigated the turbulent field for the wall sub-channel. The axial and azimuthal turbulence intensities were found to be less dependent on the angular position in the central channel than in comparable wall channels. The turbulent heat fluxes in axial and azimuthal directions were higher for the wall channel than in the central channel. The anisotropic factor was found to be very large for the case of the wall channel. Krauss and Meyer (1998) used the same geometry as Meyer (1994) and focused on the central channel with a pitch-to-diameter ratio of 1.06. It was found that in the region of maximum extent of the central channel with pitch-to-diameter ratio of 1.12, the turbulent kinetic energy and the turbulent temperature fluctuations were similar to the results obtained in a pipe. Close to the rod gap, the distributions deviate from that in pipe flow, which becomes more significant at pitch-to-diameter ratio of 1.06.

A summary of some of the important experimental investigations is provided in Table 2.1. In conclusion, it can be said that flow in tightly packed rod bundle geometries forming sub-channel arrangement present inherent differences as compared to pipe flows or regular duct flows. A high degree of anisotropy is present in sub-channel flows as compared to the fundamental flows. The turbulent transport of mass, momentum and energy through the gap region in rod bundle geometries, is primarily governed by a non-gradient type transport process. Macroscopic flow pulsations in the form of coherent structures are the cause of high turbulence intensities and kinetic energy in the small gap regions of rod bundle geometries.

2.3 Structure of turbulence in rod bundles

It is very important to have a detailed knowledge of the turbulent flow field structure in small gap regions of closely spaced rod bundle geometry, so as to correctly identify the governing mechanism for sub-channel mixing and provide a guideline for an appropriate numerical modeling methodology.

Table 2.1 Table of experimental investigations

Investigators	Sub-channel geometry (P/D or W/D)	Working fluid	Reynolds number	Available data
Rowe et al. (1974)	Square array (1.125 and 1.25)	Water	50,000-200,000	Reynolds stress
Aly et al. (1978)	Triangular array	Air	53,000-107,000	Reynolds stress Wall shear Secondary flow
Rehme (1978)	Wall sub-channel (1.07)	Air	87,000	Reynolds stress Wall shear
Seale (1979)	Wall sub-channel (1.1-1.833)	Air	30,000-300,000	Thermal mixing
Rehme (1980)	Wall and Corner sub-channels (1.1-1.4)	Air	90,000-200,000	Reynolds stress Eddy viscosity Wall shear
Hooper (1980)	Square array (1.107-1.194)	Air	48,400	Reynolds stress
Seale (1982)	Wall sub-channel (1.2)	Air	200,000	Reynolds stress Secondary flow
Renksizbulut and Hadaller (1986)	Square array (1.15)	Water	500,000	Reynolds stress Secondary flow
Rehme (1989)	Wall sub-channel (1.026-1.4)	Air	61,100-119,000	Full Reynolds stress tensor
Wu and Trupp (1993)	N/A	Air	60,000-70,000	Reynolds stress Wall shear
Krauss and Meyer (1996)	Wall sub-channel (1.12)	Air	70,000	Reynolds stress

2.3.1 Secondary flows

The secondary flows observed in rod bundle geometry arise due to the anisotropy in the Reynolds stresses and are therefore known as secondary flows of Prandtl's second kind. Secondary flows in tightly packed rod bundle geometries have proved to be very difficult to measure and some of the earliest attempts have had mixed success (Trupp and Azad, 1975; Carajilescov and Todreas, 1976). Seale (1979) measured secondary flows in a duct simulating rod bundle arrangement. Seale (1979, 1982), from the experimental and numerical investigations in a parallel sub-channel duct, concluded that secondary flows are insignificant for the high mixing rates observed experimentally. Vonka (1988) reported experimental data on secondary flows in a central sub-channel of a triangular array. It was found that the magnitude of the secondary flow velocity is less than 0.1% of the axial velocity. The general conclusion is that secondary flows in rod bundle geometries are very small. Further, they do not contribute significantly to the mixing between sub-channels of the rod bundles for small gap-to-diameter ratio, since secondary flow vortices are expected to move within the elementary cells of the sub-channels and are therefore not the reason for high mixing rates observed in sub-channel geometries with a small gap region.

2.3.2 Turbulence intensity, eddy diffusivity and anisotropy

For small pitch-to-diameter and wall-to-diameter ratios (small gap sizes), turbulent flow structure through rod bundles differs significantly in comparison to simple channels like circular tubes and parallel plates. The axial and azimuthal turbulent intensities tend to reach very high values near the open gap regions, and increase with decreasing gap width. In the gap regions, the intensities increase with increasing distance from the wall, which is the most striking feature for small gap rod bundle flows. These high intensities are neither produced by wall turbulence nor by the transport of secondary flows (Rehme, 1978). Rehme (1989) investigated the change of the maximum axial and circumferential turbulence intensity with pitch-to-diameter ratio (P/D) and wall-to-diameter ratio (W/D). It was found that the axial and azimuthal turbulence intensity increased with decreasing P/D and W/D ratios, near rod-to-rod and rod-to-wall gaps respectively. The measurements yielded the following correlations for the axial and azimuthal turbulence intensities respectively:

$$\frac{u'}{u_\tau} = 0.6 + 0.307\left(\frac{W}{D} - 1\right)^{-\frac{2}{3}} \tag{2.1}$$

$$\frac{w'}{u_\tau} = 0.6 + 0.0425\left(\frac{W}{D} - 1\right)^{-\frac{4}{3}} \tag{2.2}$$

Similar trends in the variation of the turbulence intensities with P/D or W/D ratio were found by Rowe et al. (1974), Hooper and Rehme (1984), Wu and Trupp (1993). The reason for the high turbulence intensities in the near gap region was investigated by Hooper and Rehme (1984). It was found that the auto and cross-correlation functions were periodic in nature. This periodic behavior results in high momentum exchange between sub-channels, which is a result of the flow pulsation phenomena.

The turbulent eddy diffusivity of momentum or heat is used to describe the anisotropic turbulent properties in a rod bundle geometry. From the experiments of Rehme (1978), it was observed that the maximum circumferential eddy diffusivity of momentum was higher than the maximum radial eddy diffusivity by a factor of almost 100. Rehme (1992) showed that the circumferential turbulent eddy diffusivity of momentum, measured near the gaps, strongly increases with decreasing pitch-to-diameter ratio. The radial eddy diffusivity is independent of the angular position in a rod bundle geometry. It increases from the rod wall surface similar to the case of a circular pipe. Away from the rod wall, the eddy diffusivity deviates from the circular pipe case, with a value of two times higher. Seale (1979) presented results on the anisotropic factor at the gap of a wall sub-channel. Circumferential eddy diffusivities were found to be much larger than the radial ones, which was also observed by Rehme (1978). It was also found that the anisotropy factor increases with decreasing pitch-to-diameter ratio. The anisotropy factor ranged from 3 ~ 30 with a pitch-to-diameter ratio of 1.1-1.8. Krauss and Meyer (1996) provided eddy diffusivities of heat in a wall sub-channel of a heated 37 rod bundle, with P/D = 1.12 and W/D = 1.06. It was found that the maximum circumferential eddy diffusivity of heat was higher than the maximum radial eddy diffusivity of heat by a factor of almost 100. Thus, the same anisotropy factors were obtained for both heat and momentum.

2.3.3 Macroscopic periodic flow pulsations

Experimental investigations have conclusively shown that cross sub-channel mixing is greatly enhanced by transport due to large-scale, quasi-periodic pulsations, which form across the gap. Macroscopic flow pulsations were first observed by Van der Ros and Bogaardt (1970), and Rowe et al. (1974). Rowe et al's. (1974) study showed a periodic pattern in the autocorrelation functions, which indicated a dominant frequency of turbulence. It was concluded that macroscopic flow process exists near the rod-to-rod gap. Measurements made by Hooper and Rehme (1984) in a wall bounded array and a square pitch rod cluster indicated that the axial and circumferential turbulent velocities clearly have a periodic behaviour and their peak values were about 25% of the mean axial velocity. The high magnitude of the circumferential Reynolds shear stress is also associated with the large-scale structure of the circumferential turbulent velocity. The periodic pattern in the auto and cross-correlation functions yielded a peak frequency of 92 Hz. The long length scales of the axial and circumferential turbulent velocities, relative to the gap width, emphasize the anisotropy of the turbulent transport process at the rod gap. The axial and circumferential turbulent velocities are associated with a large-scale structure. It was concluded from the study that the periodic large-scale structure in the circumferential turbulent velocity causes periodic momentum exchange through the rod-to-rod gap at low frequencies.

Möller (1991, 1992) performed a systematic study to investigate the macroscopic flow pulsations in rod bundle geometries with different aspect ratios. Hot wires and microphones were used for the measurements of velocity and wall pressure fluctuations. The data were evaluated to obtain spectra as well as auto-correlations and cross-correlations. Peaks at characteristic frequencies in the power spectra of the turbulent velocity fluctuations in the axial direction and the direction parallel to the walls were observed. The frequency varied linearly with the Reynolds number. The characteristic frequency and the maximum value of the power spectra increase with decreasing gap width. Moller showed that the non-dimensional frequency parameter, Strouhal number

($Str = \dfrac{fD}{u_\tau}$), defined with the characteristic frequency f, the rod diameter D, and the friction velocity u_τ in the gap between the rods or between the rods and channel walls, only depends on the relative gap width. Moller also proposed a phenomenological model to describe the formation of the large eddies near the gaps by adopting the concept of coherent structures (Hussain, 1983) in the gap regions of the rod bundles. The large-scale eddies are thought to move almost periodically through the gaps of the rod bundles at the characteristic frequency. Meyer and Rehme (1994) showed the presence of large-scale quasi-periodic flow oscillations using detailed measurements of mean axial velocity and Reynolds stresses in compound flow channels consisting of either two rectangular channels connected by a gap or one rectangular channel with a slot in one wall. The gap between the channels and the slot connected to one channel, strongly affected the turbulent flow features in the vicinity of the gap or the slot. The turbulence intensities and the Reynolds shear stresses were found to have very high values near the vicinity of the gap or the slot than anywhere else in the channel. Strong peaks in the power density spectra of the axial and transverse velocity components were observed, and the peak frequency varied linearly with the Reynolds number.

Guellouz and Tavoularis (2000) performed a comprehensive study of the structure of turbulent flow in a rectangular channel containing a cylindrical rod, focusing on the gap between the rod and the plane wall. Reynolds-averaged and phase-averaged measurements were performed to characterize the features of the large-scale structures. The presence of large-scale, quasi-periodic structures in the vicinity of the gap, for a range of gap widths was demonstrated through flow visualization, spectral analysis and space-time correlation measurements. The measurements identified the large-scale structures as being a street of three-dimensional, counter rotating vortices, whose convection speed and stream-wise spacing were found to be functions of the gap width. Phase-averaged measurements identified the structures as coherent vortical structures with instantaneous phase-correlated vorticity. More recently, Gosset and Tavoularis (2006) investigated the threshold Reynolds number at which the quasi-periodic flow pulsations arise in a sub-channel geometry. Experiments were conducted in the laminar flow regime on the geometry similar to the study of Guellouz and Tavoularis (2000). This was perhaps the first time, when the laminar flow instability in a channel with an internal boundary was investigated. The experimental observations revealed flow instability in the form of weak pulsations, in the gap region between the rod and the channel wall. It was found that the instability occurs at a critical Reynolds number (laminar regime), which increases as the gap size reduces. At this critical Reynolds number, the parallel flow in a rectangular channel containing a cylindrical rod becomes unstable and pulsates transversely across the narrow gap. With the increase in the Reynolds number, the intensity of the pulsations increased, and quasi-periodic laminar vortices are formed alternately on either side of the gap. With transition of the flow into the turbulent regime, the quasi-periodic nature of the stream-wise vortices are preserved. For a given geometry, the Strouhal number was found to increase with Reynolds number in the laminar flow regime, but then settled down around a constant in fully turbulent flow conditions.

From the various turbulent structural investigations in sub-channel geometries, a general consensus is reached. The large-scale coherent structures are found to exist in any longitudinal slot or groove in a wall or a connecting gap between two flow channels, provided certain geometrical parameters and flow conditions are satisfied (Meyer and Rehme, 1994; Gosset and Tavoularis, 2006). These structures, which are responsible for the flow pulsations are generated in both isothermal and non-isothermal flow conditions. The peaks in the power spectra are found to be highest for the fluctuating velocity component parallel to the wall directly in the gaps. With decreasing gap width, the peak becomes narrower in the frequency range and reaches a higher maximum value, thus the average velocity through the gap increases with decreasing gap width. For higher gap width, the peak broadens and the maximum value decreases. The large eddies move almost periodically through the gaps of rod bundles at the characteristic frequency. The cross-correlation measurements have shown that the macroscopic flow pulsation by the large eddies covers almost the full cross-section of the sub-channel. These large-scale structures are the reason for the high values of high axial and azimuthal turbulence intensities observed in the gap region of rod bundle geometries, and cause significant anisotropy in the eddy viscosity. The periodic flow pulsations across the gaps in rod bundles are the main reason for high mixing rates between sub-channels in rod bundle geometries.

2.4 Empirical modeling of turbulent interchange mixing

Empirical modeling or constitutive modeling technique is used in sub-channel analysis code like ASSERT - PV, where constitutive relations are used in order to predict the temperature distribution inside the rod bundle cluster. Turbulent interchange mixing between sub-channels is modeled using the sub-channel approach. In this approach, the average enthalpy or temperature over a sub-channel is used to determine the mixing rate. The transverse mass flow rate per unit length, called the mixing rate, between two sub-channels, i and j, is given by:

$$w_{ij}^{'} = \rho w_{eff} c \tag{2.3}$$

where w_{eff} is the effective mixing velocity and c is the gap width. This mass flow rate is a fictitious property, equal to the real mass transfer which would be needed to carry the observed amount of heat from one sub-channel to the other. The heat transported through the gap per unit length by the effective mixing velocity is:

$$q_{ij} = \rho c_p w_{eff} c \left(T_i - T_j\right) \tag{2.4}$$

where T_i and T_j are the bulk temperatures of sub-channels, i and j. The transported heat between the sub-channels per unit axial length is modeled as a diffusive process, using the turbulent eddy diffusivity. The heat transfer per unit length due to the process of turbulent diffusion is given as:

$$q_{ij} = \rho c_p \varepsilon_t c \frac{\left(T_i - T_j\right)}{z_{ij}} \tag{2.5}$$

where ε_t is the thermal eddy diffusivity and z_{ij} is the effective distance over which mixing takes place. Combining equations (2.4) and (2.5), the mixing rate is written as:

$$\frac{w_{ij}^{'}}{\mu} = \left(\frac{c}{d}\right)\left(\frac{d}{z_{ij}}\right)\left(\frac{\varepsilon_t}{\nu}\right) = \left(\frac{c}{d}\right)\left(\lambda_{ij}\right)\left(f\left(\mathrm{Re}\right)\right) \tag{2.6}$$

where d is the characteristic diameter of the rod bundle, $\lambda_{ij}(=d/z_{ij})$ is a function of the sub-channel geometry, and ε_t/ν is a function of the Reynolds number only (typically determined from friction factor correlations for pipe flow). Empirical correlations based on experimental data have been developed for the parameter λ_{ij}, which is a function of the pitch-to-diameter ratio. Different correlations have been developed for the three sub-channel pair configurations, which have mainly come from experimental studies. Eiff and Lightstone (1997) have provided a detailed review of the various correlations.

Rehme (1992) and some other researchers have used a different notation for representing the mixing rate by introducing a 'mixing factor' denoted by Y. Equation (2.5) can also be expressed in the form:

$$q_{ij} = \rho c_p \bar{\varepsilon} c Y \frac{\left(T_i - T_j\right)}{\delta_{ij}} \tag{2.7}$$

where $\bar{\varepsilon}$ is a reference eddy viscosity which is often taken as the eddy viscosity at the centre of a circular tube and δ_{ij} is the mixing distance which is assumed to be the centroid distance between the adjacent sub-channels. The mixing factor accounts for how much higher the actual mean heat eddy diffusivity is in comparison with the reference eddy viscosity and also includes a correction for the linear temperature gradient approximation. A comparison between equations (2.4) and (2.7) gives:

$$Y = \frac{w_{eff}\delta_{ij}}{\bar{\varepsilon}} \tag{2.8}$$

Correlations for the mixing factor as a function of the gap-to-diameter ratio based on experimental data has been obtained by Moller (1992) and Rehme (1992), taking into account the effect of the flow pulsation phenomena. Jeong et al. (2007) proposed a mixing factor correlation based on the eddy diffusivity of energy, which takes into account the degree of turbulent mixing of various fluids having different Prandtl numbers. This correlation is applicable for fluids with low Prandtl numbers such as liquid metals. It was found that the mixing factor correlates better to experimental data if the mixing factor correlation is made to depend on the geometrical parameter δ_{ij} / D_h (δ_{ij} is the distance between the centre of the sub-channels and D_h is the hydraulic diameter of the sub-channel) rather than the S/D ratio (S is the gap size). This is because the scatter in the mixing factor data is quite large when it is based on the S/D ratio, especially when the S/D ratio is small. The correlation is applicable for both square and triangular array rod bundles.

A non-dimensional number known as the gap Stanton number is used to characterize the effect of the gap spacing on sub-channel thermal mixing. Mathematically, the gap Stanton number is written as

$$St_g = \frac{q_{ij}}{c\left(T_i - T_j\right)\rho c_p U_b} \tag{2.9}$$

where q_{ij} is the heat transfer per unit length between the sub-channels and U_b is the bulk axial velocity. Equation (2.9) can also be reformulated into the following form:

$$St_g = \frac{Nu_g}{\mathrm{Re}_g \Pr} \tag{2.10}$$

where Nu_g and Re_g are the Nusselt and Reynolds number based on the gap spacing, and Pr is the Prandtl number of the fluid. Thus, the gap Stanton number is a modified form of the Nusselt number. Physical interpretation of gap Stanton number is given as:

$$St_g = \frac{Gap\,conductance}{Axial\,condutance} \tag{2.11}$$

Experimental investigations on sub-channel mixing have shown that the gap Stanton number increases with the decrease in gap width, indicating increased mixing levels.

Kim and Park (1997) derived the scale relations of the anisotropic factor and the mixing rate based on the flow pulsation phenomena, by assuming a hypothetical flow path which circulates with the frequency of the flow pulsation. The anisotropy in eddy viscosity was correlated with geometrical factors and the Strouhal number of the pulsating flow. The scale relation for the mixing factor agreed well with the calculated experimental data of Rehme (1992). Kim and Park (1998) used the anisotropic factor developed by Kim and Park (1997) in a two equation turbulence model and found that variation of the mixing factor with gap-to-diameter ratio can be correctly predicted. The mixing factor of Rehme (1992) was also favorably reproduced. Kim and Chung (2001) argued that the scale relation for mixing factor developed by Kim and Park (1997) is not valid for low Prandtl number fluids (Pr<<1). They developed a correlation for the mixing factor that accounts for the effects of molecular motion. The mixing factor correlation can correctly predict the trend in gap Stanton number with pitch-to-diameter ratio for low Prandtl number fluids. In general, the estimated gap Stanton number is closer to the experimental data than the Kim and Park (1997) correlation. However, the predictions are still outside the experimental error for low pitch-to-diameter ratio.

Reynolds number dependence of the turbulent mixing in fuel bundle geometries have been investigated by researchers in the past. Recently, Silin and Juanicó (2006) performed an experimental study on a triangular array bundle with a P/D ratio of 1.2, in a low pressure water loop, at Reynolds numbers between 1.4×10^3 and 1.3×10^5. The sub-channel thermal mixing was obtained with high accuracy using an improved thermal tracing technique. This allowed for a more precise determination of the influence of Reynolds number on mixing. The gap Stanton number was found to have a Reynolds number dependence of the form $St_g = CRe^m$. The exponent 'm' was found to have a value of -0.1 ± 0.005, for Reynolds number greater than 2000, in accordance with previous findings. It was reported for the first time on rod bundle geometries that for Reynolds numbers smaller than 2000, the mixing rate rapidly increases. The Stanton number was found to be five times higher for Reynolds number 1400 than for 2000.

It was previously mentioned in this section that constitutive relations are required for sub-channel analysis codes, and that these relations have been mainly derived from experimental studies. Experimental studies have the limitation that the whole spectrum of parameters cannot be tested and hence the correlations that are developed have shortcomings. In this regard, numerical investigations using CFD play a very critical role, where the studies are not limited to a range of parameters or conditions. It is expected that through numerical studies, physics based constitutive models can be developed, which can be directly incorporated into the industrial sub-channel analysis codes. The physics based constitutive models, derived from the fundamental mechanisms in the sub-channel geometries can aid in the more accurate prediction of thermal mixing in sub-channel analysis codes. Thus, as a result of increased computational power and enhanced numerical modeling methodologies, numerical based investigations have gained immense popularity in the nuclear community over the last decade or so.

2.5 CFD based numerical investigations

The numerical investigations that use steady RANS methods to predict the flow field structure, temperature field and inter sub-channel thermal mixing in rod bundle geometries with small pitch-to-diameter and wall-to-diameter ratios have not been successful. The earlier approaches based on the one-equation turbulence model with an ad-hoc specification of turbulence length scale, looked into isothermal flows. These investigations could not provide any insight into the complicated flow field structure in rod bundle geometries. Rock and Lightstone (2001) assessed the applicability of the k-ε model by applying the model to Seale's experiment (1979). They found that the k-ε model favorably predicted the radial component of the turbulent eddy viscosity, but under predicted the azimuthal component. Thus, the k-ε model failed to reproduce the experimental turbulent mixing. To account for turbulence anisotropy of the flow, Suh and Lightstone (2004) used the Reynolds Stress Transport Model of Launder, Reece, and Rodi (LRR) (1975). Isotropic eddy diffusivity model was used to characterize the turbulent heat flux. They found that the model was able to predict the secondary flows, however the inter sub-channel mixing was significantly under predicted. It was also found that the model could not predict the trend in the change of gap Stanton number with pitch-

Table 2.2 Table of numerical investigations based on steady RANS approaches.

Investigators	Momentum equation	Turbulence model	Anisotropic factor	Secondary flow
Carajilescov and Todreas (1976)	Vorticity-stream	One equation	Not used	Launder-Ying's model (1973)
Aly et al. (1978)	Vorticity-stream	One equation	Not used	Launder-Ying's model (1973)
Trupp and Aly (1979)	Vorticity-stream	One equation	Not used	Launder-Ying's model (1973)
Bartzis and Todreas (1979)	Vorticity-stream	One equation	Determined by length scale	Launder-Ying's model (1973)
Seale (1979)	Vorticity-stream	Two equation	Empirical correlation	Launder-Ying's model (1973)
Seale (1982)	Vorticity-stream	Two equation	Empirical correlation	Launder-Ying's model (1973)
Rapley and Gosman (1986)	Navier-Stokes	Two equation	Not used	Launder-Ying's model (1973)
Yang and Chieng (1987)	Navier-Stokes	Two equation	Empirical correlation	Launder-Ying's model (1973)
Kim and Park (1998)	Vorticity-stream	Two equation	Empirical correlation	Launder-Ying's model (1973)
Rock and Lightstone (2001)	Navier-Stokes	Two equation	Not used	No additional formulation required
Suh and Lightstone (2004)	Navier-Stokes	Reynolds stress transport equation	Not used	No additional formulation required

to-diameter ratio. They also assessed the applicability of anisotropic turbulent heat flux model and found that the application of the anisotropic turbulence model does not help obtain the anisotropy of the eddy diffusivity of heat near the rod-to-gap region observed in the experiments. Their study showed that macroscopic flow pulsations in the form of large-scale structures contribute significantly to sub-channel mixing as pitch-to-diameter ratio is reduced. A summary of the steady RANS approaches used for the study of sub-channel mixing problem is provided in Table 2.2.

Biemüller et al. (1996) used LES simulations to predict the flow pulsations occurring in the gap connecting two rectangular channels. To reduce computational effort, the domain represented only a portion of the actual channels with periodic boundary conditions applied in the stream-wise and span-wise directions. A coarse grid was used in the gap region and wall functions were applied to treat the no-slip walls. Because of the inherent differences between the simulated and the experimental geometries, quantitative agreement between predictions and experimental measurement was not obtained. The LES simulations were, however, found to be very promising since they were able to capture the large-scale flow pulsations in the gap region.

Tavoularis et al. (2002) used an unsteady RANS (URANS) approach to simulate an isothermal flow in a channel containing a single rod, with a gap between the rod wall and the base of the channel wall. The gap-to-diameter ratio was 0.1. They used the RNG $k-\varepsilon$ model to predict the turbulence in conjunction with a time step that was small relative to the timescales of the large scale structures. The goal of the work was to see if the flow pulsations (which appear as coherent structures) could be predicted by a URANS model. Interestingly, they found that such structures were predicted during the transient phase of the simulation. Eventually, the flow became steady and the structures washed out. They also simulated the problem using LES with a Smagorinsky subgrid-scale model. The LES simulations were not successful in capturing the coherent structures since the grid was too coarse and a significant portion of the energy containing eddies were filtered out. Predictions were compared to experiments and it was seen that the $k-\varepsilon$ results significantly over-predicted the flow oscillation timescale and the stream-wise spacing. The LES simulation under-predicted the timescale and over-predicted the spacing. Chang and Tavoularis (2005) used the URANS approach with a Reynolds stress model to simulate isothermal axial flow in a rectangular channel containing a cylindrical rod. The unsteadiness in the flow field due to the flow pulsations was reproduced (quasi-periodic character of the time history of the span-wise velocity in the centre of the gap) and coherent structure near the narrow gap region was identified. It was observed from the study that coherent components were significant in the gap region and accounted for 60% of the total kinetic energy. Chang and Tavoularis (2007) extended the project by modeling the problem for a rod bundle geometry using the Reynolds stress model (RSM). Again, by running an unsteady simulation with an appropriate time step, the presence of coherent structures was predicted.

Ikeno and Kajishima (2007) performed an LES study of turbulence in a rod bundle geometry without heat transfer. The computational domain was comprised of four sub-channels which were large enough to capture the large-scale structures. The LES study was performed for three different values of P/D ratio, where P is the distance between rod centroids and D is rod diameter. The predictions indicated that the flow was not confined to a sub-channel, which was a direct consequence of the flow pulsations through the rod gaps between sub-channels. The intensity of the gap flow increased as P/D decreased. The turbulence intensity profile in the rod gap suggested that the flow pulsation was caused by the turbulence energy transferred from the main flow to the wall tangential direction. Merzari et al. (2008) performed a detailed CFD study on assessing the applicability of unsteady turbulence modeling approaches to capture the flow pulsations in sub-channel geometries. Two different sub-channel geometries were investigated. LES was used to study flow in a rectangular duct connected by a narrow gap. The snapshots of the flow field produced from the LES results correctly revealed the presence of the flow pulsations. The predicted average frequency and wavelength associated with the pulsating flow was found to be in agreement with the experimental values (Lexmond et al., 2005). Proper orthonormal decomposition (POD) was used to analyze the time varying solution. The flow field was decomposed into a series of modes, and the primary modes that are responsible for mixing were found to have an oscillatory pattern. URANS simulation was also carried out to investigate the flow in a tight-lattice rod bundle, where coherent turbulent structures are present in the narrow gap region (Krauss and Meyer, 1998). Both, the isotropic and the anisotropic versions of the $k-\varepsilon$ models were tested. It was found from the study, that the presence of flow pulsations in experimental conditions, warrants the necessity of an unsteady simulation for accurate prediction of averaged statistics. The anisotropic version of the $k-\varepsilon$ model gave superior results as compared to the isotropic version, and compared quite well with the experimental data (Krauss and Meyer, 1998) for averaged quantities such as the turbulence kinetic energy, wall shear stress and the stream-wise velocity. The amplitude and frequency of the oscillations were correctly predicted, whereas the wavelength of the oscillations were significantly larger than the experimental value.

Home et al. (2009) have recently assessed the applicability of predicting the flow pulsation dynamics using one equation turbulence model in the URANS framework. The specific turbulence model was based on the Spalart - Allmaras approach (Spalart and Allmaras, 1992). The twin rectangular sub-channel geometry was investigated and validated against the experimental data of Meyer and Rehme (1994). This modeling approach could correctly predict the characteristics of the flow pulsations, in terms of the quasi-periodic nature of the velocity time traces, frequency and wavelength of the flow pulsations. The numerical results compared reasonably well with the experiments. The important result that transpired from the work was that this modeling approach is computationally very cost effective, easy to implement and therefore holds lot of promise for simulation of flows in more realistic sub-channel geometries formed by rod bundle arrangements.

It is very clear from the aforementioned reviews in this section, that unsteady turbulence modeling approaches are required for accurate prediction of the dynamics of the flow pulsations in sub-channel geometries. In this regard, both URANS and LES approaches have been successful at predicting flow pulsations. URANS approaches are computationally cost effective, however, LES allows for more detailed information to be captured. LES is thus, suitable for providing fundamental insights of the complex flow and hence can be used for subsequent development of physics based constitutive models for sub-channel flows. However, computational cost is a major issue for LES especially for fully wall bounded flows that occur in sub-channel flows for rod bundle geometries (Home et al., 2009). In fact, in one of the recent investigations by Merzari et al. (2009) on a sub-channel arrangement at a nominal Reynolds number, the LES study and sophisticated post analysis took three months to complete. The CPU time required to simulate a complete rod bundle arrangement at the actual reactor flow conditions would be significantly increased. This leads to an important question as to what could be an appropriate modeling approach for sub-channel flows in rod bundle geometries, which would correctly predict the underlying physics while remaining computationally cost effective. In this regard, the hybrid URANS-LES methodology which has the ingredients of both URANS and LES, combined into one approach, could be a suitable choice (Home et al., 2009). For sub-channel flows, the region of interest are the gaps where large-scale coherent vortical structures are formed, which induce the flow pulsations. The hybrid URANS-LES approach can be made to work in a way such that the LES characteristics are used in the gap region to resolve the effects of the large-scale structures, while in the near-wall region (where the problem of LES lies in terms of cost effectiveness) the URANS model is applied (Home et al., 2009). To the author's knowledge, the hybrid URANS-LES approach has never been used to investigate flows in sub-channel geometries. Thus, it is proposed in the current research work that the applicability of the hybrid URANS-LES approach be fully tested for sub-channel flows. In this context, the twin rectangular sub-channel geometry on which extensive experiments were conducted by Meyer and Rehme (1994) provides an ideal test case on which the hybrid URANS-LES approach can be applied. It is of thus, great interest to see the capability of the model to shed light on the important physics of the flow pulsation phenomena.

2.6 Summary

In this chapter, a detailed literature review on sub-channel flows in different geometries was presented. Through past and current research work, it was shown that macroscopic flow pulsations in the form of large-scale coherent vortical structures are responsible for enhanced mixing in sub-channel geometries with small gap spacing. A summary of the key investigations which have shed light on the macroscopic flow pulsations in sub-channel geometries is provided in Table 2.3. The current state of the art in numerical approaches was also presented. It is proposed that the hybrid URANS-LES approach, will be used to investigate flow in a twin rectangular sub-channel geometry. In the next chapter, the philosophy of the hybrid URANS-LES approach along with the related studies on this modeling methodology is presented.

Table 2.3 Summary of investigations on flow pulsations in sub-channel geometries.

Investigators	Approach	Domain	Working Fluid	Reynolds number	Methodology	Findings
Moller (1991)	Experimental	Channel containing four rods	Air	25,000-85,000	Anemometers, hot wires, microphones	Strouhal number depends only on the gap width
Meyer and Rehme (1994)	Experimental	Twin rectangular sub-channel geometry	Air	100,000-300,000	Hot-wire anemometry (x-wire probe), Preston tubes	Large-scale coherent structures are found to exist in any axial slot or gap between two flow channels
Guellouz and Tavoularis (2000)	Experimental	Cylindrical rod in a rectangular duct	Air	140,000	Flow visualization/ space time correlation measurements	Coherent vortical structures were identified
Chang and Tavoularis (2005)	Numerical	Cylindrical rod in a rectangular duct	Air	108,000	URANS	60% of the total kinetic energy in the gap is accounted by coherent motions
Gosset and Tavoularis (2006)	Experimental	Cylindrical rod in a rectangular duct	Water	250-2300	Dye streak motion was used to characterize the flow pulsations for different gap sizes	Critical Reynolds number for the flow pulsations to arise, was identified to be in the laminar regime
Ikeno and Kajishima (2007)	Numerical	Scaled bare rod-bundle	Not provided	3520, 6200, 9130	LES	Flow pulsation has three dimensional structure
Merzari et al. (2008)	Numerical	Rectangular channels connected by a narrow gap/ Scaled rod bundle geometry	Water	2690/ 38754	LES/URANS	POD identified most energetic modes of mixing/ Coherent structures identified

CHAPTER 3

DETACHED EDDY SIMULATION MODELING

3.1 Introduction

LES has had major success in providing information related to momentum transfer for a wide range of flow configurations. LES has been successfully used for predicting the turbulent flow field around bluff bodies, which are dominated by large scale turbulent structures (Spalart, 2000; Davidson and Dahlstöm, 2005). Accurate results are obtained for these flows using LES at a reasonable computational cost (Davidson and Billson, 2006). In contrast, wall bounded flows are a challenge for LES because of the fine grids required in the near-wall region. The near-wall region (viscous sub-layer and the buffer layer) is dominated by turbulent structures or "streaks" (Robinson, 1991) which are comprised of high speed in-rushes and low speed ejections. These structures are responsible for significant turbulence production and need to be resolved in order to obtain accurate results. The resolution required for a well resolved LES in the near-wall region in terms of wall units is approximately 1 (wall-normal direction), 50-150 (stream-wise direction) and 15-40 (span-wise direction) respectively (Davidson and Dahlstöm, 2005; Davidson and Billson, 2006; Robinson, 1991). While the cost of using LES to resolve energy carrying scales of motion away from the wall region does not depend strongly on the Reynolds number itself (Piomelli and Balaras, 2002), if the near-wall region of a boundary layer needs to be resolved, the number of grid points required strongly depends on the Reynolds number. It was estimated (Chapman, 1979), that the number of grid points required to resolve the viscous sublayer is proportional to $Re^{1.8}$, while the resolution required to resolve the outer layer of the boundary layer increases with $Re^{0.4}$. Thus, if the wall layer is completely resolved with LES, the computational costs are staggering and almost comparable to a DNS (Piomelli et al., 2003).

3.2 Wall layer models for LES

Methods based on providing approximate boundary conditions at the wall have been developed to bypass the wall layer so as to perform high Reynolds number LES at a reasonable cost. The wall layer modeling enables one to use a coarse mesh in the near-wall region, with the outer layer being solved using a normal LES approach. This strategy substantially reduces computational effort. A summary of the different wall layer modeling techniques and their key features is provided in Table 3.1. There are two wall layer modeling techniques: equilibrium law and the zonal approach (Piomelli and Balaras, 2002). Equilibrium law is based on the 'law of the wall' approach, where the viscosity affected sublayer is bridged with the outer layer using log-law or power-law based wall functions. The methodology behind this approach is to provide the outer layer flow with the wall stress (viscous stress), which cannot be computed accurately on a coarse LES grid. The wall functions are usually applied some distance away from the wall (with first grid point usually in the logarithmic region). The equilibrium flow based wall stress models in LES were proposed in the early 1970's (Deardorff, 1970; Schumann, 1975).

Table 3.1 Summary of different wall layer modeling techniques.

Method	Near-Wall Treatment	Key Points	Reference
Equilibrium law	Wall functions	Log-law/Power-law functions provide wall shear stress.	Werner and Wengle (1991), Cabot and Moin (1999), Piomelli and Balaras (2002), Temmerman et al. (2003)
Zonal - Two Layer Model	Boundary layer equations are solved	Two separate grids are used that are embedded together.	Piomelli and Balaras (2002)
Zonal - Hybrid RANS/LES	URANS model	Different RANS and SGS models are used. Switching interface plane is predefined.	Piomelli and Balaras (2002), Davidson and Dahlstöm (2005), Temmerman et al. (2005), Davidson and Billson, (2006)
Zonal - DES	URANS model	RANS and SGS models used are the same. Switching is controlled by the grid.	Spalart (2000), Piomelli et al. (2003), Constantinescu et al. (2003), Temmerman et al. (2005),

Detailed review of the various forms of the wall stress models and its application to various flows can be found in (Werner and Wengle, 1991; Cabot and Moin, 1999; Temmerman et al., 2003). Equilibrium laws have had considerable success for simple attached flows but have severe limitations in complex flow configurations like flow in a rotating channel (Balaras et al., 1996). Thus they find limited usage for engineering applications.

Zonal approaches are based on the fact that in the near-wall region a simplified set of equations will be solved or a Reynolds Averaged Navier-Stokes (RANS) approach will be undertaken, while in the outer region of the flow, LES will be solved. There are two kinds of zonal approaches: the two layer model (TLM) and the hybrid RANS-LES based method. In the conventional TLM approach two separate grids are used whereby filtered Navier-Stokes (LES) equations are solved in the core of the flow and boundary layer equations in the wall region. A detailed review of the TLM approach and its success for different flow configurations can be found in (Piomelli and Balaras, 2002). The hybrid RANS-LES method, solves unsteady RANS (URANS) in the near-wall region, and LES in the outer flow. In the URANS region, a low Reynolds number RANS turbulence model is used which is integrated to the wall, whereas in the LES region a SGS model is used. Thus, a RANS type eddy viscosity is present in the URANS region and a SGS eddy viscosity exists in the LES region. In the URANS region, the grid is usually refined in the wall-normal direction, which allows the sharp velocity gradients in the boundary layer to be captured. The no-slip boundary condition is applied at the wall. However, in the wall-parallel directions the mesh is coarse with the mesh size being larger than the local integral length scales, giving large aspect ratio cells in the RANS region. The near-wall small structures are not resolved in the URANS region. In the LES region, the grid resolution requirement is based on resolving the larger turbulent scales in the outer region of the flow, which are related to the boundary layer thickness. One of the fundamental issues surrounding the hybrid RANS-LES formulation is the operation of the RANS model (in the near-wall region) in an unsteady mode. It has been observed from the hybrid simulations that the RANS region produces significant resolved motion which lacks the small scale features. The question that arises is how realistic are the resolved scales in the URANS region, and whether the RANS models which are developed and tuned for steady flows, remain valid in highly unsteady straining (Temmerman et al., 2005). Apart from being a wall modeling approach, hybrid RANS-LES has found its most important use in providing simplified inflow boundary conditions (Hamba, 2003), which is not possible in case of a pure LES.

3.3 Hybrid URANS-LES studies

One of the earliest attempts to use the hybrid RANS-LES formulation was by Baggett (1998) where he used the $\upsilon^2 f$ RANS model (Durbin, 1995) in the near-wall region. Over the years, significant work has been done on using the hybrid RANS-LES approach for many different kinds of flow configuration (Hamba, 2001; Temmerman et al., 2002; Hamba, 2003; Davidson and Peng, 2003; Tucker and Davidson, 2004; Davidson and Dahlstöm, 2005; Temmerman et al., 2005; Davidson and Billson, 2006). One important test case to validate the hybrid RANS-LES method is the fully developed turbulent channel flow problem. Hybrid RANS-LES methods with different RANS and LES models have been tested for channel flow problem at various Reynolds number (Hamba, 2003; Davidson and Dahlstöm, 2005; Temmerman et al., 2005; Davidson and Billson, 2006). Good results have generally been obtained using the hybrid RANS-LES approach, however, a common problem in all hybrid methods arose pertaining to the turbulent scales of motion at the RANS-LES interface. In all the investigations, it was observed that there is a poor prediction of quantities such as the mean velocity profile at the RANS-LES interface, with the velocity gradient being too steep near the interface. This results in the velocity being over predicted in the outer layer of the flow. The URANS region supplies the LES region with an unsteady flow at the interface. However, the unsteady flow that is supplied lacks realistic turbulence characteristics and as a result the resolved shear stress at the interface is poorly predicted. This results in the shift of the velocity profile at the location of the matching plane. The wall shear velocity is under predicted by almost 10%-20% (Temmerman et al., 2005). To alleviate this problem, ad-hoc techniques have been developed to provide the LES region with proper interface conditions which have been successful in reducing the velocity mismatch at the interface plane and has overall improved the performance of the hybrid models (Hamba, 2003; Davidson and Dahlstöm, 2005; Davidson and Billson, 2006).

Similar to the hybrid RANS-LES concept is the DES approach, which was developed as a method to compute massively separated flows. DES is a hybrid approach that combines the solutions of the URANS in the attached boundary layer with LES in the separated regions in which the detached eddies are important. In DES, a single turbulence model is used as a RANS model in the attached regions of the boundary layer and it becomes SGS model in the LES region. The LES region is demarcated from the RANS region through the model used to calculate the turbulence eddy viscosity. It is observed in DES simulations that there is a very smooth transition of the turbulence eddy viscosity from the URANS region to the LES region, which is not observed in all hybrid RANS-LES methods (Hamba, 2003). In the original formulation of the DES, Spalart et al. (1997) used the Spalart and Allmaras (1992) model, a one-equation turbulence model in which a transport equation for the eddy viscosity is solved. This one-equation model is used both as a RANS eddy viscosity model and as a SGS eddy viscosity model in the LES region. Another DES formulation is based on the model proposed by Strelets (2001), where the Shear Stress Transport (SST) model (Menter, 1992) is used. The main advantage of the DES method is that the grid controls the switch over from RANS to the LES region. It is usually the stream-wise or the span-wise grid spacing that determines the switch over. Similar to LES, as the grid and time step is refined in DES, an increased range of turbulent length and time scales are resolved. The location of the RANS-LES interface is controlled by the grid. With grid refinement, the interface moves closer towards the wall, which means that the size of the URANS region diminishes and the LES region increases, hence resulting in increased computational effort. Thus for every problem, there is an optimum grid which is computationally cost effective, as well as, at the same time revealing the essential physics of the problem.

DES has been extensively used with great success in problems involving massive boundary layer separation like aerodynamic flows and flow over bluff bodies (Spalart et al., 1997; Travin et al., 2000; Spalart, 2000; Strelets, 2001; Constantinescu et al., 2003; Kapadia and Roy, 2003; Hamed et al., 2004). DES has also been tested for turbulent channel flow problem for a wide range of Reynolds number (Piomelli et al., 2003; Temmerman et al., 2005; Nikitin et al., 2000). Nikitin et al. (2000) performed a comprehensive study with different meshes, numerical schemes and Reynolds number ($180 \leq Re_\tau \leq 80000$). It was found from their study, that in most of the cases, the wall coefficient of friction was under predicted by approximately 15%. In all the channel flow investigations, Spalart and Allmaras model (1992) was used as the turbulence model. To the authors' knowledge, Strelets (2001) version of the DES model has not been tested for a turbulent channel flow problem. The findings of the DES model for the channel flow problem are almost the same as the other hybrid RANS-LES approaches that have been used, in that the velocity mismatch is observed at the RANS-LES interface due to the reasons mentioned earlier. Indeed, for the channel flow problem, the results from the DES approach and the hybrid RANS-LES approach are similar. Piomelli et al. (2003) used a backscatter model in the inner layer, which was based on stochastic forcing, to supply the LES region with proper turbulence scale information at the interface. This improved the prediction of the mean velocity profile and the skin friction coefficient.

3.4 Summary

In this chapter, the need of a zonal hybrid URANS-LES methodology was presented, along with a description of the success it has had in predicting flows of different nature. In terms of computational cost, it is costlier than URANS but less expensive than LES. Its major success has been in high Reynolds number flow applications, where the URANS occupies a smaller portion of the simulated flow field (restricted to the near-wall region) in comparison with LES. In the hybrid URANS-LES approach, the zones of URANS and LES are mostly predetermined with two different set of grids. The turbulence models in the URANS and LES regions are mostly different. DES, which is a zonal approach as well, is similar to the hybrid URANS-LES methodology, where a single turbulence model is used and the grid exclusively determines the URANS and LES regions. The success of DES (Spalart Allmaras version) in fully wall bounded turbulent flows without boundary layer separation has been mentioned in this chapter. From the nature and structure of the DES model, it is anticipated that it could be successful in predicting the unsteady pulsating flow and its effects in sub-channel geometries, and can provide valuable insights into the physics of the flow pulsation phenomena. Since the SST version of the DES model (Strelets, 2001) has not been applied on a completely wall bounded flow without boundary layer separation, validation of that test case is an important first step in the progression towards modeling the flow pulsation phenomena in sub-channel geometries. In the next chapter, the mathematical formulation of the Strelets (2001) version of the DES model is presented.

CHAPTER 4

MATHEMATICAL MODEL AND NUMERICAL METHODOLOGY

4.1 Governing equations

A description of the flow field is obtained by numerical solution of the governing equations for conservation of mass and momentum. For turbulent flows, depending on the turbulence modeling methodology, the conservation equations are either time averaged or spatially filtered. The time averaged operation is based on the Reynolds averaging technique (Mathieu and Scott, 1999), which is a one-point (single-point) time average and is used in statistical turbulence modeling (RANS). The governing equations for unsteady RANS (URANS) are the ensemble-averaged Navier-Stokes equations. Unlike, the Reynolds time averaging or ensemble-averaging, the filtering technique in LES is an operation in space. The filtering technique separates the large from the small scales. The fact that RANS and LES methods employ averaging in different dimensions inhibits an easy link between them. The incompressible form of Navier-Stokes equations (continuity and momentum) for the URANS and the LES region is written as:

Conservation of mass:

$$\frac{\partial \overline{u_i}}{\partial x_i} = 0 \tag{4.1}$$

Conservation of momentum:

$$\frac{\partial \overline{u_i}}{\partial t}+\frac{\partial\left(\overline{u_i}\,\overline{u_j}\right)}{\partial x_j}=-\frac{1}{\rho}\frac{\partial \overline{p}}{\partial x_i}+\nu\frac{\partial^2 \overline{u_i}}{\partial x_j^2}-\frac{\partial \tau_{ij}}{\partial x_j} \tag{4.2}$$

The overbar ($\bar{}$) symbol in Eqs. (4.1)-(4.2) has different interpretations in the RANS and the LES regions. The overbar symbol in the URANS region represents ensemble averaging, whereas in the LES region it indicates the filtering operation (spatial averaging), which gives a filtered (resolved or large-scale) variable. The filtered Navier-Stokes equations, govern the evolution of the large, energy-carrying scales of motion. The ensemble averaging or filtering operation in Eqs. (4.1) and (4.2) are implicit in nature, i.e. the grid design is solely responsible for the specific type of operation. In LES, however, an explicit filtering operation can also be used on the conservation equations (Moin, 1998). In practice, however, the filter function does not appear explicitly at all in many LES codes (Balaras et al., 1996). In Eq. (4.2), the quantity τ_{ij}, in the RANS region represents the Reynolds stress tensor (effect of all turbulent scales on the mean flow field) which represents the average momentum flux due to turbulent velocity fluctuations, whereas in the LES region it is equivalent to the SGS stress tensor (effect of the unresolved or small scales on the resolved or large scales of motion). The term τ_{ij} can be decomposed into the following form:

$$\tau_{ij}=\overline{u_i u_j}-\overline{u_i}\,\overline{u_j} \tag{4.3}$$

The Reynolds stress tensor/SGS stress tensor is formulated using the eddy viscosity concept:

$$\tau_{ij}-\frac{1}{3}\delta_{ij}\tau_{kk}=-2\nu_t\overline{S_{ij}} \tag{4.4}$$

$$\overline{S_{ij}} = \frac{1}{2}\left(\frac{\partial \overline{u_i}}{\partial x_j} + \frac{\partial \overline{u_j}}{\partial x_i}\right) \tag{4.5}$$

The eddy viscosity, ν_t, in the RANS region represents the turbulent eddy viscosity, whereas in the LES region it represents the SGS eddy viscosity. The term $\overline{S_{ij}}$ in Eqs. (4.4) and (4.5) represent the strain rate tensor. The eddy viscosity in Eq. (4.4) is obtained from the specific RANS or the SGS model. Thus, Eqs. (4.4)-(4.5) and the specific RANS/SGS model lead to the closure of Eq. (4.2).

In the next section, the hybrid URANS-LES methodology i.e. the DES model of Strelets (2001) available in ANSYS CFX 11.0 is presented. This model was used in the research work to investigate fully developed turbulent flow in a duct and flow in a twin rectangular sub-channel geometry.

4.2 DES-SST model

The DES model of Strelets (2001) uses the SST model of Menter (1992) to provide the eddy viscosity in the URANS region and the SGS viscosity in the LES region. The SST model which solves for the turbulent kinetic energy (k) and turbulent eddy frequency (ω) is a hybrid model, where a k-ω formulation is used in the near-wall region, and a k-ε (ε is the turbulence eddy dissipation) formulation in the outer part of the boundary layer (free shear-layers). For computations to be performed with one set of equations, the k-ε model is first transformed into a k-ω formulation. The difference between this formulation (transformed k-ω equation) and the original k-ω model is that an additional cross term appears in the ω-equation and the modeling constants are different.

The original model is multiplied by a function F_1 and the transformed model by the function $(1-F_1)$ and both are added together. The blending between the two regions is performed by the blending function F_1 that is designed to be unity in the near-wall region (activating the k-ω model) and zero away from the surface, activating the k-ε model. The corresponding equations of the SST model are:

$$\frac{\partial(\rho k)}{\partial t}+\frac{\partial\left(\rho \overline{u_j} k\right)}{\partial x_j}=P_k-\beta^* \rho \omega k+\frac{\partial\left[\left(\mu+\sigma_k \mu_t\right) \frac{\partial(k)}{\partial x_j}\right]}{\partial x_j} \tag{4.6}$$

$$\frac{\partial(\rho \omega)}{\partial t}+\frac{\partial\left(\rho \overline{u_j} \omega\right)}{\partial x_j}=\gamma P_\omega-\beta \rho \omega^2+2 \rho\left(1-F_1\right) \sigma_{\omega 2} \frac{1}{\omega} \frac{\partial(k)}{\partial x_j} \frac{\partial(\omega)}{\partial x_j}+\frac{\partial\left[\left(\mu+\sigma_\omega \mu_t\right) \frac{\partial(\omega)}{\partial x_j}\right]}{\partial x_j} \tag{4.7}$$

Constants in the SST model are calculated as linear combination of the constants in the k-ε and k-ω models. The weight is determined by the blending function F_1. Thus, if ϕ_1 represents any constant in the original k-ω model and ϕ_2 is any constant in the transformed k-ε model, the corresponding constant of the SST model ϕ is calculated as

$$\phi=F_1 \phi_1+\left(1-F_1\right) \phi_2 \tag{4.8}$$

In Eqs. (4.6) and (4.7) σ_k, γ, β, σ_ω are the constants of the SST model which are a combination of constants from the original k-ω and the transformed k-ε model. The values of the various constants present in the original k-ω and the transformed k-ε model are provided in Table 4.1. The eddy viscosity of the model is based on the assumption that the shear stress in a boundary layer is proportional to the turbulent kinetic energy,

Table 4.1 Constants of the Shear Stress Transport (SST) model.

Symbol	Value	Location	Description
β^*	0.09	SST- inner layer, SST - outer layer. Appears in turbulent kinetic energy equation.	Destruction term constant
σ_{k1}	0.5	SST - inner layer. Appears in turbulent kinetic energy equation.	Diffusion term constant
γ_1	5/9	SST - inner layer. Appears in turbulent eddy frequency equation.	Production term constant.
β_1	0.075	SST - inner layer. Appears in turbulent eddy frequency equation.	Destruction term constant
$\sigma_{\omega 1}$	0.5	SST - inner layer. Appears in turbulent eddy frequency equation.	Diffusion term constant
σ_{k2}	1.0	SST - outer layer. Appears in turbulent kinetic energy equation.	Diffusion term constant
γ_2	0.44	SST - outer layer. Appears in turbulent eddy frequency equation.	Production term constant.
β_2	0.0828	SST - outer layer. Appears in turbulent eddy frequency equation.	Destruction term constant
$\sigma_{\omega 2}$	0.856	SST - outer layer. Appears in turbulent eddy frequency equation.	Standard diffusion term as well as cross diffusion term constant

and is a modified form of the eddy viscosity used in the traditional k-ω model. The eddy viscosity for the SST model is given as:

$$\nu_t = \frac{a_1 k}{\max\left(a_1\omega; \Omega F_2\right)} \tag{4.9}$$

where a_1=0.31 is a constant, Ω is the absolute value of vorticity and F_2 is a blending function which is similar to the blending function F_1. The blending function F_2 extends further out into the boundary layer than F_1. The formulations of the blending functions, F_1 and F_2 are given as:

$$F_1 = \tanh(\arg_1^4) \tag{4.10}$$

$$\arg_1 = \max\left(\min\left(\frac{\sqrt{k}}{0.09\omega y}; 0.45\frac{\omega}{y}\right); \frac{400\nu}{y^2\omega}\right) \tag{4.11}$$

$$F_2 = \tanh(\arg_2^2) \tag{4.12}$$

$$\arg_2 = \max\left(2\frac{\sqrt{k}}{0.09\omega y}; \frac{400\nu}{y^2\omega}\right) \tag{4.13}$$

Turbulence models that are based on the ω equation provide an analytical expression for ω in the viscous sub-layer. The SST model allows for a near-wall formulation which automatically switches from wall function to a low Reynolds number formulation, as the grid is refined in the wall-normal direction.

A DES model can be obtained from a RANS model by appropriate modification of the length scale which is explicitly or implicitly involved in any RANS turbulence model. The basis of Strelets (2001) DES model is to switch from the RANS model (SST) to an LES model in regions where the integral length scale predicted by the RANS model is larger than the local grid spacing (filter width). The question that arises, is for which specific terms of the RANS model, should the integral length scale be replaced with the DES length scale (local grid spacing or filter width). The dissipative term of the turbulent kinetic energy transport equation is the most suitable choice because this keeps the formulation simple, and at equilibrium the resulting sub-grid model reduces to a Smagorinsky like model. This means that at equilibrium the eddy viscosity is proportional to the magnitude of the strain tensor, and to the square of the grid spacing. Thus, in the Strelets (2001) DES-SST model, the turbulent length scale, L_t, used in the computation of the dissipation rate in the equation for turbulent kinetic energy is replaced by the local grid spacing Δ, when the predicted length scale is larger than the local grid spacing.

The length scale of the SST model in terms of k and ω is:

$$L_t = \frac{\sqrt{k}}{\beta^* \omega} \tag{4.14}$$

The dissipative term of the turbulent kinetic energy transport equation in the SST (RANS) model is:

$$D^k_{RANS} = \rho \beta^* k \omega = \rho k^{3/2} / L_t \tag{4.15}$$

The dissipative term of the turbulent kinetic energy transport equation in the DES model is written as:

$$D^k_{DES} = \rho k^{3/2} / \overline{L} \tag{4.16}$$

where

$$\overline{L} = \min(L_t, C_{DES}\Delta) \tag{4.17}$$

In Eq. (4.17), Δ is the filter width, which is an algebraic combination of the grid cell dimensions. One of the most common forms of the filter width is:

$$\Delta = \max(\Delta_i) \tag{4.18}$$

The formulation in Eq. (4.18) states that the filter width is based on the maximum edge length of the grid cell in any direction. The practical reason for choosing the maximum edge length in the DES formulation is that the model should return the RANS formulation in attached boundary layers. The maximum edge length is therefore the safest estimate to ensure that demand (Strelets, 2001).

The CFX-DES modification of Strelets (2001) is formulated as a multiplier (switching function) to the destruction term in the turbulent kinetic energy equation, i.e.

$$\varepsilon = \beta^* k \omega F_{DES} \tag{4.19}$$

where F_{DES} is the switching function that switches the SST-RANS model to an LES model. The formulation of F_{DES} is given as:

$$F_{DES} = \max\left(\frac{\sqrt{k}}{\beta^* \omega C_{DES} \Delta}(1 - F_{SST}), 1\right) \tag{4.20}$$

where,

$$F_{SST} = 0 \text{ or } F_1 \text{ or } F_2 \tag{4.21}$$

In Eq. (4.20), C_{DES} is a constant and is equal to 0.61. When F_1 or F_2 (blending functions of SST model) are used in Eq. (4.20) to represent F_{SST}, it alleviates the problem of grid induced separation, which is a major issue for flows involving boundary layer separation investigated using the DES approach (Strelets, 2001). In the current research work, wall bounded turbulent flows without any boundary layer separation were investigated. The issue of grid induced separation was not of any concern and hence $F_{SST} = 0$ was used.

4.3 Numerical approach

The code in ANSYS CFX-11.0 uses finite volume discretization, with a collocated (non-staggered) grid approach to overcome the decoupling (checkerboard) problem of the pressure and velocity field (Patankar, 1980). The discrete algebraic equations are solved using an iterative solver based on algebraic multigrid accelerated incomplete lower upper (ILU) factorization technique. In this section, numerical treatment of the DES model is presented.

4.3.1 Spatial discretization

In some of the early DES investigations (Shur et al., 1999; Travin et al., 2000; Constantinescu et al., 2000) fully implicit upwind schemes were used for the advection terms. The choice of implicit upwind schemes for full DES was dictated by the hybrid nature of DES, and in particular, by the lack of stability of the less dissipative centered schemes in the flow regions where DES is operating in the RANS mode. In the LES regions of DES, however, the upwind schemes are not appropriate because they are too dissipative for LES (Moin, 1998). Excessive dissipation does not result in an unstable or meaningless solution, but it prevents the solution from taking full advantage of the grid provided. It stops the energy cascade before the SGS eddy viscosity does, or in collaboration with the eddy viscosity but still at scales that are larger than the best possible. Thus, if an upwind scheme is used for the entire DES, then numerical dissipation will exist and this needs to be treated.

In the DES methodology, different numerical treatments can be employed in the RANS and the LES regions of the domain. This is done by having a numerical switch between the upwind-biased scheme for the RANS region and central difference scheme for the LES region. This is necessary to avoid excessive numerical diffusion in the LES regions of the DES resulting from upwind-biased scheme. The switch in ANSYS CFX is performed between the second order upwind scheme (NAC - numerical advection correction) and the second order central difference (CDS) scheme in the following way:

The finite volume method approximates the advection term (inviscid flux) in the transport equation for a generic variable ψ as:

$$\nabla \bullet \rho U \psi \approx \frac{1}{\Omega_{CV}} \sum_{ip} \dot{m}_{ip} \psi_{ip} \tag{4.22}$$

where Ω_{CV} is the volume of the control volume, the index *ip* denotes the integration points on the control volume faces, $\dot{m}_{ip}$ and ψ_{ip} are the mass flow and transported variable value estimated at the integration point *ip*. The value of ψ_{ip} is obtained by interpolating from the surrounding grid nodes according to the selected discretization scheme. Blending between the upwind-biased scheme and the central difference scheme is achieved by combining the corresponding interpolation values $\psi_{ip,NAC}$ and $\psi_{ip,CDS}$ using the numerical blending function σ:

$$\psi_{ip} = \sigma \cdot \psi_{ip,NAC} + (1-\sigma) \cdot \psi_{ip,CDS} \tag{4.23}$$

A specific form of the blending function σ is:

$$\sigma = \sigma_{\max} \cdot \tanh\left(A^{C_{H1}}\right) \tag{4.24}$$

Here, the function A is defined as:

$$A = C_{H2} \cdot \max\left(\frac{C_{DES}\Delta_{\max}}{L_t m} - 0.5, 0 \right) \tag{4.25}$$

In Eq. (4.25), Δ_{max} represents the maximum neighboring grid edge size. The turbulence length scale, L_{turb} is defined using the turbulent kinetic energy and turbulent eddy frequency,

$$L_t = \frac{\sqrt{k}}{c_\mu \omega} \tag{4.26}$$

The parameter m in Eq. (4.25) is a combination of the magnitudes of the mean strain S and vorticity Ω, and is introduced to ensure the dominance of the upwind scheme in the disturbed irrotational flow regions where $\Omega \ll 1$ and $S > 0$:

$$m = \max\left(\tanh\left(B^4\right), 10^{-10}\right) \tag{4.27}$$

$$B = C_{H3} \cdot \frac{\Omega \max(\Omega, S)}{\max\left(\frac{S^2 + \Omega^2}{2}, 10^{-10} \right)} \tag{4.28}$$

A limiter based on the Courant number is used in order to avoid oscillations due to the central difference scheme, which can occur for medium and high Courant numbers. The blending function σ is limited in the following way:

$$\sigma_{\lim} = \max\left[\sigma, 1 - \min\left(\frac{CFL_{\max}}{CFL}, 1 \right)^{CFLEXP} \right] \tag{4.29}$$

The constants used in the formulation of the blending function are provided in Table 4.2. Regions where σ is close to zero, the advection scheme is virtually second order central difference and represents the LES mode of the DES model. Conversely, in the near-wall RANS regions, σ is close to 1.0 and the scheme is effectively second order upwind.

Table 4.2 Constants of the blending function.

Symbol	Value
σ_{max}	1.0
C_{H1}	3.0
C_{H2}	1.0
C_{H3}	2.0
CFL_{max}	5.0
CFL_{EXP}	1.0

4.3.2 Time advancement

For control volumes that do not deform in time, the general discrete approximation of the transient term for the nth time step, for a generic variable ψ is:

$$\frac{\partial}{\partial t}\int_V \rho\psi dV \approx V\frac{(\rho\psi)^{n+\frac{1}{2}}-(\rho\psi)^{n-\frac{1}{2}}}{\Delta t} \tag{4.30}$$

where the values at the start and end of the time step are assigned the superscripts n-1/2 and n+1/2, respectively. In ANSYS CFX, the code is fully implicit, and two different time discretization schemes are available, viz. first order backward Euler and second order backward Euler schemes. With the first order backward Euler scheme, the start and end of time step values are respectively approximated using the old and current time level solution values. The resulting discretization is:

$$\frac{\partial}{\partial t}\int_V \rho\psi dV = V\left(\frac{\rho\psi-\rho^{\circ}\psi^{\circ}}{\Delta t}\right) \tag{4.31}$$

The superscript 'o' refers to the previous time step with respect to the current time step. The scheme is robust, fully implicit, bounded, conservative in time, and does not yield a time step size limitation. This specific discretization is, however, only first order accurate in time and will introduce discretization errors that tend to diffuse steep temporal gradients and the turbulence is damped out. The behavior of this scheme is similar to the numerical diffusion experienced with the upwind difference scheme for discretizing the advection term.

With the second order backward Euler scheme, the start and end of time step values are respectively approximated as:

$$(\rho\psi)^{n-\frac{1}{2}} = (\rho\psi)^{o} + \frac{1}{2}\left((\rho\psi)^{o} - (\rho\psi)^{oo}\right) \tag{4.32}$$

$$(\rho\psi)^{n+\frac{1}{2}} = (\rho\psi) + \frac{1}{2}\left((\rho\psi) - (\rho\psi)^{o}\right) \tag{4.33}$$

Substituting Eqs. (4.32) and (4.33) into Eq. (4.30), the resulting discretized equation is:

$$\frac{\partial}{\partial t}\int_{V} \rho\psi dV \approx V\frac{1}{\Delta t}\left(\frac{3}{2}(\rho\psi) - 2(\rho\psi)^{o} + \frac{1}{2}(\rho\psi)^{oo}\right) \tag{4.34}$$

Superscript 'oo' refers to two time steps prior to the current time step. This scheme is robust, implicit, conservative in time, and does not create a time step limitation. It is second order accurate in time, but is not bounded and may create some nonphysical solution oscillations. It has been found from previous investigations (Shur et al., 1999; Travin et al., 2000; Constantinescu et al., 2000; Strelets, 2001) that time discretization using second order accurate schemes give good and meaningful results in the LES region of the DES modeling approach. Thus, second order backward Euler scheme was used for the investigations carried out in this research work (for both LES and RANS regions).

The choice of the time step size is usually determined by the requirements that numerical stability be assured, and that the turbulent motions be accurately resolved in time. In the DES modeling, the time step size requirements are usually based on the stability limit and physical constraint. The stability limit is usually set by the CFL criterion. The CFL condition requires that the numerical time step size Δt should be less than $\Delta t_c = CFL\Delta x/u$, where the maximum allowable Courant number (CFL) also depends on the numerical scheme used. Based on the spatial and temporal discretization schemes for the DES-SST model in ANSYS CFX 11.0, the maximum CFL number should be around 5. For accuracy, the average CFL number should be in the range of 0.5-1. Larger values can give stable results, but the turbulence may be damped. Also if the CFL number is in the range 0.5-1, convergence within each time step is achieved quickly. The physical constraint requires that the time step size, Δt should be less than the time scale of the smallest resolved scale of motion, $\tau \sim \Delta x/U$, where U is the convective free stream velocity.

4.4 Boundary conditions

4.4.1 Wall boundaries

At the solid walls, the momentum flux must be known. With the no-slip boundary condition, the wall velocity is assigned which allows for the determination of the convective part of the momentum flux at the wall. The wall shear stress (viscous stress) is determined by differentiating the velocity profile, which would be accurate only if the wall layer is well resolved. With increasing Reynolds number (Re $\rightarrow \infty$), the number of grid points required to resolve the steep velocity gradient in the viscous sub-layer increases substantially. Alternatively, approximate boundary conditions, or wall layer models can be used when the grid is not fine enough, to resolve the near-wall gradients. In this case, the wall layer is modeled by specifying a correlation between the velocity in the outer flow and the stress at the wall.

For the DES-SST model, in the near-wall region the RANS mode is operational. The SST model in ANSYS CFX 11.0, allows for automatic treatment of the wall, whereby the wall boundary condition switches from a wall function formulation to a low Reynolds number formulation as the grid is refined in the wall-normal direction. The wall function formulation used, is in the form of the standard logarithmic law of the wall for non-separating flow problems. For the classical (standard) wall function model to be applicable, the location of the first grid point (non dimensional distance) from the wall should satisfy the criteria, $y^+ > 30$. In the log-law region, the tangential velocity of the first grid point with respect to the wall is related to the wall shear stress, τ_w by means of a logarithmic relation. The logarithmic relation for the tangential velocity is given by:

$$u^+ = \frac{U_t}{u_\tau} = \frac{1}{\kappa}\ln\left(y^+\right) + C \tag{4.35}$$

where:

$$y^+ = \frac{\Delta y u_\tau}{\nu} \tag{4.36}$$

$$u_\tau = \sqrt{\frac{\tau_w}{\rho}} \tag{4.37}$$

In Eqs. (4.35)-(4.37), U_t is the known tangential velocity to the wall at a distance Δy from the wall, y^+ is the non dimensional distance of the first grid point from the wall, u_τ is the wall friction velocity, τ_w is the wall shear stress, κ is the Von-Karman constant and C is a log layer constant.

The limitation of the wall function approach is that the predictions depend on the location of the point nearest to the wall. It is sensitive to the near-wall meshing, refining the mesh does not necessarily give a unique solution of increasing accuracy (Grotjans and Menter, 1998). For fine meshes, the problem of inconsistencies in the wall function formulation is overcome by using the scalable wall functions, which is used in ANSYS CFX. The scalable wall function approach, limits the value of y^+ used in the log-law formulation by a lower value of:

$$\tilde{y} = \max(y^+, 11.06) \tag{4.38}$$

The number 11.06 is the intersection between the logarithmic and the linear near-wall profile. Eq. (4.38) ensures that all mesh points are outside the viscous sub-layer and all fine mesh inconsistencies are avoided, when using the logarithmic law of the wall formulation.

In the low Reynolds number formulation of the SST model, the viscous sub-layer is resolved, which requires a near-wall grid resolution of at least $y^+ < 2$. For high accuracy in computing the wall shear stress, the boundary layer should be resolved using at least 10-15 grid points normal to the wall in the low Reynolds number formulation (Menter, 1992). Thus, in the SST model of ANSYS CFX, if $y^+ < 2$ then the low Reynolds number approach is carried out, otherwise the logarithmic law of the wall (scalable wall function) formulation is used.

The advantage of the SST model is that it provides an analytical solution for the turbulent eddy frequency at the no-slip wall (Menter, 1992). If the law of the wall formulation is used, then the analytical expression for ω at the wall is:

$$\omega = \frac{\tilde{u}}{a_1 \kappa \Delta y} \tag{4.39}$$

where:

$$\tilde{u} = \max\left(\sqrt{a_1 k}, u_\tau\right) \tag{4.40}$$

$$u_\tau = \sqrt{\nu \left|\frac{\Delta U}{\Delta y}\right|} \tag{4.41}$$

For low Reynolds number formulation, the following analytical expression for turbulent eddy frequency, ω, is used at the wall:

$$\omega = \frac{6\nu}{\beta_1 (\Delta y)^2} \tag{4.42}$$

In Eqs. (4.41) and (4.42), Δy is the distance of the first grid point from the wall. ΔU is the velocity defect for the first grid point from the wall, a_1 and β_1 are the constants of the SST model (see Table 4.1). Turbulence models based on transport equation of ω give accurate results if the near-wall values of ω are sufficiently large, which is satisfied by Eqs. (4.39) and (4.42) respectively (Menter, 1992). The wall boundary condition for turbulent kinetic energy is that it is zero at the no slip walls.

4.4.2 Periodic conditions

Periodic boundary conditions have been used extensively in problems having one or more directions of spatial homogeneity, or in many practical situations where a portion of the flow field is repeated in many identical regions (eg., flow around a single turbine blade in a rotating machine). The classical case is the channel flow problem, which has been investigated extensively using DNS, LES and DES approaches. The use of periodic boundary conditions is similar to studying the time development rather than the spatial evolution of a flow. Periodic boundary conditions are advantageous since they are easy to implement, eliminate the need to specify inflow and outflow conditions, and allow the use of small computational domain, which substantially reduce the computational cost. When periodic boundary conditions are used, the computational domain must be large enough to capture the wavelength of the longest structure present in the flow. Usually two-point spatial correlations are used to determine the length of the periodic domain.

Periodic boundary conditions are implemented in a computational domain using interfaces, which set the boundaries of the domain. For periodic interfaces, flow out of one boundary is mapped onto the corresponding boundary. Periodic interface type can be either translational or rotational in nature. In case of translational periodicity, the two sides of the interface are parallel to each other such that a single translational transformation can be used to map flow from one region to the other. For rotational periodicity, the two sides of the periodic interface can be mapped by a single rotational transformation about an axis.

4.5 Summary

In this chapter, the mathematical formulation of the DES-SST model was presented. The governing (conservation) equations in the framework of hybrid URANS-LES methodology, spatial and temporal discretization schemes with respect to the DES-SST model and the boundary conditions were discussed. In the next chapter, the validation study of the DES-SST model is presented with regards to a fully developed turbulent channel flow problem without any boundary layer separation. To the author's knowledge, fully developed turbulent channel flow using the DES-SST model has not been investigated in the past.

CHAPTER 5

VALIDATION OF DES-SST BASED TURBULENCE MODEL FOR A FULLY DEVELOPED TURBULENT CHANNEL FLOW PROBLEM

5.1 Introduction

This work discusses simulations using the detached eddy simulation (DES) based turbulence model to investigate turbulent channel flows. Applicability of Strelets' (2001) version of DES model was tested for a fully developed turbulent channel flow problem in a rectangular duct. The unsteady Navier-Stokes equations were solved numerically at Reynolds number, Re_τ, of 180, 590 and 2000 respectively and compared to results obtained using direct numerical simulation (DNS) and previously published DES data. Effects of grid density and advection scheme were investigated. Overall, the model predicted the correct trends in the variation of turbulence quantities and compared reasonably well.

5.2 CFD methodology

5.2.1 Channel flow setup and mesh design

The turbulent channel flow (rectangular duct) computations were performed using ANSYS CFX-11.0, at Reynolds number, Re_τ (based on the wall friction velocity and half channel height) of 180, 590 and 2000 respectively. The domain sizes at Reynolds number of 180 and 590 were based on the DNS study of Moser et al. (1999). At Reynolds number of 2000, the domain size was based on the DES investigation of Temmerman et al. (2005). Figure 5.1 shows the domain set up, the associated coordinate axis and the velocity components (in brackets) in the respective directions. The stream-wise, wall-normal and span-wise directions are x, y and z respectively. The dimension 'h' refers to the half channel height.

Details of the simulation parameters for six different runs are provided in Table 5.1. The mesh dimensions are all indicated in wall (+) units (non-dimensional units of length based on the wall friction velocity and kinematic viscosity). In all the cases, the first grid point from the wall was maintained at $\Delta y_w^+ < 1$, to ensure the low Reynolds number formulation. The grid was stretched in the wall-normal direction using a hyperbolic meshing law, with the growth ratio between the cells of about 1.16. With this type of meshing law and growth ratio, the cost increases only logarithmically with the increase in Reynolds number (Nikitin et al., 2000; Piomelli et al., 2003). The grid was uniformly meshed in the stream-wise and span-wise directions. All cases have $\Delta x^+ \approx \Delta z^+$ which is based on the grid design suggestions for DES (Shur et al., 1999; Nikitin et al., 2000). The symbol Δy_c^+ indicates the y direction resolution in the center of the channel. The grid design led to high aspect ratio cells in the near-wall region and almost cubic cells in the core region of the channel. For example in case C5, the aspect ratio varied from 1.03 (core region) to 289 (near-wall region). The filter width in ANSYS CFX-11.0 for the DES-SST model (Strelets, 2001) is based on the maximum local grid

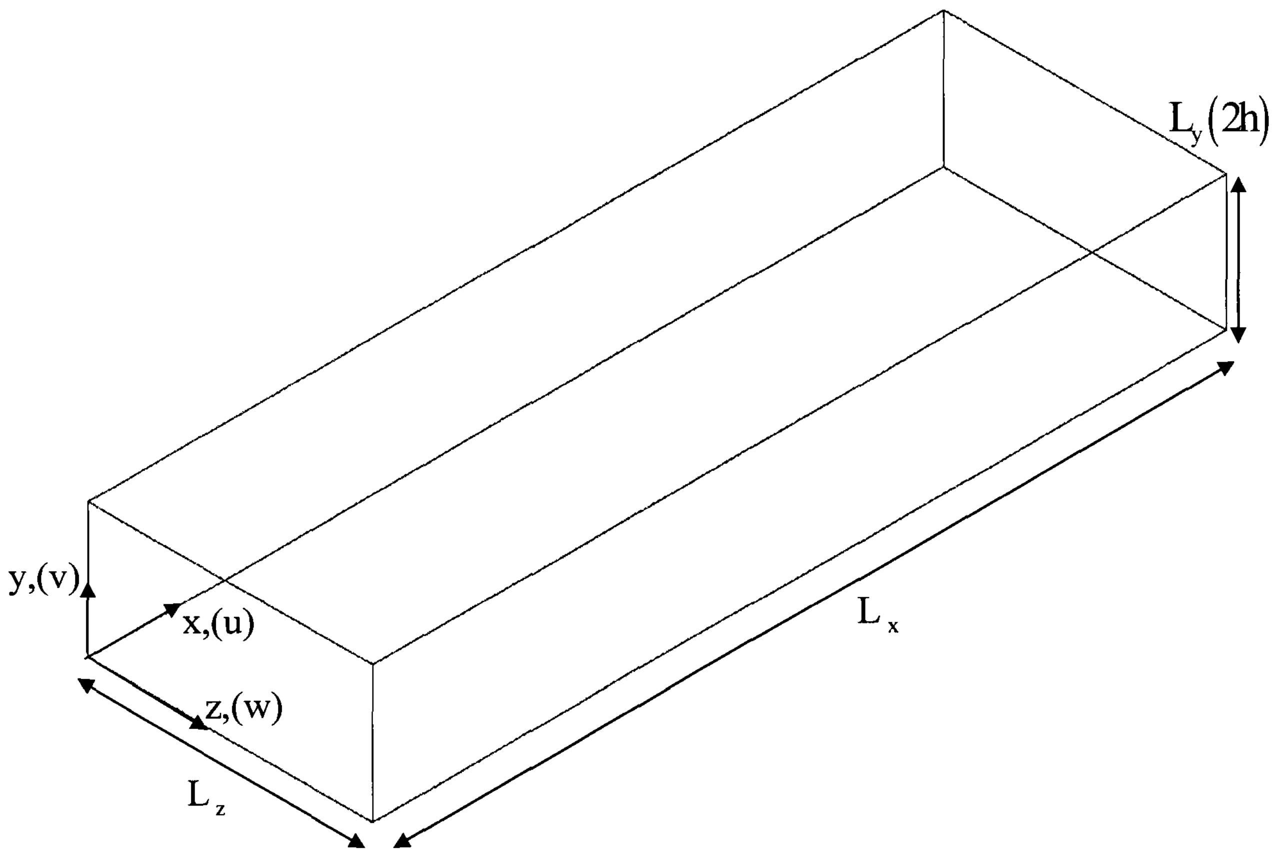

Figure 5.1 Computational domain and coordinate axes for the channel flow problem.

spacing in any direction i.e. $\Delta = \max(\Delta x, \Delta y, \Delta z)$. In all the computations, it is either the stream-wise or the span-wise grid spacing that sets the filter width.

5.2.2 Numerical approach, boundary conditions and statistical data

For the present computations, in all cases, the time discretization was carried out using the second-order backward Euler scheme. For all the equations (continuity, momentum and turbulence) in the LES region, the advection scheme used by the code is second-order central difference, which reduces the effect of numerical dissipation. However, in the URANS region, either the upwind (first-order or second-order) or the second-order central difference scheme can be used as the advection scheme. When the solver advection scheme is set as upwind, the code uses an upwind scheme in the URANS region which automatically changes to a central difference scheme once the DES model switches to LES. A central difference scheme is used throughout the domain, when the solver advection scheme is set as central difference. A summary of the test cases used is provided in Table 5.1. In all cases, except C4, the advection scheme in the URANS region was second-order central difference. For case C4, in the URANS region, the advection scheme for the continuity and momentum equations was second-order upwind and for the turbulence equations it was first-order upwind (based on CFX discretization theory guidelines). Thus, the effect of the numerical treatment on the advection scheme in the URANS region was studied between cases C3 and C4.

In the simulations, periodic boundary conditions were applied in the stream-wise (x) and span-wise (z) directions. Pressure gradient was specified in the stream-wise direction to drive the flow. Wall boundary conditions were specified for the top and

Table 5.1 Simulation parameters for the turbulent channel flow problem.

Case	Re_τ	$L_x \times L_z$	$N_x \times N_y \times N_z$	Δy^+_w	Δx^+	Δz^+	Δy^+_c	Advection Scheme
C1	180	$4\pi h \times 4/3\pi h$	125×129×42=677,250	0.06	18	18	9	Central Difference
C2	180	$4\pi h \times 4/3\pi h$	170×67×58=660,620	0.5	13	13	13	Central Difference
C3	590	$2\pi h \times \pi h$	70×64×36=161,280	0.8	54	53	53	Central Difference
C4	590	$2\pi h \times \pi h$	70×64×36=161,280	0.8	54	53	53	Upwind + Central Difference
C5	2000	$2\pi h \times \pi h$	64×64×32=131,072	0.7	199	202	232	Central Difference
C6	2000	$2\pi h \times \pi h$	128×128×64=1,048,576	0.7	100	100	101	Central Difference

bottom wall (y direction). The initial velocity field for the DES run was obtained from a steady SST simulation. The code has the ability to superimpose specified velocity fluctuations on the initial velocity field to "kick start" the process, and this was used. The steady SST run provided an estimate of the initial turbulence velocity fluctuation. The time step used for the simulations was based on a time scale estimate for the integral length scales from the steady SST run and the condition that CFL≤1 in the LES region.

The simulations were run for sufficiently long time to be statistically independent of the initial condition. Once the initial transient settled down, then statistics such as mean velocity, velocity correlations and Reynolds stresses were accumulated over sufficiently long period of time so as to obtain statistically stationary results.

5.3 Channel flow results

5.3.1 Re_τ=180

For the case C1, the grid in the y-direction was based on the DNS study of Moser et al., 1999, which used a fine grid in the near-wall region. For cubic cells to be present in the LES region, the total number of nodes for case C1 ended up being 677,250. Generally for all hybrid RANS-LES and DES methods, it is recommended that $0.5 \le \Delta y_w^+ \le 1$ (Nikitin et al., 2000). Therefore, a second case was run (C2), which used a coarser grid in the near-wall region. The grid in the y-direction for case C2 closely resembled Nikitin et al's. study (Run A1 in their study) (Nikitin et al., 2000). The overall mesh size for case C2 was 660,620 which is very close to case C1. The filter width for C2 is slightly more refined than C1, as stated in Table 5.1. The DES-SST results are compared with the DES results of Nikitin et al. (Run A1) (2000) and the DNS results of Moser et al. (1999).

Figures 5.2 and 5.3 show the time traces of the instantaneous velocity (normalized using the channel bulk velocity) at the two monitored points located at y^+=1.2 (URANS region) and y^+=120 (LES region) for case C2. It is evident from the figures that the code was successful in generating and sustaining turbulent fluctuations. The turbulent fluctuations are more intense in the LES region than in the URANS region. The time averaged (mean) stream-wise velocity profile (normalized using the time averaged wall shear velocity) for cases C1 and C2, in comparison with the DES (Nikitin et al., 2000) and DNS (Moser et al., 1999) results are shown in Figure 5.4. The approximate location of the switch over from URANS to LES, was at $y^+ = 45$ (y/h=0.25) for case C1 and $y^+ =$ 41 (y/h=0.23) for case C2. In both cases, for the outer flow region (log layer region onwards) the DES model over predicts the mean velocity. An unphysical "DES buffer layer" is formed, when the flow transitions from the RANS to LES mode, where the velocity gradient is high. Due to this, a high intercept is obtained for the logarithmic layer of the flow and in some cases an incorrect slope as well. Baggett (1998) argues that artificial streaks generated in the inner layer, causes a decorrelation between u and v fluctuations. For the balance of the stream-wise momentum flux, a higher velocity gradient is thus produced. The result of this is an under prediction in the skin friction coefficient. The skin friction coefficient was under predicted by almost 18% for the present simulations. The Von-Karman constant in the log-layer was found to be around 0.38. Nikitin et al's. (2000) DES prediction of the time averaged velocity (denoted as Run

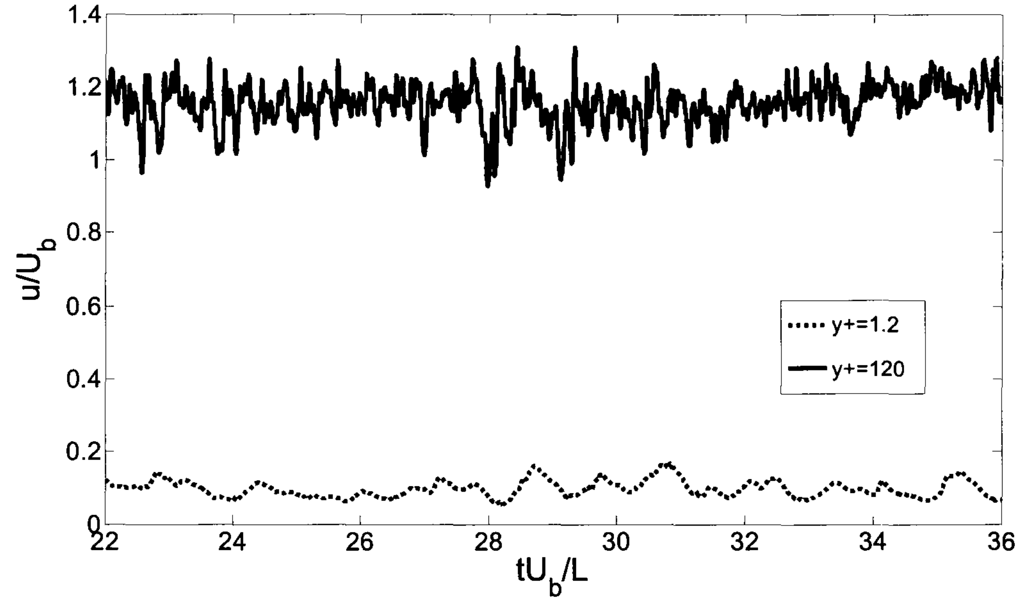

Figure 5.2 Time history of the instantaneous stream-wise velocity at Re_τ =180 for case C2.

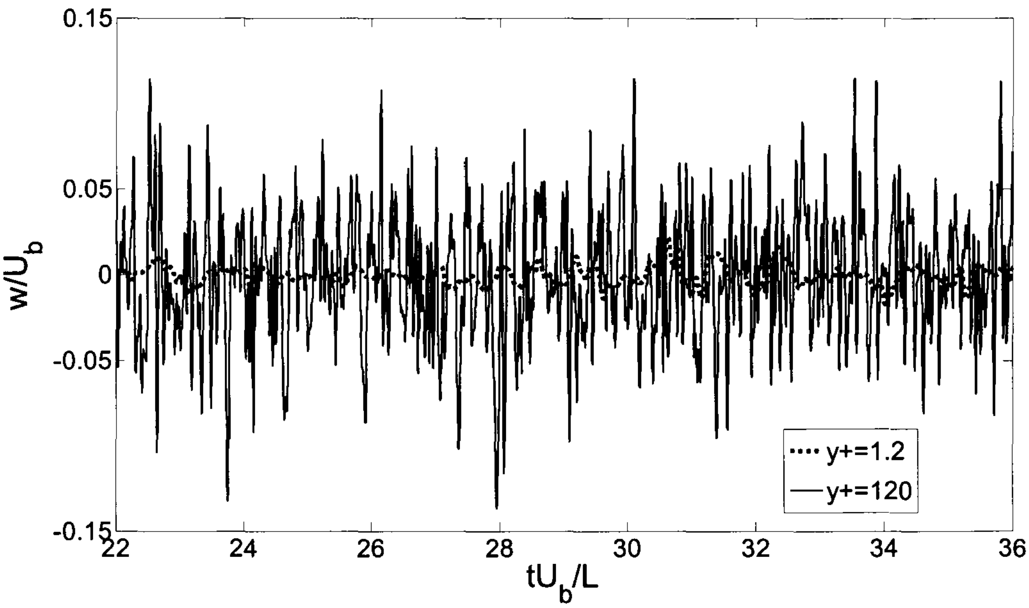

Figure 5.3 Time history of the instantaneous span-wise velocity at Re_τ =180 for case C2.

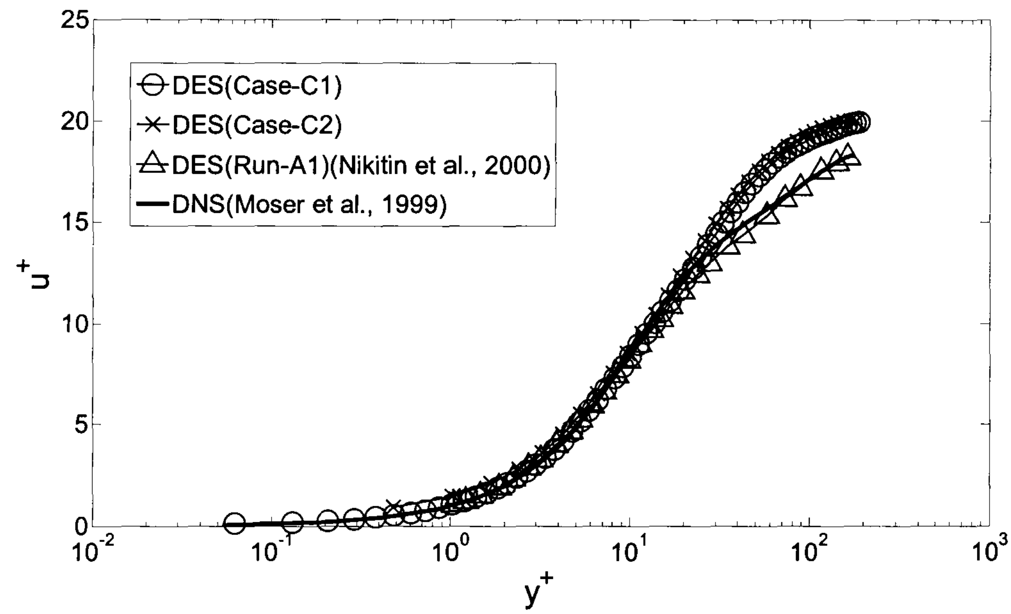

Figure 5.4 Time averaged stream-wise velocity profiles for DES-SST, DES (Run A1) (Nikitin et al., 2000) and DNS (Moser et al., 1999) at Re_τ=180.

A1 in the figure) has a near perfect agreement throughout with the DNS data (Moser et al., 1999). The characteristic feature of the DES model i.e. over prediction of the mean velocity profile in the outer region, is not present in their results.

The variation in the time averaged modeled eddy viscosity (normalized using the kinematic viscosity of fluid) is shown in Figure 5.5. As expected, the peak in the eddy viscosity is in the URANS region, and it drops down smoothly as the DES model switches from the URANS to LES mode. This clearly indicates that there is an increased level of resolved turbulence in the LES region. The eddy viscosity in the LES region is related to the grid spacing. The filter width for case C2 is smaller than C1, resulting in a reduced eddy viscosity for C2. The components of the Reynolds shear stress (modeled, resolved), viscous shear stress and the total shear stress (sum of modeled, resolved components of Reynolds shear stress and viscous shear stress) predictions for both the cases, are shown in Figure 5.6. The shear stresses are normalized using the time averaged wall shear velocity. The modeled, resolved components of Reynolds shear stress and the viscous shear stress from Nikitin et al's. (2000) study, and DNS Reynolds shear stress data (Moser et al., 1999) is also shown in Figure 5.6. It is clear that for both cases C1 and C2, significant part of the Reynolds shear stress is modeled in the URANS region and resolved in the LES region. The behavior of the shear stresses is better understood by looking into the mean momentum balance equation. For fully developed conditions, the total shear stress must always balance the driving pressure gradient. For the present channel flow simulations, the flow is homogeneous in the x and z directions. Integrating the one-dimensional Reynolds averaged equation for the stream-wise momentum flux and incorporating the appropriate boundary conditions, the mean momentum balance equation is:

$$\frac{\nu}{u_\tau^2}\frac{d\overline{u}}{dy}-\frac{\overline{u'v'}}{u_\tau^2}=1-\frac{y}{h} \tag{5.1}$$

The significance of Eq. (5.1) is that the total shear stress (sum of viscous and Reynolds shear stress) must always have a linear variation and has a fixed value at a particular *y* location, irrespective of the Reynolds number and the turbulence model. In Figure 5.6, the viscous shear stress for cases C1 and C2 is almost the same because the mean velocity profiles are nearly the same, as seen in Figure 5.4. Case C1 has a larger modeled component than case C2, consistent with the larger filter width for C1. The resolved component is higher for case C2 than case C1. Therefore, the total Reynolds shear stress (sum of modeled and resolved components) is almost the same for both the cases because of the mean momentum balance. The total shear stress for both the cases, C1 and C2 follow the linear variation as seen in Figure 5.6. In case of Nikitin et al's. (2000) study (Run A1 in the figure), the resolved component of the Reynolds shear stress has remarkably excellent agreement with the DNS data. The modeled component has extremely small contribution to the total Reynolds shear stress. In the region, y/h=0.1 to y/h=0.23, the viscous shear stress for run A1 is smaller than cases C1 and C2. This is the region where the velocity rises steeply for both the cases, C1 and C2, respectively. In the same region, the resolved component of the Reynolds shear stress is much smaller for cases C1 and C2 than run A1. Thus, the modeled component of the Reynolds shear stress is significantly larger for cases C1 and C2 as compared to run A1. From region $y/h \geq 0.44$,

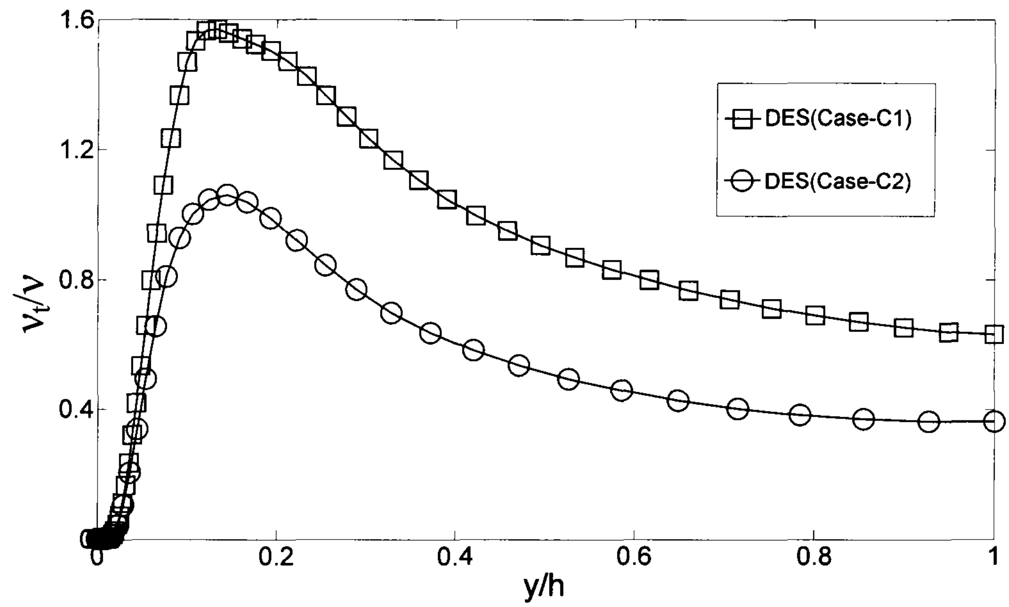

Figure 5.5 DES-SST prediction of eddy viscosity profile at Re_τ=180.

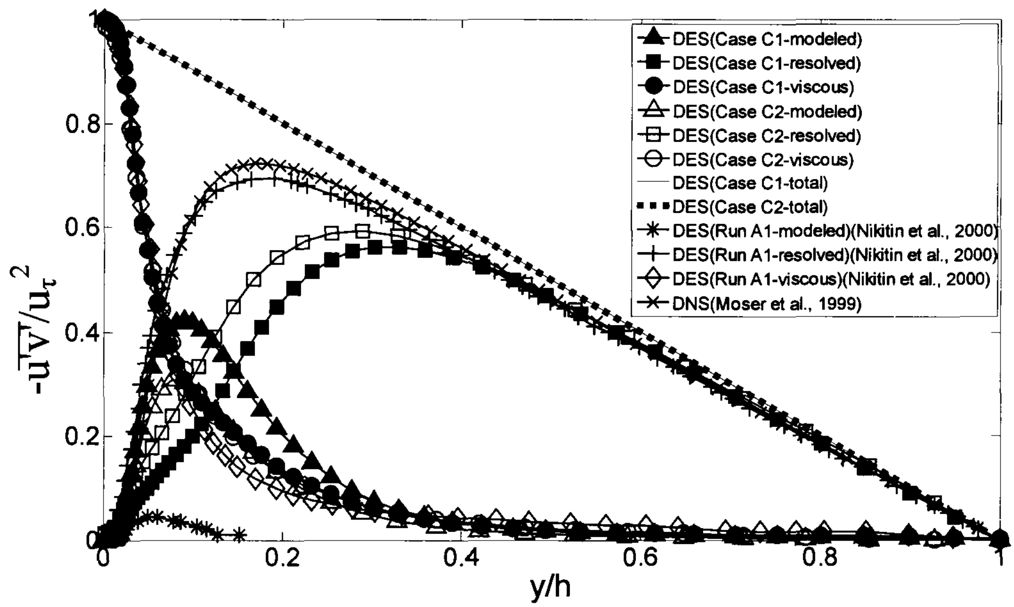

Figure 5.6 Shear stress profiles for DES-SST, DES (Run A1) (Nikitin et al., 2000) and DNS (Moser et al., 1999) at Re_τ=180.

the agreement in the resolved component of the Reynolds shear stress between the present simulations and run A1, and the DNS data is quite good. It seems that in case of run A1, the switch over from RANS to LES happened in a region much closer to the wall than the present simulations.

The modeled, resolved and total (sum of modeled and resolved) turbulence kinetic energy (normalized using the time averaged wall shear velocity) as predicted by the DES-SST model, for cases C1 and C2 are shown in Figure 5.7 and 5.8, respectively. The predicted trend in the turbulence kinetic energy for the DES model is in agreement with the DNS data. It is clear that the modeled part of the turbulence kinetic energy is mainly in the URANS region. The contribution of the sub-grid scales is quite small as compared to the resolved scales in the LES region. The nature of the resolved scales in the URANS region that contributes to the total turbulence kinetic energy is still an area of active research in the turbulence community. For case C1, the resolved and the total turbulence kinetic energy is over predicted in the LES region. This trend in predicting the turbulence kinetic energy is consistent with previous studies (Davidson and Billson, 2006). For case C2, the DES result for the total turbulence kinetic energy in the LES region, is in good agreement with the DNS data. It is expected that the relatively refined grid in the stream-wise and span-wise directions and thus the smaller filter width, led to better prediction of turbulence kinetic energy for case C2.

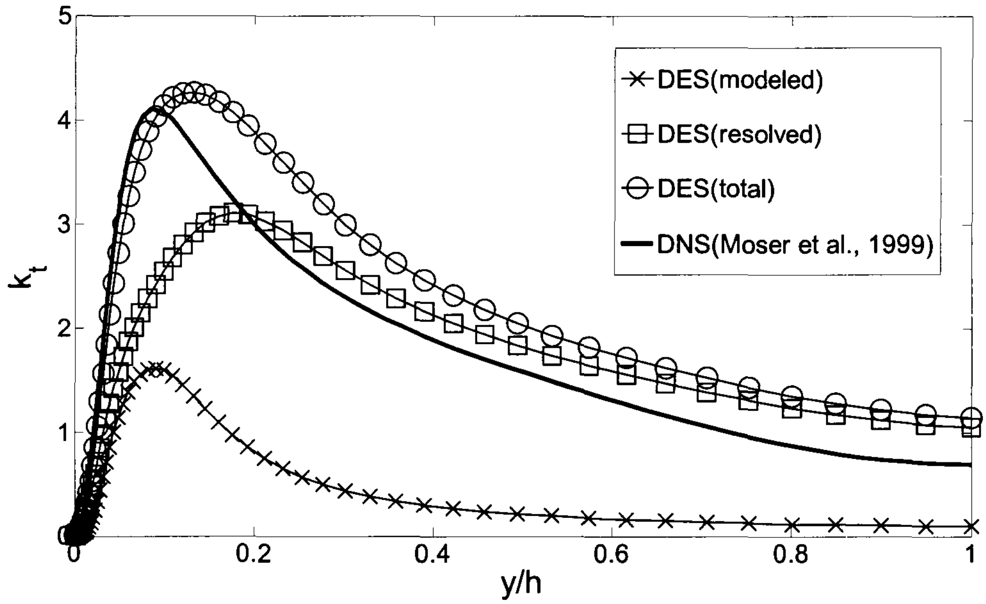

Figure 5.7 Turbulence kinetic energy profiles for DES-SST (case C1) and DNS (Moser et al., 1999) at Re_τ=180.

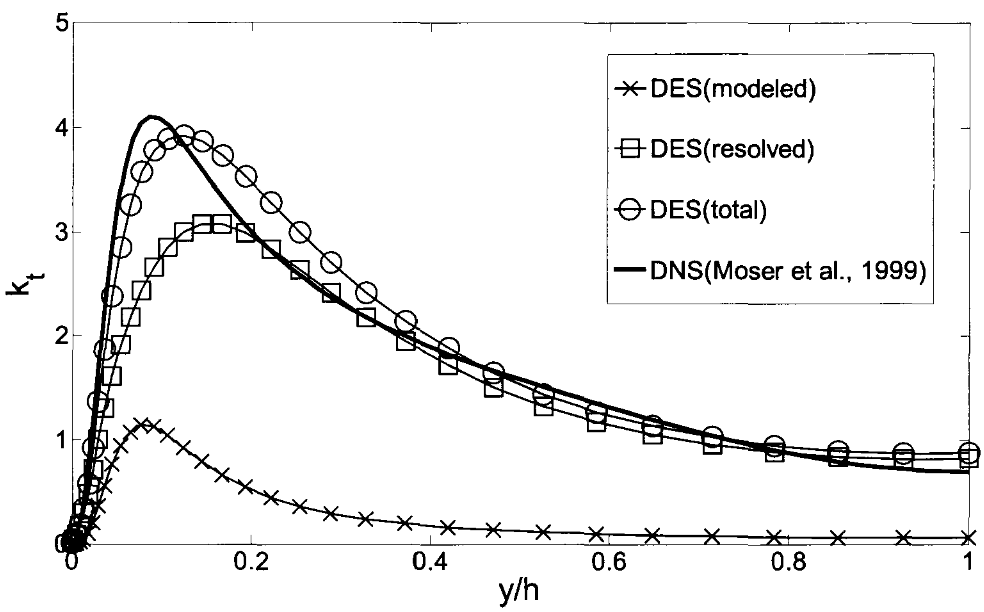

Figure 5.8 Turbulence kinetic energy profiles for DES-SST (case C2) and DNS (Moser et al., 1999) at Re_τ=180.

5.3.2 Re_τ*=590*

The same mesh was used for cases C3 and C4, at Re_τ=590, and closely resembled the mesh used in the DES study of Temmerman et al. (2005) at the same Reynolds number (mesh M1 in their study). The number of nodes in the *y*-direction are exactly the same. For case C3, a second-order central difference advection scheme was used throughout the domain, whereas for case C4, in the URANS region an upwind scheme was used and in the LES region a second-order central difference advection scheme was implemented. The DES-SST results are compared with the DES study of Temmerman et al. (2005) (denoted as DES (M1) in the figures) and DNS data of Moser et al. (1999). For these simulations (cases C3 and C4), the approximate location of switch over from URANS to LES, was at y^+=91 (y/h=0.15). The time history of the flow variables were monitored at points y^+=10 (URANS region) and y^+=458 (LES region) respectively. It was found from the present simulations, that the differences in the statistical description of the flow between cases C3 and C4 were extremely small. In fact, the time averaged velocity profiles from both the cases yielded similar results. The maximum difference in the time averaged modeled eddy viscosity between the two cases was around 1%. This showed that changing the advection scheme in the URANS region had no effect on the predictions of the DES-SST model. Therefore, in the present discussion results are presented for case C3. Figure 5.9 shows the time trace of the instantaneous stream-wise velocity (normalized using the channel bulk velocity) at both the monitored points. The effect of unsteady straining in the URANS region is evident. As stated earlier, the nature of resolved fluctuations in the URANS region is not clear and is an area of active research. The time averaged (mean) stream-wise velocity profile (normalized using the time averaged wall shear velocity) from the DES-SST model, in comparison with the DES (Temmerman et al., 2005) and DNS (Moser et al., 1999) results are shown in Figure 5.10. The DES-SST and DES (Temmerman et al., 2005) (DES (M1) in the figure) gave similar predictions for the mean velocity profile. In the LES region, both the DES models over predict the mean velocity, which was expected. The Von-Karman constant in the log-layer was found to be around 0.26. For the present simulations, the skin friction coefficient was under predicted by almost 14%. The DES prediction of the mean velocity profile is in qualitative agreement with the DNS result.

The variation in the time averaged modeled eddy viscosity (normalized using the kinematic viscosity of the fluid) is shown in Figure 5.11. The peak value of the eddy viscosity is in the URANS region and it drops down smoothly towards the LES region. The components of Reynolds shear stress (modeled, resolved), viscous shear stress and the total shear stress (sum of modeled, resolved components of Reynolds shear stress and viscous shear stress) variation as predicted by the DES-SST model is shown in Figure 5.12. The shear stresses are normalized by the time averaged wall shear velocity. Also shown in Figure 5.12 are the modeled, resolved components of Reynolds shear stress from Temmerman et al. (2005) (DES (M1) in the figure), and DNS Reynolds shear stress (Moser et al., 1999). For the present simulations, the modeled part of the shear stress is primarily in the URANS region, with its contribution being extremely small in the LES region. In the LES region, the Reynolds shear stress is essentially resolved. The agreement between the components (modeled, resolved) of the Reynolds shear stress for

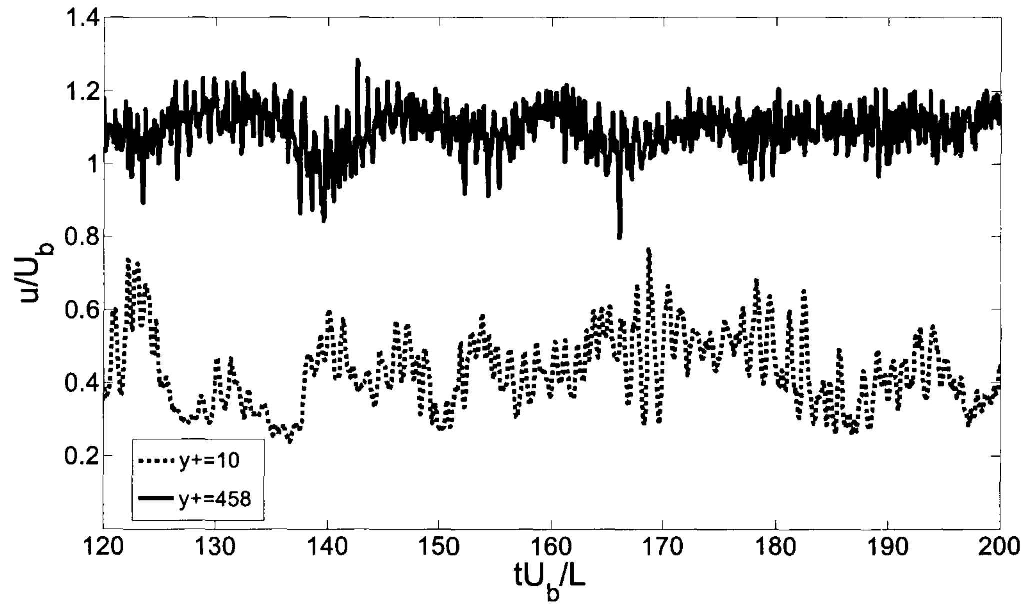

Figure 5.9 Time history of the instantaneous stream-wise velocity at Re_τ=590 for case C3.

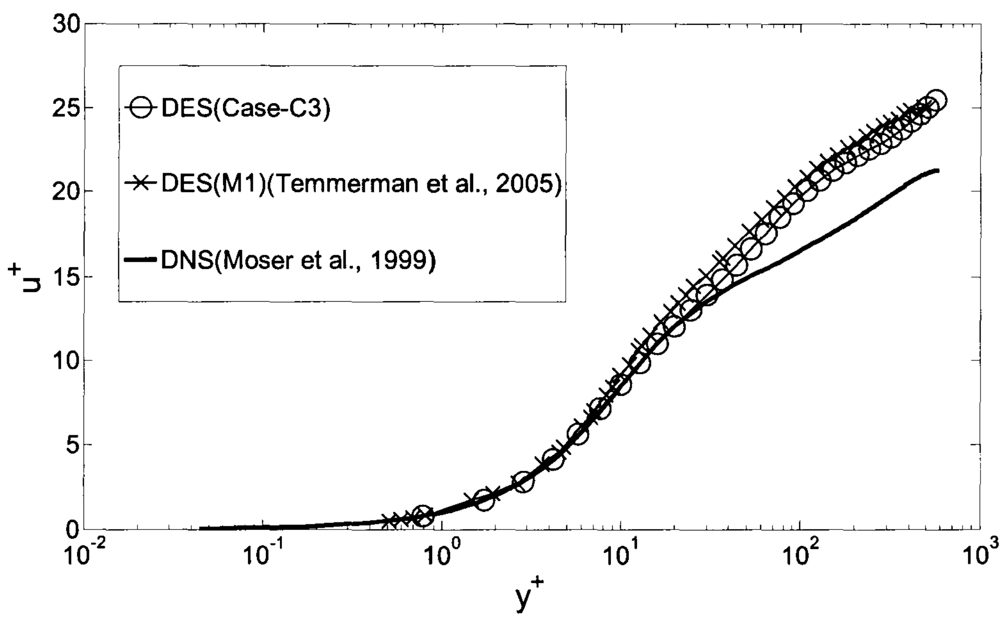

Figure 5.10 Time averaged stream-wise velocity profiles for DES-SST, DES (M1) (Temmerman et al., 2005) and DNS (Moser et al., 1999) at Re_τ=590.

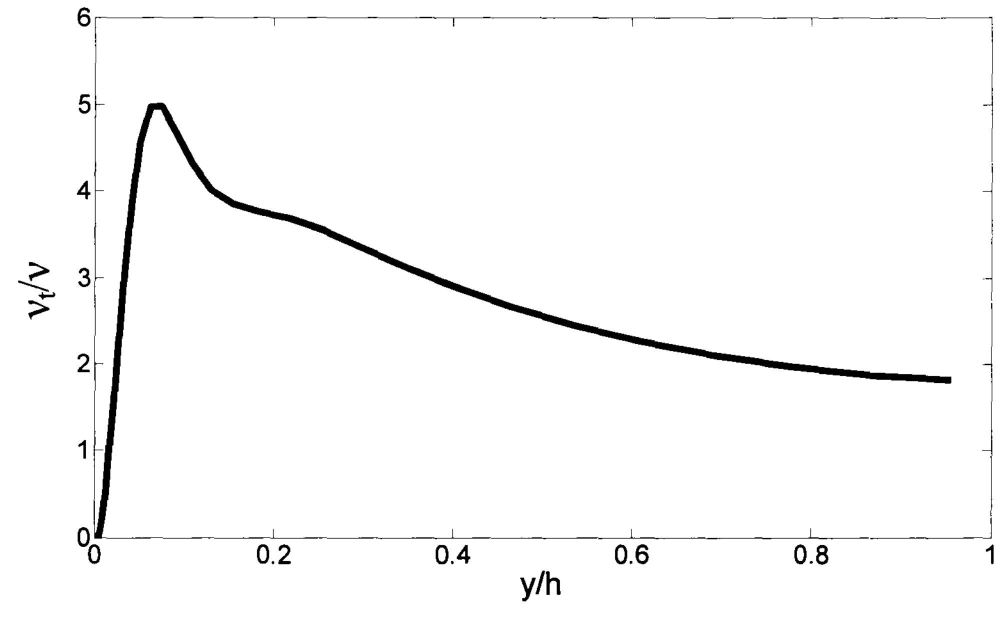

Figure 5.11 DES prediction of eddy viscosity profile at Re_τ=590.

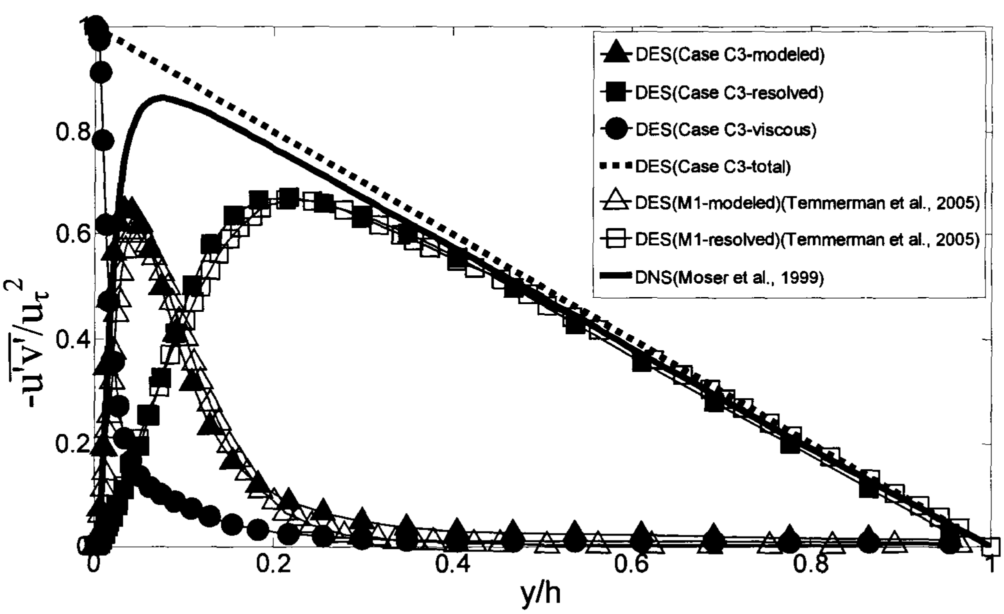

Figure 5.12 Shear stress profiles for DES-SST, DES (M1) (Temmerman et al., 2005) and DNS (Moser et al., 1999) at Re_τ=590.

the DES-SST model and DES study of Temmerman et al. (2005) is quite good.

The RMS fluctuations (normalized using the time averaged wall shear velocity) as predicted by the DES-SST model in comparison with the DNS data are shown in Figure 5.13. The fluctuation in the stream-wise direction (u'') is over predicted in the core of the LES region by the DES model and is consistent with previous findings (Davidson and Dahlstöm, 2005; Davidson and Billson, 2006). The DES model correctly predicts the peak value of the u'' fluctuation. The fluctuations in the wall-normal (v'') and span-wise (w'') directions are under predicted by the DES model, which is also consistent with findings from previous studies (Davidson and Dahlstöm, 2005; Davidson and Billson, 2006). In the near-wall region, the mesh for DES and hybrid RANS-LES methods are coarse in the wall-normal and span-wise directions. This is the reason why, v'' and w'' fluctuations are under predicted. The DES model correctly predicts that the v'' and w'' fluctuations reach the same value as the centre of the channel is approached, which is also shown by the DNS results.

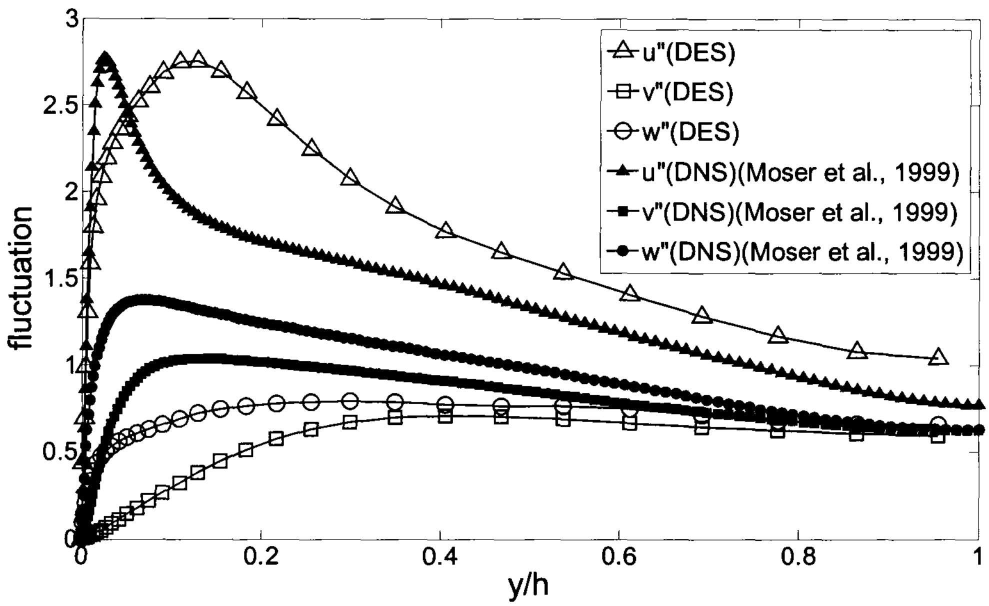

Figure 5.13 Turbulence intensity profiles for DES-SST and DNS (Moser et al., 1999) at Re_τ=590.

5.3.3 Re_τ=2000

The mesh for case C5 is similar to the DES study of Temmerman et al. (2005) at Re_τ=2000 (mesh M3 in their study). Case C6 had double the number of nodes in each of the three directions as compared to case C5. Thus, the effect of refining the filter width on the performance of the DES-SST model was studied between cases C5 and C6. The approximate location of the switch over from URANS to LES, was at y^+=320 (y/h=0.16) for case C5 and at y^+=180 (y/h=0.09) for case C6. Figure 5.14 shows the time trace of the instantaneous stream-wise velocity (normalized using the channel bulk velocity) for case C5, at the two monitored points, y^+=14 (URANS region) and y^+=1653 (LES region) respectively. The characteristic patterns in the time traces for the URANS and LES points in Figure 5.14 are very similar to the time traces at Re_τ=590. The DES-SST predicted time averaged stream-wise velocity profiles (normalized using the time averaged wall shear velocity) in comparison with the DES and LES results of Temmerman et al. (2005) is shown in Figure 5.15. Temmerman et al. (2005) performed LES simulations for the same channel dimensions as in the current study at Re_τ=2000. The LES model used was Smagorinsky SGS model (with constant C_s=0.1). The SGS viscosity was damped in the viscous sub-layer using the following damping function:

$$f_{v,SGS} = 1 - \exp\left(\frac{y^+}{5}\right) \tag{5.2}$$

In Figure 5.15, LES (M3) and LES (M4), denote the LES studies of Temmerman et al. (2005) for two different meshes M3 and M4. The mesh M3 was similar to the mesh of the present DES study i.e. case C5. The mesh M4 had 64 times the total number of nodes of

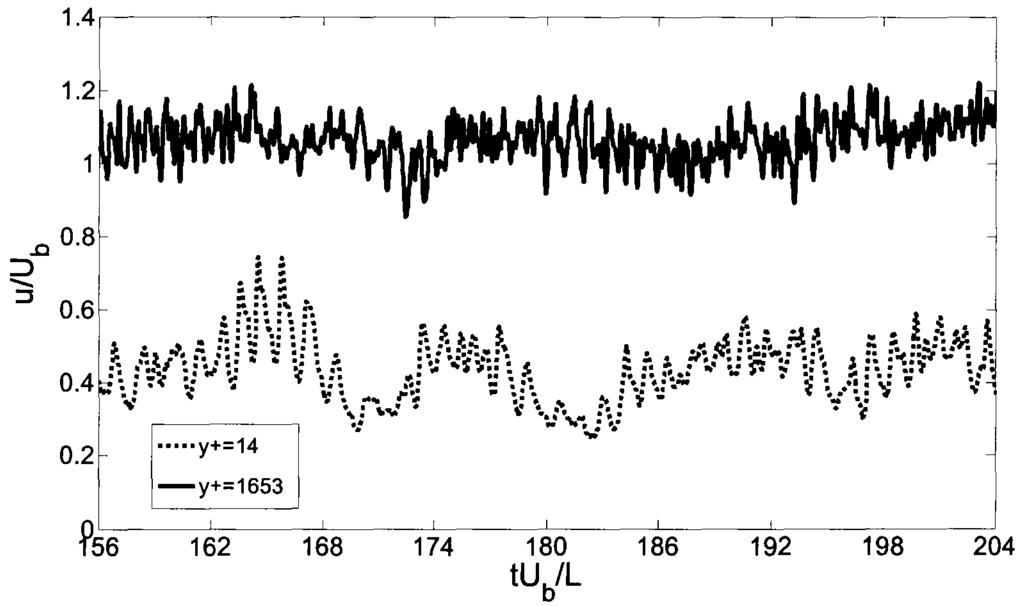

Figure 5.14 Time history of the instantaneous stream-wise velocity at Re_τ=2000 for case C5.

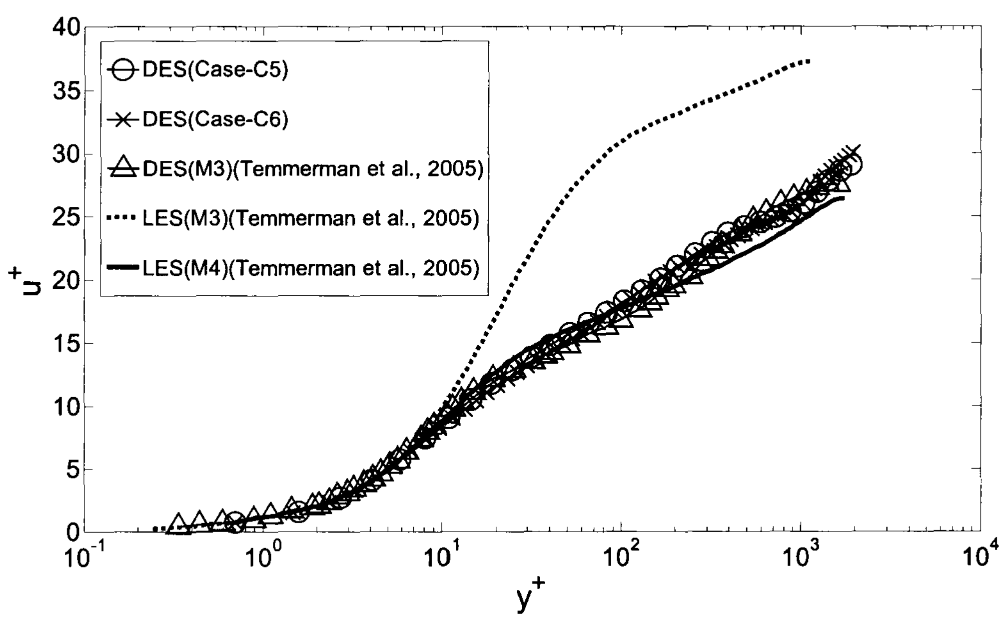

Figure 5.15 Time averaged stream-wise velocity profiles for DES-SST and DES, LES (Temmerman et al., 2005) at Re_τ=2000.

mesh M3, and was thus a highly refined mesh. The details of meshes M3 and M4 is provided in Temmerman et al. (2005). It is clear from Figure 5.15, that the DES-SST predictions of the time averaged velocity for both the cases, C5 and C6 are in good agreement with the DES results of Temmerman et al. (2005). The DES results are also in reasonably good agreement with the LES study (mesh M4). There is no significant difference in the prediction of the time averaged velocity between cases C5 and C6. The classical over prediction in the DES-SST mean velocity profiles (with reference to LES-M4) takes place around y^+=140. For the present simulations, the skin friction coefficient was under predicted by approximately 10%. The Von-Karman constant in the log-layer was found to be around 0.28. Temmerman et al.'s (2005) results (M3 and M4) indicate a strong sensitivity to the grid for the LES simulations. In contrast, the DES results reported here are much less sensitive to the grid (even though case C5 used a relatively coarse mesh similar to Temmerman et al.'s M3 grid). Thus, if computational cost is an issue at high Reynolds number, then performing a DES study is more appropriate than carrying out a coarse LES simulation.

The DES-SST predicted time averaged modeled eddy viscosity (normalized using the kinematic viscosity of the fluid) is shown in Figure 5.16. For both the cases, the peak in the eddy viscosity is in the URANS region, and it drops down smoothly in the LES region. The filter width for case C6 was smaller than case C5 by a factor of 2. The interface plane between the URANS and the LES region moved closer towards the wall as the filter width was reduced. The eddy viscosity (SGS viscosity) for case C6 is lower than case C5 by almost a factor of 3. Thus, as expected, refining the mesh (filter width)

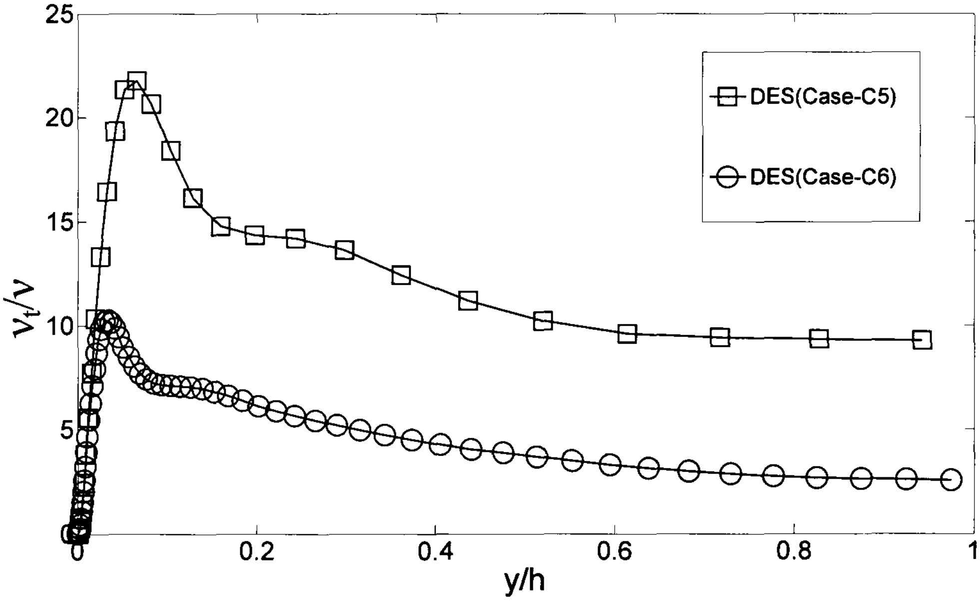

Figure 5.16 DES-SST prediction of eddy viscosity profile at Re_τ=2000.

reduces the contribution of the modeled scales in the total turbulence quantities. Figure 5.17 shows the comparison between cases C5 and C6, for the components of Reynolds shear stress (modeled, resolved), viscous shear stress and the total shear stress (sum of modeled, resolved components of Reynolds shear stress and viscous shear stress). The shear stresses are normalized using the time averaged wall shear velocity. The viscous shear stress for both the cases is the same since the mean velocity profiles are nearly the same. Case C5 has a larger modeled component than case C6, consistent with the larger filter width and eddy viscosity for C5. The resolved component is higher for case C6 than case C5. The total Reynolds shear stress (sum of modeled and resolved components) is the same for both the cases. Both cases predict the same linear variation of the total shear stress consistent with Eq. (5.1). Figure 5.18 shows the comparison of the modeled, resolved and total (sum of modeled and resolved components) Reynolds shear stress for case C5 and the DES study (mesh M3) of Temmerman et al. (2005). In the region, $0.02 \leq y/h \leq 0.5$, the modeled component of DES (M3) is larger than case C5. In the same region, the resolved component for case C5 is larger than DES (M3). From $y/h > 0.5$, the trend in the comparison of the resolved and modeled components for case C5 and DES (M3) reverses. The total Reynolds shear stress for case C5 and DES (M3) are very similar. Case C5, has a slightly smaller total Reynolds shear stress than DES (M3), in the region $y/h \geq 0.24$. It seems from the velocity profile, Figure 5.15, that case C5 has slightly steeper velocity than DES (M3) for the same region. From this comparison between the DES-SST model (case C5) and DES (M3) study based on the Spalart and Allmaras (1992) model, the DES-SST model and the Spalart and Allmaras

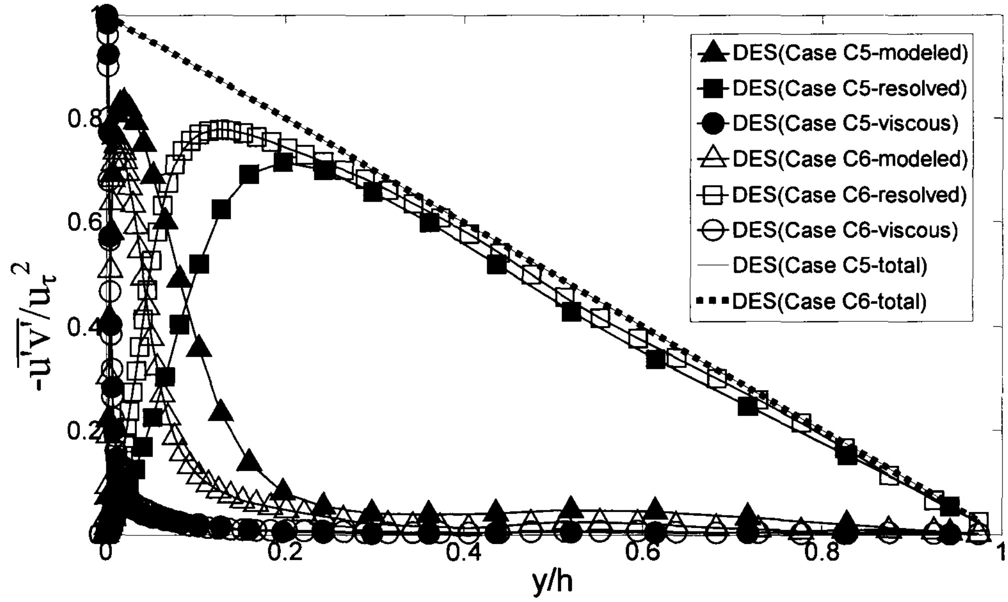

Figure 5.17 Shear stress profiles for DES-SST at Re_τ=2000.

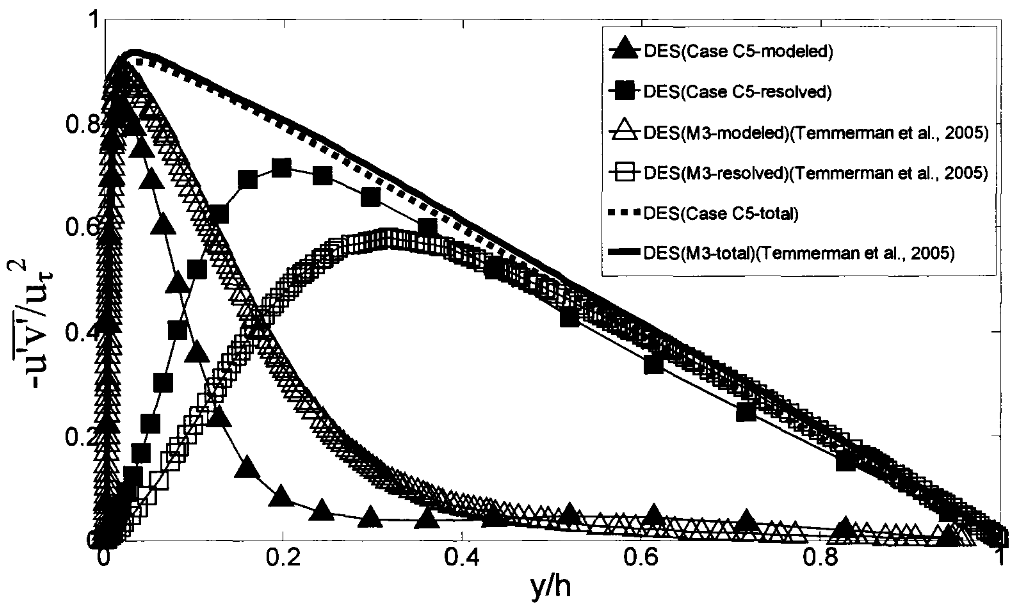

Figure 5.18 Reynolds shear stress profiles for DES-SST (case C5) and DES (Temmerman et al., 2005) at Re_τ=2000.

model have nearly the same performance.

Turbulence kinetic energy (normalized using the time averaged wall shear velocity) profiles for the modeled and the resolved components as predicted by the DES-SST model for case C5 and C6 in comparison with the DNS data of Davidson and Billson (2006) is shown in Figure 5.19. Davidson and Billson (2006) performed DNS study for a turbulent channel flow problem at Re_τ=2000. The dimension of the channel in their study was 4πh (stream-wise)×2h (wall-normal)×2πh (span-wise). The aspect ratio of the plane parallel to the flow was thus the same for the present case and the study of Davidson and Billson (2006). The DNS study of Davidson and Billson (2006) was performed using a 96^3 mesh (which is coarser than the grid employed for C6). The contribution of the modeled scales for case C6 is smaller than case C5 because of the fine mesh employed for case C6. It is clear from Figure 5.19, that the resolved component for case C6 is in relatively good agreement with the DNS data. It can be concluded that as the mesh is refined, the over prediction in the turbulence kinetic energy is reduced in the core of the LES region. Finally, the turbulence intensity (RMS fluctuations) profiles (normalized using the time averaged wall shear velocity) for case C6 in comparison with the DNS data of Davidson and Billson (2006) are shown in Figure 5.20. Similar to the lower Re_τ case, the DES model over predicts the anisotropy of the flow, but provides the correct trends seen in the DNS data.

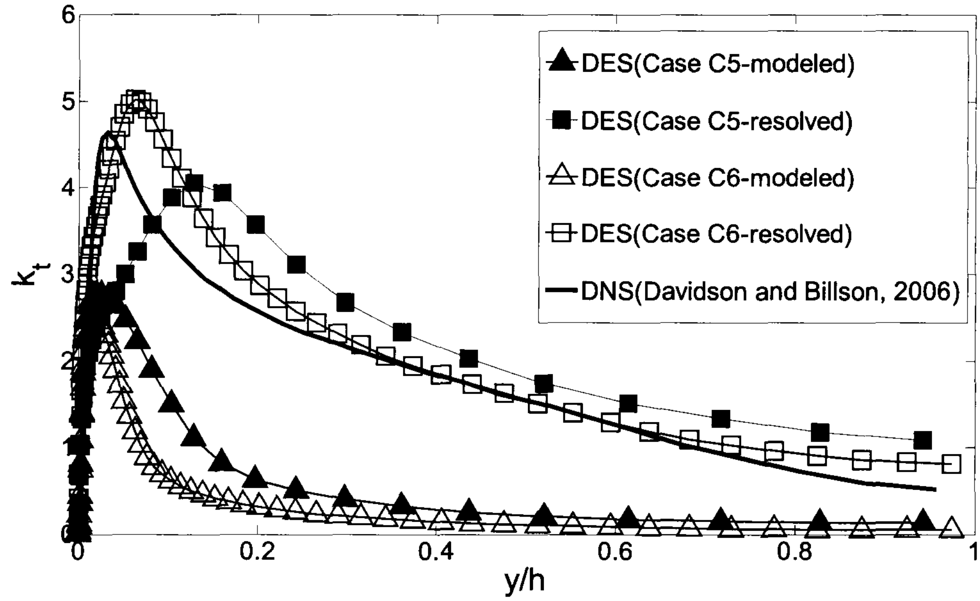

Figure 5.19 Turbulence kinetic energy profiles for DES-SST and DNS (Davidson and Billson, 2006) at Re_τ=2000.

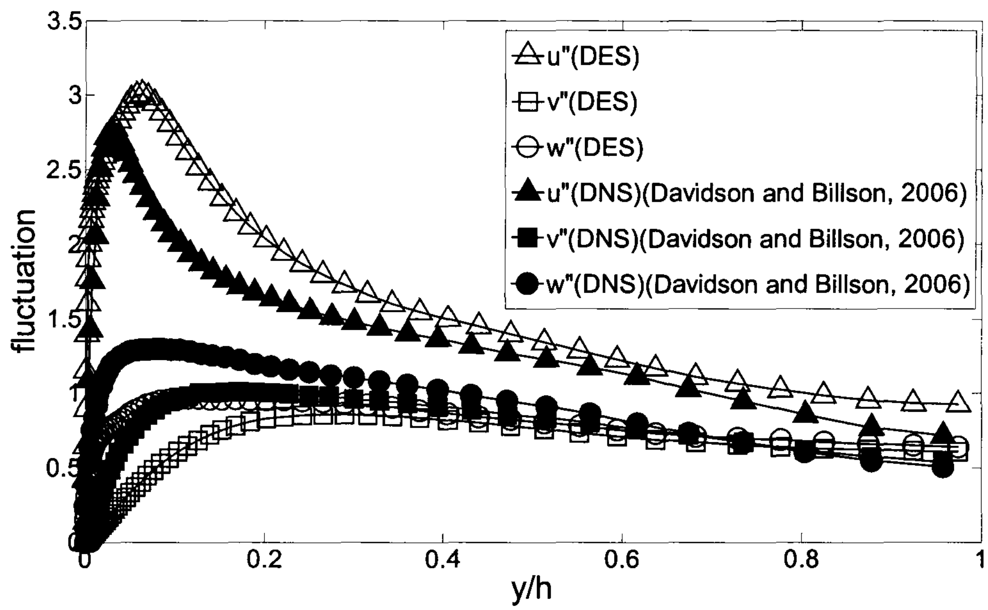

Figure 5.20 Turbulence intensity profiles for DES-SST (case C6) and DNS (Davidson and Billson, 2006) at Re_τ=2000.

5.4 Conclusion

Results of fully developed turbulent channel flow simulations using the DES-SST model of Strelets (2001) have been presented in this chapter. Simulations were performed for a wide range of Reynolds number and the results were compared to previously published DES, LES and DNS results for the same problem. The trends predicted in the statistical results were in agreement with the standard DES, LES and DNS data. In some cases, the quantitative agreement in the statistical data was quite good as well. The classical velocity mismatch was observed in the LES region of the DES model where the mean velocity profile was over predicted. This appears as a kink in the velocity profile in the interface region. This is due to the fact, that the LES region is supplied with incorrect turbulent scales from the URANS region. The anomaly in the mean velocity profile from the interface region onwards has been dealt by some previous researchers (Piomelli et al., 2003; Davidson and Billson, 2006) by the means of external forcing to the momentum equations, where proper turbulent fluctuations (from DNS data) are added as momentum sources. It was found from the present study that moving the interface closer towards the wall, did not have an effect on the mean velocity profile. As the mesh is refined or the filter width is reduced, a wider range of turbulent scales are resolved and the modeling aspect of the DES approach is minimized. The refinement coincides with an increase in the computational cost. It can be concluded from this study and previous investigations (Temmerman et al., 2005) that the hybrid RANS-LES or the DES approach gives better solutions than a coarse LES grid. Hybrid approaches are especially suitable for high Reynolds number computations, where information related to the large scale turbulent structures can be obtained using computational grid which is very cost effective, as has been shown in the current study. In fact, the grid for Re_τ=2000, i.e. case C5 had just 1.5% the number of mesh points of the fine LES grid of Temmerman et al. (2005) and provided fairly acceptable results.

CHAPTER 6

TWIN RECTANGULAR SUB-CHANNEL GEOMETRY: CFD ANALYSIS

6.1 Overview

In this chapter, numerical results from the DES-SST investigation on the twin rectangular sub-channel geometry are presented and discussed. The numerical results are compared and validated against the experimental dataset of Meyer and Rehme (1994). Meyer and Rehme (1994) have provided detailed results for channel no. 9 (see Table 6.1), so this forms the baseline case for the comparison. In addition to this, parametric studies were also carried out. The results presented are in the form of averaged flow field quantities and second order turbulence statistics, structural analysis, transient flow field analysis, anisotropic characteristics of the flow field, secondary flows, sectional plane contours of the vorticity fields, coherent structure identification and characterization of the fluid flow pulsations. A physics based theoretical model is proposed for the origin and cause of the instability mechanism, which leads to quasi-periodic fluid flow pulsation in the sub-channel geometry. Similarities and differences between the flow in sub-channel geometry and classical shear layer dominated flows are also highlighted.

6.2 Experimental description

Meyer and Rehme (1994) experimentally investigated the fluid flow in compound rectangular channels. The geometry investigated is shown in Figure 6.1, where the flow configuration was a vertical straight duct of rectangular cross section. The channel was made out of Perspex and had a length of L = 7000 mm. The channel was subdivided by inserts of Perspex into two rectangular sub-channels that were connected by a gap. The cross sectional view of the twin rectangular sub-channel geometry is shown in Figure 6.2. Overall 18 different geometrical configurations were studied by varying the gap depth d and the gap width g. Table 6.1 lists the dimensions of the geometries investigated. For the first nine geometries, the aspect ratio of the sub-channels were almost identical, but were connected by gaps of different sizes. Channel no. 11 was asymmetric, the cross section of one sub-channel was twice the cross section of the other sub-channel. Geometries 12 to 18 are termed as 'slots', which consisted of only one channel connected to gaps of the same width but different depths.

The fluid used in the experiments was air at room temperature and atmospheric pressure. The air was driven into the test section by a centrifugal blower. Care was taken to ensure that a symmetric flow distribution was obtained at the entrance of the channel.

6.2.1 Measurements

The experiments (Meyer and Rehme, 1994) were conducted in the Reynolds number (based on the bulk velocity and the hydraulic diameter of a single channel neglecting the gap) range of 1.25×10^5 to 3.12×10^5. The measurements were performed at five different flow rates, with a total variation of the velocity by a factor of 2.

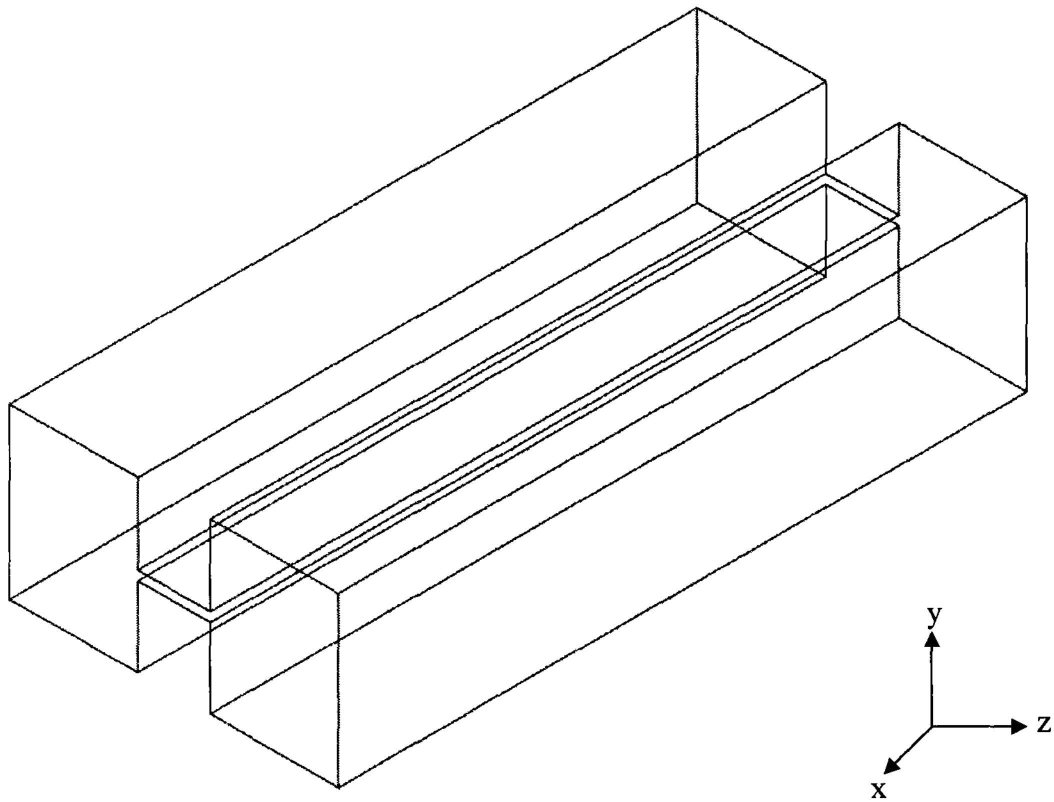

Figure 6.1 Isometric view of the twin rectangular sub-channel geometry with the associated coordinate directions.

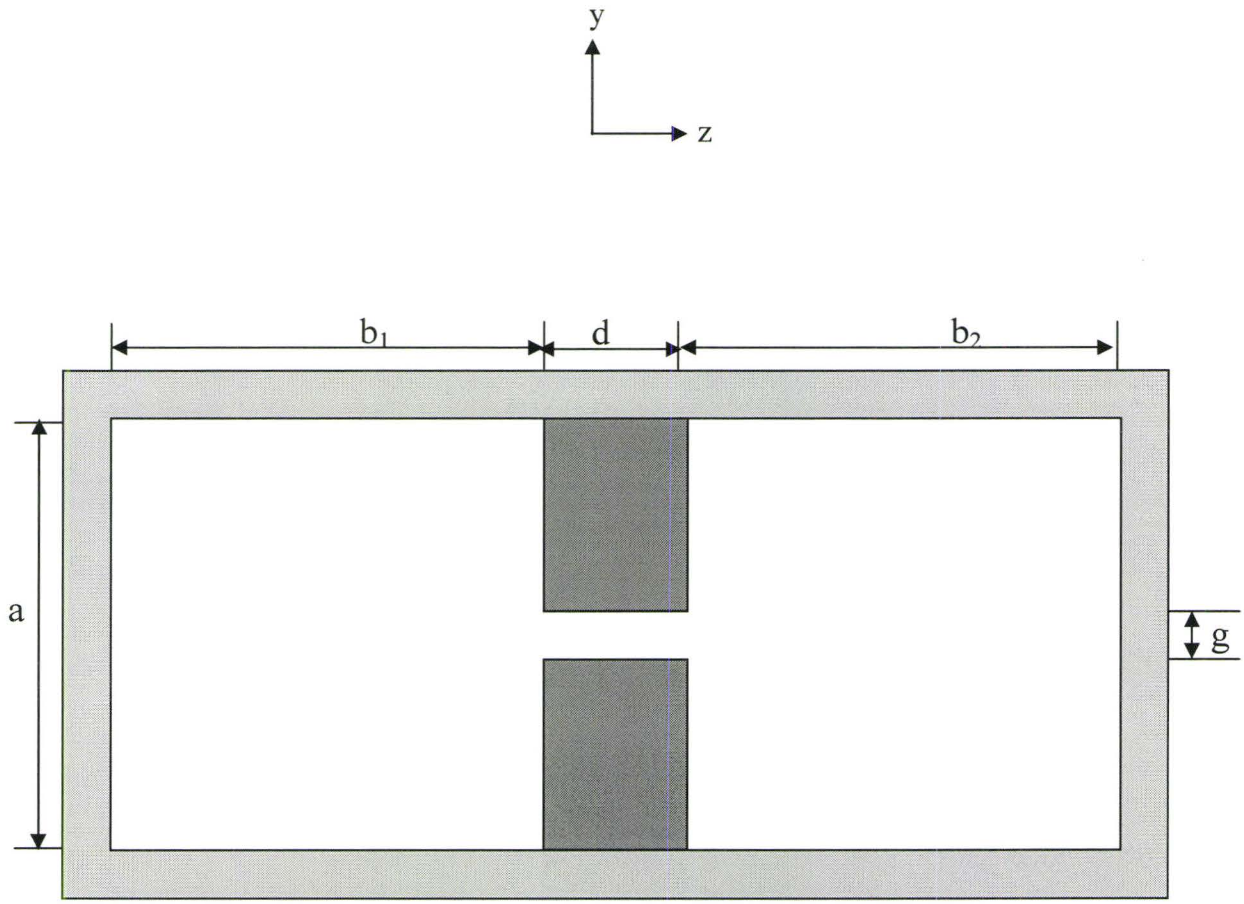

Figure 6.2 Cross sectional view of the twin rectangular sub-channel geometry.

Table 6.1 Dimensions of the twin rectangular sub-channel geometry investigated by Meyer and Rehme (1994).

Channel no	a (mm)	b_1 (mm)	b_2 (mm)	d (mm)	g (mm)
1	180.0	170.0	169.7	9.88	1.80
2	180.0	170.0	169.7	9.88	4.95
3	180.1	170.0	169.7	9.88	9.81
4	180.1	165.9	164.4	20.29	2.45
5	180.1	164.6	164.7	20.30	5.05
6	180.1	154.9	154.1	40.63	5.20
7	180.1	136.5	136.1	76.96	5.09
8	180.0	154.5	154.5	40.60	10.20
9	**180.0**	**136.4**	**136.2**	**76.96**	**10.00**
10	180.0	67.75	67.75	76.96	10.00
11	180.0	67.75	136.4	76.96	10.01
12	180.0	-	136.2	76.96	10.00
13	180.0	-	136.2	68.00	10.00
14	180.0	-	136.2	57.80	10.00
15	180.0	-	136.2	48.60	10.00
16	180.0	-	136.2	36.90	10.00
17	180.0	-	136.2	29.00	10.00
18	180.0	-	136.2	16.60	10.00

The measurements were taken at a position of 30 mm upstream of the open outlet. It was ensured that the length to hydraulic diameter ratio of the measurement plane was at least $L/D_h = 40$. The time averaged values of the axial velocity and the wall shear stresses were measured by Pitot and Preston tubes. The turbulent normal and shear stresses were measured using hot-wire anemometry with an x-wire probe. The maximum absolute uncertainties in the experimental results, including the drift of the anemometer, were estimated to be ± 3% for the instantaneous velocity in the stream-wise (x) direction and ± 0.2 m/s for the normal (y) and span-wise (z) velocities. The uncertainty in the turbulence intensities was found to be of the order of ± 1%. The maximum error in the turbulent shear stresses was found to be around ± 5% near the vicinity of the walls. The uncertainty in the velocity measurements was estimated to be ± 0.7% and that of the wall shear stress was found to be ± 1%.

The measurements were performed using a fully automated system, with a signal conditioner having four channels, filter, offset and amplification. The signals were digitized at a sampling rate of 2 kHz per channel. The overall measurement time was 48 sec and the total number of samples taken in a continuous stream were 96,000 per channel. Measurements were taken in the full rectangular channel at 493 to 783 points depending on the size of the cross section of the channel. The measurements of the turbulence intensities and the Reynolds stresses were performed with the low pass filter set at 10 kHz. The autocorrelation functions and the power spectral densities of the fluctuating velocities in the stream-wise (x) and span-wise (z) directions, and the cross correlation and cross spectra were measured at a number of positions in the gap and in the channel in the vicinity of the gap. The correlation and spectra measurements were performed at a sampling rate of 1.3 kHz, and the low pass filters were set to 500 Hz in order to avoid errors due to aliasing. The spectra and correlations were determined on-line by fast Fourier transform (FFT) using 128 blocks with 1024 sampling data points. It was found that in the stationary flow conditions, the statistical error is less than 10%.

6.3 CFD methodology

6.3.1 Computational considerations

The simulations were performed using ANSYS CFX 11.0. The computations were conducted on the PC-SHAKA cluster at the Nuclear Safety Analysis group in McMaster University. The cluster is configured with 6 nodes and each node is comprised of 4 individual Quad core processors, with a processor speed of 1024 MHz and an overall RAM of 32 Gb. A single node was used for the computations and the code was locally parallelized into 4 partitions using the MPICH parallelization algorithm. On an average, it took approximately 6 weeks for a simulation to complete.

6.3.2 Twin rectangular channel flow setup

The simulations were performed on the computational domain shown in Figure 6.3. The stream-wise, normal and span-wise directions are indicated by x, y and z respectively. The instantaneous velocity components (in brackets) in the respective directions are also shown in the figure. The bulk (mean) flow was in the stream-wise direction. The time history of the flow variables were monitored at points 1-9, situated along the span-wise direction. The normal coordinate of the monitor points was fixed at y

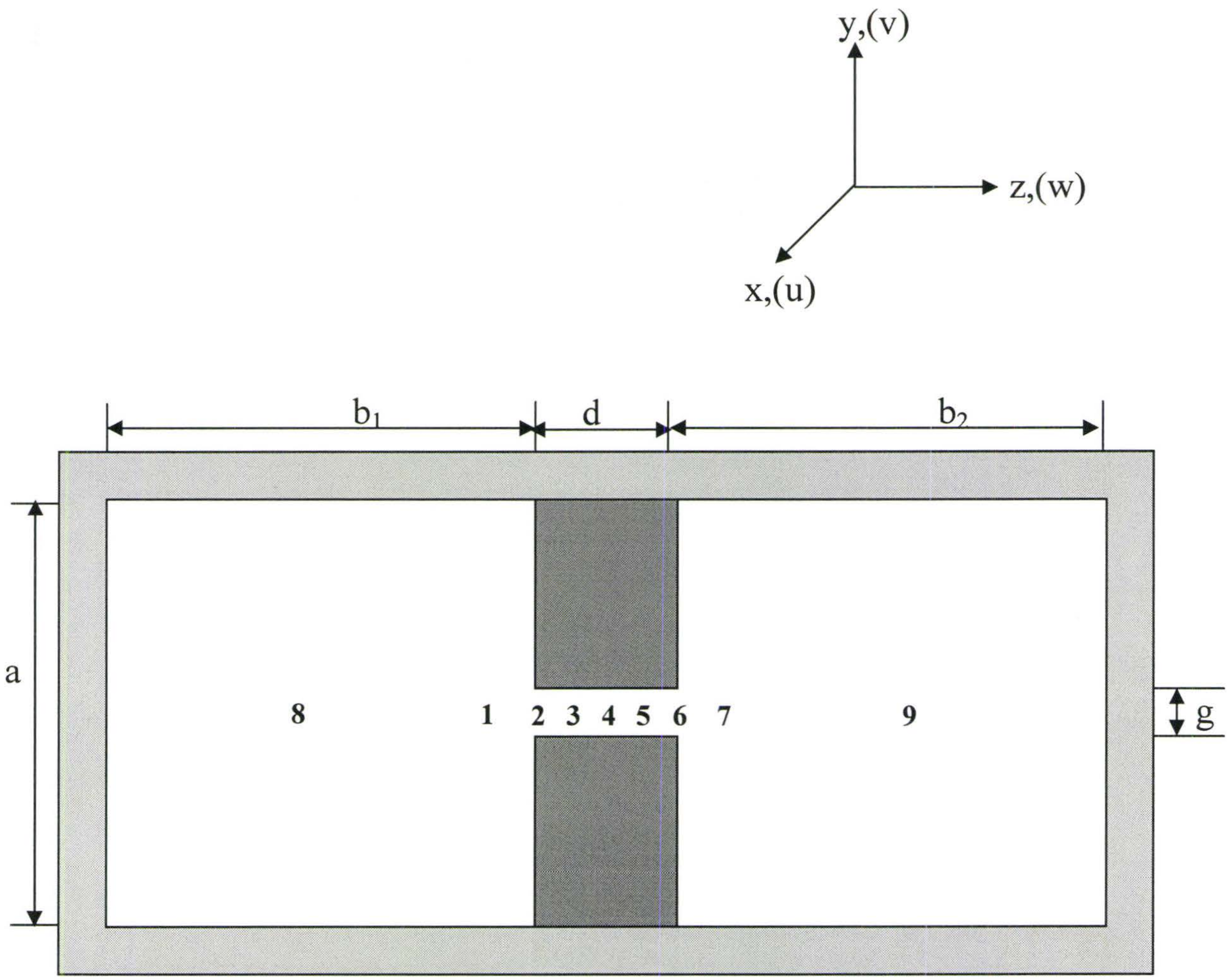

Figure 6.3 Computational domain for the twin rectangular sub-channel geometry.

= *a/2*. The z-coordinate of the monitor points 1-7, were obtained from the experiments of Meyer and Rehme (1994). Monitor points 2-6 are located along the length of the gap. Monitor points 2-6 are equidistant from one another, with a separation distance of 10 mm between the respective points. Monitor point 4 is located at the centre of the gap and monitor points 2 and 6 are situated at the two edges of the gap respectively. The distance between monitor points 1 and 2, and, 6 and 7 is 19.2 mm. Monitor points 8 and 9 are located at the centre of the two sub-channels respectively. In addition to this, 11 monitor points were set axially along each of the two edges of the gap respectively, with a separation distance of 40 mm between the subsequent points. Additional monitor points were set in order to obtain spatial cross-correlation functions.

6.3.3 Choice of computational domain length and case studies

The flow under consideration is fully developed turbulence and is statistically homogeneous in the stream-wise direction. Under these conditions, either periodic boundary conditions or inlet/outlet boundary condition can be used in the homogeneous direction. The use of inlet/outlet boundary conditions presents several challenges. The fundamental issue deals with the required length of the computational domain. With coupled inlet/outlet boundary condition, the length of the computational domain is usually very long and to simulate the exact experimental length of the test section, in the present case i.e. 7000 mm (Meyer and Rehme, 1994), is computationally unfeasible with the available computational resources. Therefore, the use of inlet/outlet boundary conditions was not a viable option.

Periodic boundary conditions in the stream-wise direction have been successfully used to simulate flows in regular channels or ducts (Moser et al., 1999) and substantially reduce the computational cost in comparison to an inlet/outlet boundary condition. The length of the domain in this case is usually determined using two point spatial correlations in the stream-wise direction, which has to be lower than an arbitrarily low threshold value, in order to ensure that the periodic boundary condition has been correctly implemented (Pope, 1999). Experimental studies on regular duct flows have also provided information on the wave number spectra. The correct determination of the two point correlation function depends on how accurately the wave number spectra is correctly reproduced by a given domain length and mesh size. For a uniform grid in the stream-wise direction, the set of wave numbers that the numerical simulation can correctly reproduce is given by:

$$\overrightarrow{k_m} = \frac{2\pi}{L_x} m \overrightarrow{u_x} \tag{6.1}$$

where L_x is the length of the domain in the stream-wise direction, $\overrightarrow{u_x}$ is the versor of the stream-wise direction and $m \in \left[0, \left(L_x / \Delta_x\right)\right]$, where Δ_x is the mesh size in the stream-wise direction. In regular channel flow computations, the size of the turbulent structures is small compared to the length of the domain. The determination of the length of the domain using Eq. (6.1) is therefore, a reasonable estimate.

The present investigation of sub-channel flow has some fundamental differences with regular channel or duct flow. Large-scale coherent structures are present in the stream-wise direction which lead to quasi-periodic flow pulsations. The presence of coherent structures cause large-scale phase correlation in the turbulence quantities at significant distances both in the stream-wise and span-wise directions. The length of the computational domain in this case should be such that it can hold the essential wave numbers associated with the flow pulsation phenomena. If a resolution limit is available on the wave number spectra, then the length of the domain can be estimated as:

$$L_x > \frac{2\pi}{k_{res}} \tag{6.2}$$

Since information related to wave number spectra is not available from the experiments (Meyer and Rehme, 1994), an estimate of the length of the domain is not possible using Eq. (6.2). Intuitively, for the sub-channel flow an optimal computational length could then be based upon the numerical simulation capturing sufficient number of integer structures in the domain. It is expected that this philosophy would be suitable to correctly reproduce the effect of periodic boundary condition on the domain, in terms of accurate prediction of frequency and wavelength associated with the flow pulsations. Meyer and Rehme (1994) have provided information on the wavelength of the fluctuations or the stream-wise spacing between the large-scale structures formed near the gap. This data was used to estimate the computational length of the domain.

Table 6.2 provides the details of different test cases that were investigated in terms of the length of the domain in the stream-wise direction, Reynolds number Re (based on the hydraulic diameter of the sub-channel and bulk velocity) and Re_τ (based on the time averaged wall shear velocity and half gap height 'g/2'), and the cross-sectional dimensions of the twin rectangular sub-channel geometry (Figure 6.3). Case C1 will be referred to as

Table 6.2 Description of the case studies investigated for the twin rectangular sub-channel flow.

Cases	L_x (mm)	Re	Re_τ	a (mm)	b_1 (mm)	b_2 (mm)	d (mm)	g (mm)
C1(reference)	730	2.2×10^5	299	180	136.4	136.2	76.96	10
C2	**330**	2.2×10^5	299	180	136.4	136.2	76.96	10
C2(a)	**330**	2.2×10^5	299	180	136.4	136.2	76.96	10
C3	**992.8**	2.2×10^5	299	180	136.4	136.2	76.96	10
C4	730	2.2×10^5	149.5	180	136.4	136.2	76.96	**5**
C5	730	2.4×10^5	326	180	**67.75**	**67.75**	76.96	10
C6	730	$\mathbf{3.12\times10^5}$	424	180	136.4	136.2	76.96	10

the reference case for which detailed results will be provided, and compared to the base line case of Meyer and Rehme (1994). The experimental wavelength of the large-scale structures was reported as 200 mm (Meyer and Rehme, 1994). The length of the domain was set to 730 mm, which is larger than the experimental wavelength by a factor of 3.6. This length is sufficiently long enough to capture approximately four structures each of two alternating sequences, in a very idealized sense. Sensitivity to this length was tested by performing simulations with two other channel lengths viz. 330 mm and 992.8 mm, which are represented by cases C2 , C2(a) and C3 respectively. The length of the longer channel (992.8 mm) was chosen to avoid an integer multiple of the reference case channel length (730 mm) while allowing for computational costs to not be too overwhelming. The channel length of 992.8 mm was longer than the channel length of 730 mm by a factor of 1.36. A shorter channel with a length of 730 mm was also considered. Note that the channel length of 992.8 mm was longer than the channel length of 330 mm by a factor of 3.01, and was thus roughly an integer multiple of it. The channel length of 330 mm would completely capture two structures of each sequence. The difference between cases C2 and C2(a) was in the number of nodes in the normal direction that was used to resolve the flow in the gap region. Differences between these two cases will be presented in more detail in the next sub-section. The channel length of 992.8 mm would completely capture five structures of each sequence. However, with this length, a sixth structure of one sequence would be partially truncated.

Parametric studies in relation to the reference case C1, are represented by cases C4, C5 and C6 respectively. The effect of gap height 'g' and the width 'b_1', 'b_2' of the sub-channels on the dynamics of the flow pulsations were studied, and are represented by cases C4 and C5 respectively. Case C4 had a gap height smaller than case C1 by a factor of 2. The width of the sub-channels for case C5 were smaller than case C1 by a factor of 2. The effect of Reynolds number was investigated and is depicted by case C6.

6.3.4 Mesh design

The mesh design concept was same for all the cases and was based on a multi block structure. It was found from preliminary studies on mesh design for the sub-channel geometry, that using a 5 block structure can make the DES-SST model operate in the LES mode in the gap region, without having an overly large number of grid points in the domain. For the sub-channel geometry shown in Figure 6.3, a total of 5 blocks were created and were snapped onto the geometry. The 5 block structure on the sub-channel geometry is shown in Figure 6.4. Blocks 1, 2, 3, 4 created quarter sub-channels in the domain. Block 5 is the central block that covers the entire gap region and spans through the sub-channels as well. The nodal points are distributed along the edges of the blocks, which then gets translated to the curves of the sub-channel geometry. With the multi block structure, hexahedral elements are created in the volume of the domain.

The cross-sectional distribution of nodes for blocks 1, 2, 3, 4 were same. Bi-exponential meshing law was used in these regions to expand the mesh in the normal and span-wise directions. With this kind of meshing law, the grid expansion factor (growth ratio of cells) can be controlled. A grid expansion factor of about 1.03 was used in both the directions. The interfaces between block 5 and the remaining blocks were meshed exactly in the same way for the span-wise direction, as was done for the individual

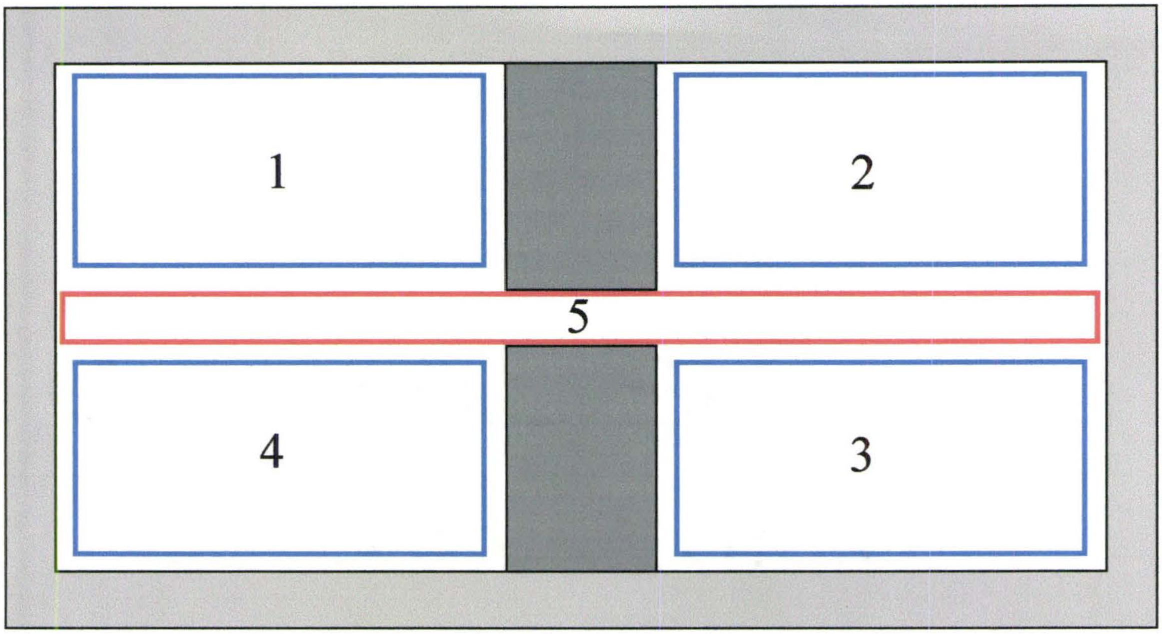

Figure 6.4 Concept of the multi block structure for mesh generation in sub-channel geometry.

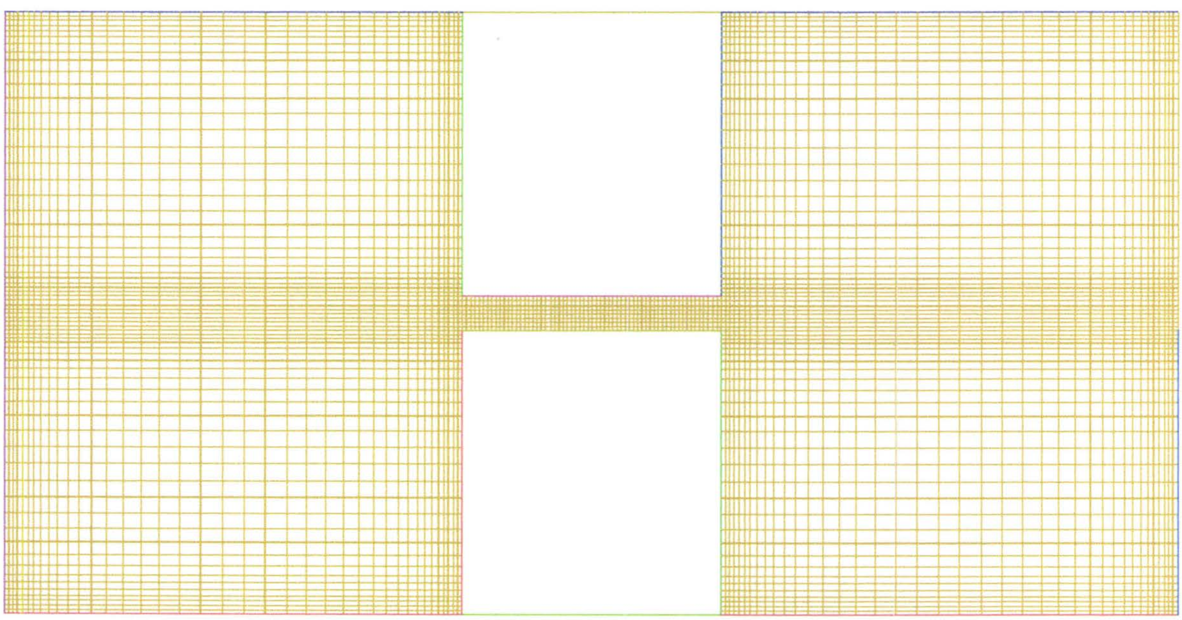

Figure 6.5 Cross-section of a mesh for the sub-channel geometry (case C1).

blocks 1, 2, 3, 4. For the entire block 5, the grid points in the normal direction were uniformly distributed. Inside the gap region, a uniform mesh was applied for the distribution of nodes in the span-wise direction. The cross-sectional distribution of the nodes ensured that the cells at the edges of the gap and sub-channels have the same aspect ratio. It was also ensured that the cells at the interfaces between block 5 and the remaining blocks have the same aspect ratio (except for case C2(a)). In the stream-wise direction, a uniform mesh was applied. A typical cross-section of a mesh is shown in Figure 6.5. As mentioned before, mesh cross-sectional design was same for all cases.

For the different cases investigated, tables 6.3 and 6.4 provide the details of the distribution of nodes and the mesh size respectively. From table 6.3, for case C1, the total number of grid points in the domain was 590,900 (N_{total}). In the stream-wise direction, 100 nodes (N_x) were used. In the quarter sub-channels (represented by blocks 1, 2, 3, 4) 30 nodes were used in the normal direction (N_{ysub}) and 40 nodes in the span-wise direction (N_{zsub}). The gap was modeled using 9 grid points in the normal direction (N_{ygap}) and 63 grid points in the span-wise direction (N_{zgap}). A square cross-section of the face of the grid cell normal to the flow was obtained in the gap region. The aspect ratio of the grid cells for case C1 varied from 1.43 to 5.94. With reference to case C1, the number of grid points in the steam-wise direction changed proportionately with the length of the channel for cases C2 and C3 respectively. For these two cases, the cross-sectional distribution of the nodes was exactly the same as case C1. The effect of grid resolution in the gap was studied between cases C2 and C2(a). Case C2 had 9 grid points, whereas case C2(a) had 18 grid points in the normal direction to resolve the flow in the gap region.

Table 6.3 Distribution of nodes for the test cases investigated.

Cases	N_{total}	N_x	N_{ysub}	N_{zsub}	N_{ygap}	N_{zgap}	Aspect Ratio
C1	590,900	100	30	40	9	63	1.43-5.94
C2	271,814	46	30	40	9	63	1.43-5.91
C2(a)	330,188	46	30	40	18	63	1.43-12.5
C3	803,624	136	30	40	9	63	1.43-5.92
C4	622,900	100	32	40	9	63	1.16-11.6
C5	590,900	100	30	40	9	63	3.44-5.94
C6	944,240	110	33	50	12	84	1.31-7.37

Table 6.4 Details of mesh for the test cases investigated.

Cases	Δx (mm)	Δy_{wsub} (mm)	Δz_{wsub} (mm)	Δy_{maxsub} (mm)	Δz_{maxsub} (mm)	Δy_{gap} (mm)	Δz_{gap} (mm)	Δy^+_{wsub}	Δz^+_{wsub}	Δy^+_{wgap}
C1	7.37	1.25	1.25	5.14	6.47	1.25	1.24	70	72	62
C2	7.37	1.25	1.25	5.14	6.47	1.25	1.24	70	72	62
C2(a)	7.37	1.25	1.25	5.14	6.47	0.59	1.24	70	72	29
C3	7.37	1.25	1.25	5.14	6.47	1.25	1.24	70	72	62
C4	7.37	0.64	1.24	6.38	6.49	0.64	1.24	36	72	30
C5	7.37	1.25	1.25	5.14	2.14	1.25	1.24	116	122	112
C6	6.69	0.91	0.93	5.09	5.2	0.91	0.93	66	68	59

Figures 6.6 and 6.7 show the cross-section of the mesh in the gap for cases C2 and C2(a) respectively. The total number of grid points was slightly larger for case C4 in comparison to case C1 but the grid point distribution in the gap was exactly the same. Case C5 had exactly the same number of grid points as case C1. The higher Reynolds number case represented by C6 had a larger number of grid points in the cross-section.

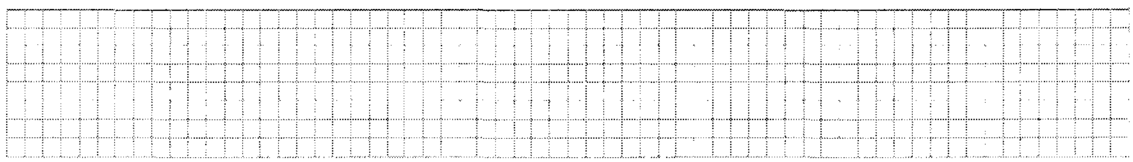

Figure 6.6 Cross-section of the mesh at the gap for case C2.

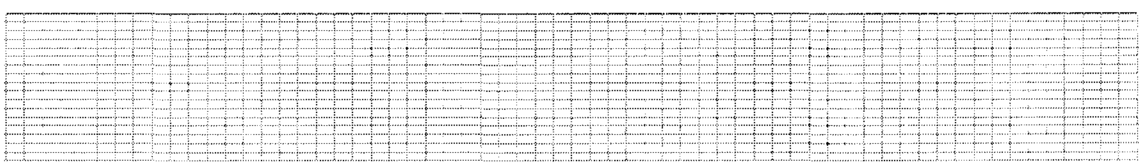

Figure 6.7 Cross-section of the mesh at the gap for case C2(a).

Table 6.4 provides the details of mesh spacing for the stream-wise grid cells, and the first nodal points with respect to the walls of the sub-channel geometry. The mesh dimensions are also indicated in wall (+) units (non-dimensional units of length based on the time averaged wall friction velocity and fluid kinematic viscosity). In all the computations, it was the stream-wise grid spacing, Δx that set the filter width. The normal and the span-wise distance of the first nodal point from the sub-channel walls are indicated by Δy_{wsub} and Δz_{wsub} respectively. The maximum cell dimension in the normal and span-wise directions for the regions where the grid was expanded are indicated by Δy_{maxsub} and Δz_{maxsub} respectively. The normal and the span-wise cell size in the gap are indicated by Δy_{gap} and Δz_{gap} respectively. The distance of the first grid point from the walls of the gap in terms of wall units is represented by Δy^{+}_{wgap}.

6.3.5 Numerical approach, boundary conditions and statistical data

For all the cases, the numerical approach was same. The time discretization was carried out using the second order backward Euler scheme. For all the equations (continuity, momentum and turbulence) in the LES region, the advection scheme used by the code is second-order central difference, which reduces the effect of numerical dissipation. However, in the URANS region, either the upwind (first-order or second-order) or the second-order central difference scheme can be used as the advection scheme. When the solver advection scheme is set as upwind, the code uses an upwind scheme in the URANS region which automatically changes to a central difference scheme once the DES model switches to LES. A central difference scheme is used throughout the domain, when the solver advection scheme is set as central difference. Home et al. (2009) had found that changing the advection scheme in the URANS region had no effects on the prediction of the DES-SST model. For the present simulations, in the URANS region, the advection scheme for the continuity and momentum equations was second-order upwind and for the turbulence equations it was first-order upwind.

The fluid used in the simulations was air at room temperature and atmospheric pressure. In the simulations, periodic boundary conditions were applied in the stream-wise direction. Wall boundary conditions were applied in the normal and span-wise directions. In the experiments of Meyer and Rehme (1994), the bulk axial velocity was reported. This data was used to calculate the overall mass flow rate for the sub-channel geometry. Mass flow rate was thus specified in the stream-wise direction to drive the flow. The time step used in the simulations was based on the frequency of the flow pulsations observed in the experiment (Meyer and Rehme, 1994). The time step size was chosen such that there is sufficient temporal resolution to capture the dynamics of the flow pulsations and that the average CFL number is less than one. The initial velocity field for the DES-SST runs were obtained from a steady shear stress transport (SST) simulation. The code has the ability to superimpose specified velocity fluctuations on the initial velocity field to "kick start" the process, and this was used. The initial turbulent velocity fluctuation used in the simulation was taken from the experimental data on the maximum turbulent intensity, as reported by Meyer and Rehme (1994). Table 6.5 provides the mass flow rates, the time step size and the initial velocity fluctuation for the various test cases.

The simulations were run for a sufficiently long time to be statistically independent of the initial condition. The simulations were run till 5000 time steps yielding an equivalent ($L/D_h = 70$), at which point statistics such as mean velocity, velocity correlations and Reynolds stresses were accumulated for another 5000 time steps, i.e. total of 10,000 simulation time steps. For the reference case C1 and case C6, the simulation was extended beyond 10,000 time steps and was run for a total of 20,000 time steps. It was found that the statistical significance of results for 10,000 time steps was the same as that of 20,000 time steps.

Table 6.5 Simulation parameters for the different test cases.

Cases	Mass flow rate (kg/s)	Time step (sec)	Velocity fluctuation (m/s)
C1	1.2697	10^{-4}	3.14
C2	1.2697	10^{-4}	3.14
C2(a)	1.2697	10^{-4}	3.14
C3	1.2697	10^{-4}	3.14
C4	1.2634	10^{-4}	3.14
C5	1.1112	10^{-4}	3.14
C6	1.65	7×10^{-5}	4.08

6.4 Effect of grid resolution

The grid resolution study was performed in the gap in order to determine the threshold number of grid points so as to perform a well resolved LES in the gap region. A well resolved LES in the gap can correctly reproduce the dynamics of the flow pulsations in the gap region. The effect of grid resolution was studied by varying the number of grid points in the normal direction in the gap region. The cases chosen for the grid resolution study are represented by C2 and C2(a), having 9 and 18 grid points respectively in the normal direction in the gap region. The grid structure for cases C2 and C2(a) was similar (see Tables 6.3 and 6.4), except for the number of grid points in the normal direction in the gap. For case C2, out of the 9 grid points in the gap, 2 grid points were on the respective walls of the gap, with the remaining 7 grid points in the LES region. For case C2(a), out of the 18 grid points in the gap, 2 grid points were on the respective walls of the gap, 6 grid points were in the URANS region and 10 grid points in the LES region respectively. The approximate switch over from URANS to LES was at $y^+ \sim 61$ for case C2 and at $y^+ \sim 117$ for case C2(a). Quantitative comparison between the two cases for the time averaged wall shear velocity (for the gap walls), time averaged bulk velocity in the gap and the computed skin friction coefficient is provided in Table 6.6. The skin friction coefficient was calculated as:

$$C_f = \frac{\tau_{w,avg}}{\frac{1}{2}\rho U_{b,gap}^2} = 2\left(\frac{u_{\tau,avg}}{U_{b,gap}}\right)^2 \tag{6.3}$$

In Eq. (6.3), $\tau_{w,avg}$ is the time averaged wall shear stress at the gap walls, $U_{b,gap}$ is the time averaged bulk velocity in the gap and $u_{\tau,avg}$ is the time averaged wall shear velocity. The predicted time averaged wall shear velocity for both the cases are very similar. This possibly indicates that the time averaged axial pressure drop in the gap should be similar for both the cases. The bulk velocity in the gap is larger for case C2 as compared to case C2(a). Meyer and Rehme (1994) have not provided data related to the time averaged bulk velocity in the gap. A comparison of the span-wise variation for the time averaged axial velocity (normalized using the time averaged channel bulk velocity) between cases C2 and C2(a) is shown in Figure 6.8. These profiles were obtained along the centre line (located at $y = a/2$) in the span-wise direction. The z-axis (span-wise length) is normalized with the distance between the centre of the sub-channels, which is represented by 'b'. Thus, z/b = 0 and z/b = 1, represent the centre of the sub-channels respectively. The edges of the gap are located at z/b = 0.31 and z/b = 0.69 respectively. The velocity profile in Figure 6.8 was obtained by averaging the cross-section (span-wise) profiles in the stream-wise direction. In the stream-wise direction, 30 different locations were chosen and for each location the span-wise variation in the time averaged axial velocity was obtained. A composite velocity profile was thus created by averaging these 30 profiles. The averaging process helped to smooth out and remove the statistical inconsistencies if any, in the velocity profiles. This process of averaging in the stream-wise direction was applied to different cross-sectional profiles and contours, which will be presented in the subsequent sections of this chapter. It is clear from Figure 6.8, that the axial velocity in the central region of the gap is larger for case C2 as compared to case C2(a). This is consistent with the data obtained for the overall bulk velocity, as indicated in Table 6.6.

Table 6.6 Comparison of predicted variables for grid resolution study.

Cases	$u_{\tau,avg}$ (m/s)	$U_{b,gap}$ (m/s)	C_f
C2	0.769	13.65	0.00635
C2(a)	0.772	12.85	0.00722

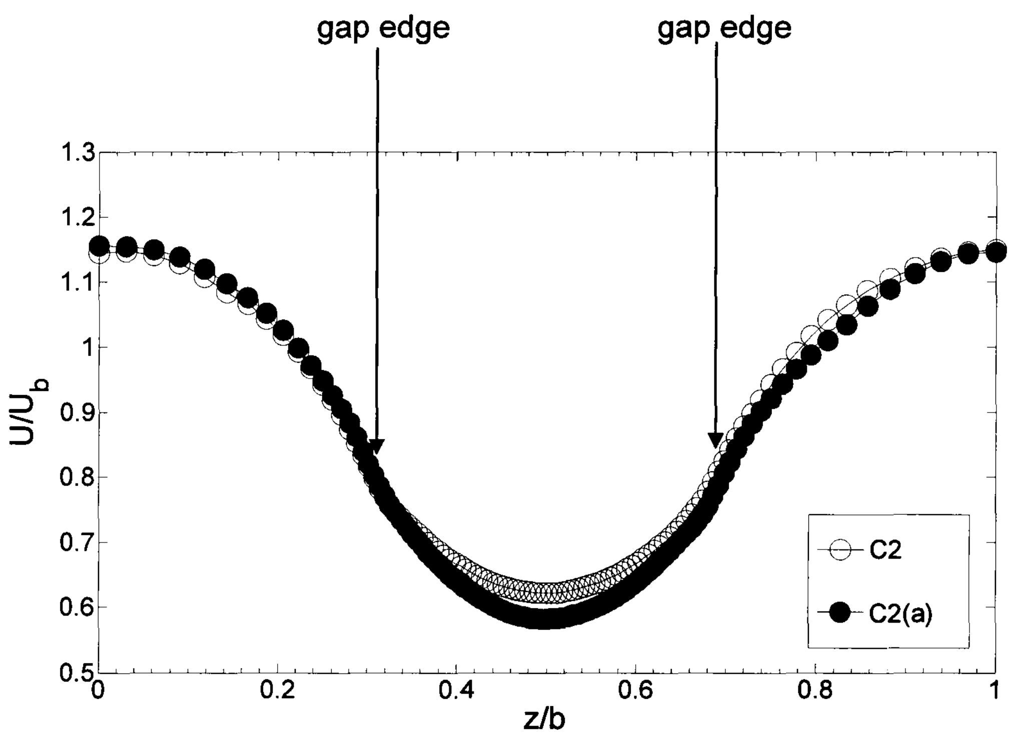

Figure 6.8 Comparison of the span-wise variation in the time averaged axial velocity for the grid resolution study (U_b = 21.5 m/sec, z/b: normalized span-wise length, b: distance between centre of sub-channels).

Overall, the difference in the velocity profiles for the two cases is not very significant. Figure 6.9 shows the variation in the modeled, resolved components of turbulent kinetic energy and total (sum of modeled and resolved) turbulent kinetic energy profiles for cases C2 and C2(a) respectively. The turbulent kinetic energy is normalized using the experimental time averaged wall shear velocity, which was reported as 0.924 m/s (Meyer and Rehme, 1994). The reported experimental wall shear velocity included all the walls except the walls in the gap. It is clear from Figure 6.9, that for both the cases, the modeled component of turbulent kinetic energy is the same. Case C2(a) with a finer grid resolution in the gap as compared to case C2, resolves more turbulent kinetic energy in the gap, as evident from Figure 6.9. As a result, the total turbulent kinetic energy predicted in the gap is larger for case C2(a) as compared to case C2. Results from the grid resolution study for the resolved turbulent kinetic energy are as expected, since, complete grid independent results for resolved components of turbulent flow field quantities cannot be obtained for LES based simulations using implicit filtering. Both the cases predict similar peak values in the turbulent kinetic energy profiles at the edges of gap. It can be concluded from both the cases that a significant amount of turbulent kinetic energy was resolved rather than modeled around the gap region. The characteristics of the turbulent kinetic energy profiles will be discussed later on in this chapter.

The success of a simulation for the sub-channel geometry problem primarily depends on how accurately the dynamics of the flow pulsation phenomena are predicted at the macroscopic level. Accurate prediction of the flow pulsation dynamics, will lead to accurate prediction in the correct levels of sub-channel mixing. Figure 6.10 shows a

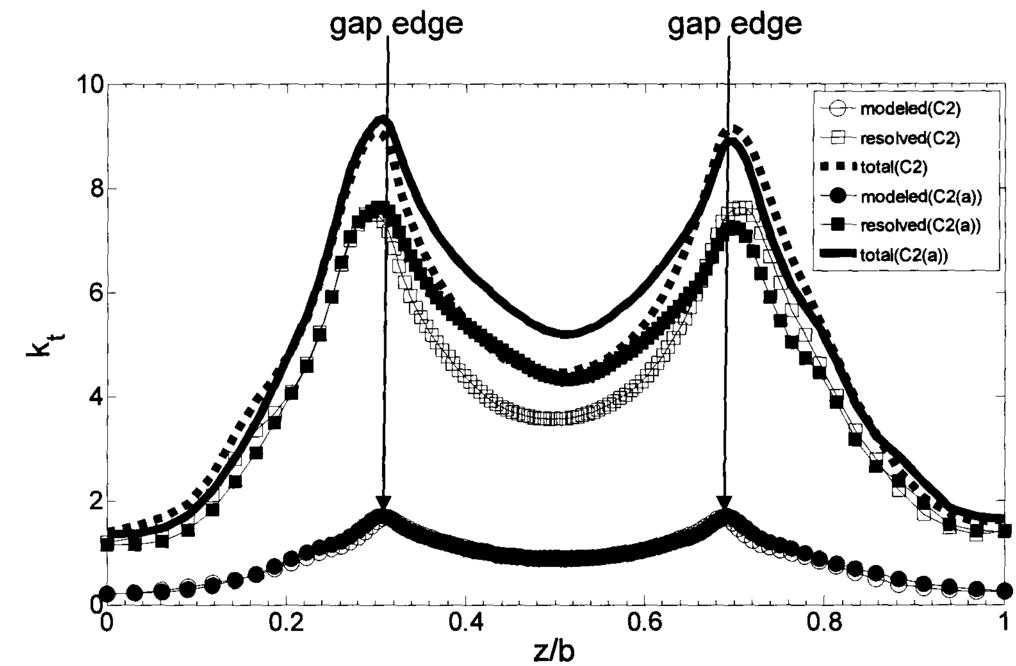

Figure 6.9 Comparison of the span-wise variation in the turbulent kinetic energy for the grid resolution study (z/b: normalized span-wise length, b: distance between centre of sub-channels).

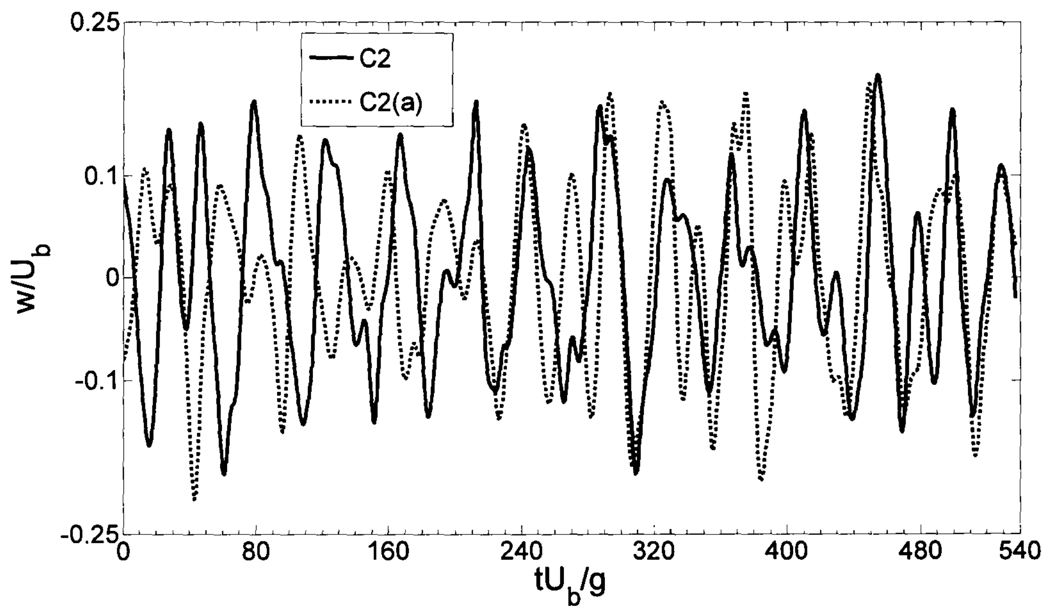

Figure 6.10 Comparison of the time trace of the span-wise velocity for the grid resolution study.

comparison in the time traces of the span-wise velocity (normalized using the channel bulk velocity) at the gap can centre for cases C2 and C2(a) respectively. Both cases show similar trends for the span-wise velocity in terms of the quasi-periodic nature and amplitude levels of the velocity. It was found from the grid resolution study that both the cases predict similar dynamical characteristics (frequency, wavelength, amplitude levels of velocity) associated with the flow pulsations. Thus, from an overall perspective, it can be concluded that the difference in the predictions from both the cases is not very significant. The gap in a sub-channel geometry acts as a conduit for the mass and momentum transfer across the sub-channels, and having 9 grid points in the normal direction in the gap was found to be sufficient to accurately predict the statistical and dynamical characteristics associated with the flow pulsation phenomena. It is not important to have an overly refined grid in the gap (particularly in the normal direction) as long as the grid can correctly predict the velocity profile shown in Figure 6.8 which is the cause of the instability mechanism (description discussed in Section 6.5.7) responsible for flow pulsations. However, the grid should have sufficient resolution capability in the span-wise direction near the gap edge region to capture the velocity defect (discussed in Section 6.5.7) shown in Figure 6.8. In the next section, detailed results for the reference case C1 and comparison with the experimental results (Meyer and Rehme, 1994) will be presented.

6.5 Results and analysis for case C1

6.5.1 Blending regions and mesh resolution

It is important to identify the zones of URANS and LES in the flow field in order to determine if the designed mesh has the capability of switching the DES-SST model from the URANS mode to LES mode in the regions of interest. For the present case, it is the gap region and its vicinity that are of great interest. The DES blending function in the DES-SST model is used to switch the numerical scheme from an upwind to a central difference scheme. It provides an indication of where LES is applied and where URANS is used. Figure 6.11 shows the contour plot of the DES blending function. A value of 0 (dark blue region) indicates pure LES numerics (central difference) and a value of 1 (dark red region) indicates pure RANS numerics (second order upwind). A value between 0 and 1 indicates that the advection term is computed as a blend of central and upwind schemes. An expanded view of Figure 6.11 is shown in Figure 6.12, concentrating on the gap region. For the gap, it is around the central region, where the pure central difference scheme is operating. It is clear that for almost the entire sub-channel region, the central difference scheme is operational. It was found that the numerics pertaining to the URANS zone is concentrated to a very thin near-wall region. The approximate location of pure central difference numerics in the gap and sub-channel regions is around $y^+ \sim 124$ and $y^+ \sim 141$ respectively. A more precise criteria for demarcating the regions of LES and URANS is the switching function, F_{DES} given by Eq. (4.20). Figure 6.13 shows the contour plot of the switching function, and Figure 6.14 shows its expanded view. A value greater than 1 indicates the LES region while the URANS region is indicated by a value less than 1. In the contour plot, the thin green regions near the walls indicate the URANS zones. The red regions indicate the LES zones. It is clear that the LES mode is dominant in the gap and the sub-channels. In the central region (location of the monitor points) of the gap, the LES mode is operational. The distribution of the nodal points in the gap in the different zones is exactly the same as case C2. It can be thus concluded that the designed mesh was successful in exploiting the zonal features of the DES-SST model. The designed mesh was also successful in limiting the URANS zones to very thin regions near the wall, and made the LES mode operational in the regions of interest.

In DES based simulations, it is of fundamental importance to see the capability of the mesh to resolve important scales of motion. It was shown in the previous section that the mesh for case C2 has sufficiently good resolution capability. The grid spacing used for case C1 is identical to that used for C2, but a longer domain is used for case C1. A further discussion on the resolving ability of the mesh for case C1 is provided, focusing primarily in and around the gap region. The variation of modeled and resolved components of turbulent kinetic energy (normalized using the experimental wall shear velocity) along the gap height is shown in Figure 6.15. This profile was obtained along a line that is located equidistant from the edges of the gap. The final profile was obtained by stream-wise averaging of profiles at different axial locations. It is clear that there is significant resolved motion, especially in the vicinity of the central region of the gap, where the LES mode is operational. The resolved component of turbulent kinetic energy is larger by almost a factor of 4 as compared to the modeled component, in the central region of the gap. On an average, approximately 73% of the turbulent kinetic energy in

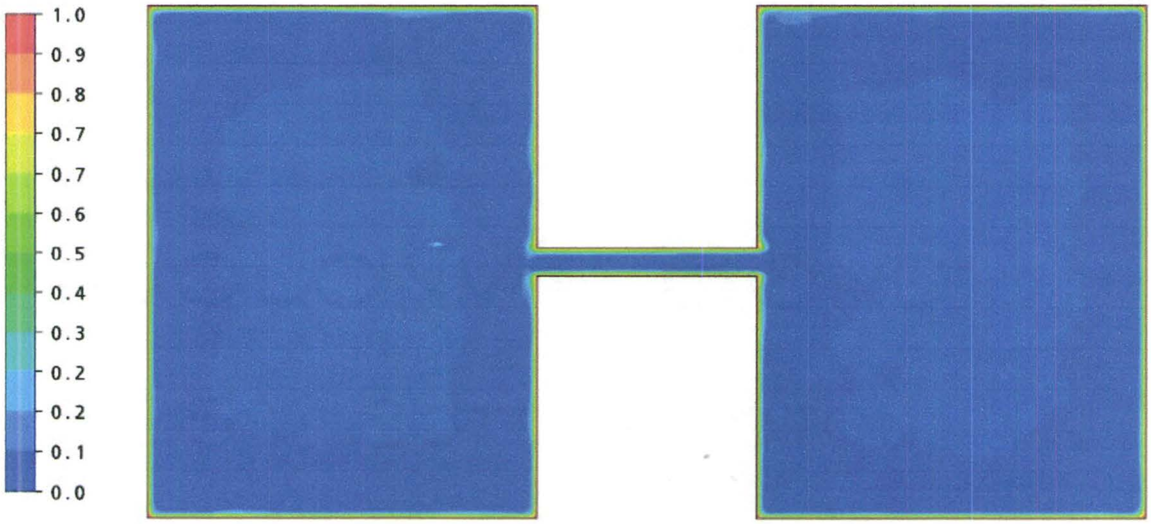

Figure 6.11 Contour of the DES blending function (Dark blue: Pure central difference scheme, Dark red: Pure second order upwind scheme).

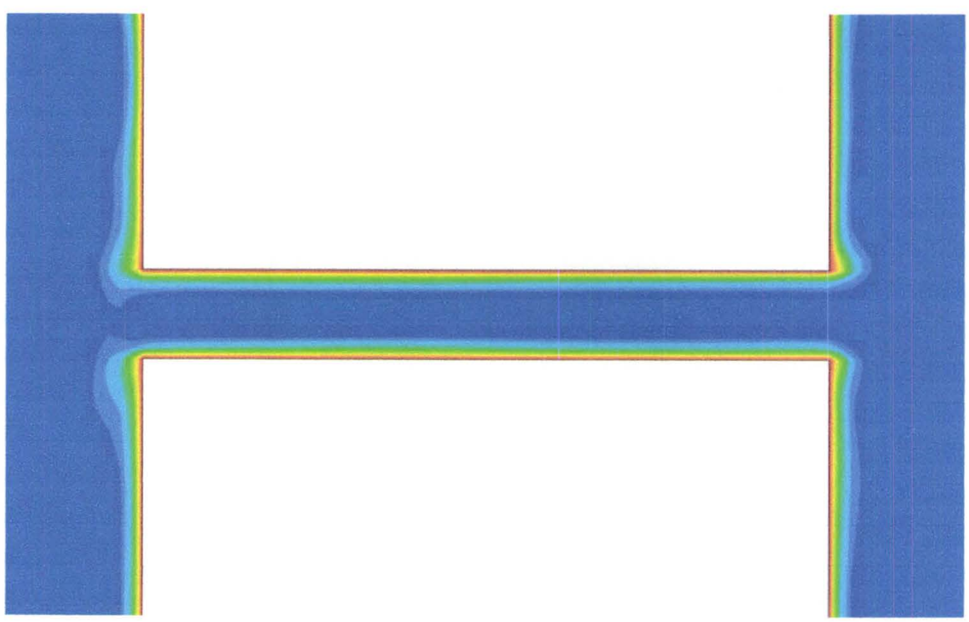

Figure 6.12 Expanded view of the DES blending function.

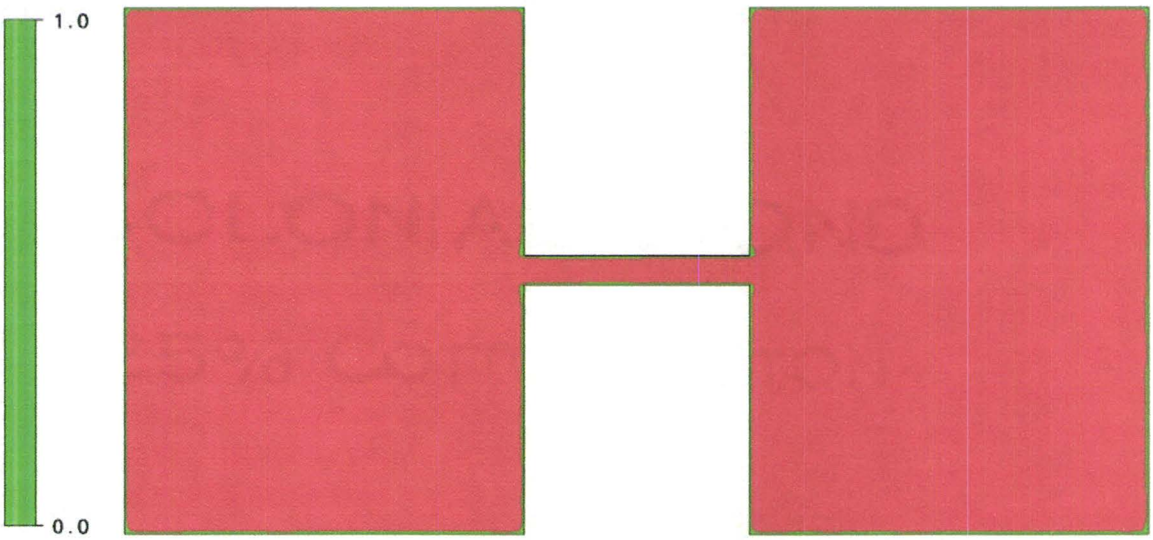

Figure 6.13 Contour of the DES-SST switching function (Red region: LES zones, Green region: URANS zones).

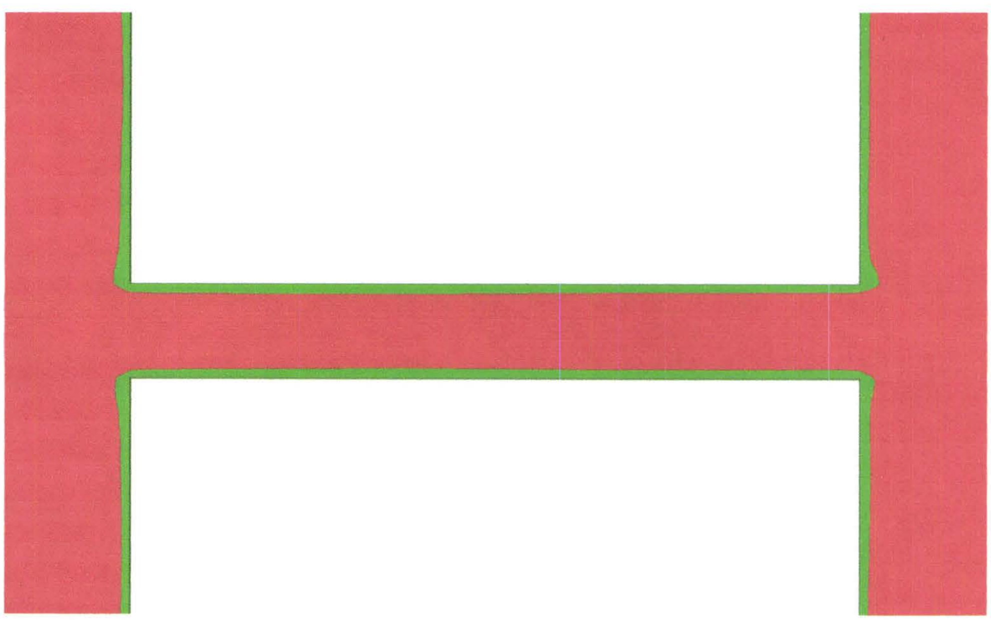

Figure 6.14 Expanded view of the DES-SST switching function.

the LES region ($0.12 \le y/g \le 0.87$) is provided by the resolved scales of motion. Figure 6.16 shows the variation of modeled, resolved components of turbulent kinetic energy and total turbulent kinetic energy (normalized using the experimental wall shear velocity) along the span-wise direction. Figure 6.16 was created exactly the same way as Figure 6.9. It is clear from Figure 6.16 that the resolved component of turbulent kinetic energy is significantly larger than the modeled component. At the edges of the gap, the resolved component is larger than the modeled component by almost a factor of 5. The peaks in turbulent kinetic energy at the edges of the gap, is a characteristic feature of flows in sub-channel geometries. This feature will be discussed in more detail in the subsequent sections of this chapter. Approximately 80% of the turbulent kinetic energy in the central region of the gap, where the LES mode is operational, is provided by the resolved scales of motion. Thus, from Figures 6.15 and 6.16 it is concluded that the designed mesh for the DES-SST model was able to resolve a significant portion of the flow field.

6.5.2 Averaged flow fields and quantitative comparison

The averaged flow fields discussed in this section, have been obtained through both temporal, and spatial averaging in the stream-wise direction. As mentioned earlier, the temporal averaging was performed for 0.5 sec of simulation time. This averaging time was chosen, in order to have convergence for the stream-wise velocity, and stream-wise turbulent intensity in the gap region. The time averaging operation was performed for a sufficiently long time so as to obtain time independent statistical profiles. Nevertheless, spatial averaging was performed in the stream-wise direction to remove any statistical inconsistencies. The averaged flow field helps to assess the quality of the simulation.

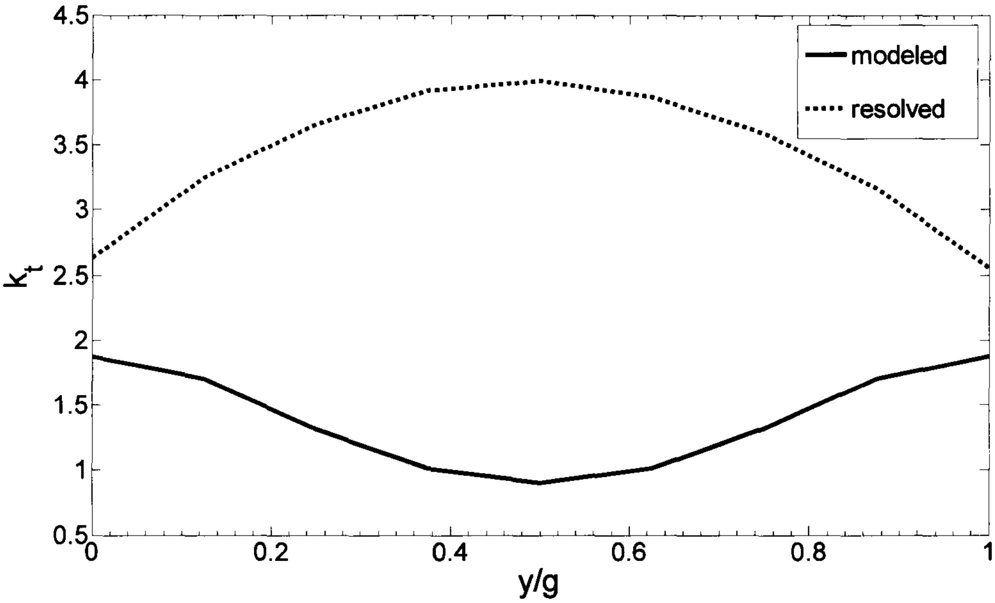

Figure 6.15 Variation of turbulent kinetic energy in the gap.

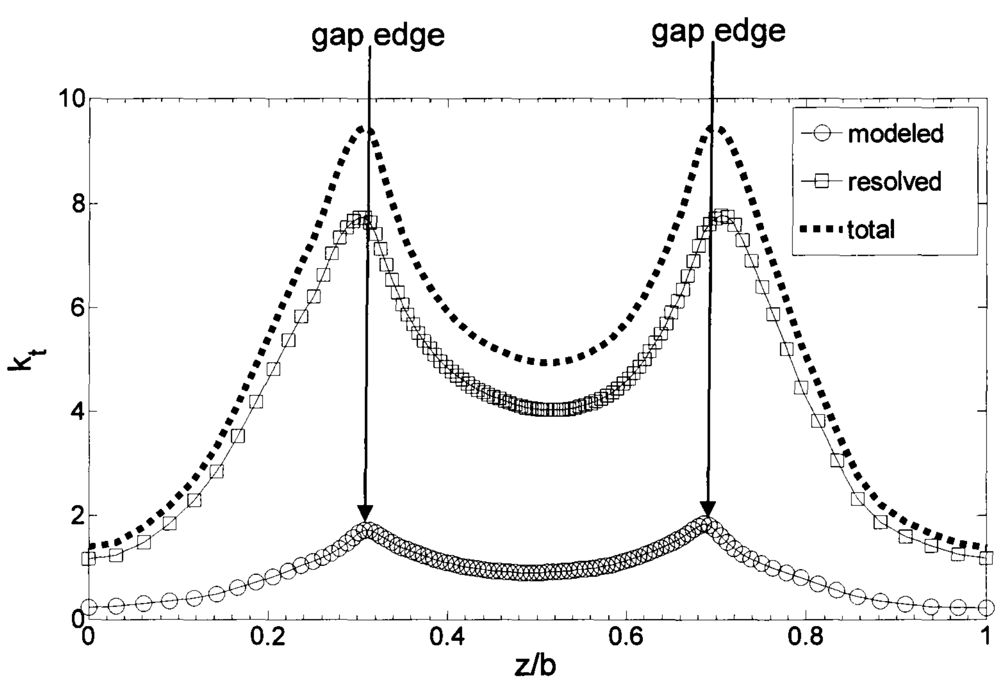

Figure 6.16 Variation of turbulent kinetic energy in the span-wise direction (z/b: normalized span-wise length, b: distance between centre of sub-channels).

A typical contour of the time averaged axial velocity (normalized by the channel bulk velocity) in the channel cross-section as predicted by the DES-SST model is shown in Figure 6.17. The symmetry of the contours for the left sub-channel, with respect to the axis of symmetry through the gap is good. However, for the right sub-channel, the velocity contours have a fair degree of asymmetry involved. Meyer and Rehme (1994) have reported asymmetry in the velocity contours as less than $\pm 1\%$. The most pronounced feature of the flow in the sub-channel geometry is the bulging of the isovels near the gap region, which was reported in the experiments. It is evident from Figure 6.17 that the numerical simulation was able to successfully capture this bulging. The outward bulging of the velocity contours near the gap region is due to the roughly periodic cross flow through the gap. This cross flow through the gap which occurs at a threshold frequency is referred to as the flow pulsations. The presence of secondary flows in the duct causes the velocity contours to bulge near the four corners of the duct, which is seen in Figure 6.17. The mean flow at the centre of the sub-channel was under predicted by the numerical simulation by 3.3% as compared to the experimental data (Meyer and Rehme, 1994). The under prediction could possibly be due to the relatively coarse mesh used in the sub-channels. The contour in Figure 6.17 can be represented as a 3-D surface plot, which is shown in Figure 6.18. It is seen that the stream-wise velocity distribution is perturbed. The axial velocity through the gap is much smaller than the axial velocity through the core of the sub-channels since the flow resistance is higher in the gap. A 2D coloured surface plot of the time averaged axial velocity (normalized by the channel bulk velocity) at (x, z) symmetry plane (mid plane) through the gap ($y = a/2$) is shown in Figure 6.19.

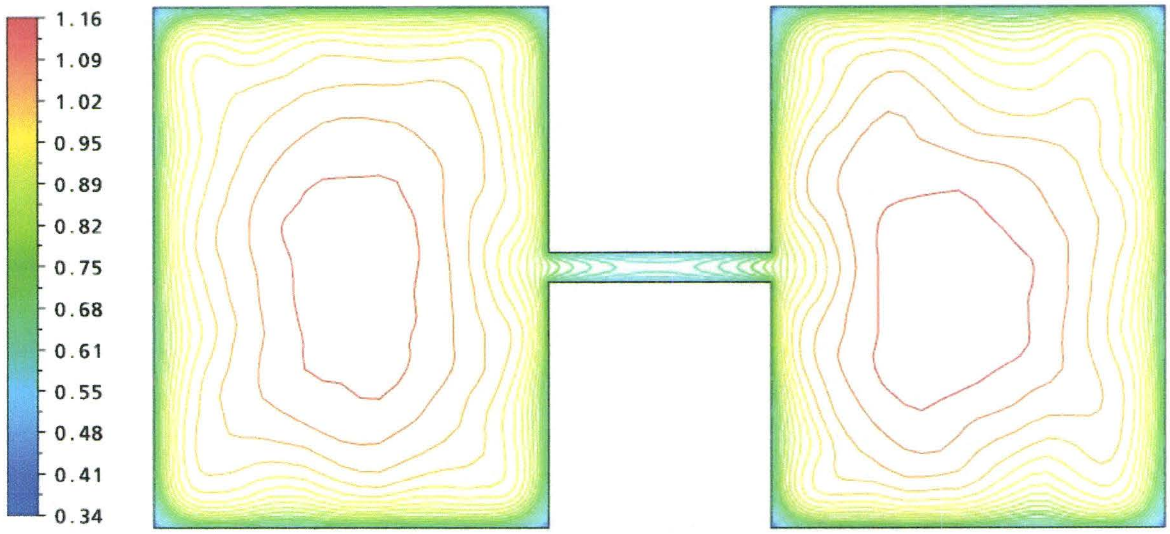

Figure 6.17 DES- SST prediction of the contour plot of time averaged axial velocity contour.

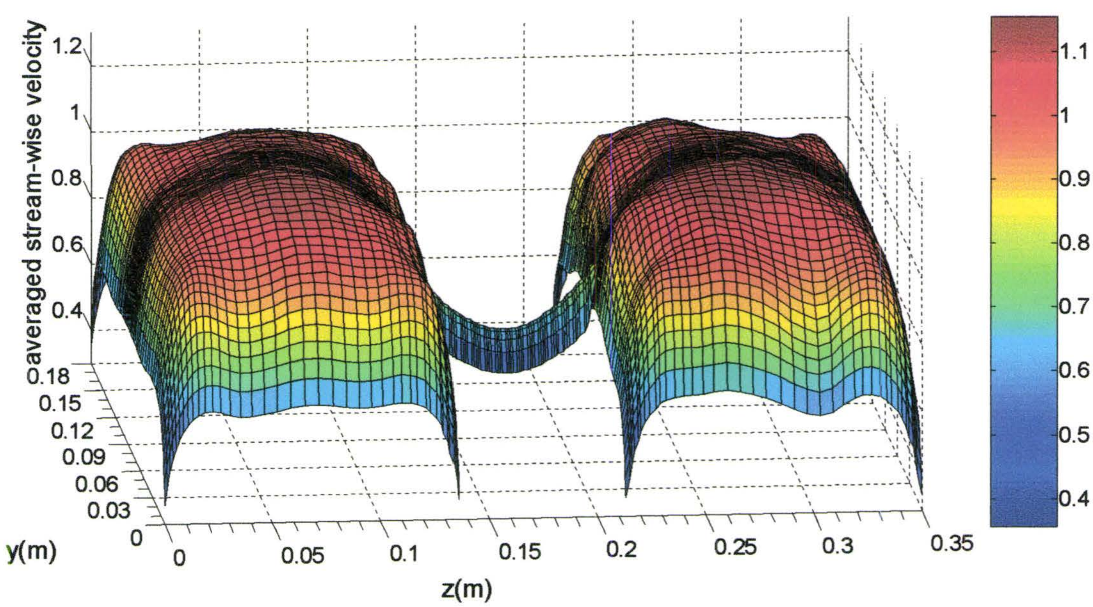

Figure 6.18 3-D surface plot of the time averaged axial velocity.

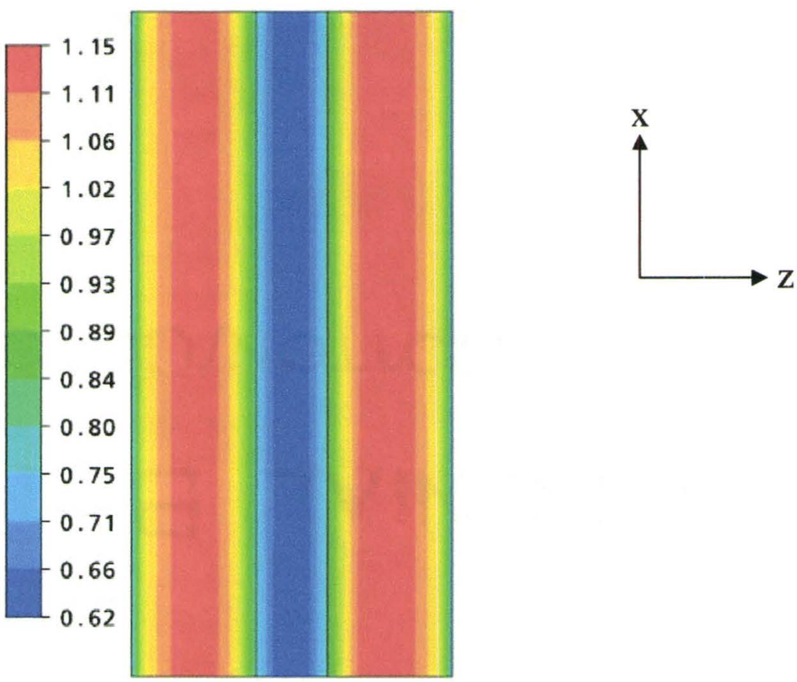

Figure 6.19 DES-SST prediction of the time averaged axial velocity.

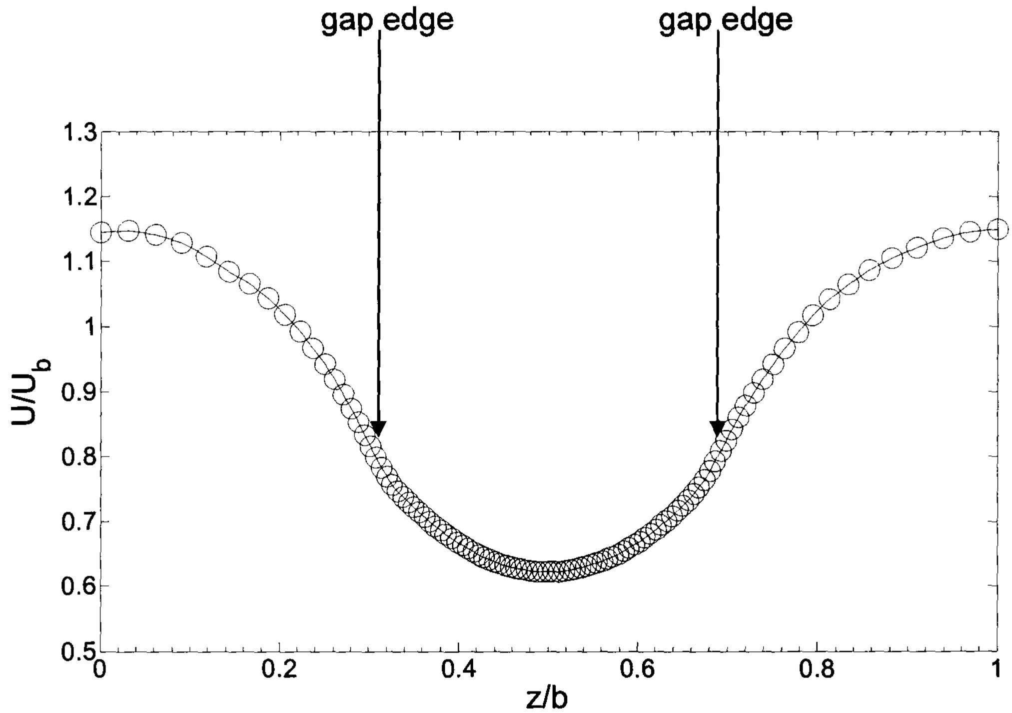

Figure 6.20 Span-wise variation in the time averaged axial velocity (z/b: normalized span-wise length, b: distance between centre of sub-channels).

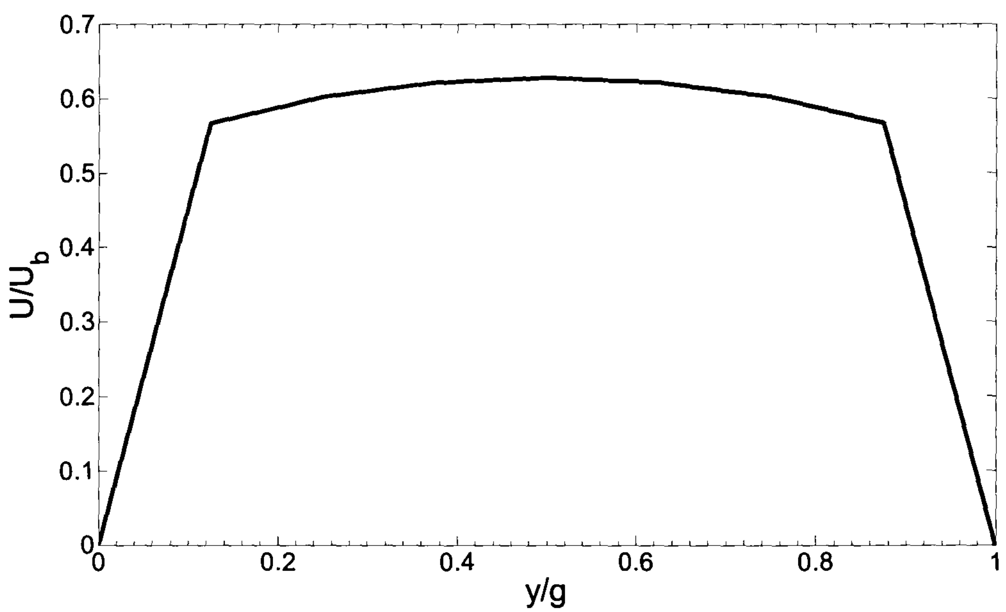

Figure 6.21 Variation of the time averaged axial velocity in the gap.

[The symmetry plane through the gap is shown in Figure 6.52]. Figure 6.19 clearly shows low velocity fluid through the gap and high velocity fluid through the core of the sub-channels. The span-wise variation for the time averaged axial velocity (normalized by the channel bulk velocity) is shown in Figure 6.20. This velocity profile is exactly the same as case C2 shown in Figure 6.8. Discussion on the characteristics and implication of the profile shown in Figure 6.20 is presented in section 6.5.7 of this chapter. The variation of the time averaged axial velocity (normalized by the channel bulk velocity) along the gap height is shown in Figure 6.21. Figure 6.21 was obtained similar to the way Figure 6.15 was created. The velocity profile in Figure 6.21 has a characteristic pattern similar to turbulent velocity profile for a duct flow. The overall effect of the flow pulsation on the mean velocity was well captured by the numerical model and matched well with the experiment (Meyer and Rehme, 1994).

The turbulence variables discussed are non-dimensionalized using the experimental wall friction velocity. The contour and the corresponding 3-D surface plots for the stream-wise turbulent intensity, u" is shown in Figures 6.22 and 6.23 respectively. It is clear that u" has large values near the vicinity of the gap edge region, with symmetric peaks located at the respective edges of the gap. The contours have a familiar bulging near the corners of the gap, which signifies the transport of the low intensity fluid by the secondary flows from the centre of the sub-channel towards the corners. The contour of the turbulent intensity, v" in the y-direction is shown in Figure 6.24. Very high values of v" are noticeable near the vicinity of the edges of the gap. The 3-D surface plot in Figure 6.25 clearly shows that the turbulent intensity v" has two peaks near both the edges of the gap.

The transverse turbulent intensity in the z-direction (parallel to the gap), w" is very high along the entire length of the gap, as shown in Figures 6.26 and 6.27 respectively. The high turbulent intensities observed in and around the vicinity of the gap has direct implication on the distribution of the turbulent kinetic energy. The contour and 3-D surface plots of the resolved and total (sum of modeled and resolved) turbulent kinetic energy is shown in Figures 6.28, 6.29, 6.30 and 6.31 respectively. It is clear that a significant portion of turbulent kinetic energy is resolved rather than modeled near the gap region. The turbulent kinetic energy is very high in the region close to the gap, and has symmetric peaks located at the respective edges of the gap. The peak value near the gap region is much higher than the highest values at the other walls without a gap. The Reynolds shear stresses were found to be much higher near the gap than other regions in the channel. Figures 6.32 and 6.33 show the contour and 3-D surface plot for the Reynolds shear stress, $\overline{u'v'}$. It is clear that strong peaks are observed at the edges of the gap. The shear stress $\overline{u'v'}$ has two peaks, a positive and a negative one, at each of the individual edges of the gap. The contour and 3-D surface plots for the gap parallel (planar) Reynolds shear stress, $\overline{u'w'}$ are shown in Figures 6.34 and 6.35 respectively. The shear stress $\overline{u'w'}$ is zero at the symmetry line between the two channels at the centre of the gap. The planar Reynolds shear stress has peaks located around the respective edges of the gap. The two peaks are of the same magnitude but of opposite signs, with the positive peak located near the left edge and the negative peak at the right edge of the gap. Peaks of opposite signs for the Reynolds shear stresses ($\overline{u'v'}$, $\overline{u'w'}$) around the vicinity of the gap edges possibly indicate that there is lateral flow directed from the sub-channels towards the gap region, causing lateral mixing at an instantaneous time scale. The unusually high turbulent intensities, turbulent kinetic energy and Reynolds shear stresses that are observed near the gap region suggests that there is additional production of turbulence near the vicinity of the gap, and its effect is felt throughout the entire length of the gap region. The additional production of turbulence could be associated with an instability mechanism (description discussed in Section 6.5.7), which arises near the gap region. This instability leads to quasi-periodic flow pulsations through the gap, that results in high levels of turbulence in the near gap region. The high levels of turbulence results in higher levels of mixing which is a characteristic feature of flows in sub-channel geometries.

Table 6.7 provides the quantitative comparison between the numerical results and the reported experimental data (Meyer and Rehme, 1994) for the peak values in the turbulence variables. All the variables reported, were normalized using the experimental wall shear velocity. The variable k_t represents the total turbulent kinetic energy (sum of modeled and resolved components). The simulations were in excellent agreement with the experiment in detecting the location of the peak values. The predicted peak values compare well with the experimental data. Tables 6.8-6.11 provide the comparison between numerical and reported experimental results (Meyer and Rehme, 1994) for flow variables pertaining to different monitor points located along the gap. The time averaged velocity, U is over predicted for all the points by approximately 17%. The normal Reynolds stress, $\overline{w'w'}$ is very well predicted, and is in excellent agreement with the experimental data for all the monitor points. This probably suggests that the grid resolution in the span-wise direction was sufficiently fine. The planar Reynolds shear stress, $\overline{u'w'}$ has reasonably good agreement with the reported experimental results. In general, the qualitative and quantitative descriptions pertaining to the flow in the twin rectangular sub-channel geometry were well predicted by the DES-SST model.

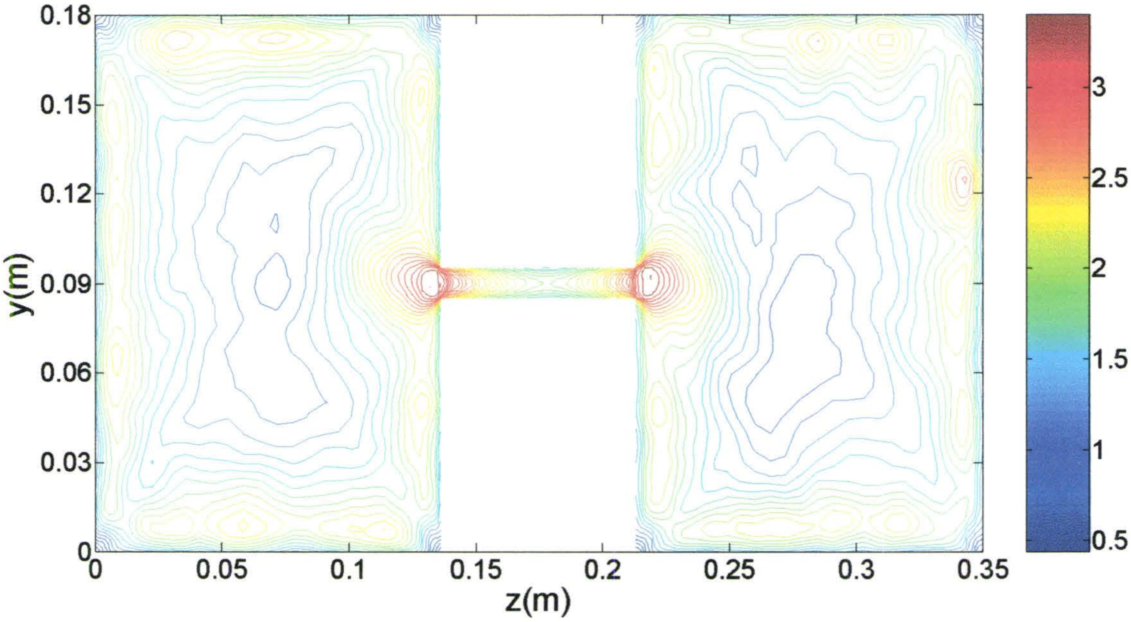

Figure 6.22 DES-SST prediction of the contour plot of stream-wise turbulent intensity.

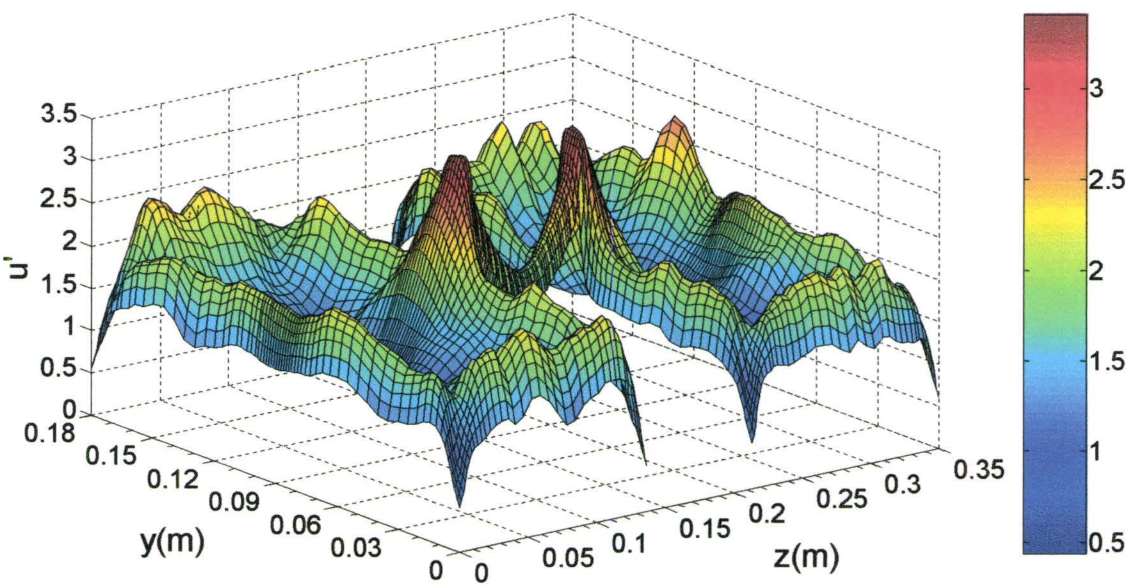

Figure 6.23 3-D surface plot of the stream-wise turbulent intensity.

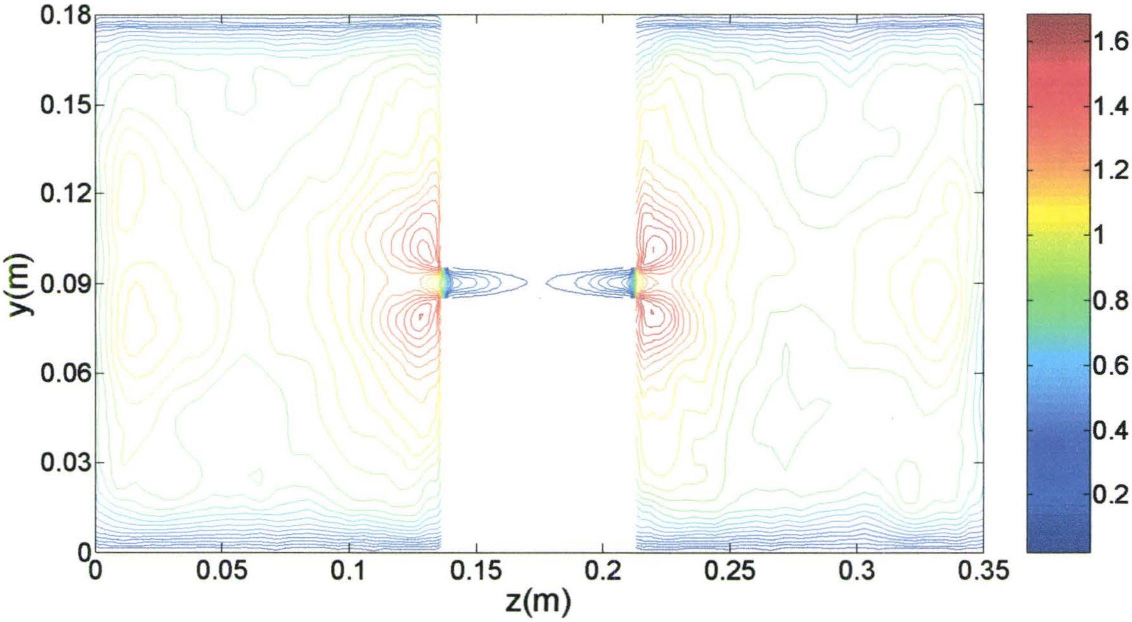

Figure 6.24 DES-SST prediction of the contour plot of the turbulent intensity in the y-direction.

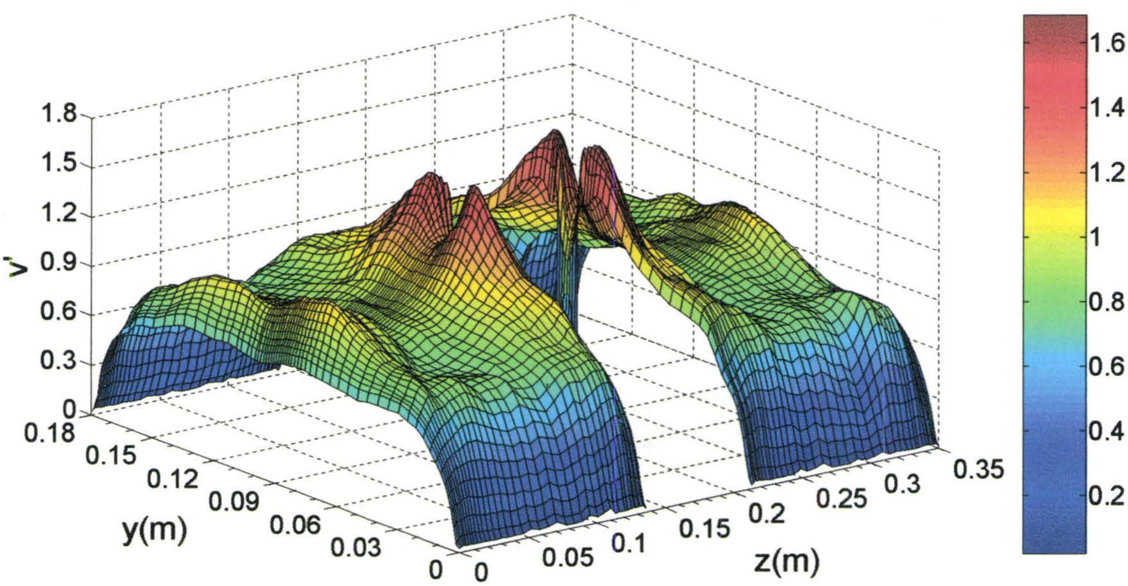

Figure 6.25 3-D surface plot of the turbulent intensity in the y-direction.

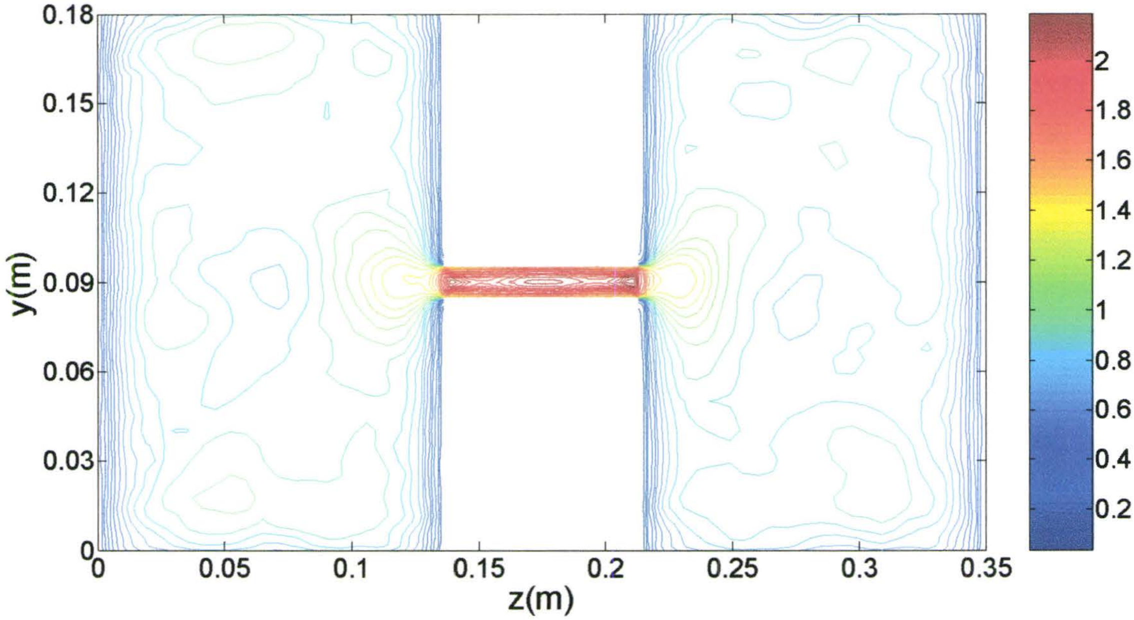

Figure 6.26 DES-SST prediction of the contour plot of span-wise turbulent intensity.

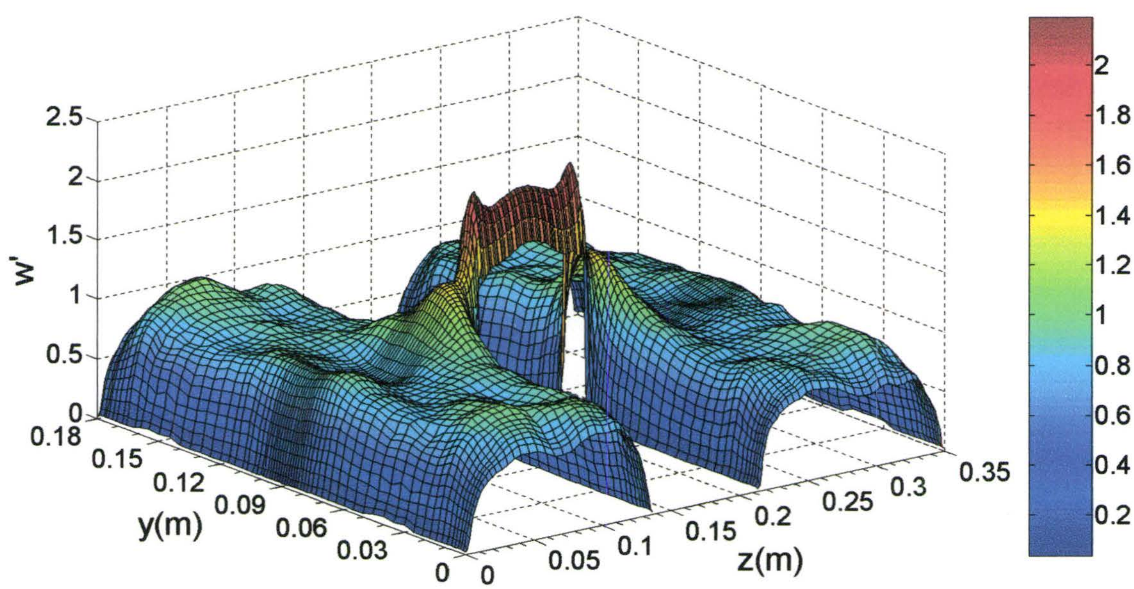

Figure 6.27 3-D surface plot of the span-wise turbulent intensity.

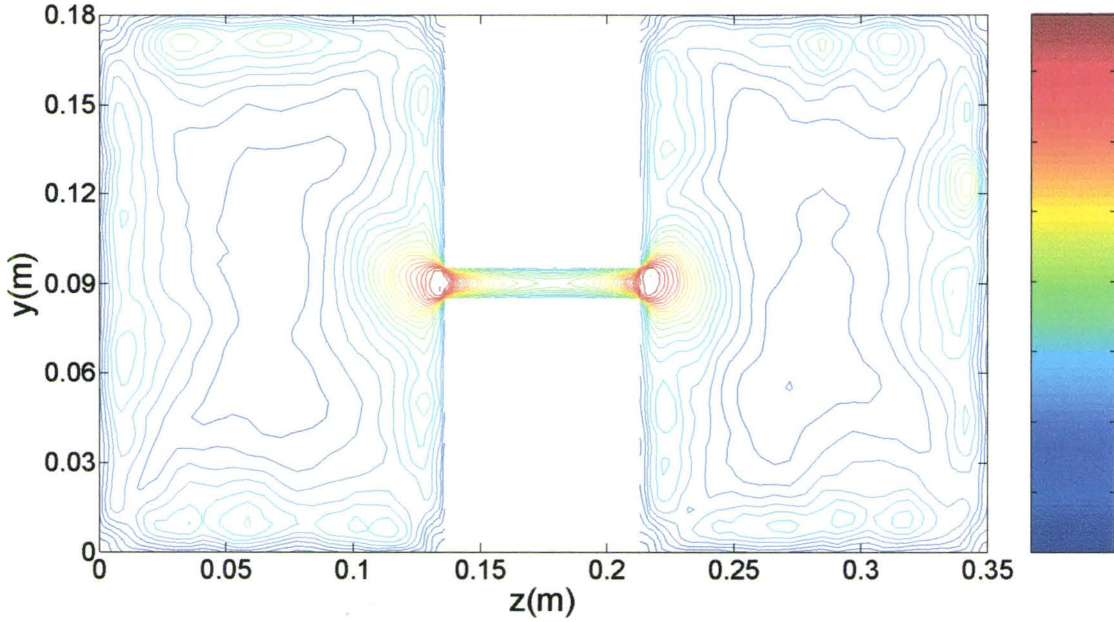

Figure 6.28 DES-SST prediction of the contour plot of the resolved component of turbulent kinetic energy.

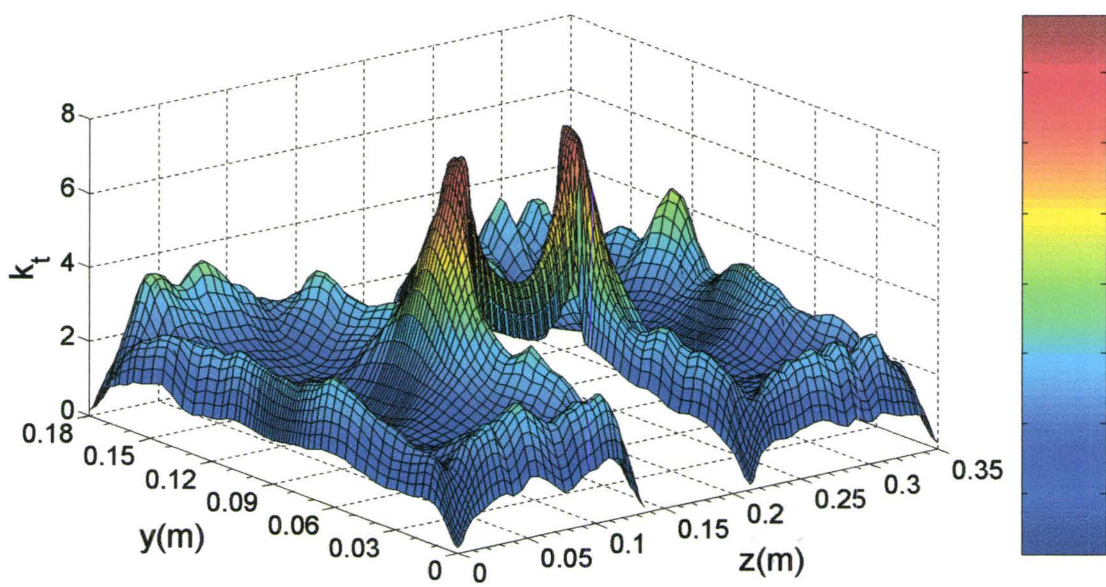

Figure 6.29 3-D surface plot of the resolved component of turbulent kinetic energy.

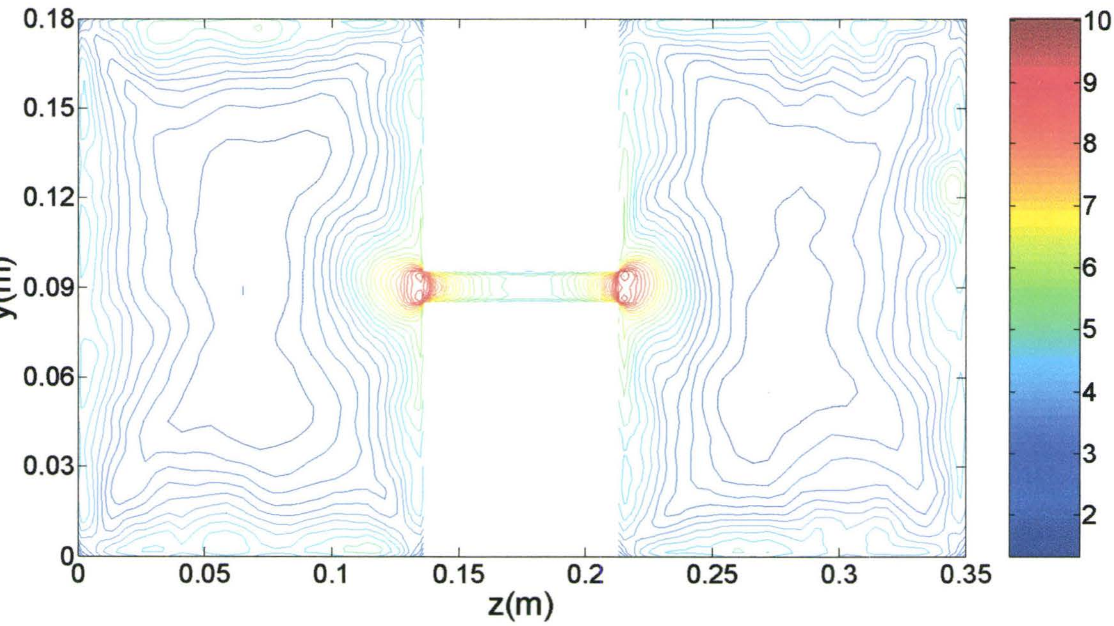

Figure 6.30 DES-SST prediction of the contour plot of the total turbulent kinetic energy.

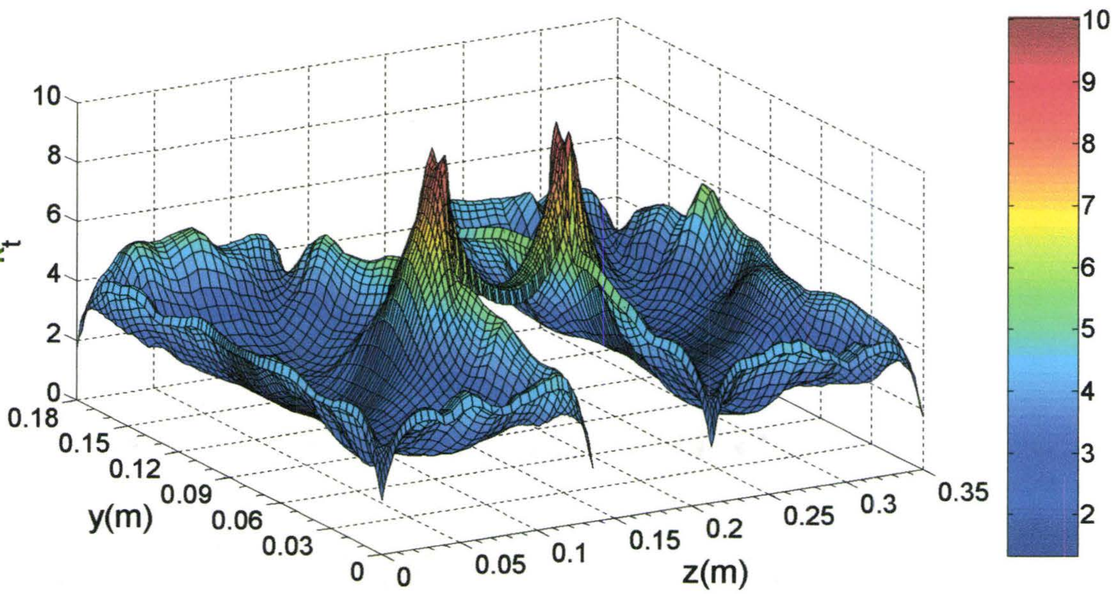

Figure 6.31 3-D surface plot of the total turbulent kinetic energy.

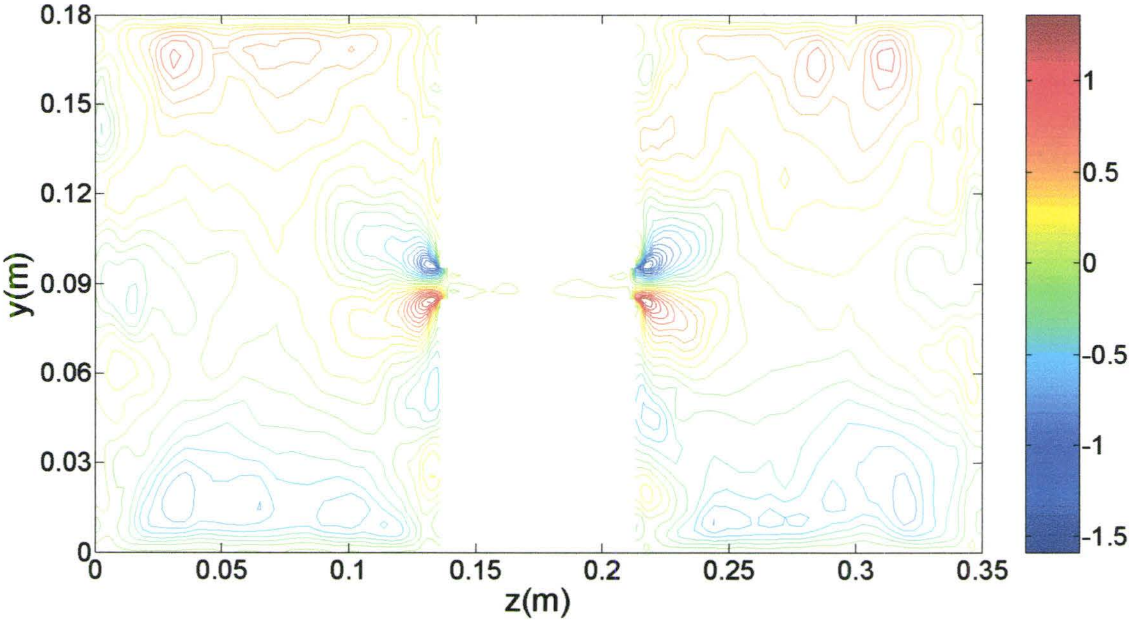

Figure 6.32 DES-SST prediction of the contour plot of the Reynolds shear stress, $\overline{u'v'}$.

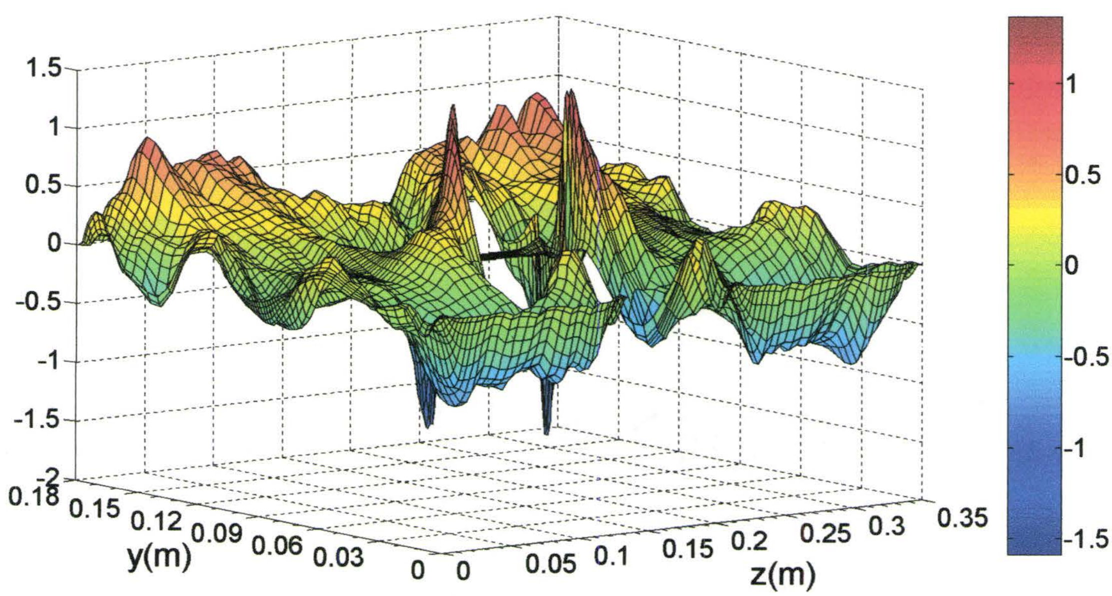

Figure 6.33 3-D surface plot of the Reynolds shear stress, $\overline{u'v'}$.

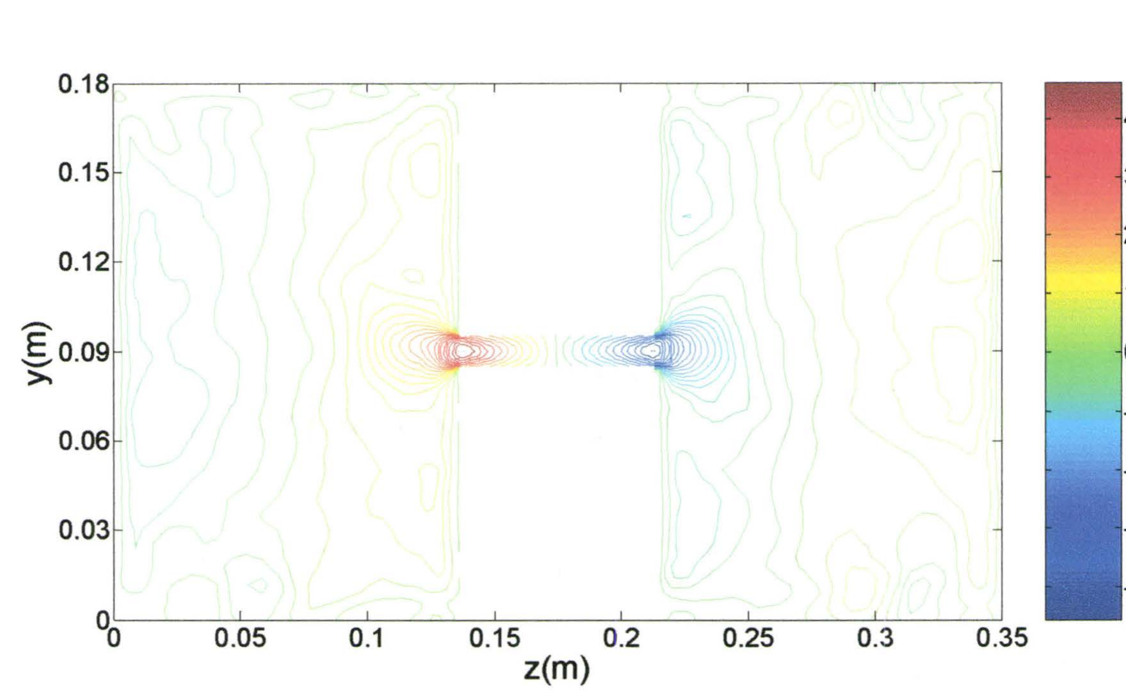

Figure 6.34 DES-SST prediction of the contour plot of the gap parallel Reynolds shear stress, $\overline{u'w'}$.

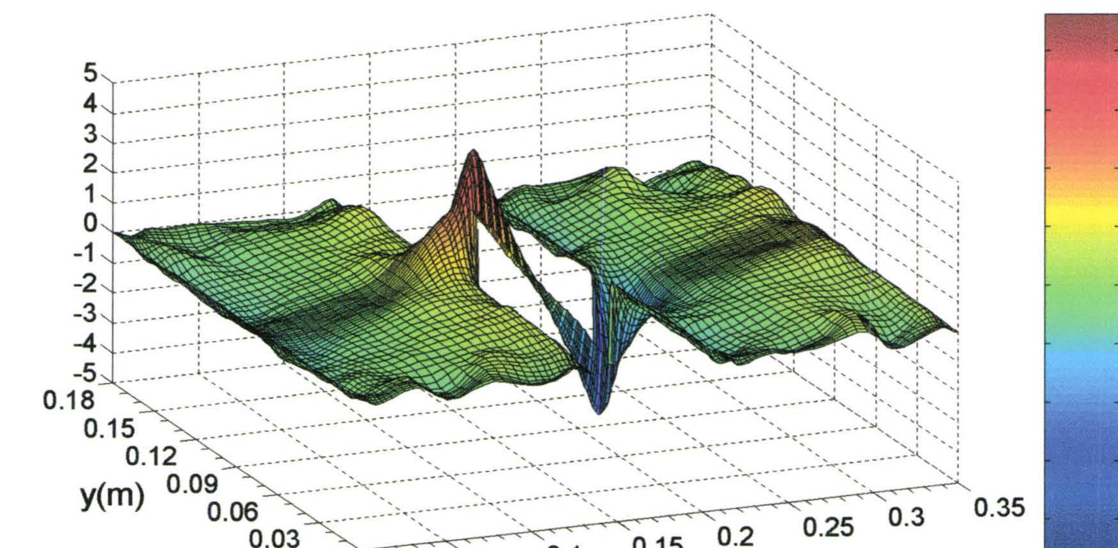

Figure 6.35 3-D surface plot of the Reynolds shear stress, $\overline{u'w'}$.

Table 6.7 Comparison of peak values in the turbulence variables.

Variables	Numerical	Experimental
u''	3.4	3.4
v''	1.7	2.0
w''	2.2	2.0
k_t	10.1	9.2
$\overline{u'v'}$	+1.4, -1.6	±2.4
$\overline{u'w'}$	4.6	4.4

Table 6.8 Flow data pertaining to monitor point 4 (gap centre).

Variables	Numerical	Experimental
U (m/s)	13.47	11.54
$\overline{w'w'}$ (m^2/s^2)	3.749	3.596
$\overline{u'w'}$ (m^2/s^2)	-0.27	-0.172

Table 6.9 Flow data pertaining to monitor point 5.

Variables	Numerical	Experimental
U (m/s)	14.48	12.40
$\overline{w'w'}$ (m^2/s^2)	3.616	3.712
$\overline{u'w'}$ (m^2/s^2)	-2.015	-1.731

Table 6.10 Flow data pertaining to monitor point 6 (gap edge).

Variables	Numerical	Experimental
U (m/s)	17.45	14.73
$\overline{w'w'}$ (m^2/s^2)	3.556	3.061
$\overline{u'w'}$ (m^2/s^2)	-3.977	-3.095

Table 6.11 Flow data pertaining to monitor point 7.

Variables	Numerical	Experimental
U (m/s)	20.07	16.77
$\overline{w'w'}$ (m^2/s^2)	1.754	1.066
$\overline{u'w'}$ (m^2/s^2)	-2.444	-1.338

6.5.3 Dynamics of the flow pulsations

The time variations of the instantaneous span-wise velocity at the gap centre and at the gap edge, and the instantaneous axial velocity at the gap centre and at the gap edge are shown in Figures 6.36-6.39. The numerical predictions from the DES-SST model are compared to the experimental data (Meyer and Rehme, 1994). The velocity time traces are normalized using the channel bulk velocity. The x-axis represents the normalized flow time units. It is clear from Figures 6.36 and 6.37 that there is significant velocity directed in the span-wise direction. The figures indicate the quasi-periodic nature associated with the flow, which is different from a pure turbulent flow. This quasi-periodic nature is a characteristic feature of the flow pulsation phenomena. The quasi-periodic flow is responsible for enhanced mixing and is associated with a characteristic time scale (frequency). The amplitudes of the predicted span-wise velocities are similar to the experimental velocities. The clear negative skewness in the time trace of the span-wise velocity at the gap edge (Figure 6.37) is well captured by the DES-SST model and is in accordance with the experimental velocity. It is clear from Figure 6.37 that a greater number of harmonics are associated with the predicted velocity as compared to the experimental one. The predicted and the experimental axial velocities at the gap centre shown in Figure 6.38 have a very erratic trend, closely resembling a turbulent flow pattern. The experimental axial velocity at the gap edge, shown in Figure 6.39 has a quasi-periodic nature and is much smoother than the predicted axial velocity. In general, for the axial velocity at the gap edge, the predicted amplitude is higher than the reported experimental data. The time averaged axial velocity for the gap centre from Figure 6.38 is

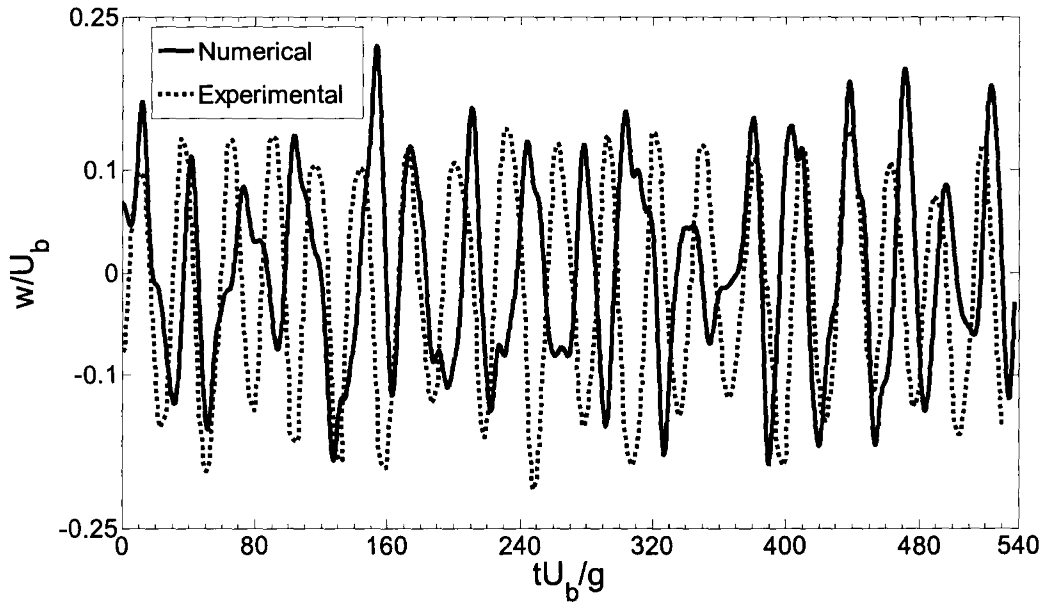

Figure 6.36 Time trace of the span-wise velocity at the gap centre.

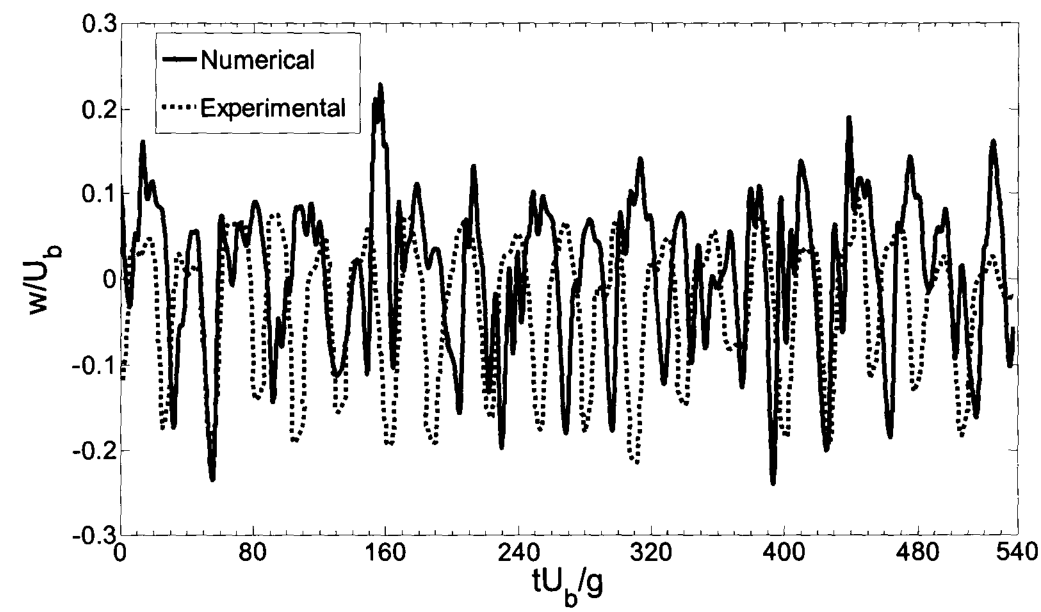

Figure 6.37 Time trace of the span-wise velocity at the gap edge.

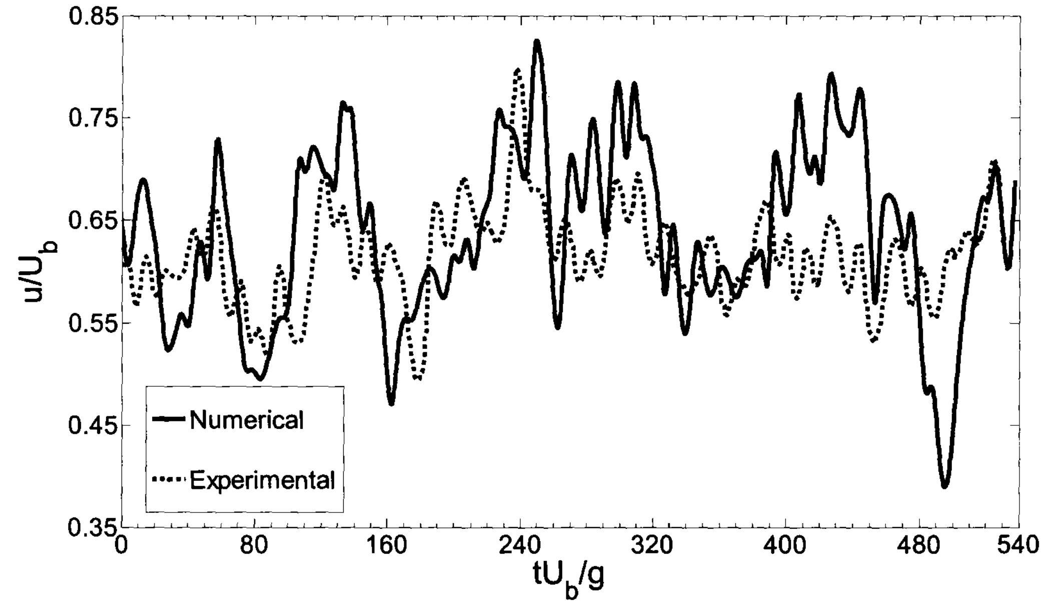

Figure 6.38 Time trace of the stream-wise velocity at the gap centre.

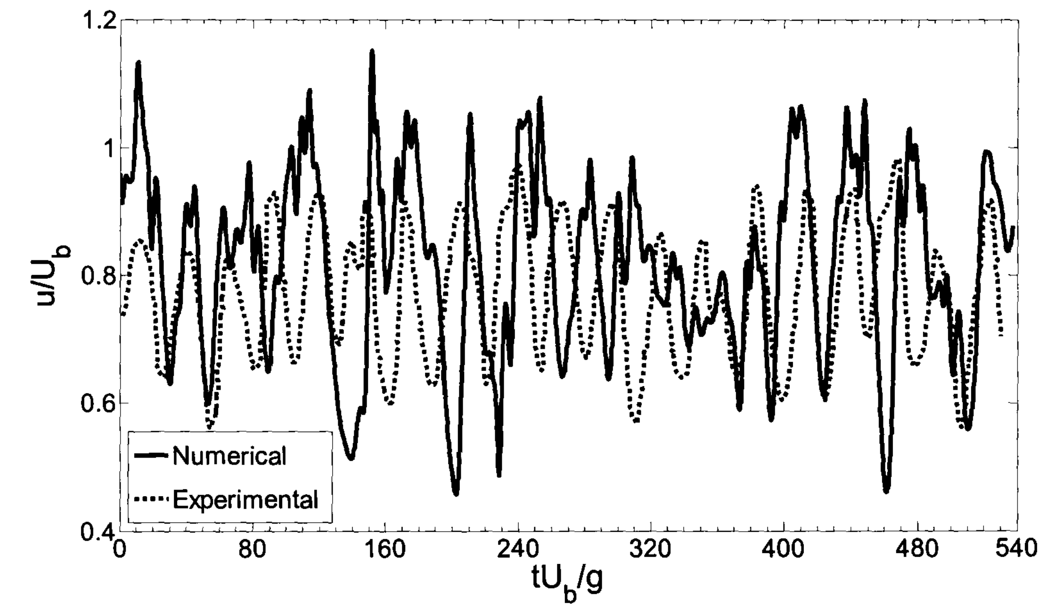

Figure 6.39 Time trace of the stream-wise velocity at the gap edge.

13.5 m/s from the numerical prediction and 13.3 m/s from the experimental data. The time averaged axial velocity for the gap edge from Figure 6.39 is 17.5 m/s from the numerical prediction and 17.0 m/s from the experimental data. The probability density functions (PDF) for the span-wise and the stream-wise velocities for the different monitor points is shown in Figures 6.40 and 6.41 respectively. The PDF was obtained over a simulation time of 2 sec. The non-symmetric shape of the PDF for the span-wise velocity at the gap edge (monitor point 6) clearly indicates the skewness associated with the velocity (Figure 6.37). The PDF of the span-wise velocity at the gap centre (monitor point 4) has two peaks located symmetrically with respect to the centre, indicating quasi-periodicity associated with the velocity (Figure 6.36). The PDF of the span-wise velocity at monitor point 5 is non-symmetric. A symmetric PDF is obtained for the span-wise velocity at monitor point 7. The PDF of the axial velocity at the gap centre (monitor point 4) is close to a Gaussian distribution, which is in accordance with its velocity time trace (Figure 6.38).

The power spectra for the instantaneous span-wise velocity was obtained using 2048 Fourier modes at a sampling frequency of 10,000 Hz. Figures 6.42 and 6.43 show the power spectra for the span-wise velocity at the gap centre and gap edge respectively. It is clear from Figure 6.42 that there is one dominant (peak) frequency of 68.4 Hz. In addition to the peak frequency, there are smaller (power magnitude) harmonics present as well. The contribution of the other harmonics to the overall spectra is significantly smaller than the peak frequency. In Figure 6.43, the peak frequency is again 68.4 Hz but there are a

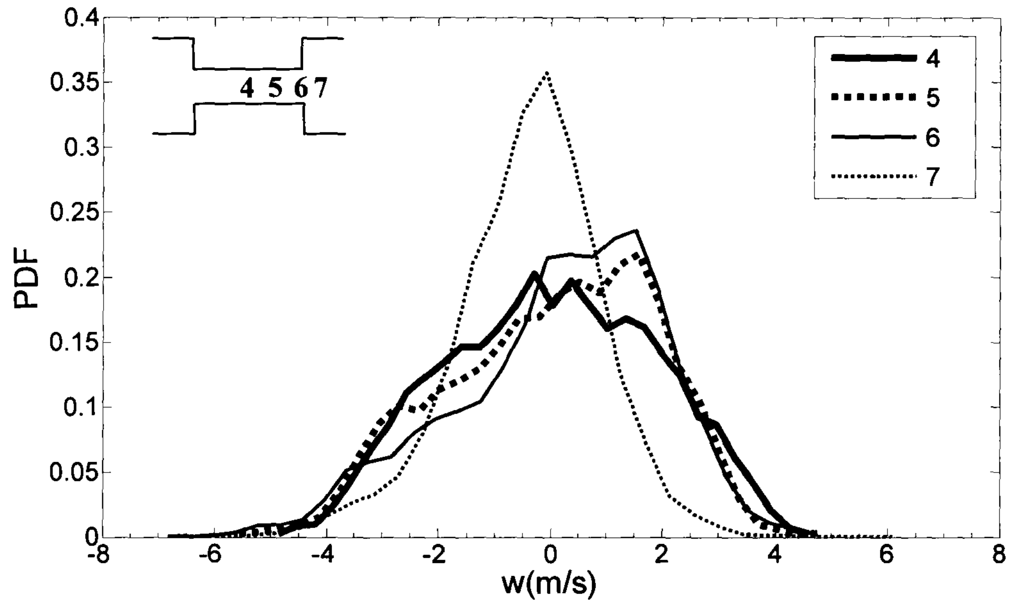

Figure 6.40 DES-SST prediction of the probability density function for the span-wise velocity.

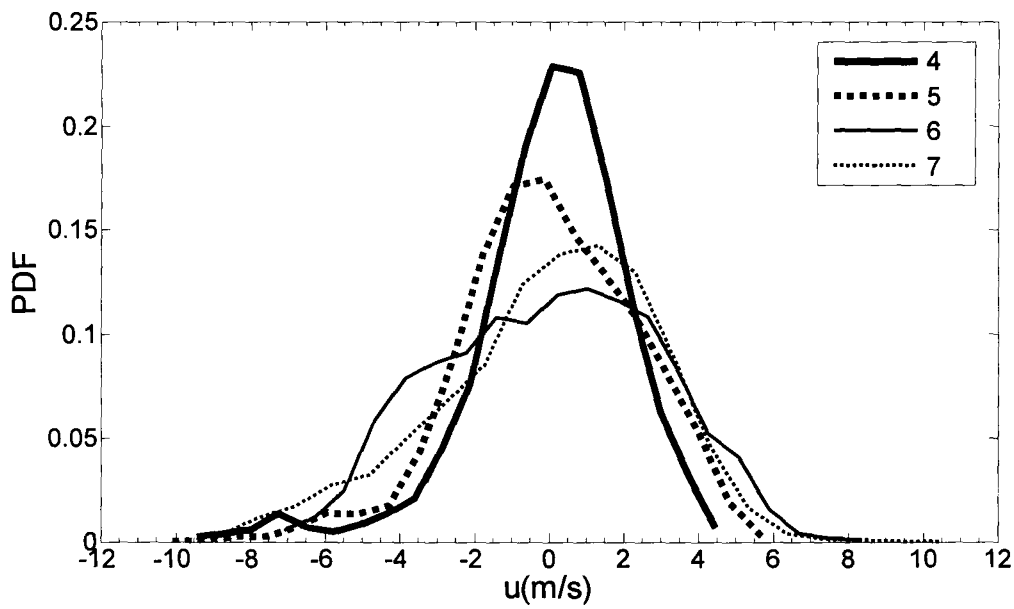

Figure 6.41 DES-SST prediction of the probability density function for the stream-wise velocity.

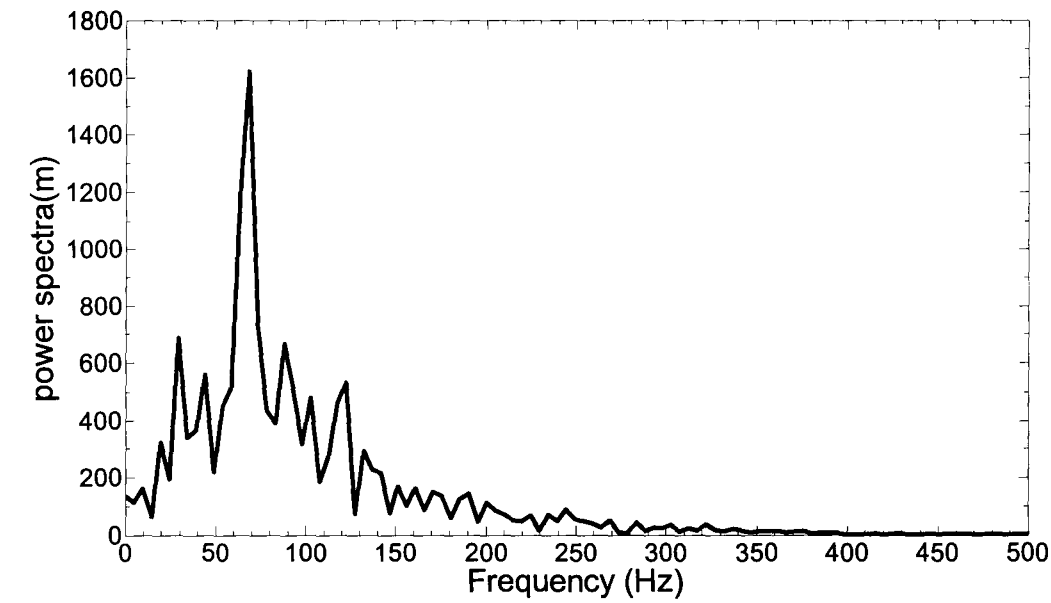

Figure 6.42 DES-SST prediction of the power spectra for the span-wise velocity at the gap centre.

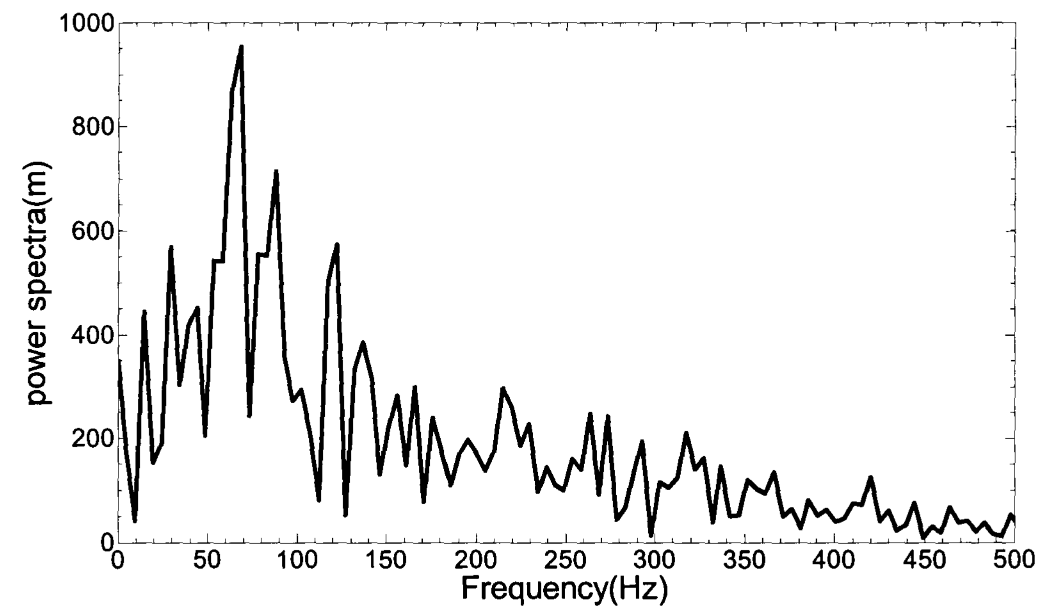

Figure 6.43 DES-SST prediction of the power spectra for the span-wise velocity at the gap edge.

greater number of harmonics present in comparison to Figure 6.42. The presence of number of other harmonics in addition to the peak frequency in Figure 6.43, is in accordance with the time trace of the span-wise velocity at the gap edge (Figure 6.37). The dominant quasi-periodic frequency of 68.4 Hz from Figures 6.42 and 6.43 has the physical implication that the flow traverses back and forth in the span-wise direction at a characteristic time scale and this is the frequency at which the flow pulsation phenomena occurs. In general, the flow is said to pulsate at the dominant frequency, which is responsible for enhanced mixing in the sub-channel geometry. The instantaneous momentum transfer from one sub-channel to the other is associated with a pressure difference pulse, which possibly arises from an instability near the gap edge region. The transverse pressure difference is a response to the instability mechanism (description discussed in Section 6.5.7). Figure 6.44 shows the time traces of pressure (normalized using the dynamic velocity head) at the monitor points 2 and 6, located at the edges of the gap. It is clear that the pressure at the two locations have an anti-phase relationship. Figure 6.45 shows the power spectra of the pressure difference between the two edges of the gap. A peak is noticeable at a dominant frequency of 68.4 Hz, which is consistent with the frequency obtained from the velocity spectra. The transverse pressure difference across the sub-channels results in mass and momentum transfer from one sub-channel to the other in an alternate fashion (along the length of the duct) at an instantaneous time scale. This transverse pressure difference exists along the length of the duct and causes significant cross flow. Figures 6.46-6.51 show the 3-D surface plot of the instantaneous cross flow (span-wise) velocity on the stream normal plane at different axial locations

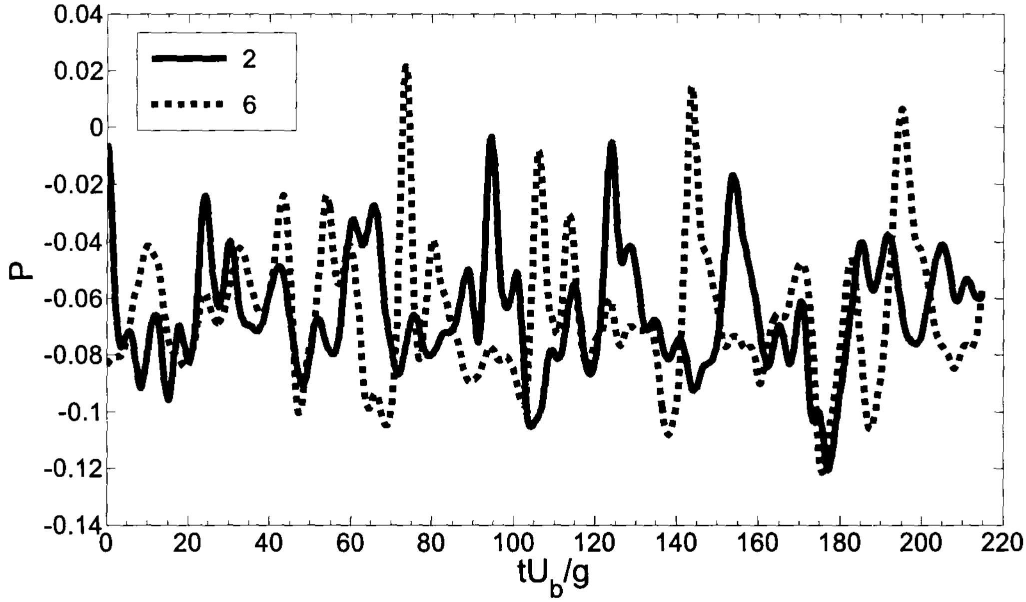

Figure 6.44 Instantaneous pressure at the monitor points located on the gap edge.

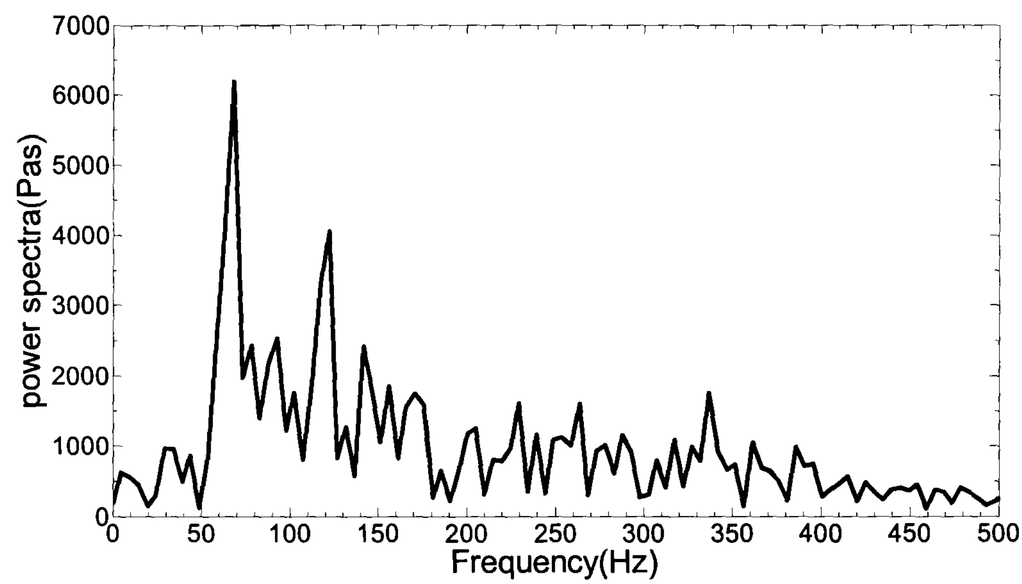

Figure 6.45 Power spectra of the pressure difference with respect to the two edges.

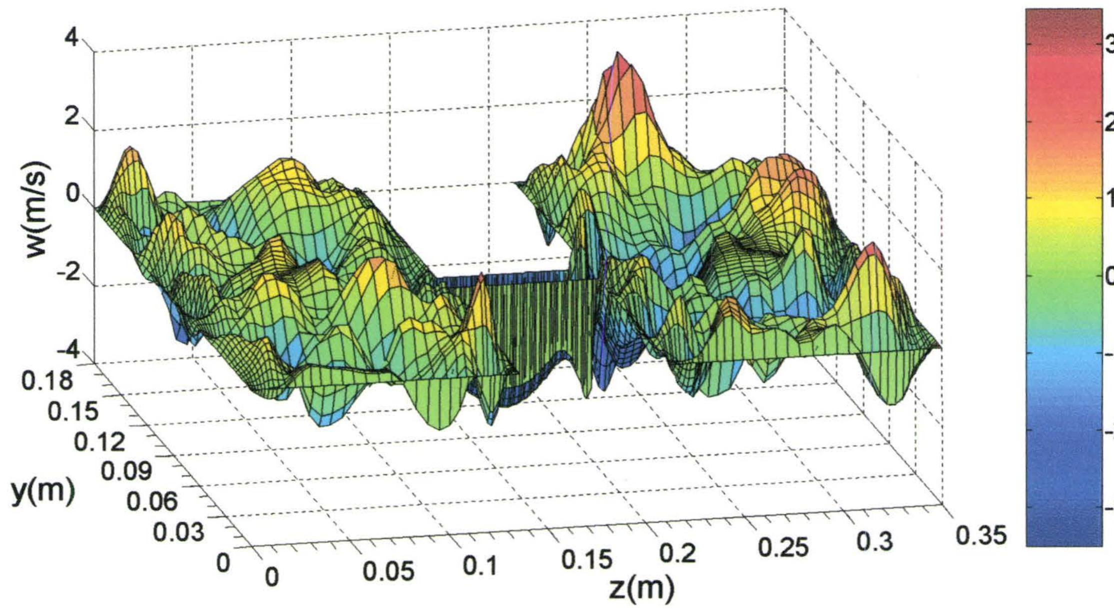

Figure 6.46 Span-wise velocity at the cross-sectional plane located at z = 30 mm.

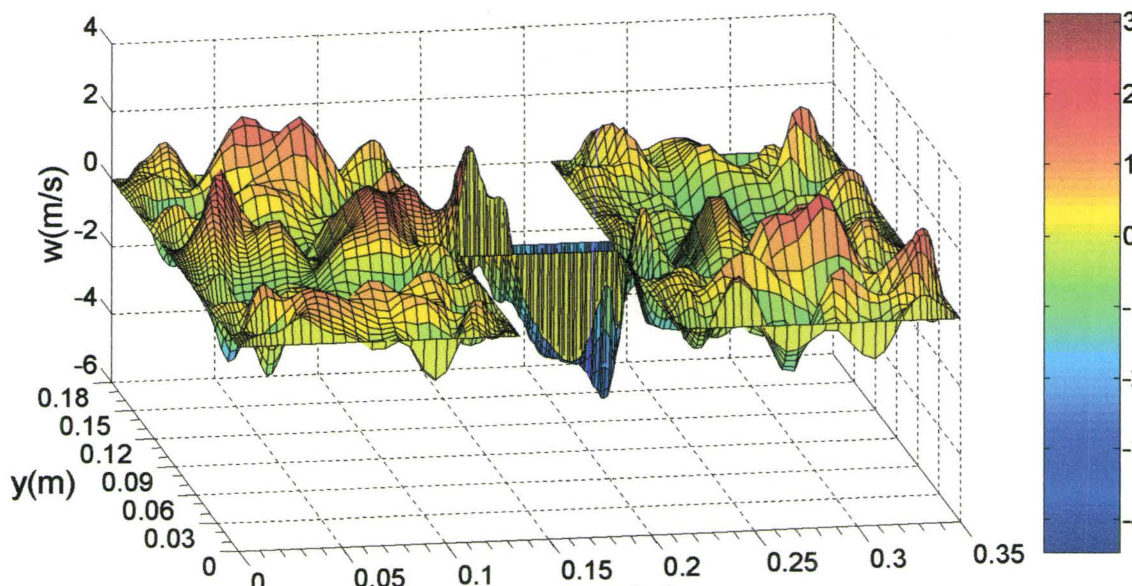

Figure 6.47 Span-wise velocity at the cross-sectional plane located at z = 180 mm.

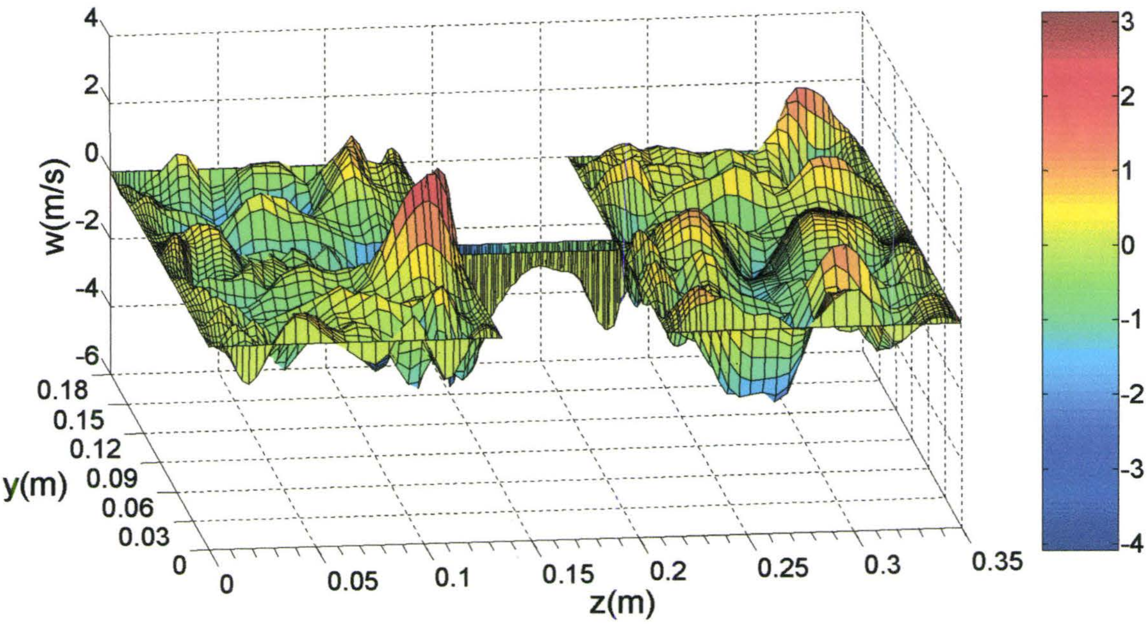

Figure 6.48 Span-wise velocity at the cross-sectional plane located at z = 330 mm.

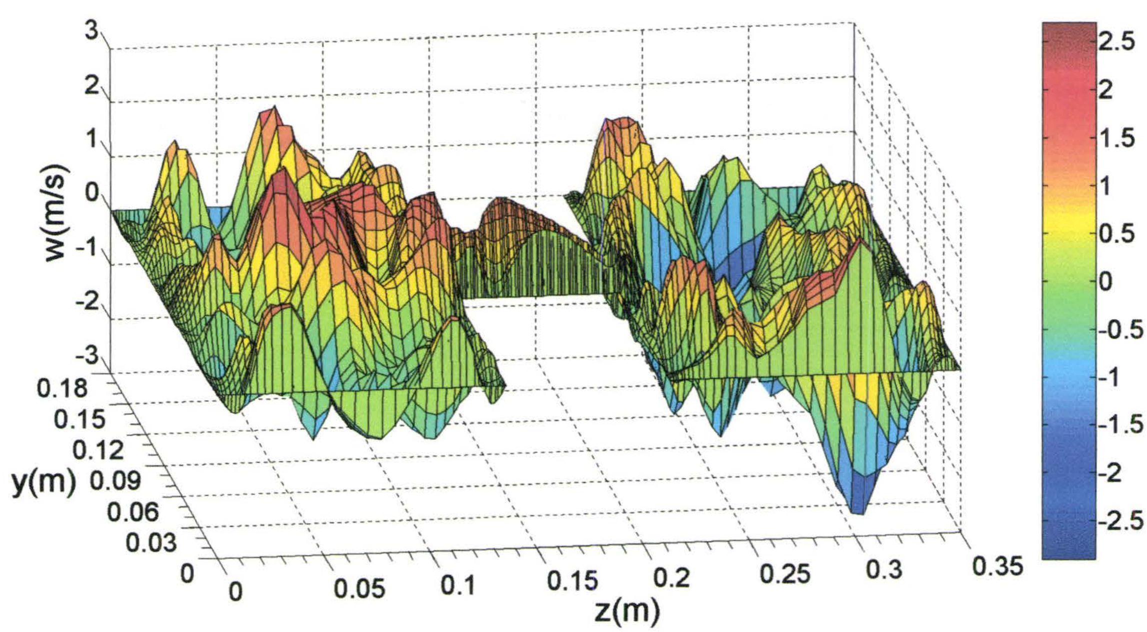

Figure 6.49 Span-wise velocity at the cross-sectional plane located at z = 480 mm.

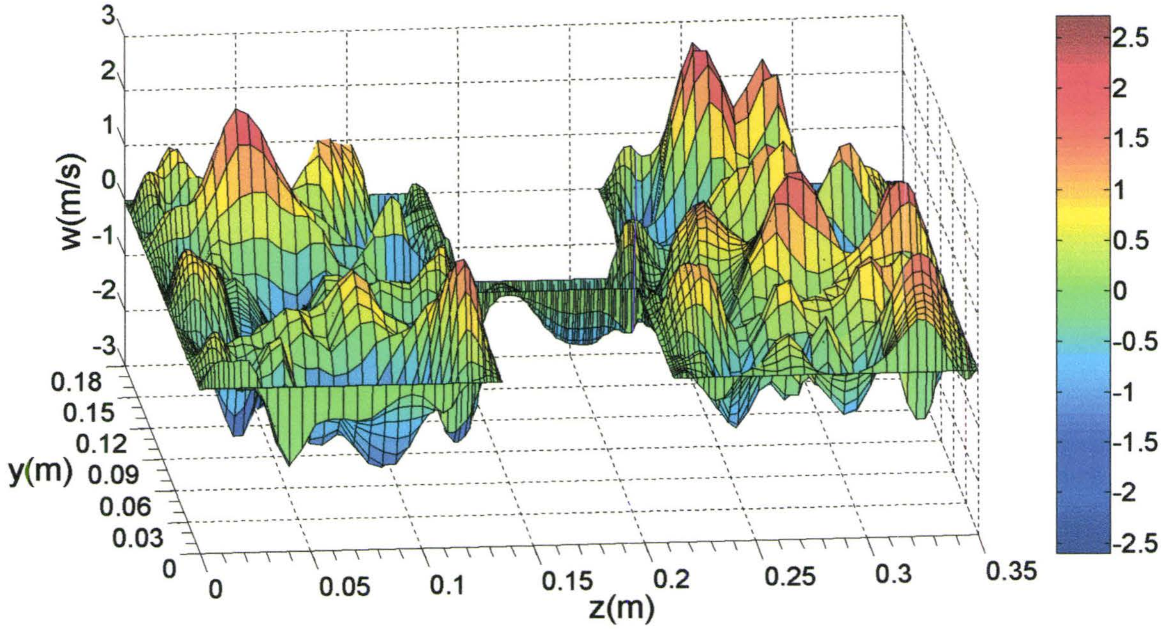

Figure 6.50 Span-wise velocity at the cross-sectional plane located at z = 630 mm.

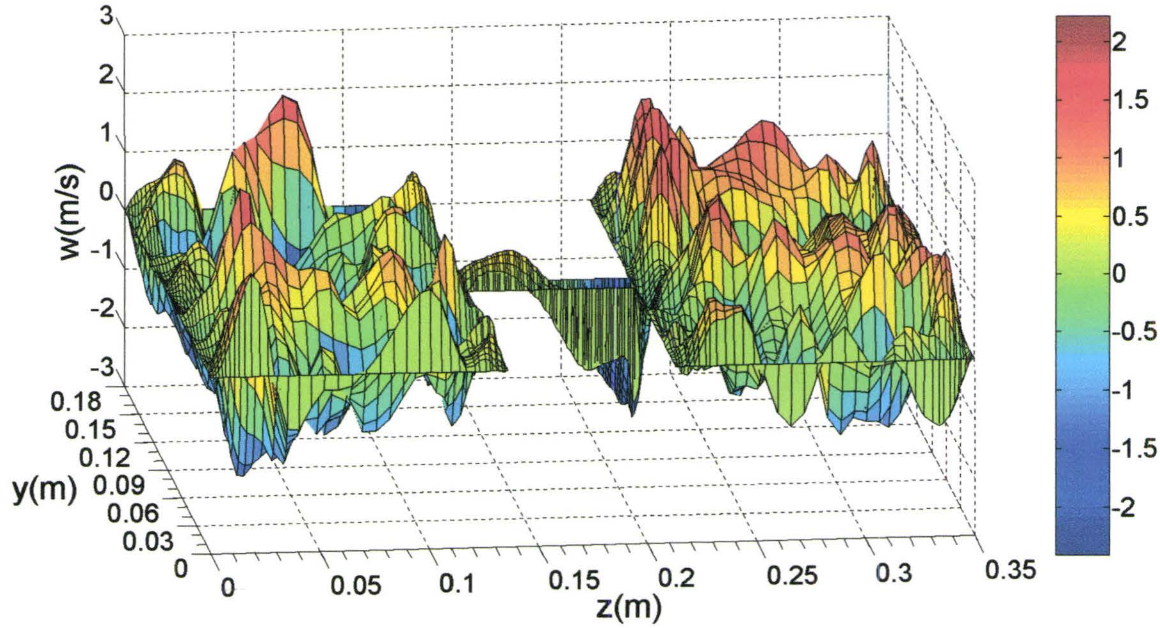

Figure 6.51 Span-wise velocity at the cross-sectional plane located at z = 700 mm.

(arbitrarily chosen). It is clear from the figures that the amplitudes of the velocity are quite significant compared to the channel bulk velocity of 21.5 m/s, and there is significant perturbation associated with the cross flow. At certain locations for instance (z = 30, 180, 480, 700 mm) there is significant velocity directed through the gap. The velocity directed through the gap is from either of the sub-channels to the other one. A very clear picture on the effect of the flow pulsations is observed by looking into the velocity contour, streamlines and velocity vector plots at the (x, z) symmetry plane (mid plane) through the gap (y = a/2). An isometric view of the twin rectangular sub-channel geometry showing the symmetry plane (plane parallel to the bulk flow) through the gap is shown in Figure 6.52. The instantaneous span-wise velocity contour and streamlines at the symmetry plane are shown in Figures 6.53 and 6.54 respectively. The gap region is demarcated from the sub-channels by two thick black lines. It is clear from the velocity contour plot, that alternate sequence of positive and negative velocities are present, and are directed across the gap (z-direction). This is a clear indication of the cross flow mixing between the sub-channels, which is present along the entire length of the duct and is a very efficient process for thermal mixing. The amplitudes of the velocity directed across the gap are quite significant. Figure 6.53 possibly indicates the presence of an alternate pattern of large-scale flow structures, with centres located around the vicinity of the gap region. From the streamline pattern in Figure 6.54, it is clear that the presence of alternate sequence of flow structures causes the fluid to follow a zig-zag path or a wiggly pattern in the entire gap region along the whole channel length. Figure 6.55 shows the instantaneous velocity vector in the span-wise direction at the symmetry plane, which

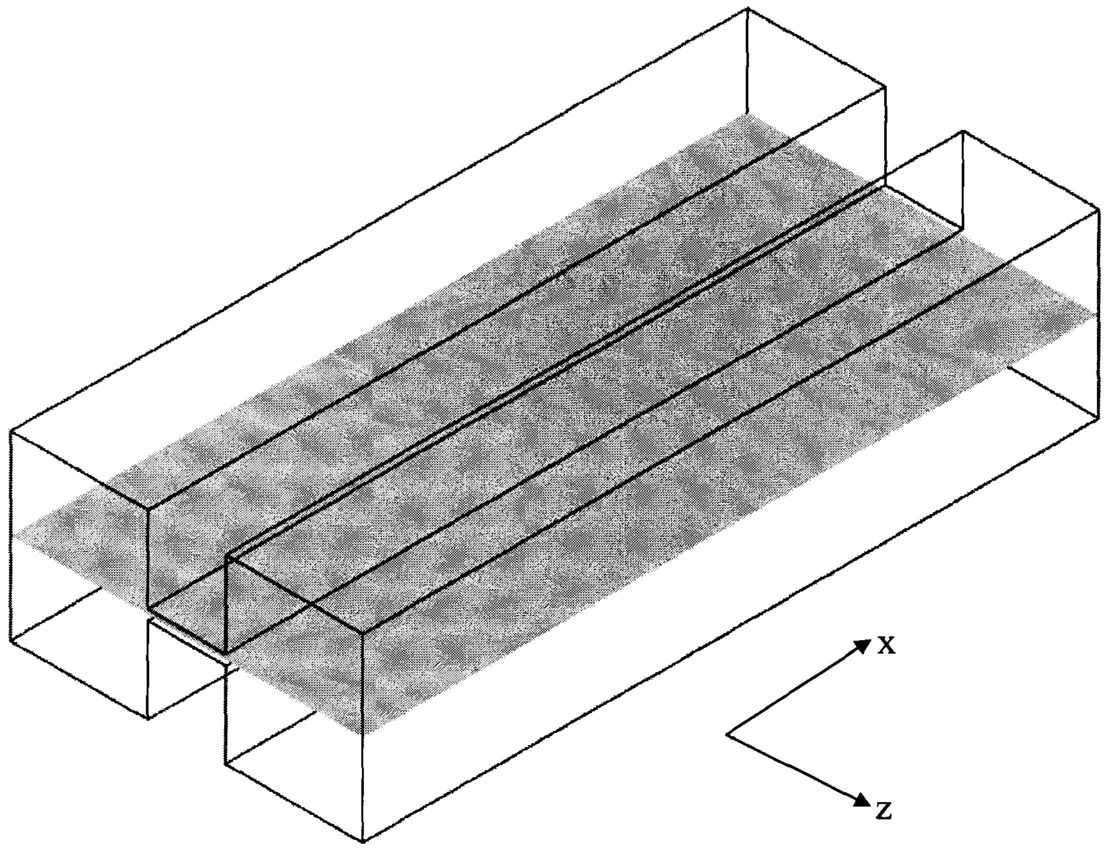

Figure 6.52 View of the symmetry plane through the gap.

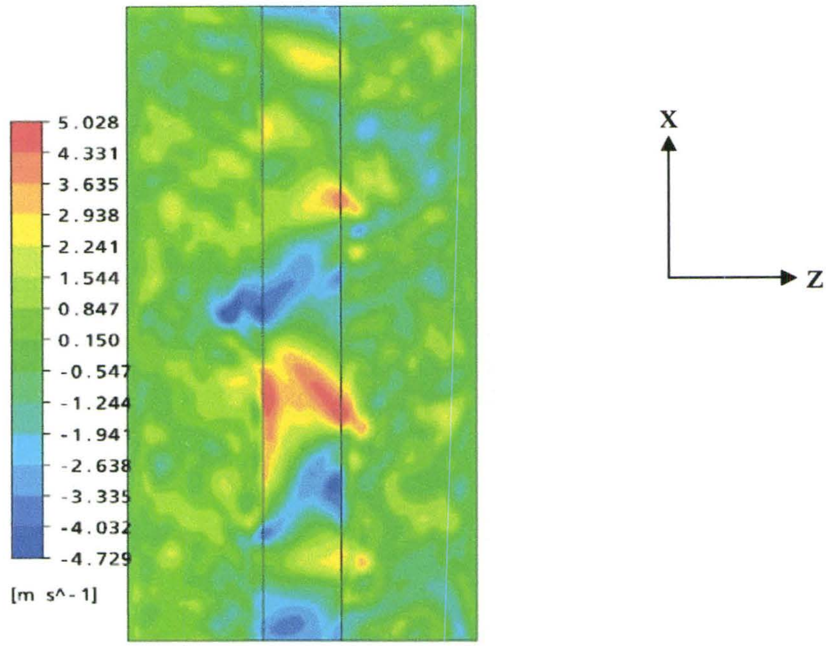

Figure 6.53 Snapshot of the span-wise velocity contour at the symmetry plane.

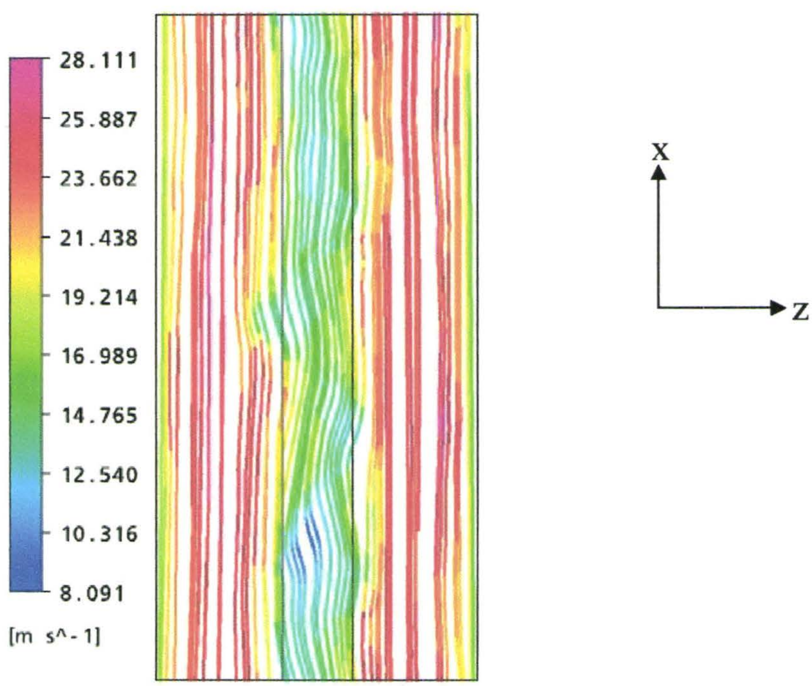

Figure 6.54 Snapshot of the streamline pattern at the symmetry plane.

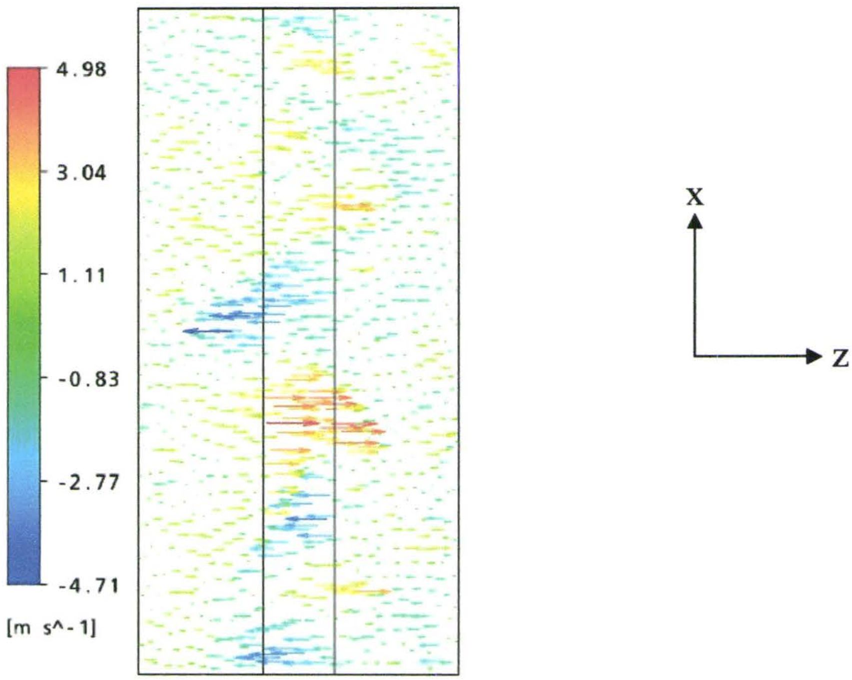

Figure 6.55 Snapshot of the velocity vector in the span-wise direction at the symmetry plane.

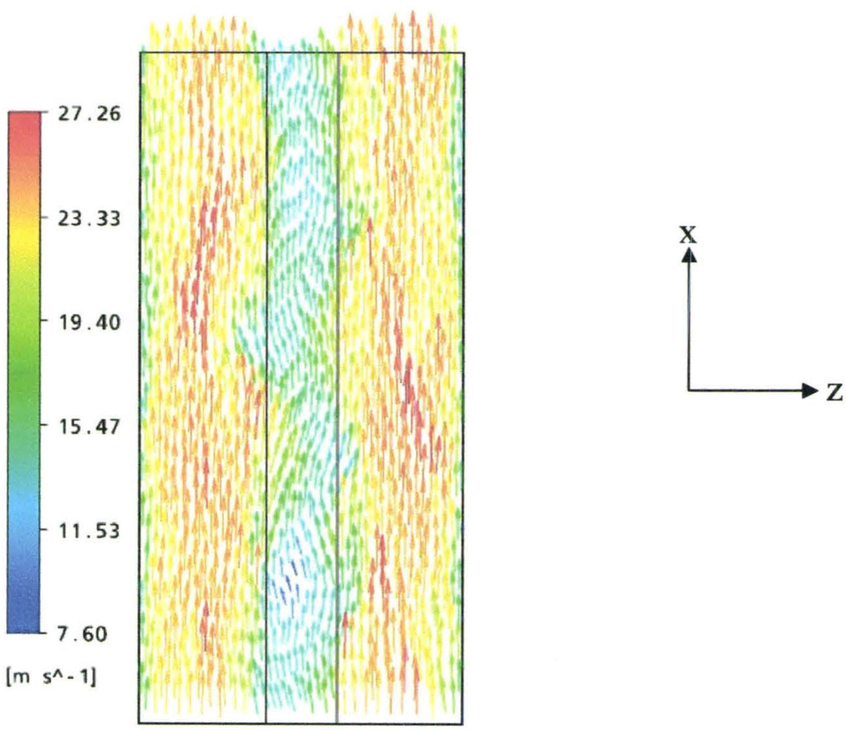

Figure 6.56 Snapshot of the overall velocity vector at the symmetry plane.

further reiterates the presence of alternate sequence of flows across the gap. Finally, the overall instantaneous velocity vector at the symmetry plane is shown in Figure 6.56. The velocity vectors too show a wiggly pattern in and around the vicinity of the gap region, similar to the streamline pattern.

6.5.4 Lateral flow and pressure field

The instantaneous lateral flow which is basically the tangential projection of the velocity vector, at two different cross sectional planes arbitrarily chosen in the stream-wise direction is shown in Figures 6.57 and 6.58. In Figure 6.57, the flow is flushed in from the right sub-channel to the left, and in Figure 6.58, the flow is driven from the left sub-channel to the right. In these cases, the flow passes through the gap and ejects out into the sub-channels at high velocities, and mixes in the respective sub-channels. The time averaged projection of the lateral flow is shown in Figure 6.59. The time averaged slice shown, is after a time integration of 1.5 sec. In the time averaged projection (longer time scale), large-scale vortices are evident and there is practically no flow through the gap. Figure 6.59 clearly shows the secondary flow patterns. Around the vicinity of the edges of the gap, a pair of counter-rotating vortices are formed (for each edge location), as indicated in Figure 6.59. These secondary flow vortices are confined to regions inside the sub-channel and do not cross the gap. The direction of rotation of these vortices (in the time averaged frame) is determined by how the flow ejects out of the gap and mixes in the sub-channels (at an instantaneous time scale) creating two swirling zones with opposite sense of rotations. The flow pulsations create additional anisotropy in the Reynolds stresses near the gap region, and this anisotropy possibly produces the

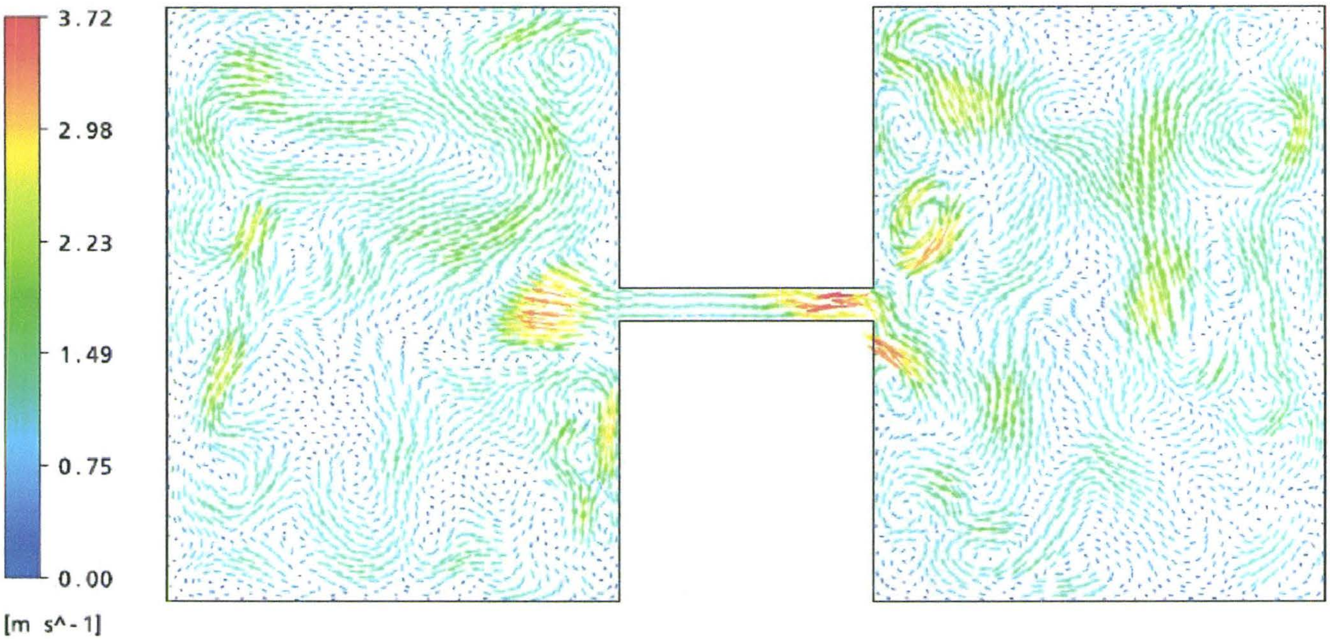

Figure 6.57 Instantaneous tangential projection of the velocity vectors.

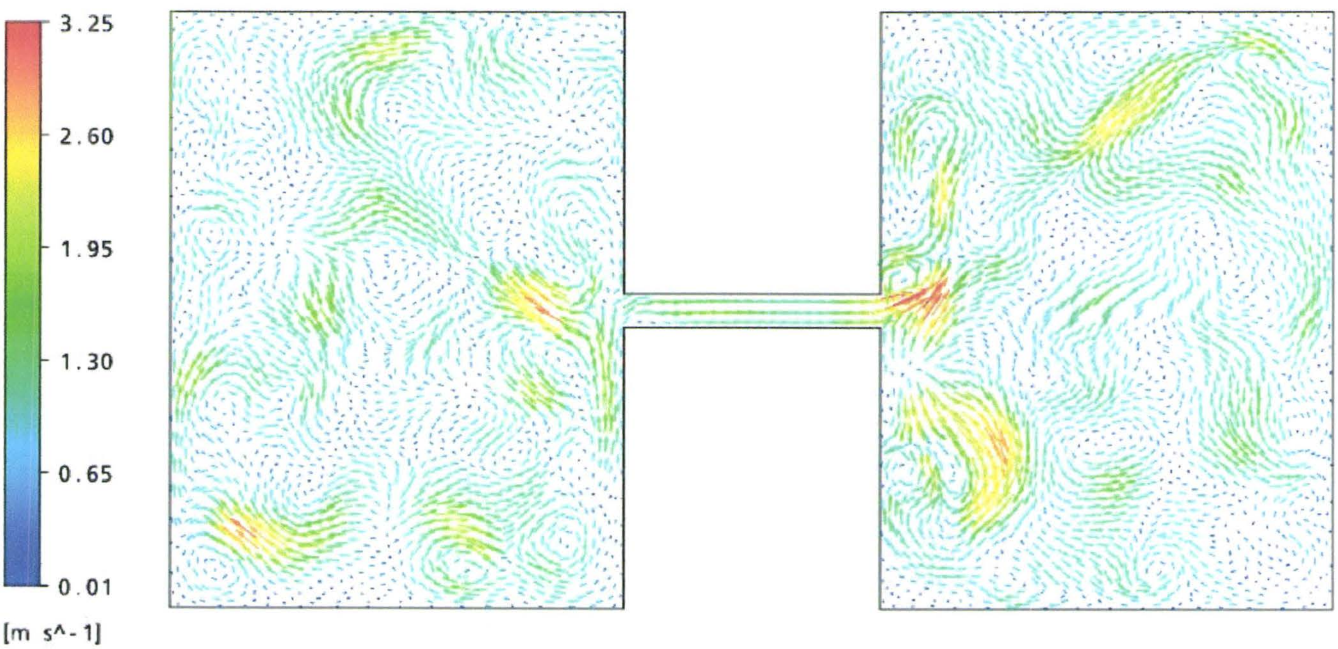

Figure 6.58 Instantaneous tangential projection of the velocity vectors.

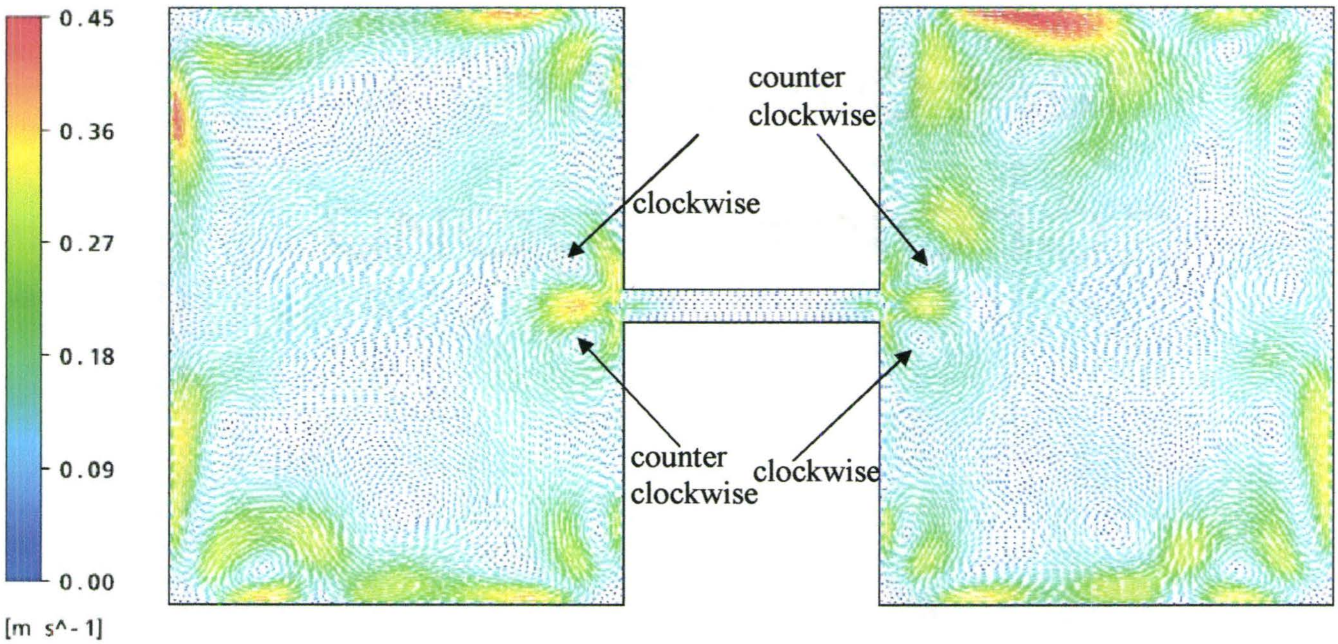

Figure 6.59 Time averaged projection of the velocity vectors.

secondary flows near the vicinity of the gap region. A pair of counter rotating vortices are also observed with respect to the bisector line for the corners of the sub-channels, which is reminiscent of secondary flow vortices formed in pure duct flows. The maximum magnitude of the secondary flows is around 2% of the bulk velocity, which reiterates the fact that secondary flows are not responsible for high mixing rates observed in sub-channel geometries with a small gap region. The flow pulsations through the gap shown in Figures 6.57 and 6.58, exist at a much shorter time scale than the secondary flow vortices, and cause mass and momentum transport between sub-channels. This mass and momentum transport can be associated to an unsteady convection that promotes heat transfer in sub-channels, which is stronger than that in isotropic turbulence.

The local pressure field was analyzed at different axial locations in order to describe the lateral flow from the sub-channels towards the gap region, and in this process different flow mixing patterns were identified. The following analysis was performed at an instantaneous time of 1 sec and at different stream-wise locations. Figures 6.60 and 6.61 show the velocity vectors and pressure field at the cross-sectional plane located at 200 mm from the origin. It is clear from the velocity vectors that streams of fluid from the core of the sub-channels come and converge (mix) at the gap. Very intense eddy motions exist in the right sub-channel, which break and form into streams of fluid, which travel towards the gap region as a result of the momentum of the fluid and the local pressure difference. An intense low pressure core exists around the gap edge towards the left sub-channel. This low pressure core causes fluid streams to be sucked in from the left sub-channel towards the gap at very high velocities. Figures 6.62 and 6.63 show the velocity

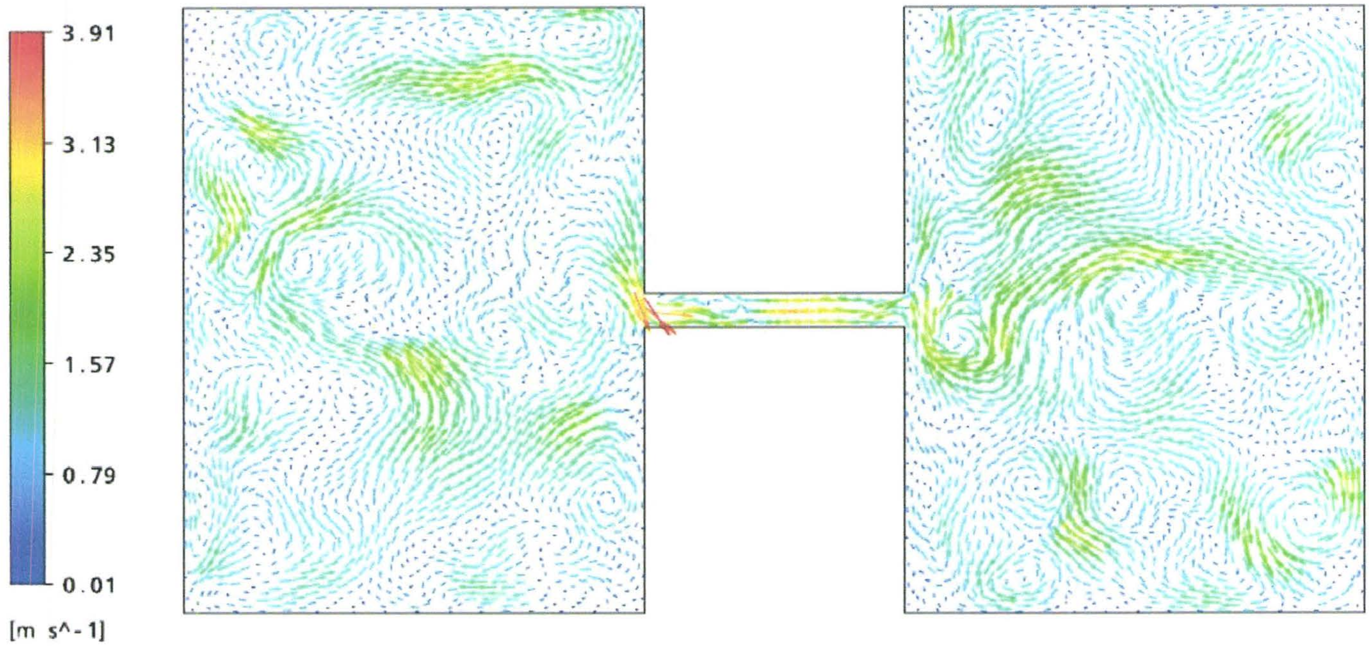

Figure 6.60 Instantaneous tangential projection of the velocity vectors at the cross-sectional plane located at x = 200 mm.

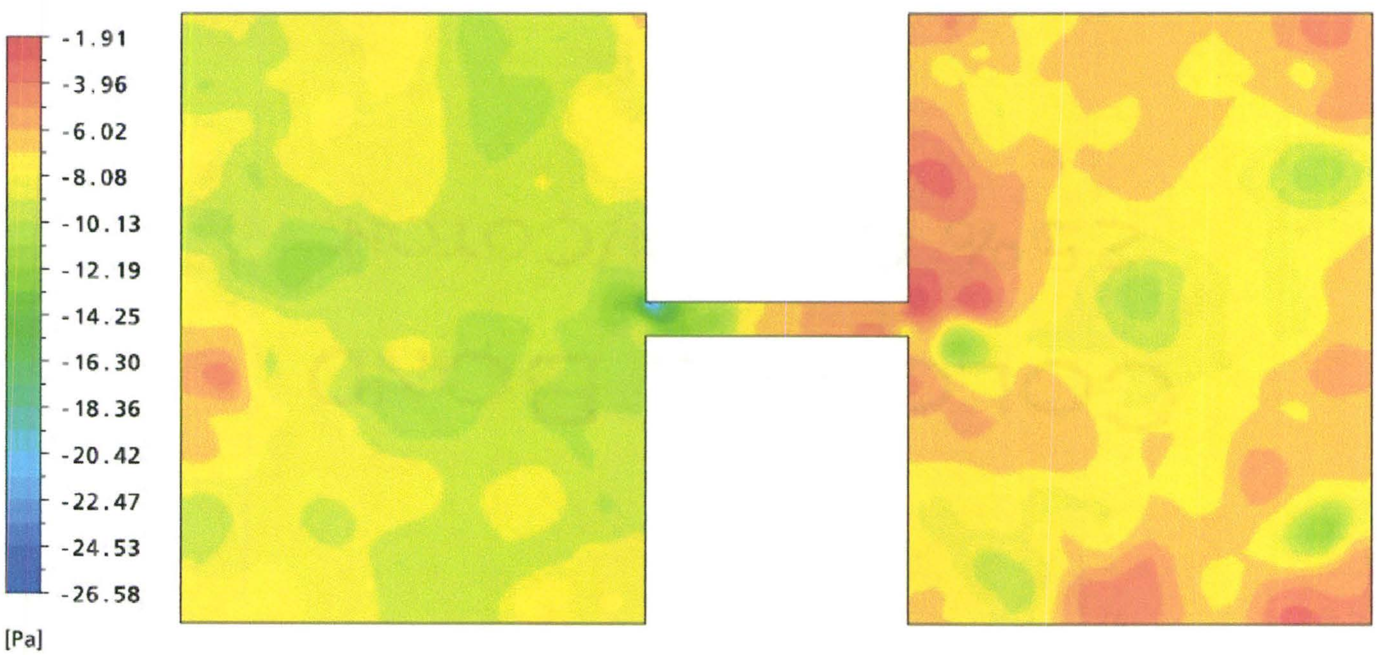

Figure 6.61 Instantaneous pressure contour at the cross-sectional plane located at x = 200 mm.

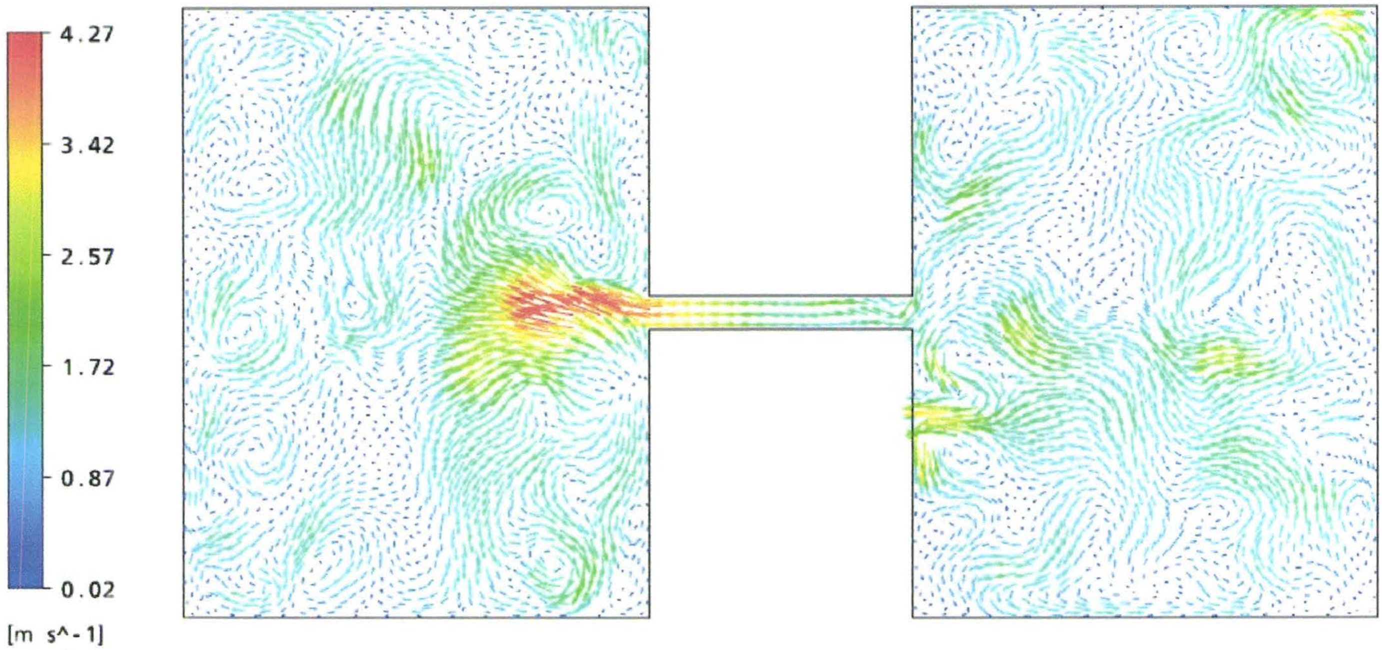

Figure 6.62 Instantaneous tangential projection of the velocity vectors at the cross-sectional plane located at x = 390 mm.

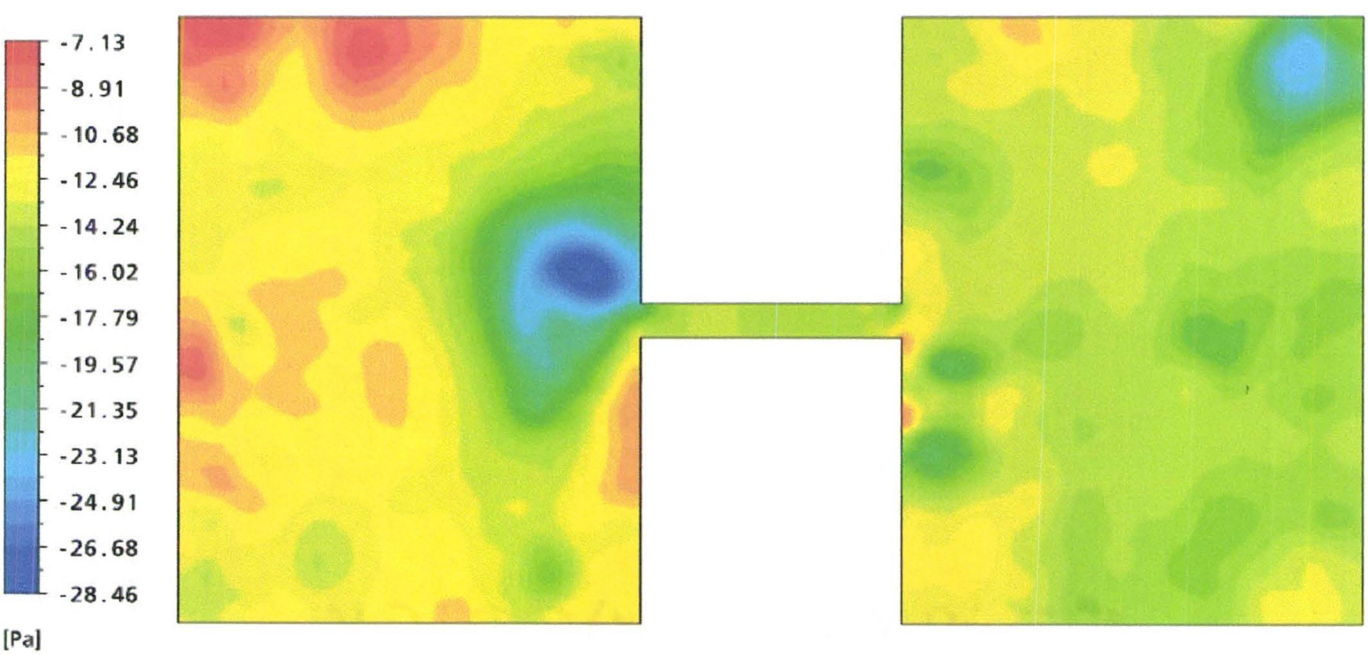

Figure 6.63 Instantaneous pressure contour at the cross-sectional plane located at x = 390 mm.

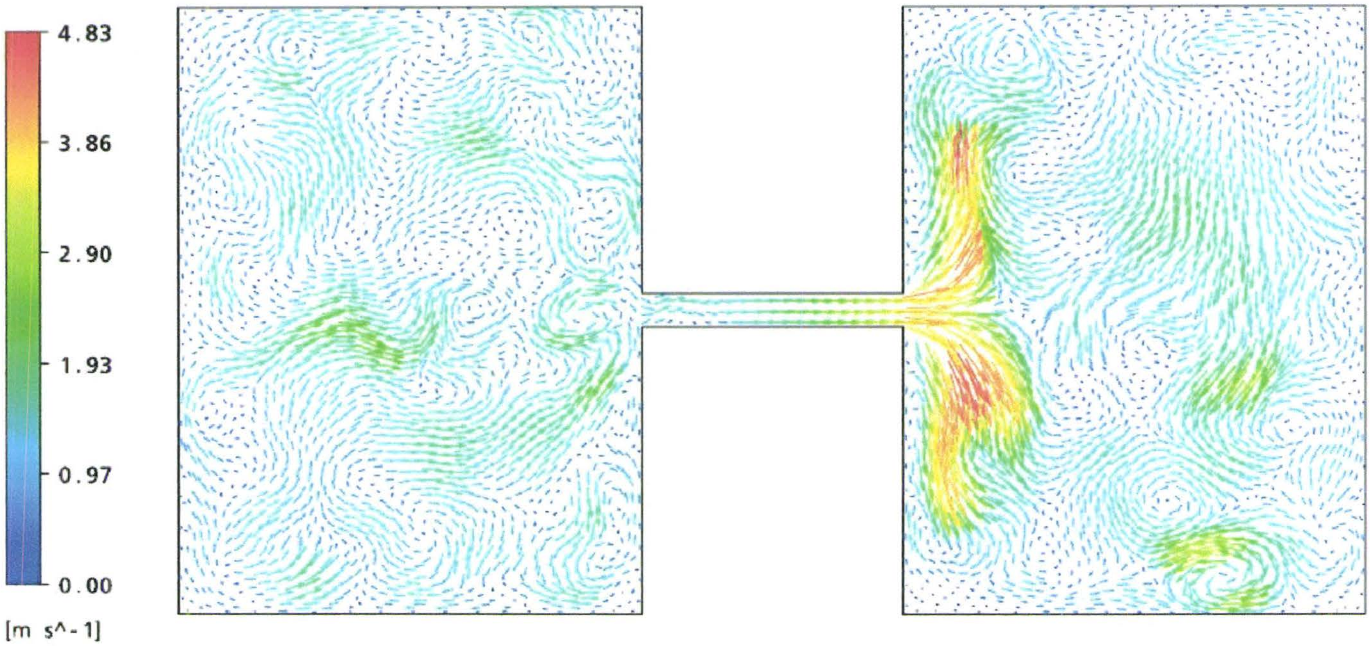

Figure 6.64 Instantaneous tangential projection of the velocity vectors at the cross-sectional plane located at x = 500 mm.

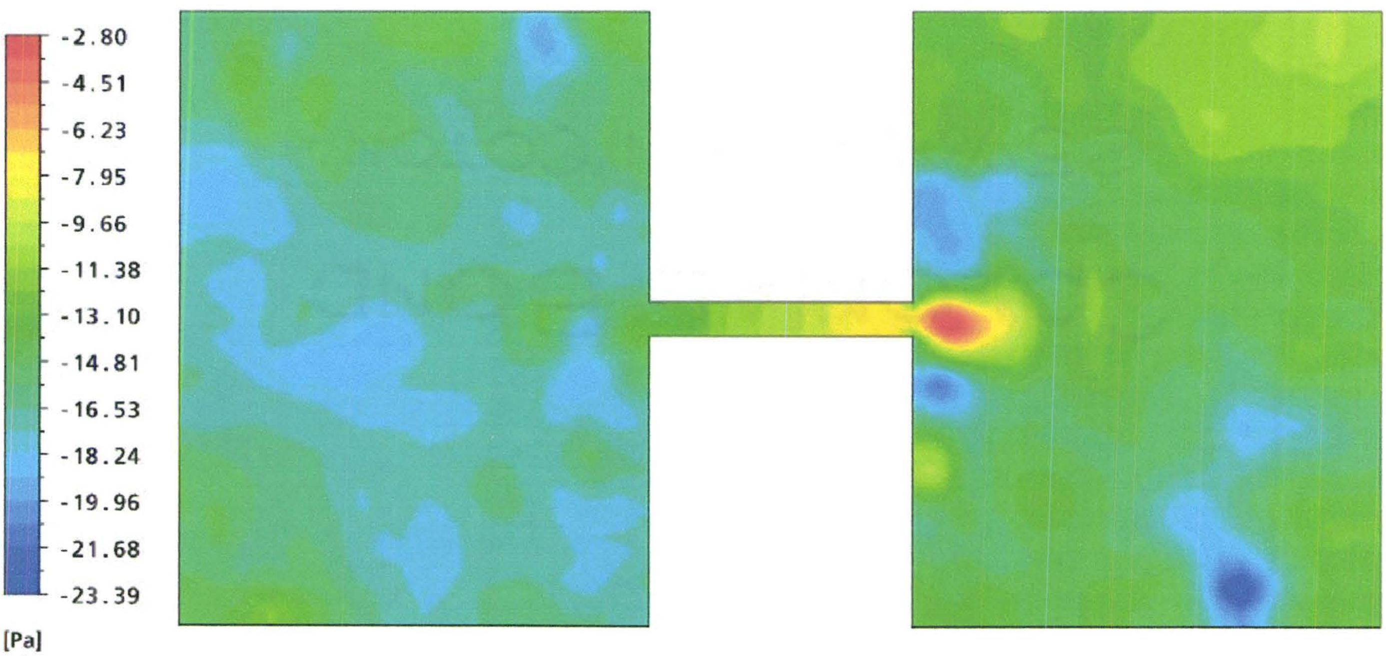

Figure 6.65 Instantaneous pressure contour at the cross-sectional plane located at x = 500 mm.

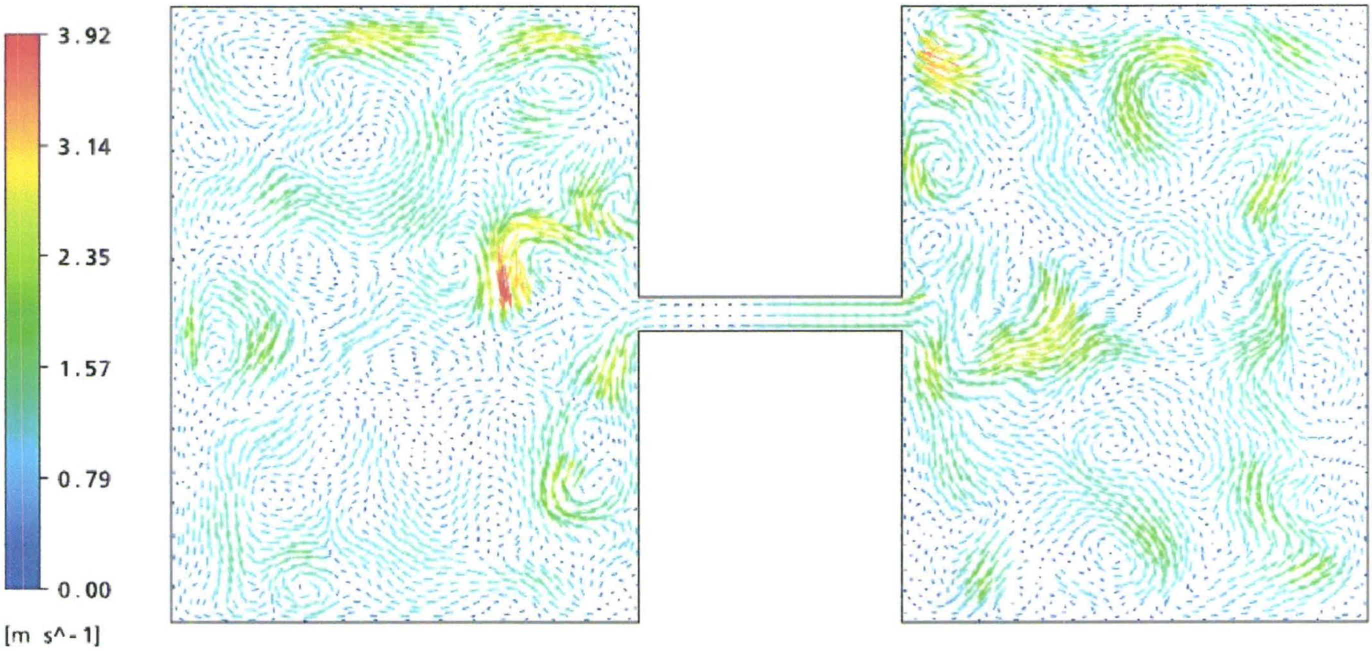

Figure 6.66 Instantaneous tangential projection of the velocity vectors at the cross-sectional plane located at x = 650 mm.

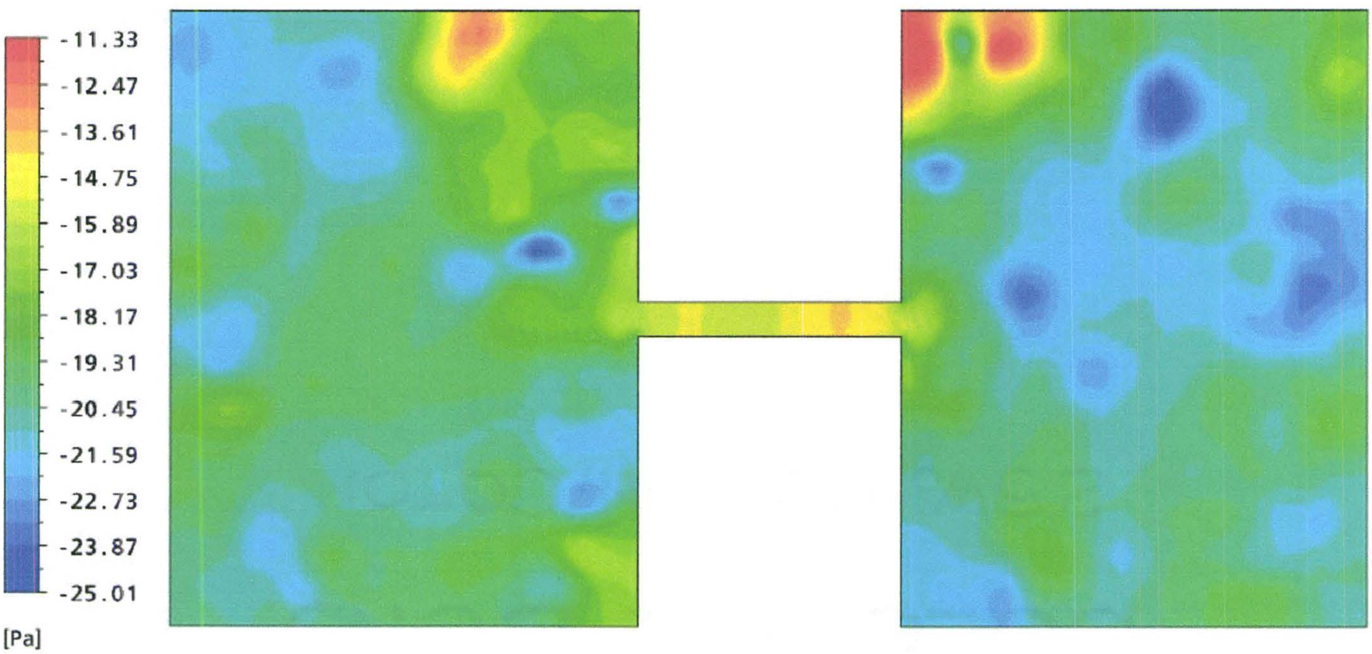

Figure 6.67 Instantaneous pressure contour at the cross-sectional plane located at x = 650 mm.

vectors and pressure field at the cross-sectional plane located at 390 mm from the origin. It is clear from the velocity vectors that fluid streams from the core of the right sub-channel travel through the gap and flush into the left sub-channel at very high velocities. An intense low pressure region is formed near the gap region of the left sub-channel, which causes the fluid mixing to occur from the right towards the left sub-channel. Figures 6.64 and 6.65 show the velocity vectors and pressure field at the cross-sectional plane located at 500 mm from the origin. At this location, streams of fluid from the left sub-channel travel through the gap and flush into the right sub-channel at high velocities. A local high pressure core is formed near the gap region of the right sub-channel, which acts to block the fluid from exiting the gap. As a result the fluid from the gap is diverted towards the top or bottom of the sub-channel. Figures 6.66 and 6.67 show the velocity vectors and pressure field at the cross-sectional plane located at 650 mm from the origin. In this case, low velocity fluid diverges out from the gap towards the respective sub-channels. The local pressure in the gap is higher than the nearby regions of the sub-channels, which causes the fluid to be pushed outwards into the sub-channels.

The above analysis has identified three different mixing patterns. Similar observations were made at different instants of time. The dominating mixing pattern at an instant in time occurs when the fluid streams coming from either of the sub-channels flushes into the other sub-channel. This mixing pattern decides the sense of rotation of the secondary flow zones around the edges of the gap region. In a sub-channel geometry, the flow is transported from the region of high momentum (sub-channels) to the narrow gap along the walls and it is transported back to the region of low shear. The fluid flow pulsation is based on the combination of the high momentum fluid streams breaking away from the eddy zones, and the local pressure field difference.

6.5.5 Coherent structure characterization and vorticity field

The secondary flow patterns formed near the gap (Figure 6.59) could be associated with quasi-periodic stream-wise coherent structures, which appear as a street of counter-rotating vortices on both sides of the gap. The identification of the turbulent structures in the flow field is critical, since they significantly affect both the momentum and heat transfer for processes such as mixing (Hunt et al., 1988). In the present investigation, the turbulent structures were identified using the Q-criterion proposed by Hunt et al. (1988). The Q-criterion was chosen for the present study because it has been widely used; the Q variable is easy to formulate and is applicable for a wide range of turbulent flows. Hunt et al. (1988) identified four different turbulent structures viz., eddies, convergence zones, shear zones and streams. The turbulent structures are identified based on the balance between the irrotational strain and vorticity, and a pressure (p) threshold restriction. The Q variable is defined as the second invariant of the velocity gradient tensor and is formulated as:

$$Q = -\frac{1}{2}\left(\Omega_{ij}\Omega_{ji} + S_{ij}S_{ji}\right) \tag{6.4}$$

where Ω_{ij} and S_{ij} are the local rotation and strain rate tensors, and are formulated as:

$$\Omega_{ij} = \frac{1}{2}\left(\frac{\partial u_i}{\partial x_j} - \frac{\partial u_j}{\partial x_i}\right) \tag{6.5}$$

$$S_{ij} = \frac{1}{2}\left(\frac{\partial u_i}{\partial x_j} + \frac{\partial u_j}{\partial x_i}\right) \tag{6.6}$$

The rotation and strain rate tensors can be expressed in terms of the vorticity vector (ω_k) and the strain modulus (S) respectively.

$$\Omega_{ij} = -\frac{1}{2}\varepsilon_{ijk}\omega_k \tag{6.7}$$

$$S = \sqrt{S_{ij}S_{ij}} \tag{6.8}$$

The Q variable can thus be written in terms of the vorticity modulus (ω) and the strain modulus:

$$Q = \frac{1}{4}\left(\omega^2 - 2S^2\right) \tag{6.9}$$

Thus, from Eq. (6.9) it is evident that the Q variable represents the relative importance of vorticity and strain.

Combining Eq.s (6.4), (6.5) and (6.6), the Q variable is written in a very convenient form.

$$Q = -\frac{1}{2}\frac{\partial u_i}{\partial x_j}\frac{\partial u_j}{\partial x_i} \tag{6.10}$$

The description of the different turbulent structure regions and their identification criteria are based on Hunt et al., 1988. The regions are identified based on velocity, pressure and their derivatives. The reason for including pressure as an identification variable is that it brings in a broad region of information about the flow field, owing to its elliptic dependence on velocity. The mathematical classification of the different zones is based on a combination of intuition and numerical optimization. The optimization consists of observing a tentative classification against a background of various flow quantities, such as velocity vectors, pressure or vorticity fields, eigenvalues and invariants of the strain and deformation tensors, etc. The different zones are identified as follows:

(i) Eddies: Eddies are regions of rotational flow where vorticity dominates irrotational strain. These are regions of swirling zones, with net circulation and are thus regions of low pressure, where the streamlines curve around. The two simultaneous criteria that is used to define zones of eddy region are:

$$Q > 0.5Q_{rms} \text{ and } p < -0.5p_{rms}$$

(ii) Shear zones: Shear zones are defined to be vortical flow regions with no circulation and so are regions of moderate pressure. The criteria that is used to define the shear zones are:

$$Q > 0.5Q_{rms} \text{ and } -0.5p_{rms} < p < p_{rms}$$

(iii) Convergence zones: The convergence zones are defined to be regions where there is irrotational straining motion, with converging and/or diverging streamlines. These zones are identified based on the following criteria:

$$Q < -Q_{rms} \text{ and } p > p_{rms}$$

(iv) Streams: Streams are regions of high speed but weak deformation, where the flow is relatively fast and not very curved. The flow in the streams does not converge or diverge strongly. These zones are the main transport for fluid or particles across the flow. Streams are identified based on the following criteria:

$$|Q| < \min(0.5Q_{rms}, Q_{rms}) \text{ and } |u| > |u|_{rms}$$

In the analysis, the Q variable was evaluated using Eq. (6.10) and the different regions were identified based on the aforementioned criteria. Sub-volumes were created in the domain and the average representation of the space occupied by the structures was estimated. At a given time step, the Q criterion classified approximately 31% of the total volume into eddies, shear zones and streams. Streams were found to be the largest structures, occupying approximately 20% of the total volume. Eddies and shear zones occupied approximately 10% and 1% of the total volume respectively. Figure 6.68 shows the snapshot for the isosurface plot of the Q variable at a specific threshold value of Q_{norm}, where $Q_{norm} = Q/(0.5\times Q_{rms})$. The isosurface plot is colored by the pressure variable, and was specifically created to show the eddy and the shear zone regions. In Figure 6.68, the red regions indicate the eddies and the remaining structures represent the shear zones. It is clear that the eddies and the shear zones are concentrated in the two sub-channels and that the shear zones surround the eddies. Figure 6.69 shows a snapshot of the contour plot for the Q variable, superimposed by the projection of the fluid velocity. The eddies (based on the identification criteria) are the dense white regions, with swirling structures of the velocity vectors. Intuitively, a general picture can be formed on the dynamical interaction between the eddies, shear zones and the streams. From the velocity vectors for the lateral flow and the isosurface plot shown in Figure 6.68, it appears that the eddies are flanked by the less swirling shear zones that transport the fluid along the high speed streams. These streams bring the high momentum fluid from the core of the sub-channel towards the gap region. As mentioned before, it is the combination of high speed streams and the instantaneous pressure difference across the sub-channels that causes the fluid to pulsate from one sub-channel to the other. It appears that the coherent vortical structures formed

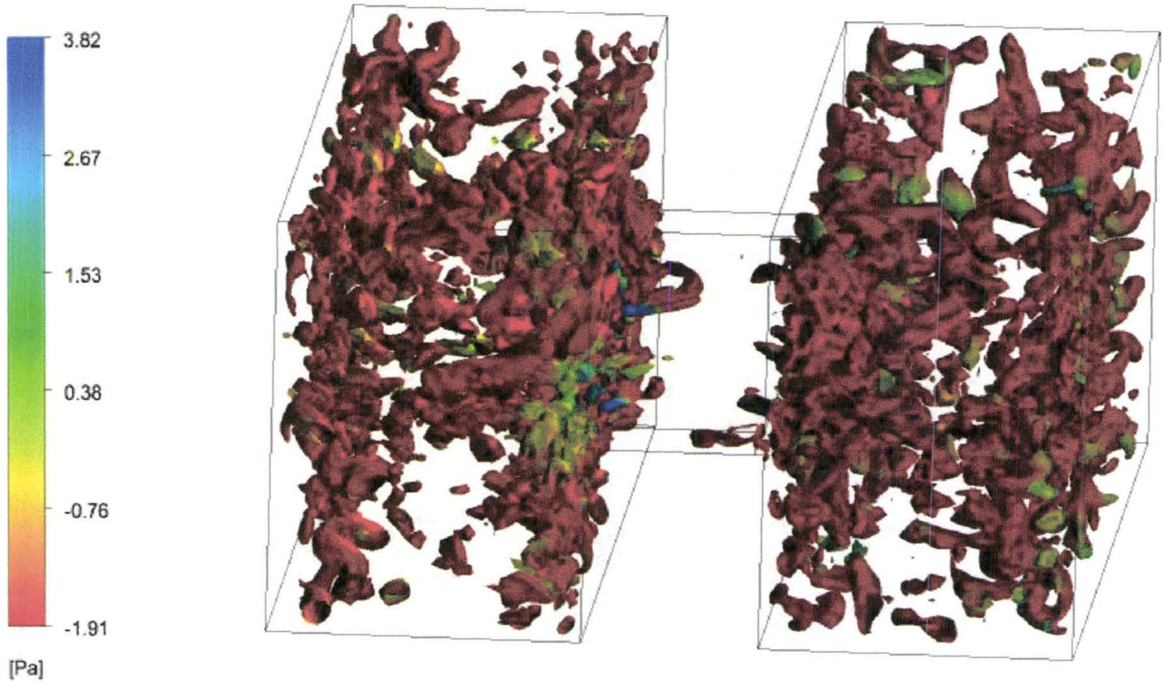

Figure 6.68 Isosurface of the Q (Q_{norm} = 1.2) variable showing the eddies and the shear zones.

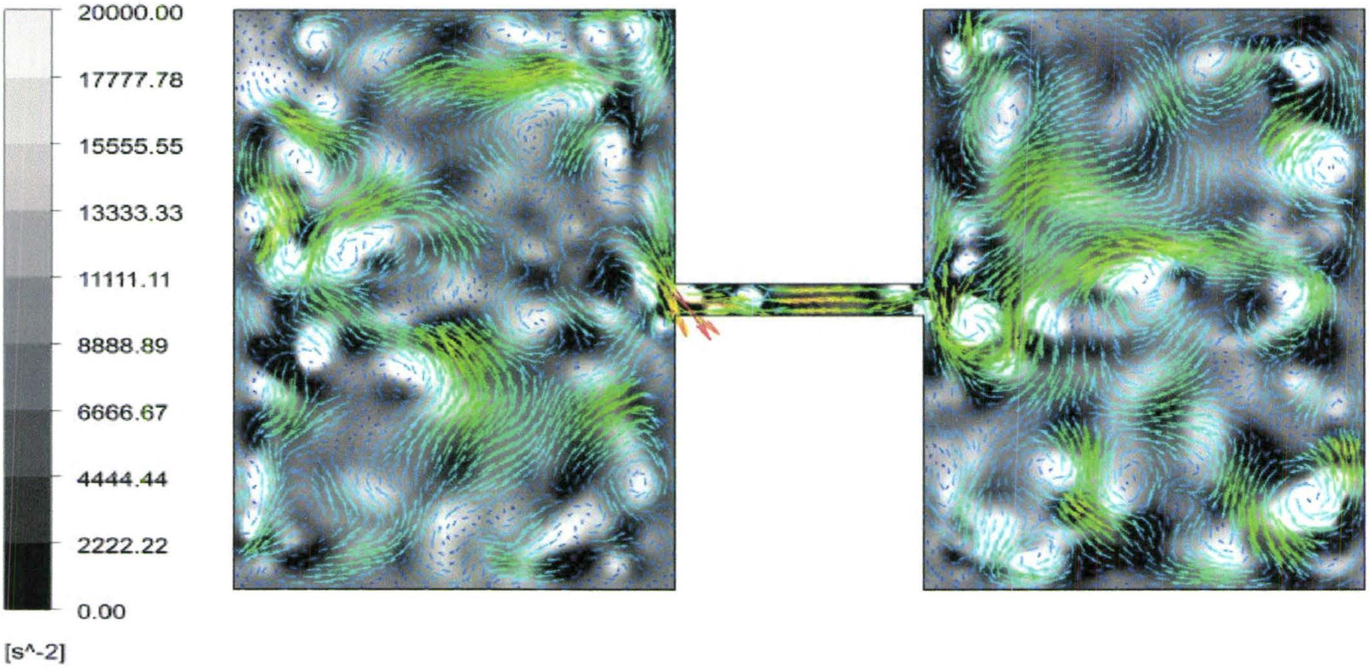

Figure 6.69 Superposition of the tangential velocity vectors on the Q profile.

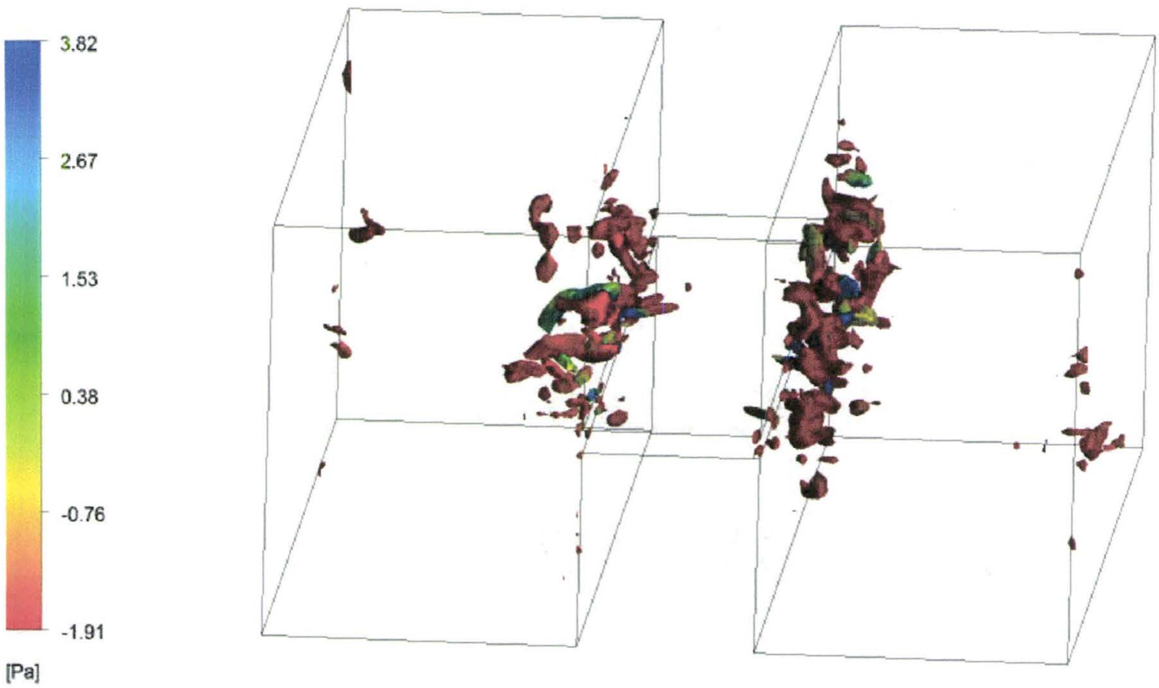

Figure 6.70 Isosurface of the Q (Q_{norm} = 5) variable showing the eddies and the shear zones.

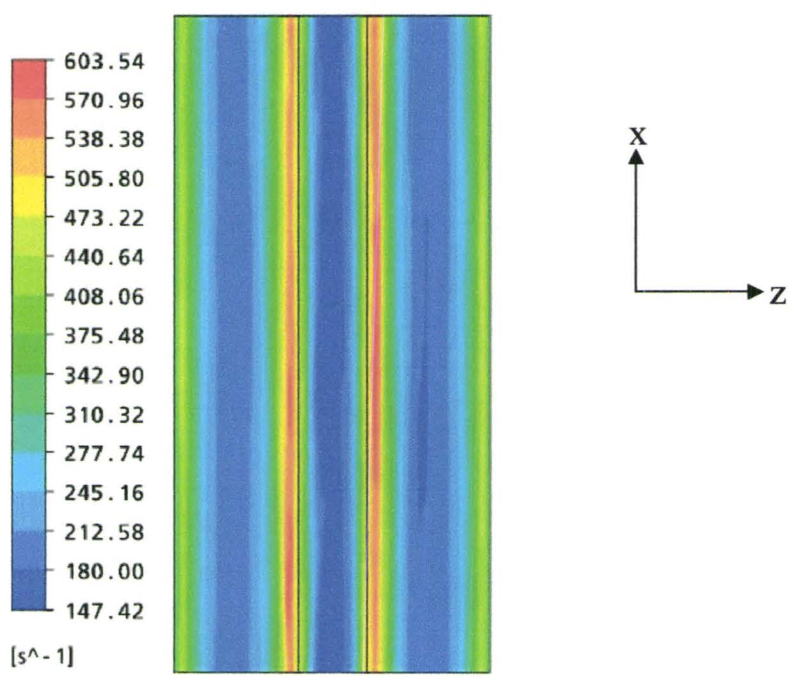

Figure 6.71 Contour of the vorticity fluctuation at the symmetry plane.

near the vicinity of the gap edge region are responsible for altering the pressure difference field across the sub-channels. Figure 6.70 depicts the snapshot of the isosurface plot of the Q variable at a very high threshold value of Q_{norm} , which primarily shows the eddy regions with very few shear zones, along the entire length of the gap edge region. This isosurface plot was created by employing the identification criteria's for the eddy and the shear zone structures. The high value of Q_{norm} basically indicates that intense vortical activity is specifically concentrated near the gap edge region, and that the coherent vortical structures in the form of eddies formed near the gap edge are associated with high vorticity. These eddy structures are pockets of low pressure region in the flow field. The specific characteristics of the eddy structures near the gap edge is obtained by looking into the vorticity field. Figure 6.71 shows the contour plot for the vorticity fluctuation at the symmetry plane through the gap. A trail of high vorticity is observed near the vicinity of the gap edge region, throughout the entire channel length along the stream-wise direction. It is of interest to see the individual components of vorticity and their contribution to the overall vorticity. Contour plots of the instantaneous vorticity in the normal (y) direction at the symmetry plane for different simulation times are shown in Figure 6.72. It is clear that patches of high values of positive and negative vorticity are present at the respective edge vicinities of the gap. The positive and negative vorticity is in accordance with the shear layer interaction at the edges of the gap. The shear layer interaction between the high velocity and the low velocity fluid around the gap edge region, causes the high velocity fluid to rollup towards the low velocity fluid. The positive vorticity is due to the counter-clockwise interaction (rollup) between the shear

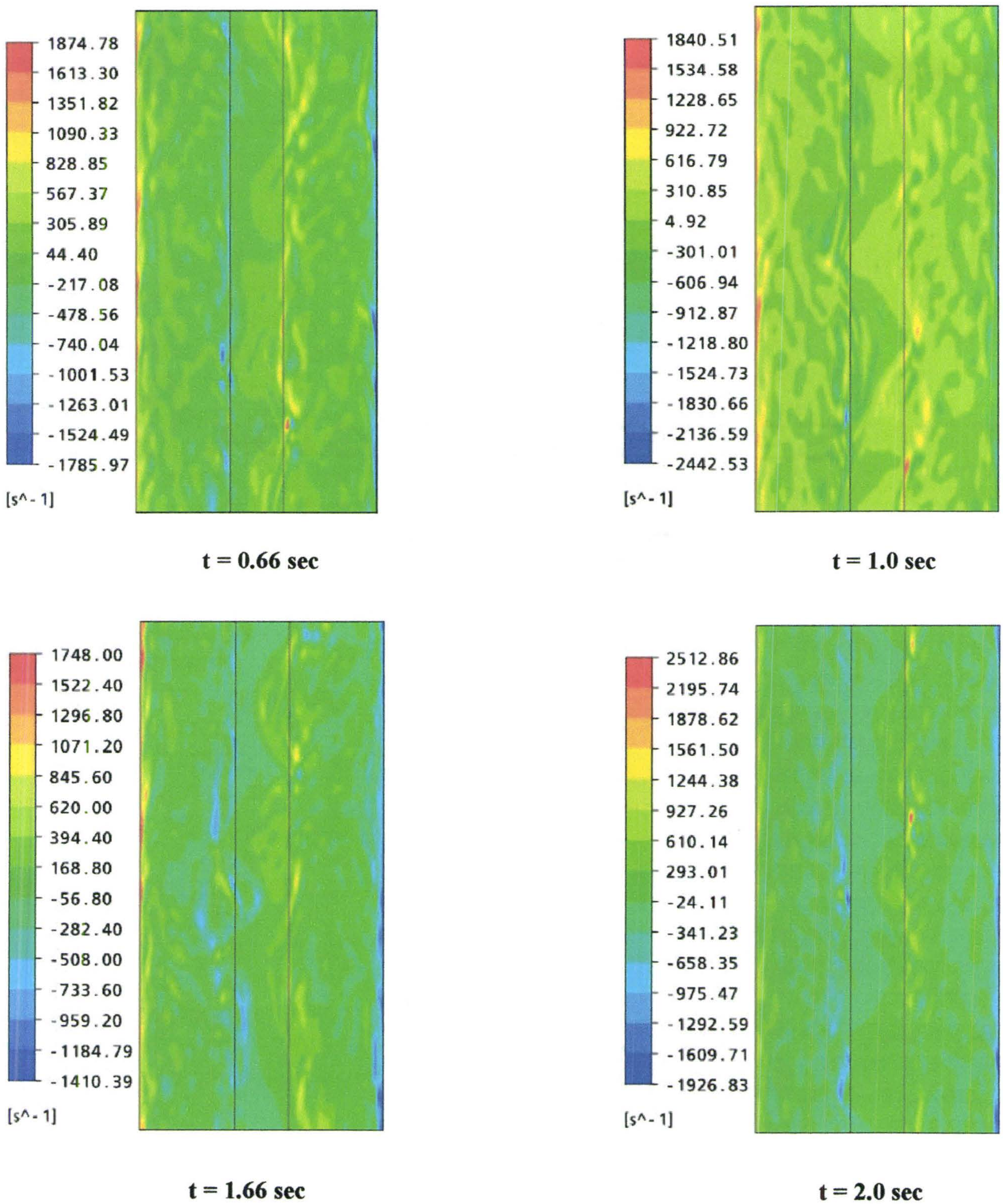

Figure 6.72 Snapshots of vorticity in the normal direction at the symmetry plane.

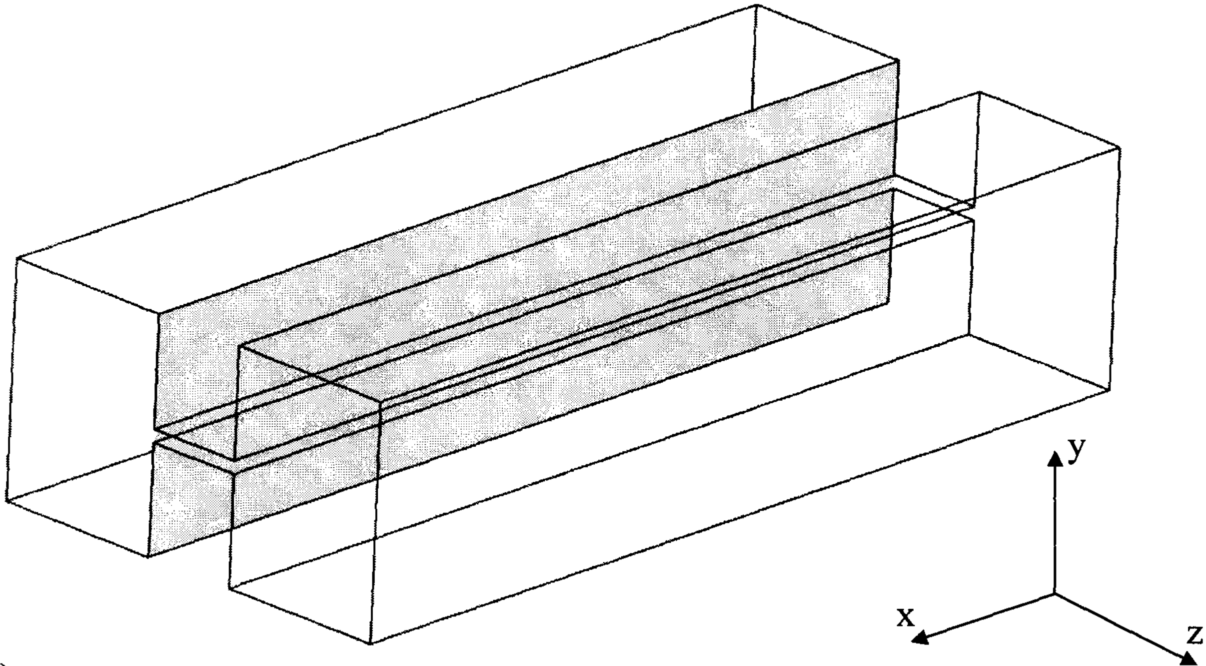

(a)

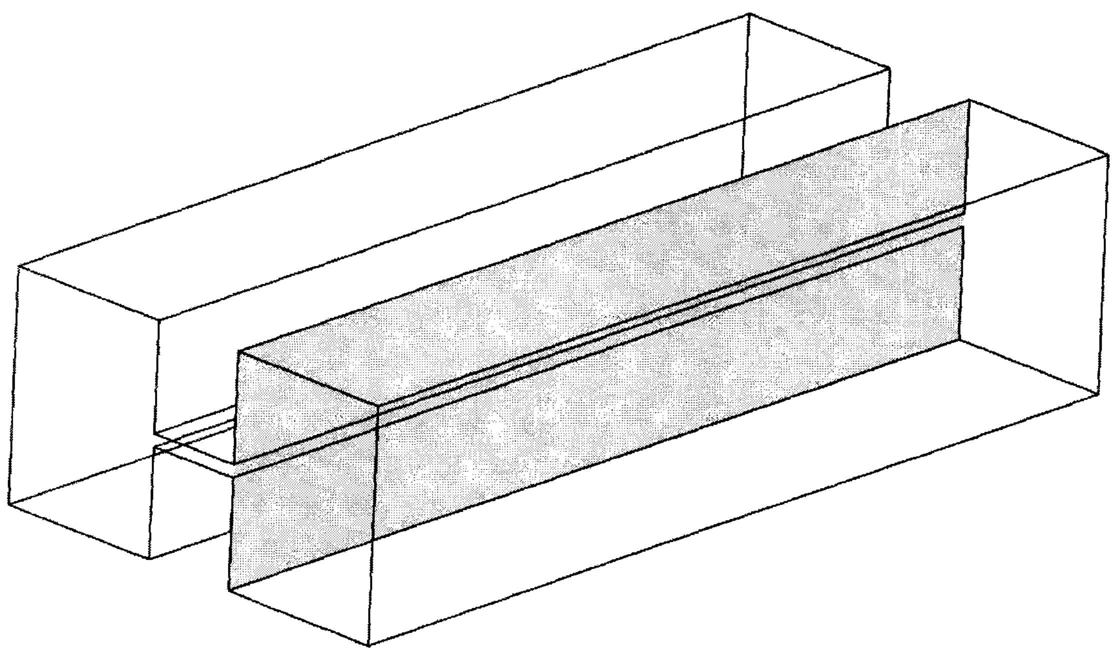

(b)

Figure 6.73 Location of planes (a) Left plane (LP) and (b) Right plane (RP).

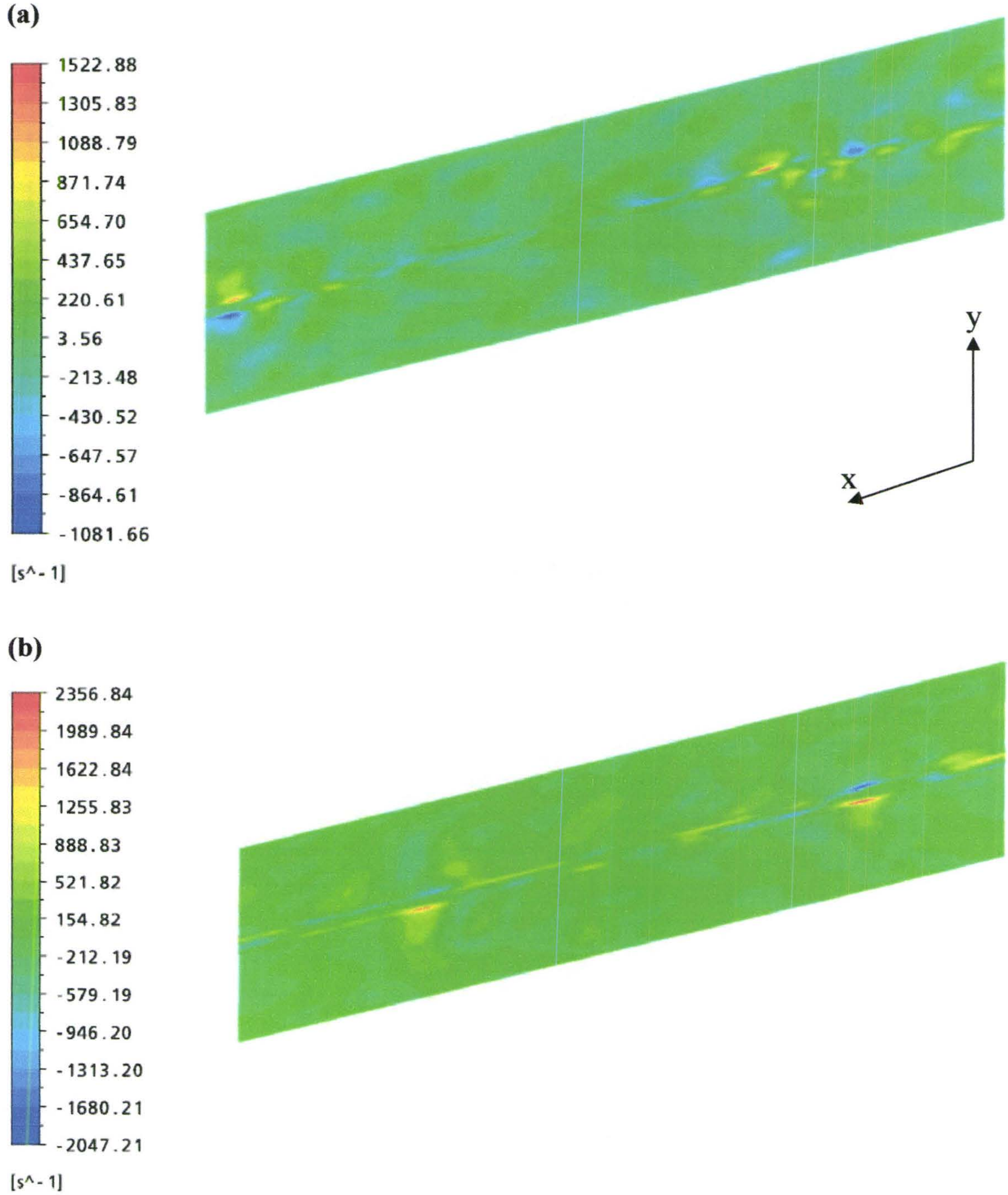

Figure 6.74 Snapshot of the stream-wise vorticity at time t = 0.66 sec (a) LP location and (b) RP location.

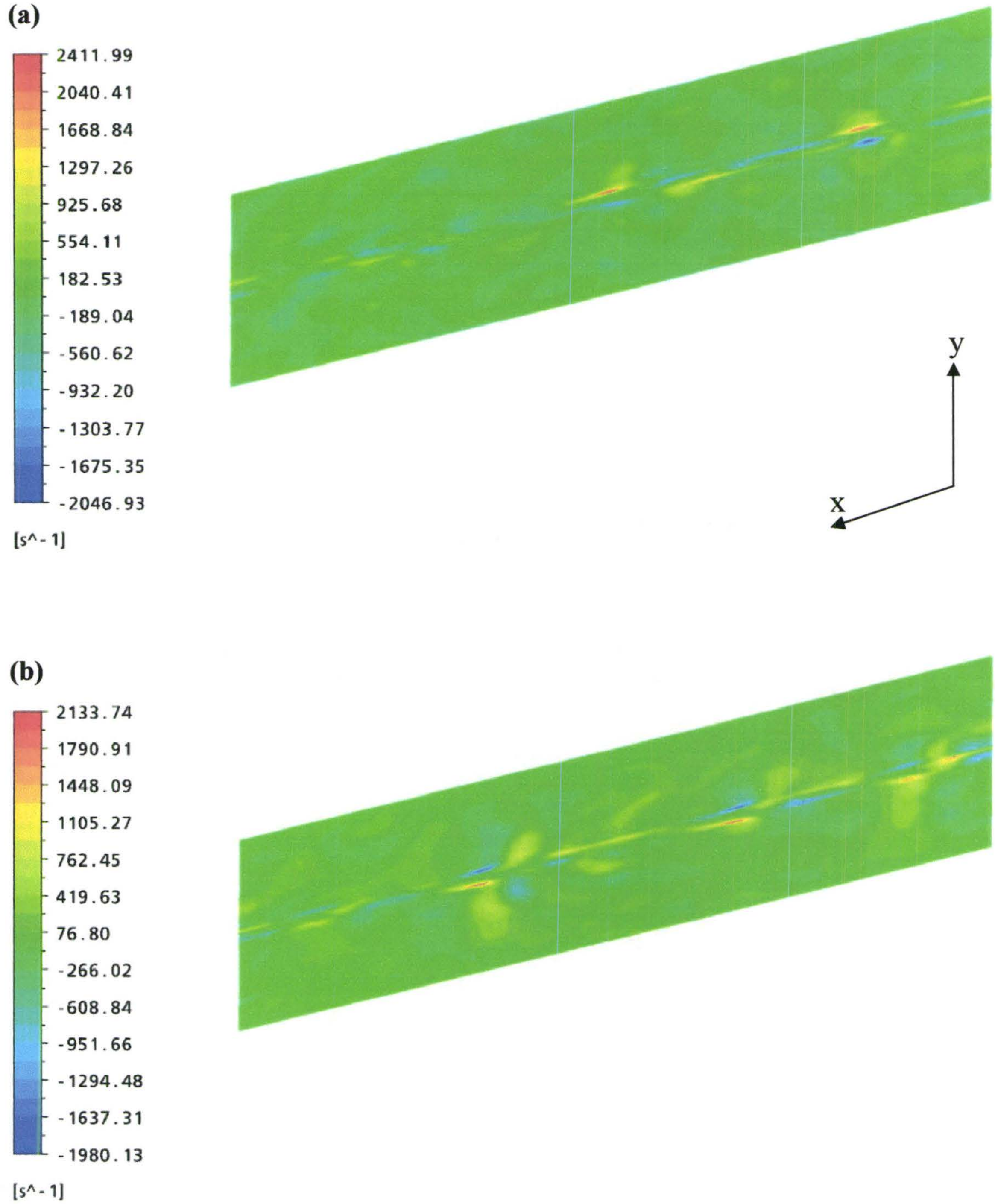

Figure 6.75 Snapshot of the stream-wise vorticity at time t = 1.0 sec (a) LP location and (b) RP location.

(a)

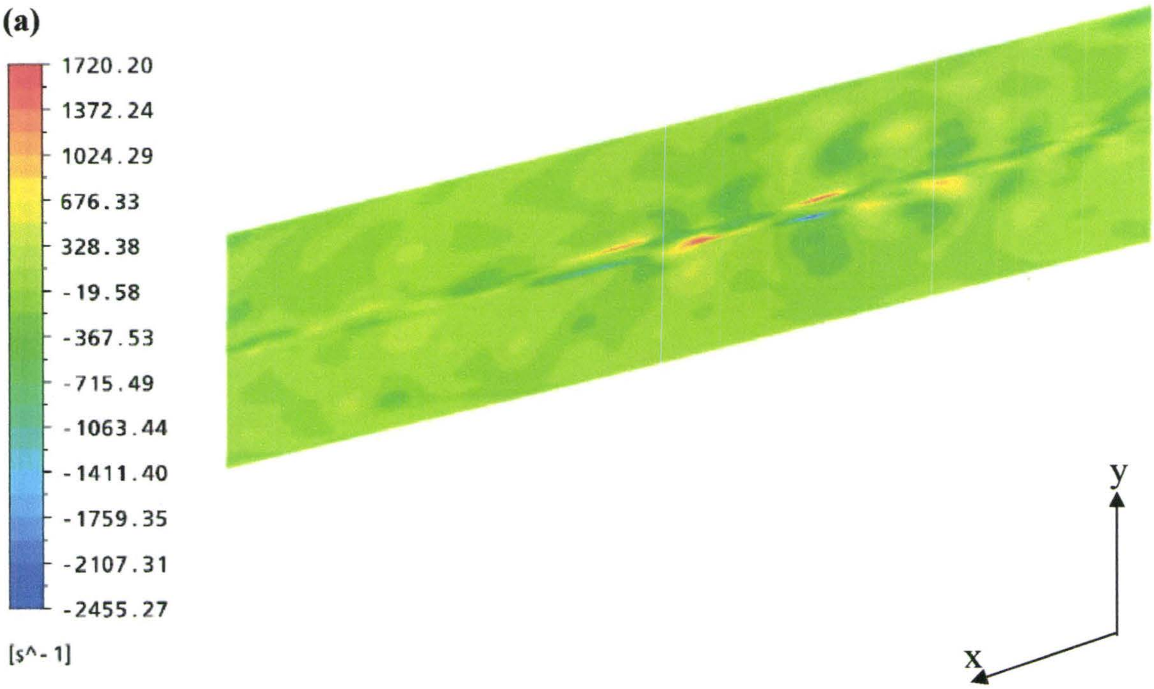

(b)

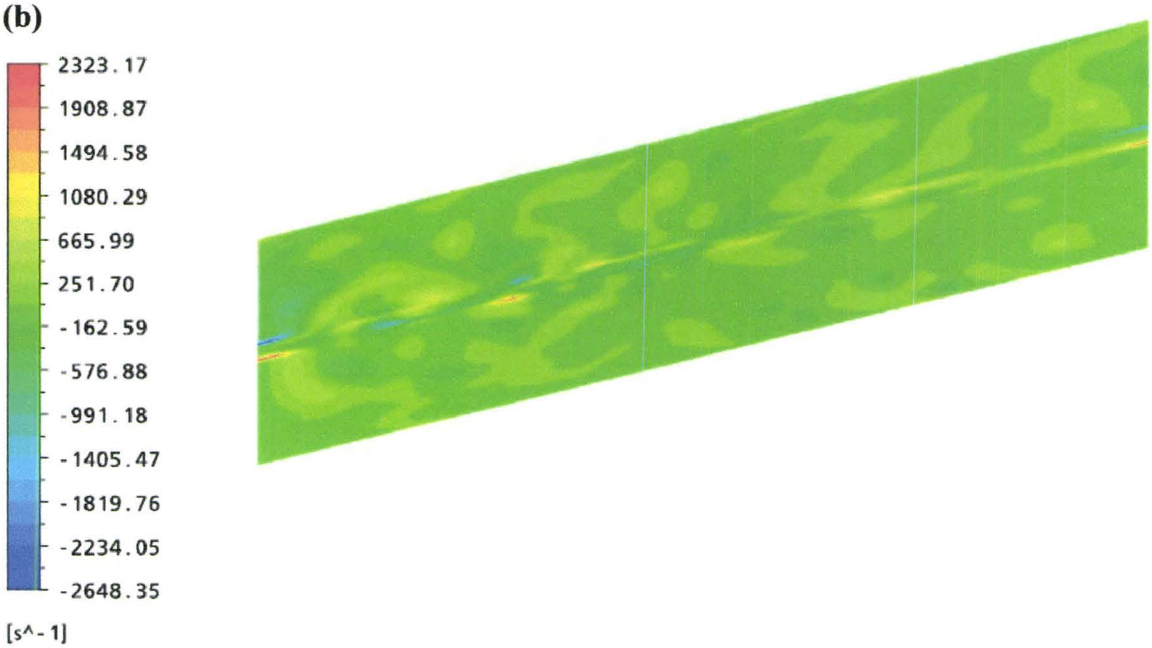

Figure 6.76 Snapshot of the stream-wise vorticity at time t = 1.66 sec (a) LP location and (b) RP location.

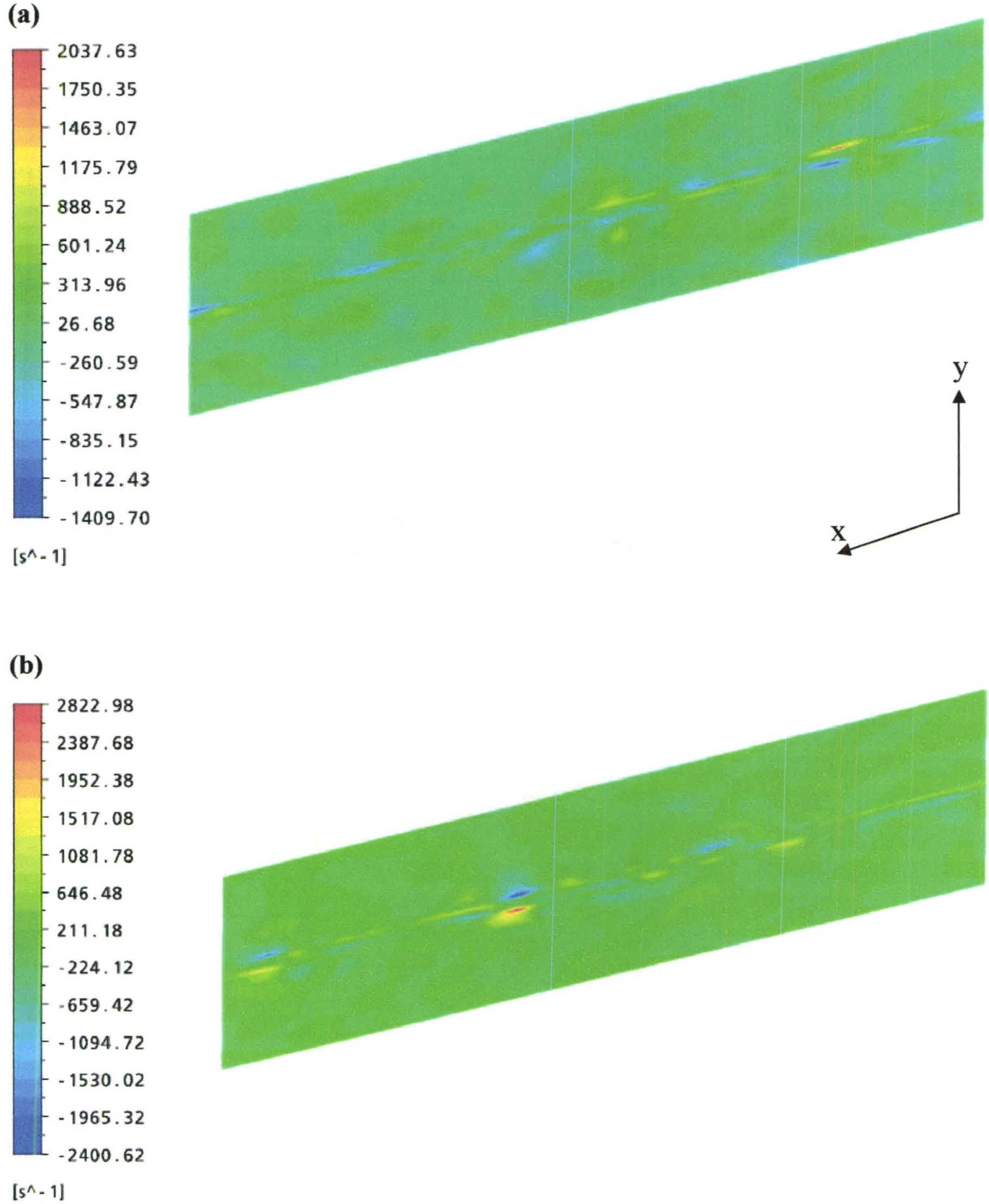

Figure 6.77 Snapshot of the stream-wise vorticity at time t = 2.0 sec (a) LP location and (b) RP location.

layers and the negative vorticity is due to clockwise interaction (rollup) between the shear layers. This shear layer interaction at the vicinity of the edges of the gap and the local vorticity causes the fluid to meander and follow a zig-zag path in and around the gap region, as seen from the velocity vector plot shown in Figure 6.56. The stream-wise vorticity was analyzed at the two planes shown in Figure 6.73. The two planes are located at the interface between the sub-channels and the gap, and are named as left plane (LP) and right plane (RP) for convenience. Figures 6.74-6.77 show the contour plot of the stream-wise vorticity at the two planes for different simulation times. Generally, it is observed from the contour plots that at the respective edges of the gap, high values of positive and negative vorticity are present. The positive and negative vorticity seem to exist in a quasi-periodic pattern. High values of the span-wise vorticity was also found at the gap edge regions. The quasi-periodic vortical structures formed at the edges of the gap are thus, associated with a three-dimensional vorticity field.

6.5.6 Structural analysis

The quasi-periodic vortical structures formed near the gap edge region are coherent structures which cause large-scale phase correlation in the turbulence quantities, both temporally as well as spatially in the stream-wise and span-wise directions. The temporal correlation functions were obtained using 2301 data points, and were sampled at a base frequency of 10,000 Hz. The three temporal auto-correlation functions are defined as:

$$R_{ww} = \frac{\overline{w^{'}(x,y,z,t)\, w^{'}(x,y,z,t+\Delta t)}}{\sqrt{\overline{w^{'}(x,y,z,t)^{2}}}} \tag{6.11}$$

$$R_{uu} = \frac{\overline{u^{'}(x,y,z,t)u^{'}(x,y,z,t+\Delta t)}}{\sqrt{\overline{u^{'}(x,y,z,t)^{2}}}} \tag{6.12}$$

$$R_{uw} = \frac{\overline{u^{'}(x,y,z,t)w^{'}(x,y,z,t+\Delta t)}}{\sqrt{\overline{u^{'}(x,y,z,t)^{2}}}\sqrt{\overline{w^{'}(x,y,z,t)^{2}}}} \tag{6.13}$$

Figures 6.78 and 6.79 show the predicted and experimental temporal auto-correlation function respectively, for the span-wise velocity component (R_{ww}) at different monitor points. The time on the abscissa of the figures correspond to the time lag (Δt) between the velocity component (signal). The DES-SST model was successful in predicting the oscillating pattern in the auto-correlation function seen experimentally. At the gap centre (monitor point 4), the span-wise velocity component is the most correlated. The predicted and experimental temporal auto-correlation function for the stream-wise velocity component (R_{uu}) at the different monitor points is shown in Figures 6.80 and 6.81 respectively. The oscillating pattern in the auto-correlation function is captured by the DES-SST model. The stream-wise auto-correlation function at the gap centre (monitor point 4) does not show a periodic trend, instead it de-correlates with time, which is shown by both the predicted and experimental data. The two correlation functions, R_{ww} and R_{uu} suggest that there is a dominant period associated with the two signals. The period of the auto-correlation function is obtained by taking the inverse of the time at which the correlation functions obtain their second maximum (Meyer and Rehme, 1994). In general, the period obtained from the DES-SST prediction is 0.0146 sec, whereas the reported experimental period is 0.0147 sec (Meyer and Rehme, 1994). The predicted temporal auto-correlation function associated with the cross velocity components, u and w, i.e. R_{uw}

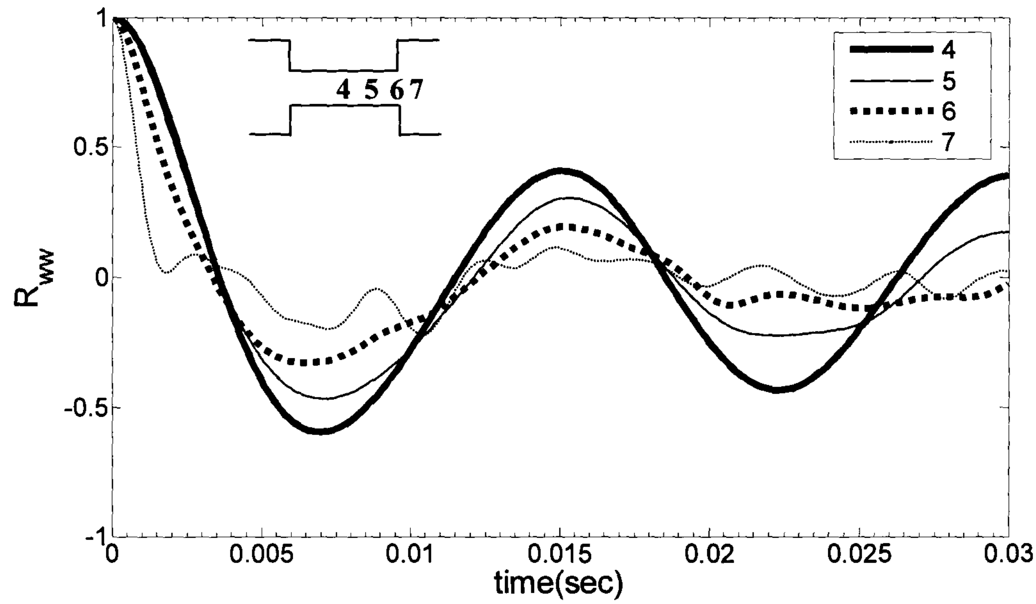

Figure 6.78 DES-SST prediction of span-wise temporal auto-correlation function.

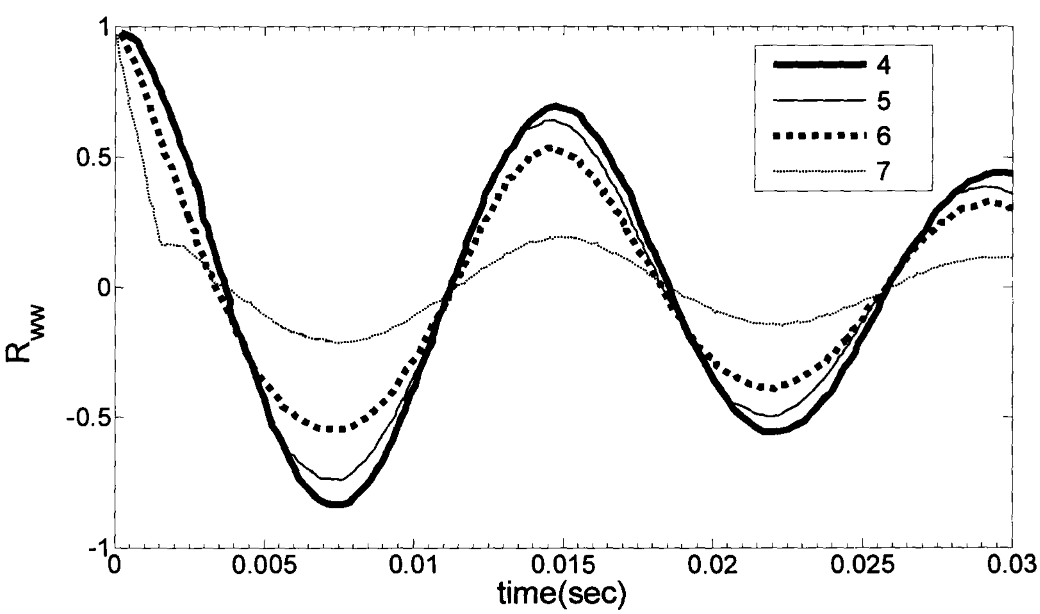

Figure 6.79 Span-wise temporal auto-correlation function (Meyer and Rehme, 1994).

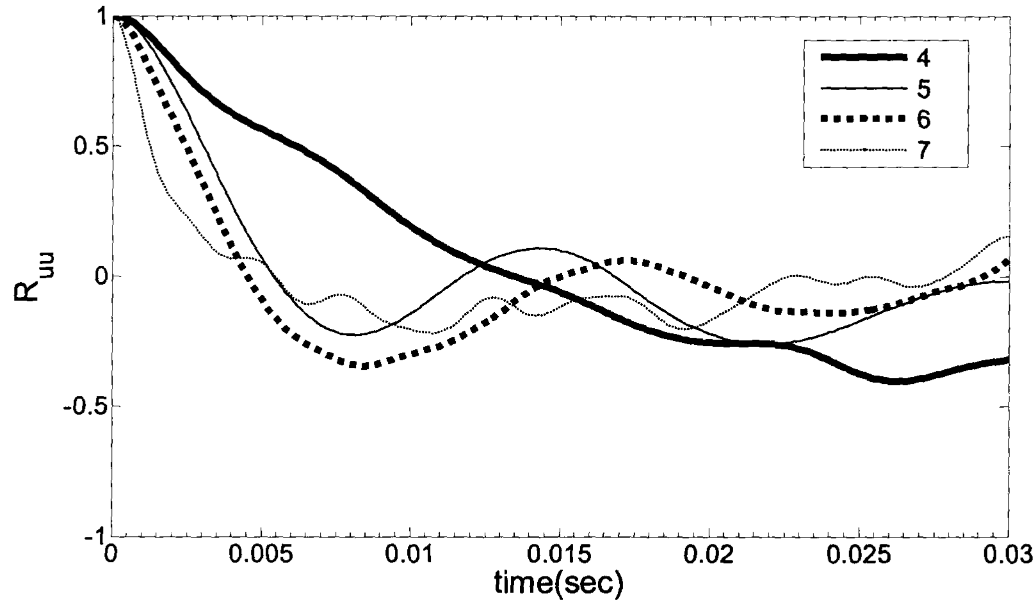

Figure 6.80 DES-SST prediction of stream-wise temporal auto-correlation function.

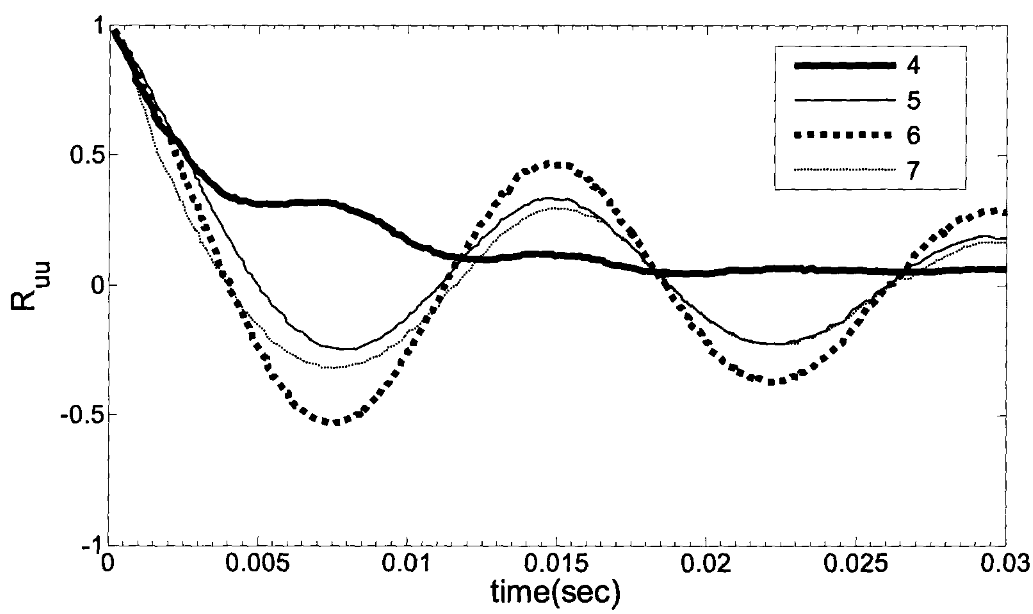

Figure 6.81 Stream-wise temporal auto-correlation function (Meyer and Rehme, 1994).

is shown in Figure 6.82. It is clear that there is a periodic behavior associated with the correlation function R_{uw}, similar to that of the correlation functions R_{ww} and R_{uu}. It appears that there is a phase shift between the signals for different positions. The dominant period for the correlation function R_{uw} was found to be similar to the dominant periods for the correlation functions R_{ww} and R_{uu}. It is concluded from the above observations that there is temporal coherence associated with the auto-correlation functions and that the flow field is highly correlated in time. This shows that the flow is not purely turbulence dominated, but is superimposed by quasi-periodic oscillations. The periodic behavior of the auto-correlation functions clearly indicate the presence of large-scale flow pulsations in the flow field.

Two-point temporal correlations were defined by fixing one point at the edge of the gap (monitor point 6) and moving the second point through the entire length of the gap. In this case, the points are located at different span-wise positions (z) but at the same axial location (x). The two-point temporal correlations for the velocity components in the span-wise (w) and stream-wise (u) directions are defined as:

$$R_{w1w2} = \frac{\overline{w_1'(x,y,z_1,t)\,w_2'(x,y,z_2,t+\Delta t)}}{\sqrt{\overline{w_1'(x,y,z_1,t)^2}}} \tag{6.14}$$

$$R_{u1u2} = \frac{\overline{u_1'(x,y,z_1,t)\,u_2'(x,y,z_2,t+\Delta t)}}{\sqrt{\overline{u_1'(x,y,z_1,t)^2}}} \tag{6.15}$$

In the above Eq.s (6.14) and (6.15), subscript 1 refers to the fixed point and subscript 2 refers to the variable point that is moving. For the present formulation, the correlation functions are evaluated with monitor point 6 as the fixed point and the remaining points

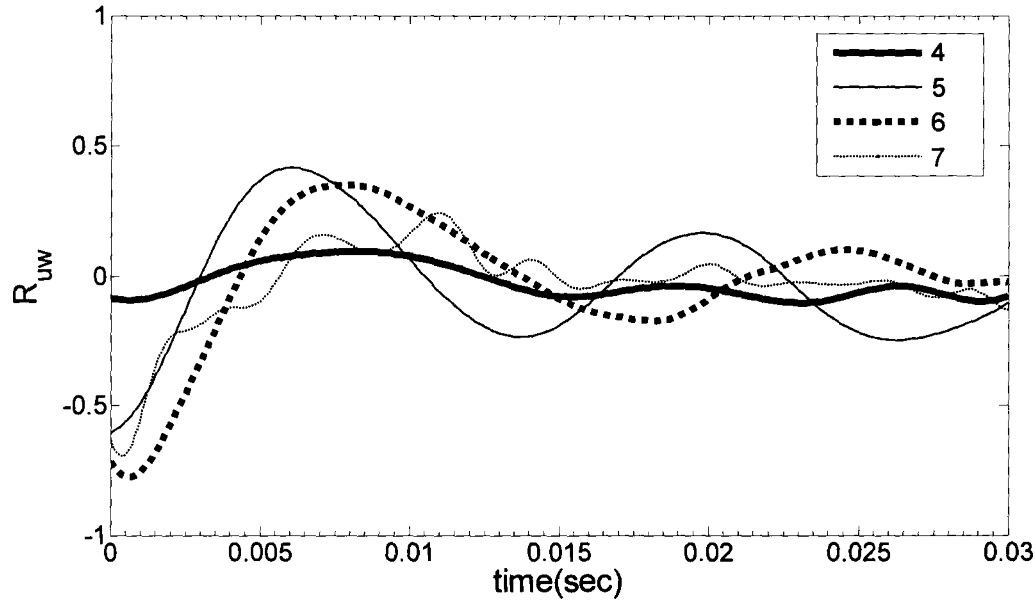

Figure 6.82 DES-SST prediction of temporal auto-correlation function for the cross velocity components.

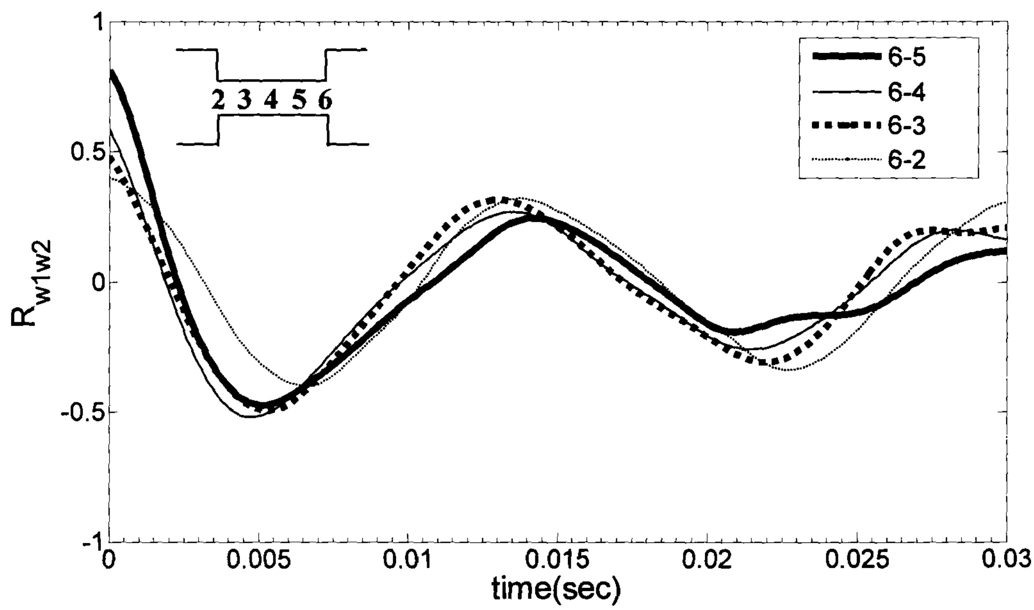

Figure 6.83 DES-SST prediction of temporal correlation function for spatially separated span-wise velocity components.

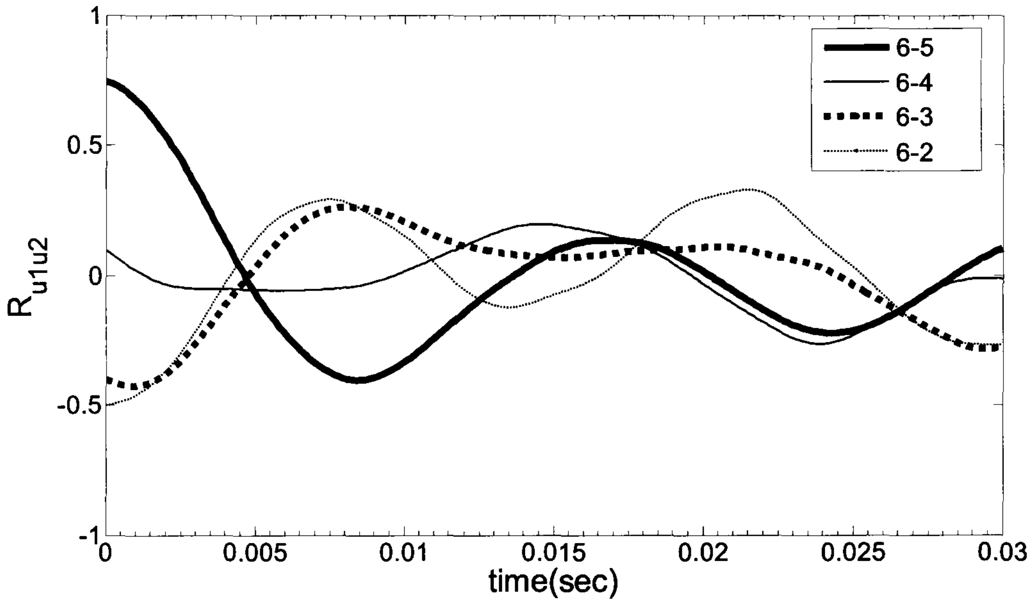

Figure 6.84 DES-SST prediction of temporal correlation function for spatially separated stream-wise velocity components.

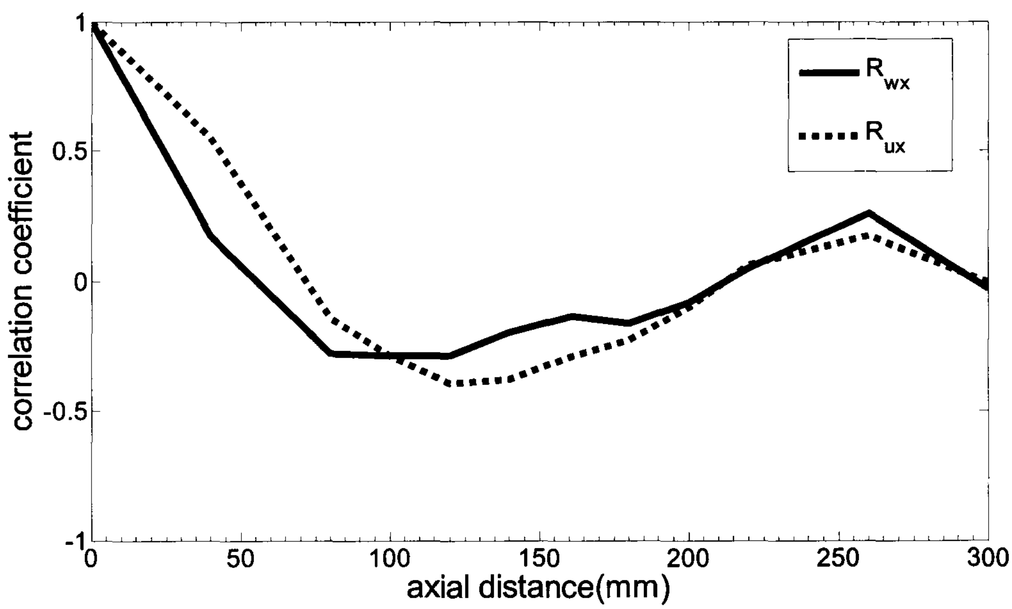

Figure 6.85 DES-SST prediction of the spatial cross-correlation function.

inside the gap form the variable points. Thus, the two-point temporal correlation functions are formed for the following pairs of points: monitor points 6 and 5, monitor points 6 and 4, monitor points 6 and 3, and monitor points 6 and 2. Figures 6.83 and 6.84 show the variation of the two-point temporal correlation functions for the span-wise and axial velocities respectively. The correlation function R_{w1w2} has a very clear periodic pattern and the phase shift between the different components is small. The dominant period of the correlation function R_{w1w2} is the same as the temporal auto-correlation functions. The correlation function R_{u1u2} also has a very clear periodic pattern. For the correlation function R_{u1u2}, the axial velocity fluctuations on the same side of the symmetry line of the gap (vertical line passing through the centre of the gap) show very small phase shift, however, for velocities taken at different sides of the symmetry line, the phase shift is nearly 180^0 (i.e. comparing the curves denoted as 6-5 and 6-2 in Fig 6.84). The two-point temporal correlations have clearly shown that the flow field is highly correlated in time for spatial distances across the gap. It was also found that the two-point temporal correlations for points varying in the axial direction but at the same span-wise location, were also highly correlated. The presence of quasi-periodic flow pulsations in the sub-channel geometry causes the time correlation of events spatially, both in the span-wise and stream-wise directions.

The spatial scale of the flow structure in the gap region was investigated by calculating the spatial cross-correlation coefficient. The spatial cross-correlation coefficient in the axial direction, for the span-wise (w) and stream-wise (u) velocity components is formulated as:

$$R_{wx} = \frac{\overline{w^{'}(x,y,z,t)\,w^{'}(x+\Delta x,y,z,t)}}{\sqrt{\overline{w^{'}(x,y,z,t)^{2}}}} \tag{6.16}$$

$$R_{ux} = \frac{\overline{u^{'}(x,y,z,t)\,u^{'}(x+\Delta x,y,z,t)}}{\sqrt{\overline{u^{'}(x,y,z,t)^{2}}}} \tag{6.17}$$

Figure 6.85 shows the spatial cross-correlation functions. The minimum value of the correlation function represents a length scale characteristic of the velocity component. The results show that the instantaneous flow field is highly correlated spatially. The spatial correlations are unaffected by the computational domain length. Figure 6.85 indicates that the span-wise and stream-wise velocity have spatial length scales of approximately 85 mm and 130 mm respectively in the stream-wise direction. A wavelength (axial spacing) associated with the alternate sequence of velocity structures was estimated from the spatial cross-correlation function. From the spatial cross-correlation function of the span-wise velocity component, the wavelength associated with alternate sequence of structures was found to be approximately 260 mm (the point of second maximum of the correlation function). The wavelength can also be estimated based on an average number of structures contained in a series of snapshots, i.e.

$$\lambda = \frac{L_x}{N_{seq}} \tag{6.18}$$

In the above equation, λ is the wavelength, L_x is the length of the domain in the stream-wise direction and N_{seq} is the average number of alternate sequence of span-wise velocity structures. The estimated wavelength using Eq. (6.18) was approximately 182 mm. The experimental wavelength was reported to be 200 mm (Meyer and Rehme, 1994).

The temporal correlations showed periodic behavior, which is an indication of the large-scale flow pulsations. The fundamental frequencies of the flow pulsations are obtained by taking the power spectra of the temporal auto-correlation functions. The power spectra was extracted using the FFT algorithm in MATLAB. The FFT was obtained using 1024 data points in the auto-correlation functions, sampled at a base frequency of 10,000 Hz. This sampling frequency helped to remove any aliasing errors that would have occurred in the power spectra. Figures 6.86-6.88 show the power spectra of the span-wise temporal auto-correlation function at the respective monitor points. The power spectral plots show one clear peak frequency at 68.4 Hz. Other than the main peak frequency, there are some local maximums in the power spectral plot (monitor point 6), which is in accordance with the quasi-periodic nature of the flow field (Figure 6.37). The power spectral plots for the stream-wise temporal auto-correlation function at the respective monitor points is shown in Figures 6.89-6.90. The dominant frequency from these plots is 68.4 Hz, whereas the secondary maximum is around 29 Hz. Finally, the power spectral plots associated with the temporal correlation function R_{uw}, at different monitor points are shown in Figures 6.91-6.93. The peak frequency from these plots also occurs at 68.4 Hz and the secondary maximum is around 29 Hz. The secondary maximum frequency in the power spectral plots implies that there is an intermittency of the structures which is also evident from the velocity contour plots (Figure 6.53). The intermittency indicates that the flow pulsations are quasi-periodic in nature. The flow pulsations are associated with a base (fundamental) frequency and these pulsations can intermittently occur at the secondary maximum frequency.

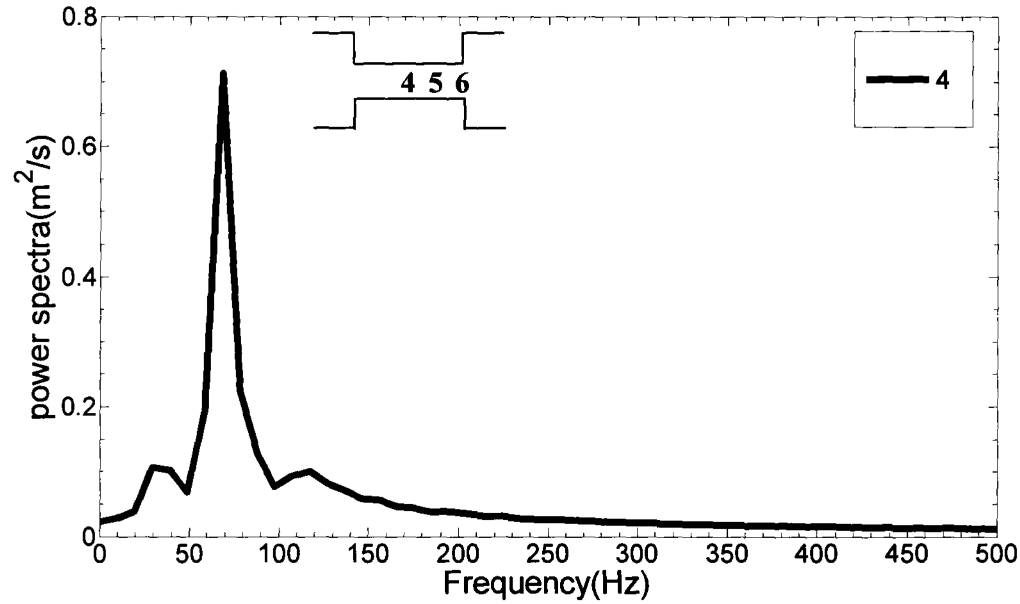

Figure 6.86 DES-SST prediction of the power spectra for the span-wise temporal auto-correlation function, R_{ww} at monitor point 4 (gap centre).

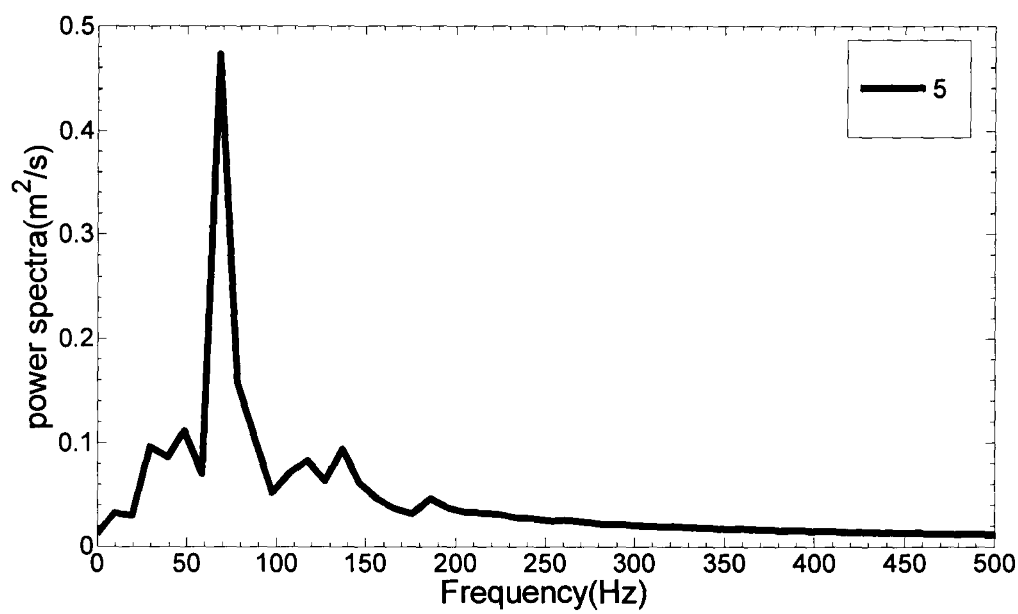

Figure 6.87 DES-SST prediction of the power spectra for the span-wise temporal auto-correlation function, R_{ww} at monitor point 5.

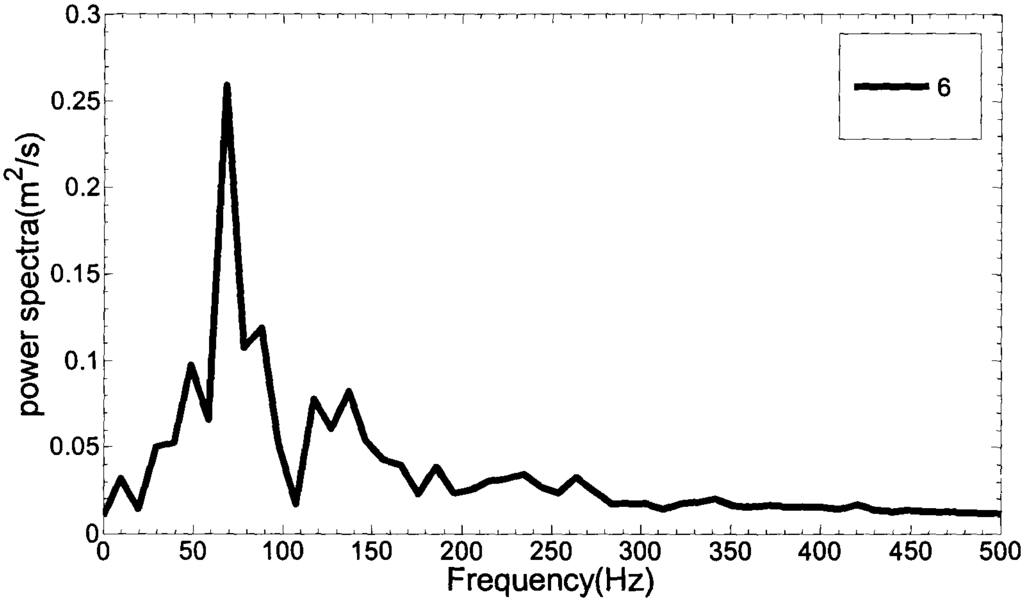

Figure 6.88 DES-SST prediction of the power spectra for the span-wise temporal auto-correlation function, R_{ww} at monitor point 6 (gap edge).

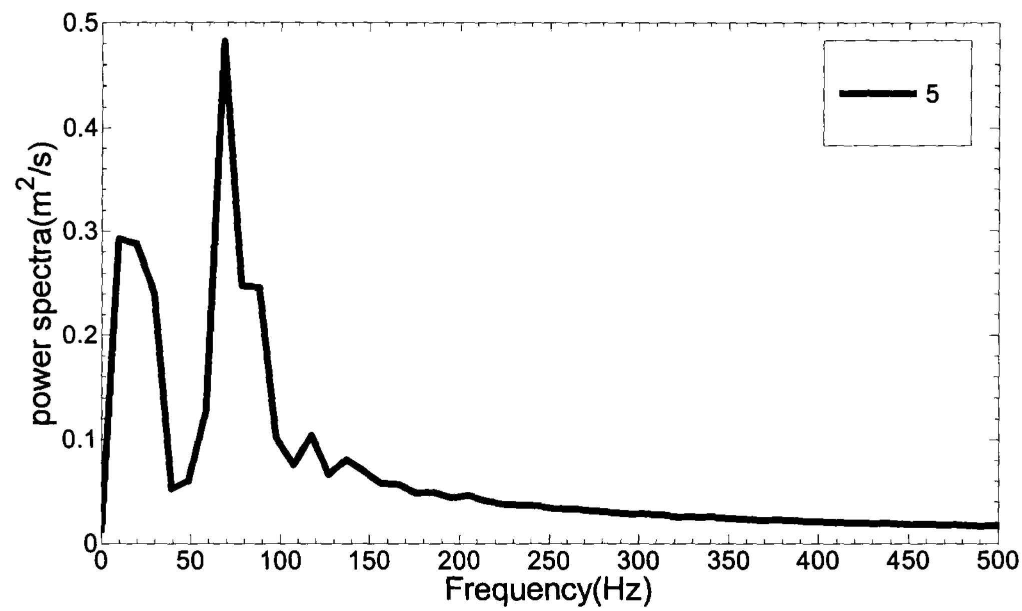

Figure 6.89 DES-SST prediction of the power spectra for the stream-wise temporal auto-correlation function, R_{uu} at monitor point 5.

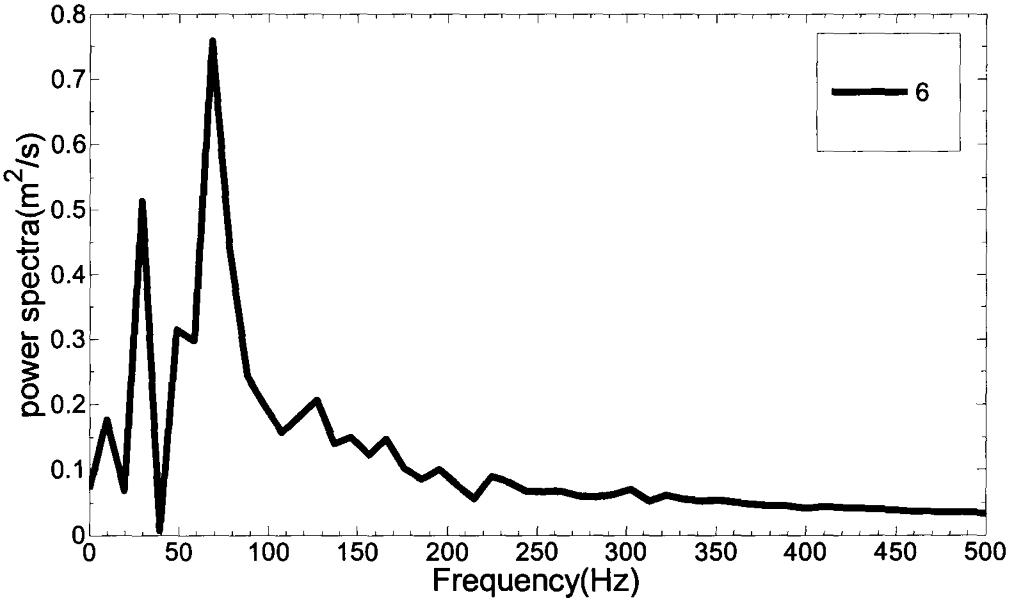

Figure 6.90 DES-SST prediction of the power spectra for the stream-wise temporal auto-correlation function, R_{uu} at monitor point 6 (gap edge).

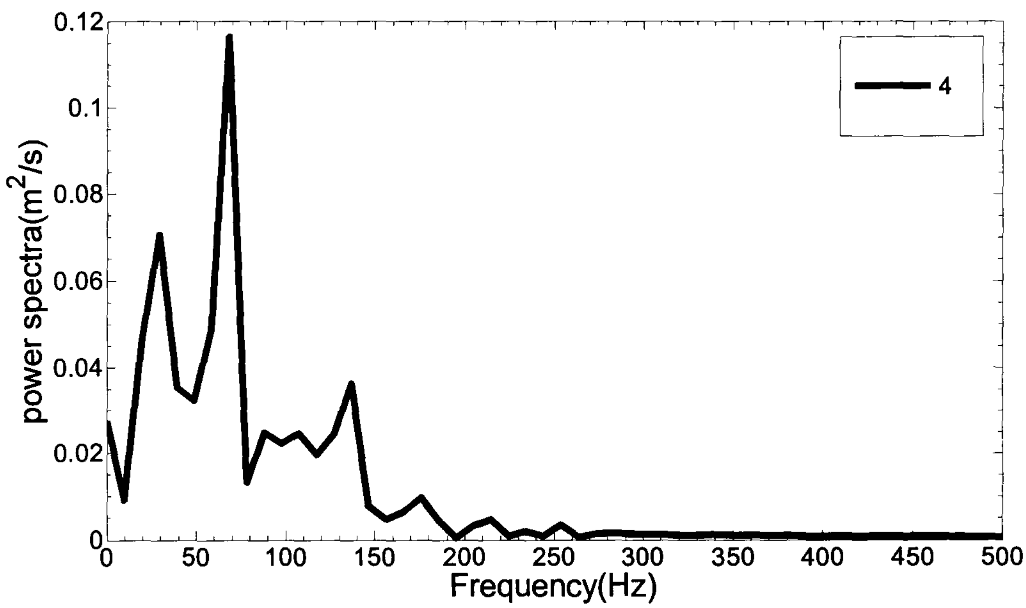

Figure 6.91 DES-SST prediction of the power spectra for the temporal correlation function, R_{uw} at monitor point 4 (gap centre).

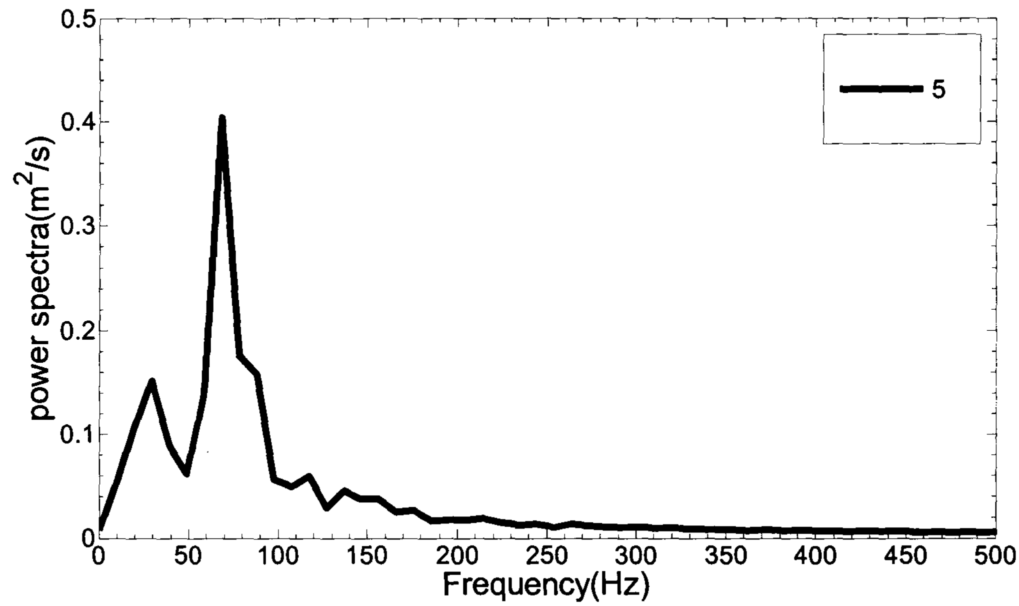

Figure 6.92 DES-SST prediction of the power spectra for the temporal correlation function, R_{uw} at monitor point 5.

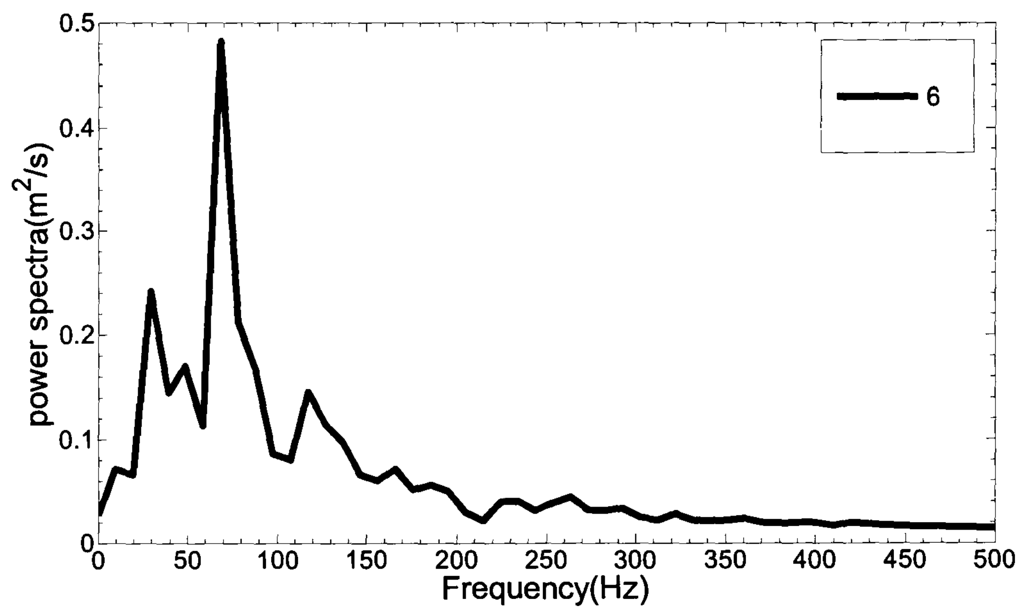

Figure 6.93 DES-SST prediction of the power spectra for the temporal correlation function, R_{uw} at monitor point 6 (gap edge).

The dominant (peak) frequency associated with the quasi-periodic flow pulsations as predicted by the DES-SST model is 68.4 Hz. The experimental peak frequency was reported as 68 Hz (Meyer and Rehme, 1994). Thus, the numerical prediction is in excellent agreement with the experimental result. In general, it can be said that the predictions from the DES-SST model captures the dynamics of the flow pulsations and is in agreement with the experiments.

The fundamental frequency or peak frequency of the flow pulsations can be represented in a dimensionless form known as the Strouhal number, which is used to describe oscillating flow mechanisms. The gap Strouhal number is defined based on the peak frequency of the flow pulsations, a velocity scale and a length scale. The Strouhal number was formulated based on the following equation:

$$Str_g = \frac{f\left(gd\right)^{1/2}}{U_e} \tag{6.19}$$

In Eq. (6.19), f is the frequency, g is the gap height, d is the gap width and U_e is the time averaged velocity at the edge of the gap. The experimental Strouhal numbers based on Eq. (6.19) for all the channels were found to be constant within ±16%. In the experiments (Meyer and Rehme, 1994), the gap size ratio g/d varied between 0.06 and 1.0, and the Reynolds number varied in the range 1.6×10^5 to 3.2×10^5. The mean Strouhal number was reported as 0.115 (Meyer and Rehme, 1994). The Strouhal number predicted from the DES-SST model was found to be 0.109, which is around 5% less than the experimental value.

6.5.7 Discussion

The frequency analysis has clearly shown that there is a dominant frequency associated with the flow pulsations. This results in strong peaks in the near gap region for the turbulence kinetic energy and Reynolds stresses. The flow pulsations can cause redistribution of the thermal energy, by transporting fluid from the core of the sub-channels and across the gap into the adjoining open flow region. The flow pulsations are a result of the quasi-periodic vortical structures formed at the gap edge region and moving in the stream-wise direction. The large-scale structures formed in the near gap region cause temporal and spatial coherence both in the axial and span-wise directions for the turbulence variables. The origin of the flow pulsations or the instability arises from the near gap region, where there is an interaction between the low and high speed fluids as seen in Figure 6.94 (repetition of Figure 6.20). Figure 6.94 shows that the shear experienced by the fluid in the near gap region causes the span-wise variation of the time averaged axial velocity profile to be inflectional in nature. In inflectional profiles, the curvature of the profile changes around a point of inflection. At the inflection point, the curve changes from being concave upwards (positive curvature) to concave downwards (negative curvature), or vice versa. There are two inflectional points on the velocity profile, as indicated in Figure 6.94. These two points are located symmetrically with respect to the centre of the gap. The approximate location of the inflectional points was found to be around the respective edges of the gap. This kind of velocity profile is a characteristic feature of some classical shear dominated flows. Inflectional velocity profiles are also observed in non-bounded external flows like wake flows (cross flows

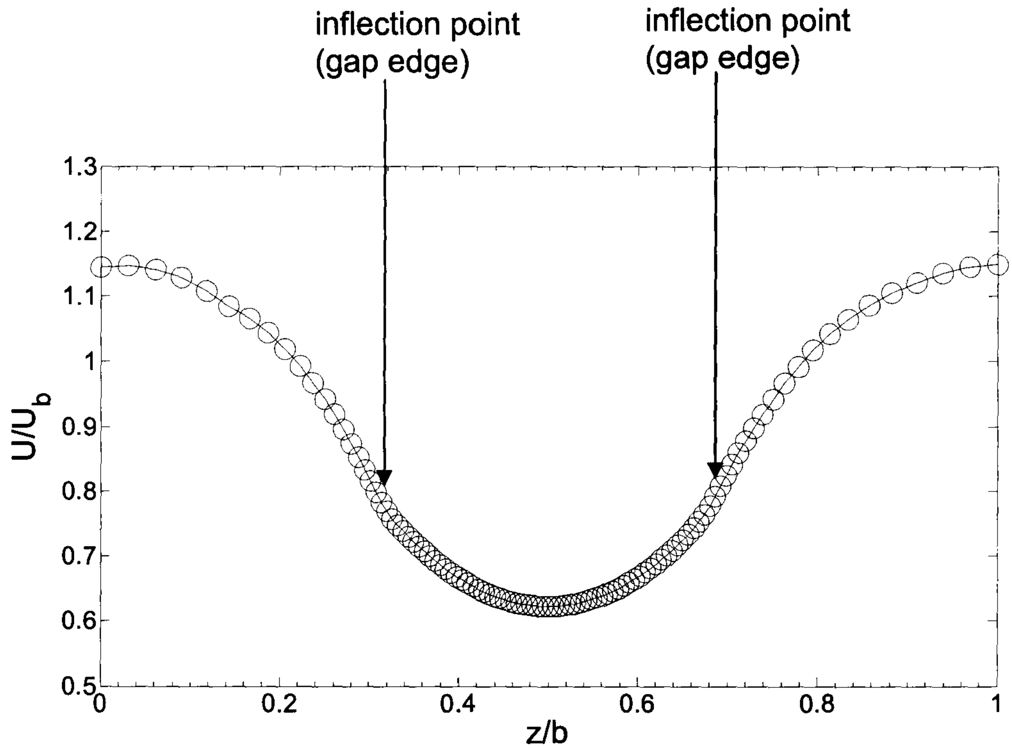

Figure 6.94 Span-wise variation in the time averaged axial velocity (z/b: normalized span-wise length, b: distance between centre of sub-channels).

over bluff bodies like cylinder, sphere), and also in the near-wall flow over a flat plate (boundary layer flow). In the near-wall flow over a flat plate, an anti-symmetric mode of instability is developed which is dominated by the wake type instability of span-wise velocity distributions across a near-wall low speed streak (Asai et al., 2002). This inflectional velocity profile is highly unstable in nature and a small perturbation in the flow condition can lead to instability. This instability in the anti-symmetric mode evolves into a train of quasi stream-wise vortices with vorticity of alternate sign. The meandering of the low speed streaks takes place in the anti-symmetric mode, similar to the meandering of the fluid around the vicinity of the gap region for sub-channel flows. In sub-channel flows with small gap size, the fluid at the edge of the gap entails high shear and strain, because of the velocity defect, which probably causes a shear layer rollup similar to boundary layer separation and wake formation in flows over blunt bodies. There is formation of quasi-periodic vortices, with high vorticity fluctuation and a three dimensional vorticity field, along the gap edge region in the entire length of the duct. It appears that the vortex street that is formed for sub-channel flows has some resemblance and analogy with the Von-Karman vortex street for cross flows over bluff bodies. The rise of instability in sub-channel flow takes place at a critical Reynolds number (Merzari et al., 2008) which is in the laminar flow regime. For the present case, the flow is in a fully developed turbulent mode where the instability causing the flow pulsation is completely sustained. The intensity of the flow pulsations becomes stronger as the Reynolds number increases. For sub-channel flows at a given gap size, the Strouhal number increases with the increase in Reynolds number and attains a constant value, when the flow is in a fully turbulent regime (Möller, 1991; Meyer and Rehme, 1994). For cross flow over bluff bodies, the variation of Strouhal number with Reynolds number is quite similar to sub-channel flows. In these cases, the Strouhal number asymptotically reaches a value of 0.2 at fully turbulent flow regime. In the investigations of Meyer and Rehme (1994), the Strouhal number was found to be approximately 0.115.

The internal flow inside the sub-channel geometry provides some fundamental difference with flows over bluff bodies and near-wall boundary layer flow over a flat plate. The low speed fluid in a sub-channel geometry is constrained inside the gap region along the entire length of the duct. In flow over a bluff body and near-wall flow over a flat plate there is no spatial constraint on the fluid or the near-wall low speed streaks. The flow inside a sub-channel geometry is highly correlated temporally and spatially as compared to the counter part flows. The quasi-periodic stream-wise vortices are formed due to the shear layer interaction and are present along the entire length of the duct, whereas, vortices formed from the boundary layer separation over bluff bodies diffuse after certain distance from the body due to viscous effects. For cross flow over bluff bodies, the separation of the boundary layer is delayed (location of the separation point moves further downstream) as the flow regime changes from laminar to turbulent mode, which is accompanied by a lower pressure drag. Thus, the wake formation and the generation of Von-Karman vortex street is also delayed, and their occurrence is strictly dependent on the type of flow regime. In the present case, once the instability causing the flow pulsations is triggered, which happens to be in the laminar flow regime (Merzari et al., 2008), it remains sustained throughout as the flow transitions from laminar to turbulent mode. For sub-channel flows, the flow regime is not responsible for when the quasi-periodic vortices are generated. In case of near-wall flow over a flat plate, there is also a symmetric type of instability due to a single point inflectional velocity profile in the wall normal direction (Asai et al., 2002). This symmetric type of instability is similar to a Kelvin-Helmholtz instability, where the growth of symmetric mode leads to the formation of hairpin vortices. The wall normal velocity profile inside the gap region of a sub-channel flow is like a Poiseuille flow profile, which is non-inflectional in nature and hence the symmetric mode of instability is absent. Thus, the important connection between sub-channel flow and the fundamental flows is the wake like velocity distribution in the span-wise direction as shown in Figure 6.94.

6.6 Sensitivity to the channel length

Sensitivity to the length of the channel was carried out by comparing the results of the reference case C1 (channel length of 730 mm), with the results of cases C2 (channel length of 330 mm) and C3 (channel length of 992.8 mm) respectively. The length of the domain for the reference case C1 was based on the experimental wavelength information (Meyer and Rehme, 1994) for the alternate sequence of structures. The length of the domain for case C3 was chosen to avoid an integer multiple of the reference case channel length. The shortest channel represented by case C2 was also considered and its domain length was smaller than case C3 by approximately a factor of three. As was previously described in the section on mesh design, the grid structure and the aspect ratio of the cells was the same for all the three channel lengths. The simulation setup for all the three channel lengths was the same in terms of boundary conditions, mass flow rate and the advection scheme. It was found that the time averaged axial velocity distribution for all the channel lengths were similar. The distribution of the turbulent kinetic energy was found to be the same for the three channel lengths. The approximate location of the peak value for the turbulent kinetic energy was found to be the same for all the three channel lengths. The peak value in the turbulent kinetic energy slightly differed (maximum difference of 2%) amongst the three channel lengths. Tables 6.12-6.15 show the quantitative comparison of time averaged quantities for the three channel lengths at different monitor points. In general, the predictions for the time averaged quantities for the three channel lengths at the different monitor points is quite similar. Figures 6.95 and 6.96 show the instantaneous span-wise velocity contours at the (x, z) symmetry plane for

Table 6.12 Comparison of time averaged quantities at monitor point 4 (gap centre).

Variable	Case C1	Case C2	Case C3
U (m/s)	13.47	13.36	13.33
u" (m/s)	1.749	1.562	1.802
v" (m/s)	0.052	0.051	0.059
w" (m/s)	1.937	1.90	1.797
k_t (m^2/s^2)	4.175	3.787	3.987
$\overline{w'w'}$ (m^2/s^2)	3.749	3.629	3.228
$\overline{u'w'}$ (m^2/s^2)	-0.27	-0.05	-0.124

Table 6.13 Comparison of time averaged quantities at monitor point 5.

Variable	Case C1	Case C2	Case C3
U (m/s)	14.48	14.19	14.26
u" (m/s)	2.071	2.006	2.248
v" (m/s)	0.166	0.145	0.164
w" (m/s)	1.89	1.809	1.743
k_t (m^2/s^2)	4.895	4.534	4.947
$\overline{w'w'}$ (m^2/s^2)	3.616	3.272	3.037
$\overline{u'w'}$ (m^2/s^2)	-2.015	-1.897	-1.881

Table 6.14 Comparison of time averaged quantities at monitor point 6 (gap edge).

Variable	Case C1	Case C2	Case C3
U (m/s)	17.45	17.09	17.22
u" (m/s)	2.924	2.938	2.937
v" (m/s)	0.883	0.861	0.901
w" (m/s)	1.892	1.763	1.817
k_t (m^2/s^2)	8.01	7.702	7.886
$\overline{w'w'}$ (m^2/s^2)	3.556	3.108	3.303
$\overline{u'w'}$ (m^2/s^2)	-3.977	-3.712	-3.758

Table 6.15 Comparison of time averaged quantities at monitor point 7.

Variable	Case C1	Case C2	Case C3
U (m/s)	20.07	19.55	19.63
u" (m/s)	3.005	2.922	3.032
v" (m/s)	1.145	1.211	1.129
w" (m/s)	1.332	1.325	1.386
k_t (m^2/s^2)	7.075	6.843	7.229
$\overline{w'w'}$ (m^2/s^2)	1.754	1.755	1.921
$\overline{u'w'}$ (m^2/s^2)	-2.444	-2.57	-2.845

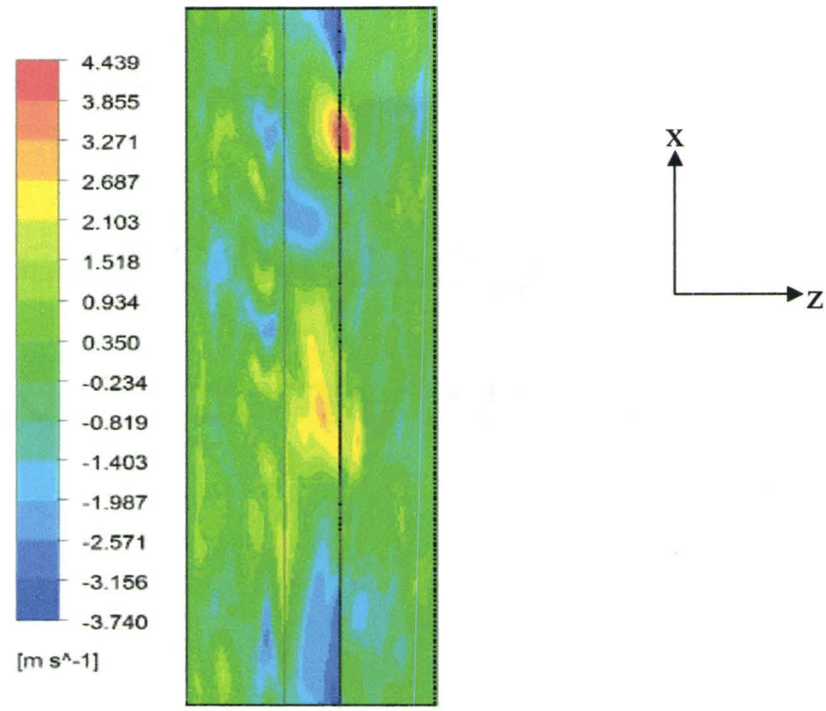

Figure 6.95 Snapshot of the span-wise velocity contour at the symmetry plane for case C2.

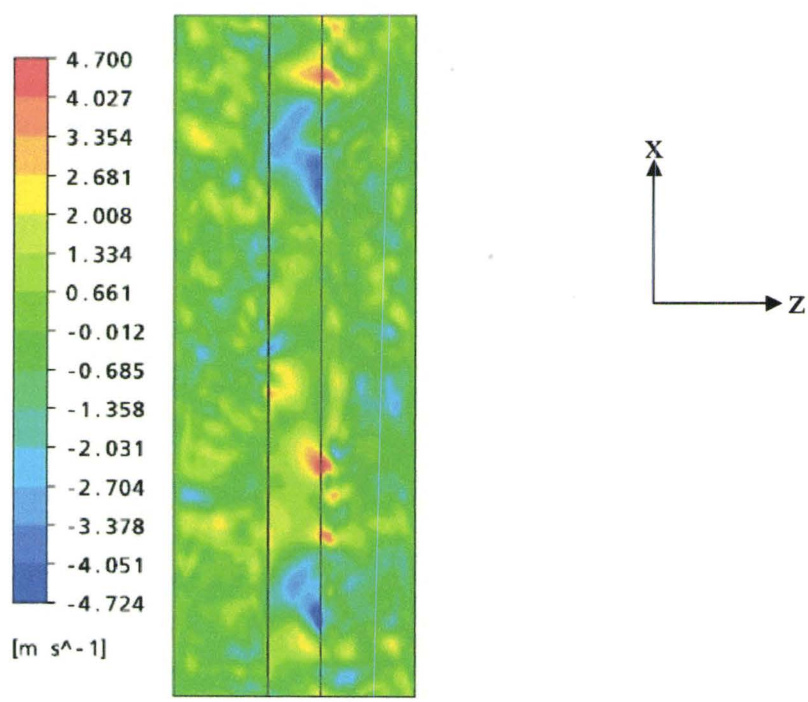

Figure 6.96 Snapshot of the span-wise velocity contour at the symmetry plane for case C3.

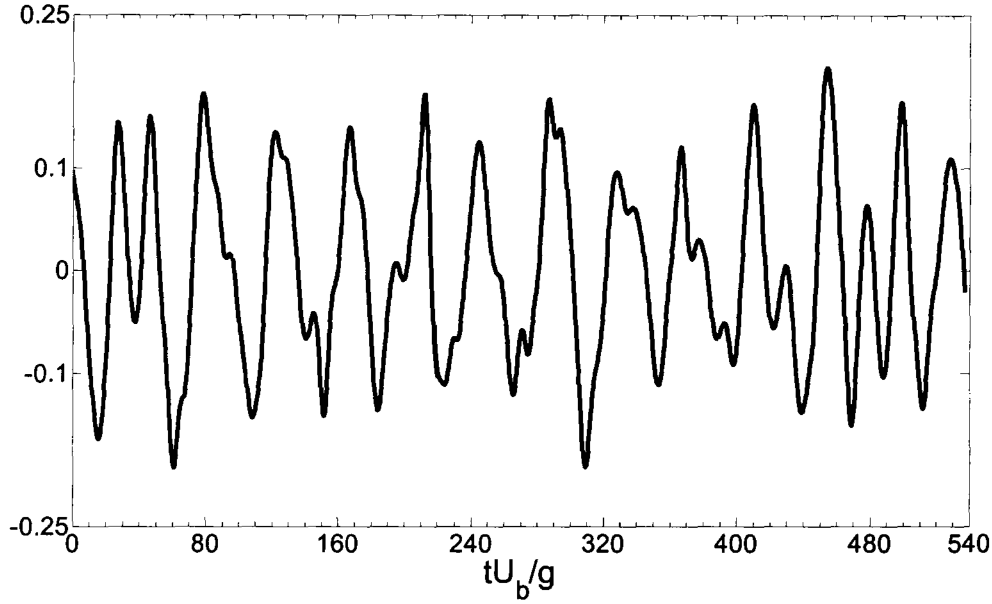

Figure 6.97 Time trace of the span-wise velocity at the gap centre for case C2.

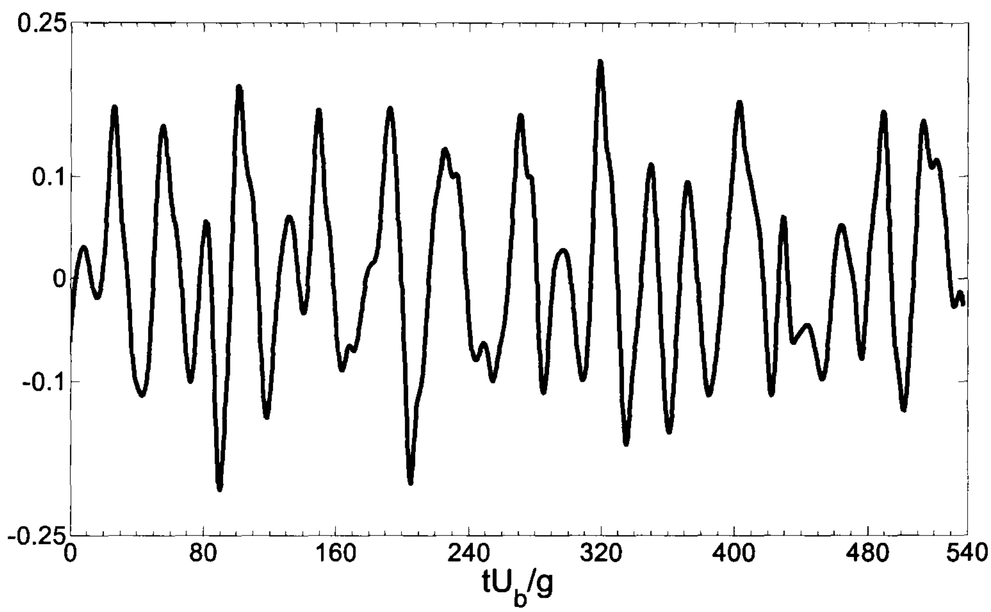

Figure 6.98 Time trace of the span-wise velocity at the gap centre for case C3.

cases C2 and C3 respectively. The peak magnitudes of the span-wise velocities for cases C2 and C3 are similar to case C1. It is clear, as expected, that the shortest channel (330 mm) holds a smaller number of structures in the domain in comparison to the other two channel lengths. Time traces of the span-wise velocity at the gap centre for cases C2 and C3 are shown in Figures 6.97 and 6.98 respectively. It is clear that the characteristic pattern in the velocity for cases C2 and C3 is similar to case C1 (Figure 6.36). Figures 6.99 and 6.100 show the time trace of the span-wise velocity at the gap edge for cases C2 and C3 respectively. In general, it was found that the velocity time traces had the same amplitude range and negative skewness for all the three channel lengths. The span-wise temporal auto-correlation functions at different monitor points for cases C2 and C3 are shown in Figures 6.101 and 6.102 respectively. The correlation functions show an oscillating pattern similar to case C1 (Figure 6.78), however the fundamental period associated with the flow pulsations is different for cases C2 and C3 as compared to case C1. Case C2 shows a higher degree of correlation as compared to cases C1 and C3. Figures 6.103 and 6.104 show the power spectra of the span-wise temporal auto-correlation function at the gap centre. The peak frequency was found to be 49 Hz for both the cases, C2 and C3. The peak frequency predicted from case C1 was 68.4 Hz. The wavelength of the fluctuations as predicted for case C3 (longer channel of length 992.8 mm) from the spatial cross-correlation function of the span-wise velocity component was approximately 260 mm, which is exactly the same as predicted from case C1. Thus, frequency independent results were not obtained from the channel length studies. In general, it was found that studies with different channel lengths in the stream-wise

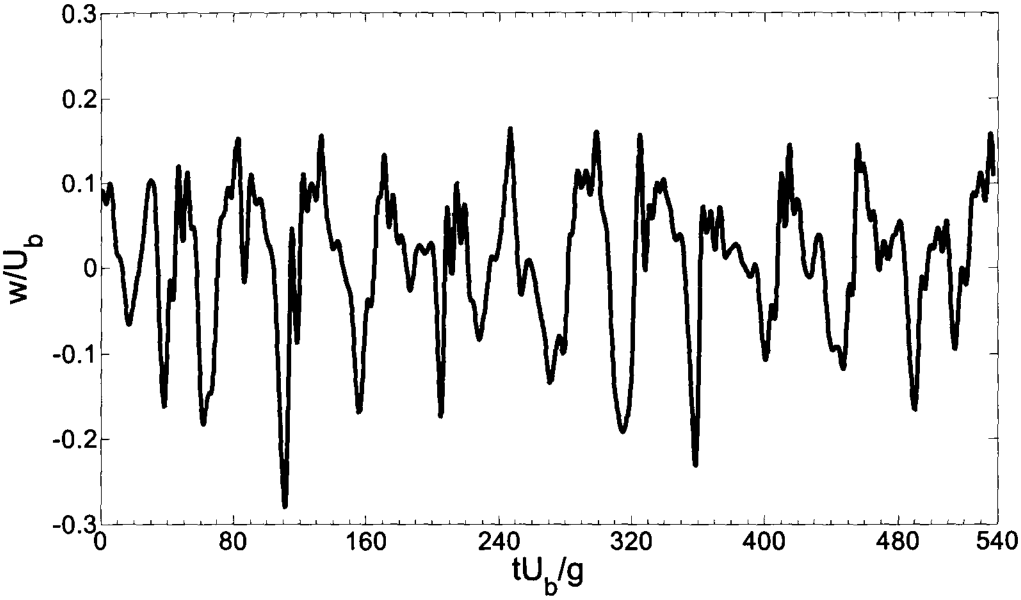

Figure 6.99 Time trace of the span-wise velocity at the gap edge for case C2.

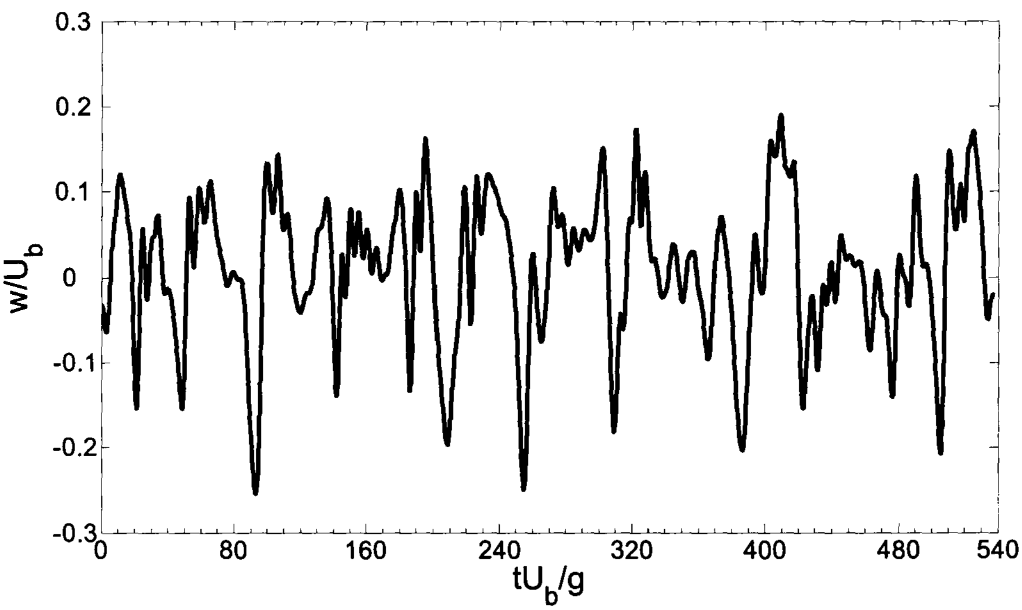

Figure 6.100 Time trace of the span-wise velocity at the gap edge for case C3.

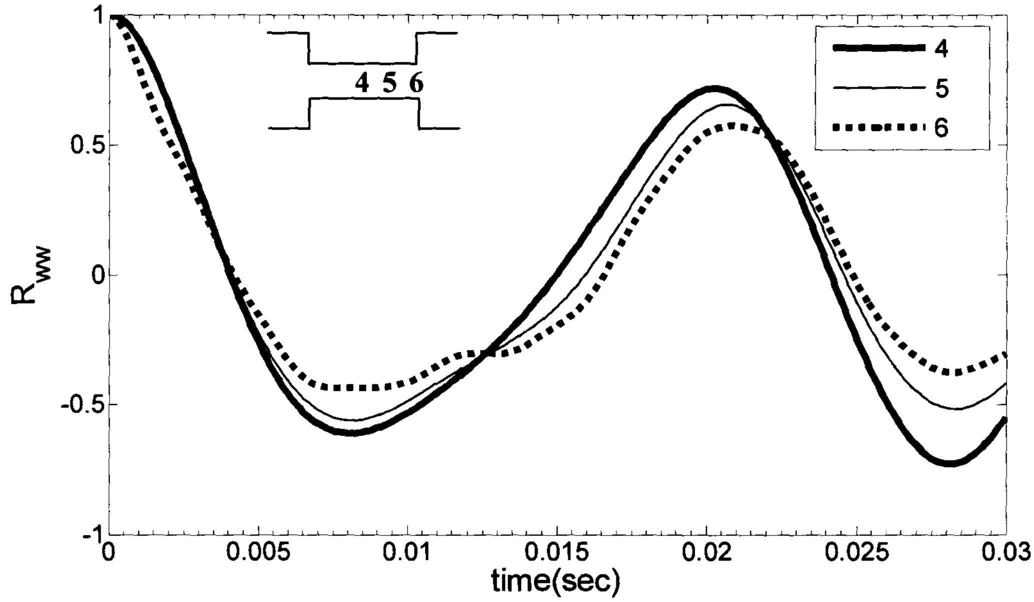

Figure 6.101 DES-SST prediction of span-wise temporal auto-correlation function for case C2.

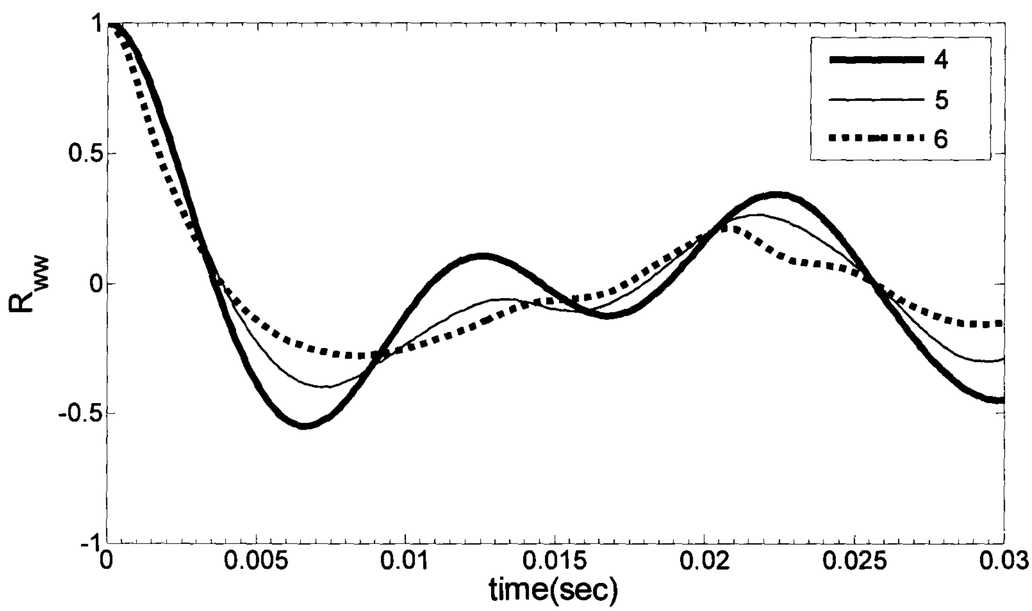

Figure 6.102 DES-SST prediction of span-wise temporal auto-correlation function for case C3.

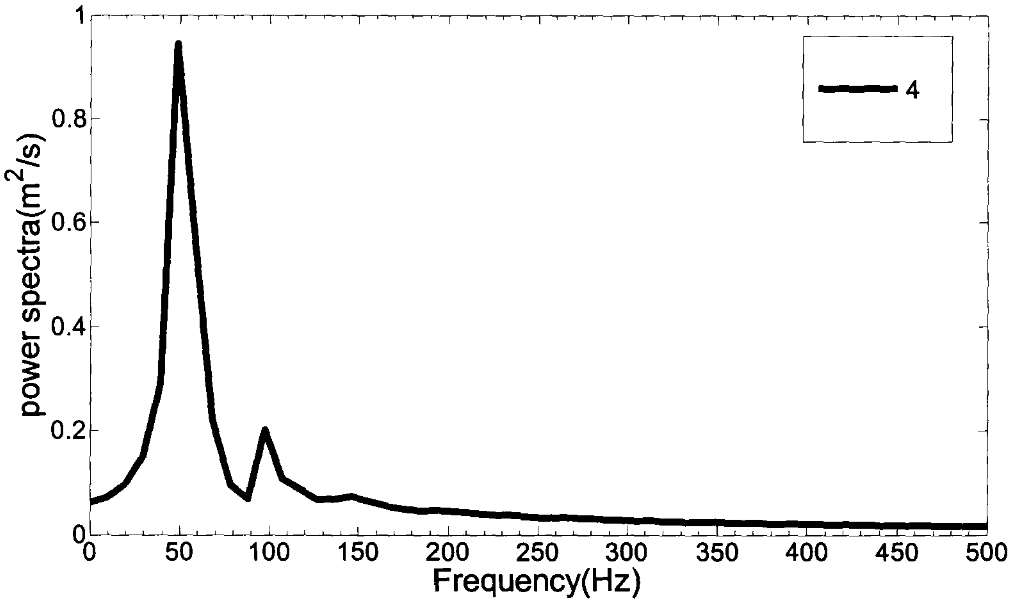

Figure 6.103 DES-SST prediction of the power spectra for the span-wise temporal auto-correlation function, R_{ww} at monitor point 4 (gap centre) for case C2.

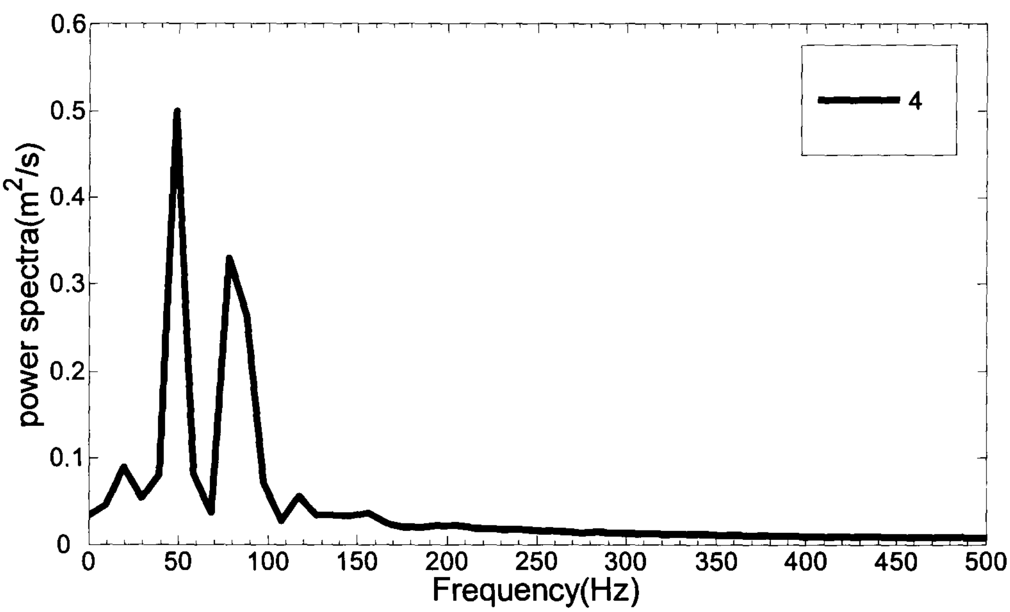

Figure 6.104 DES-SST prediction of the power spectra for the span-wise temporal auto-correlation function, R_{ww} at monitor point 4 (gap centre) for case C3.

direction gave similar results for the prediction of the averaged statistical characteristics of the flow field. The channel lengths studied did not significantly affect the dynamics of the flow pulsations and provided the correct order of span-wise velocities.

6.7 Effect of gap and sub-channel size

Table 6.2 provides the details for cases C4 and C5, that were used to study the effect of gap and sub-channel size, respectively, on the cross flow mixing, in relation to the reference case C1. The Reynolds number for case C5 was slightly larger than cases C1 and C4. Case C4 had a gap height which was reduced by 50% as compared to the reference case C1. Case C5 had a sub-channel width which was reduced by approximately 50% as compared to the reference case C1. A representative scale drawing showing the geometrical difference between cases C4 and C5 in relation to the reference case C1 is shown in Figure 6.105. Figures 6.106 and 6.107 show the predicted time traces of the span-wise velocity at the gap centre for cases C4 and C5 respectively, in comparison with case C1. The velocity time traces for cases C4 and C5 have similar quasi-periodic characteristic pattern as case C1. The velocity time trace for case C5 has a larger number of harmonics associated with it as compared to case C1. It is clear from both the figures that higher span-wise velocities are obtained for both the cases C4 and C5, in comparison to case C1. Snapshots of the span-wise velocity contour at the symmetry plane for cases C4 and C5 are shown in Figures 6.108 and 6.109 respectively. Clear pattern of alternate sequence of velocity structures is evident from the figures. In general, it was found that by reducing the gap height and the sub-channel size, the

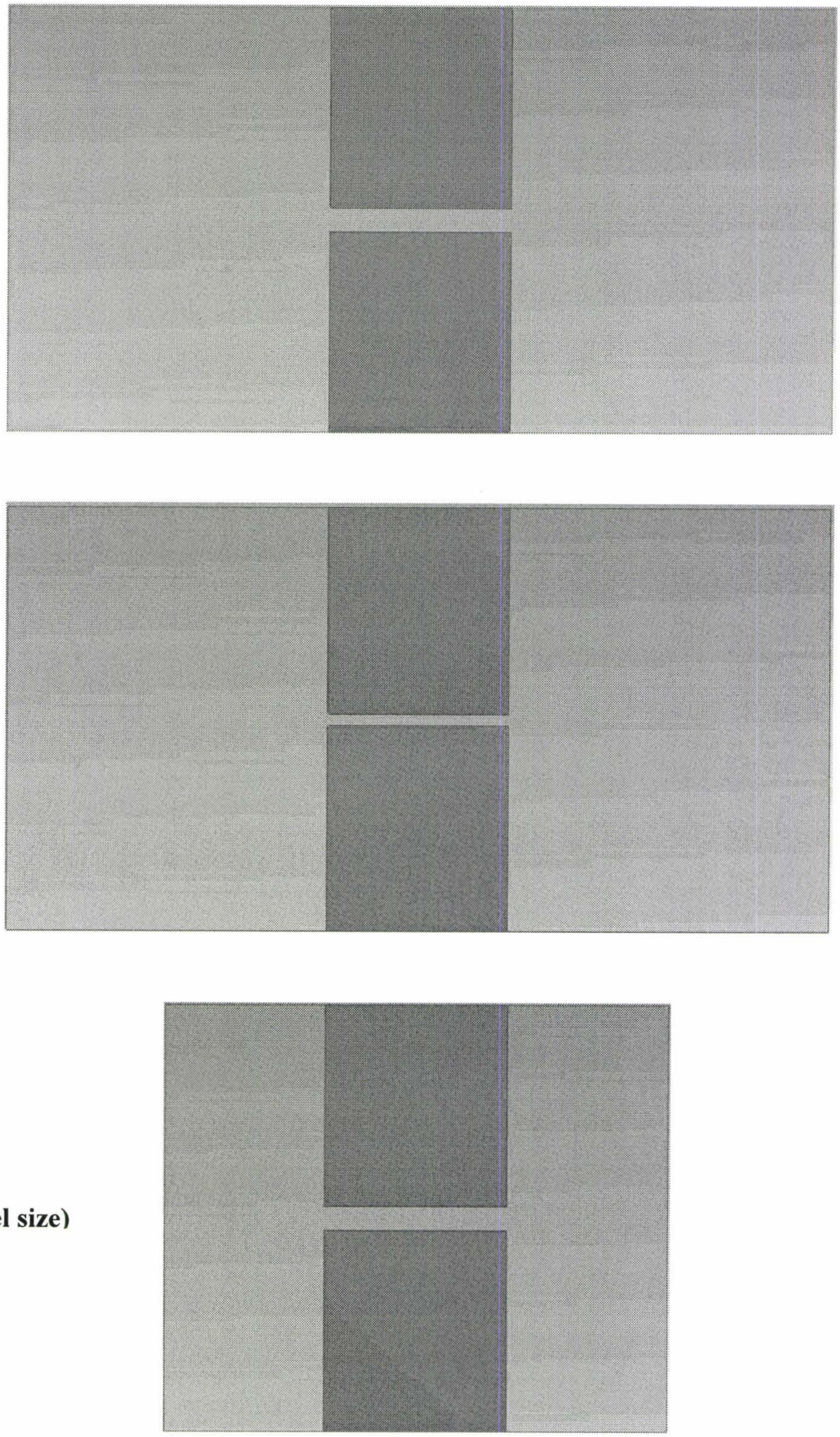

ase C1 (reference case)

se C4 (reduced gap height)

se C5 (reduced sub-channel size)

Figure 6.105 Scale drawing of the sub-channel cross-section for cases C1, C4 and C5.

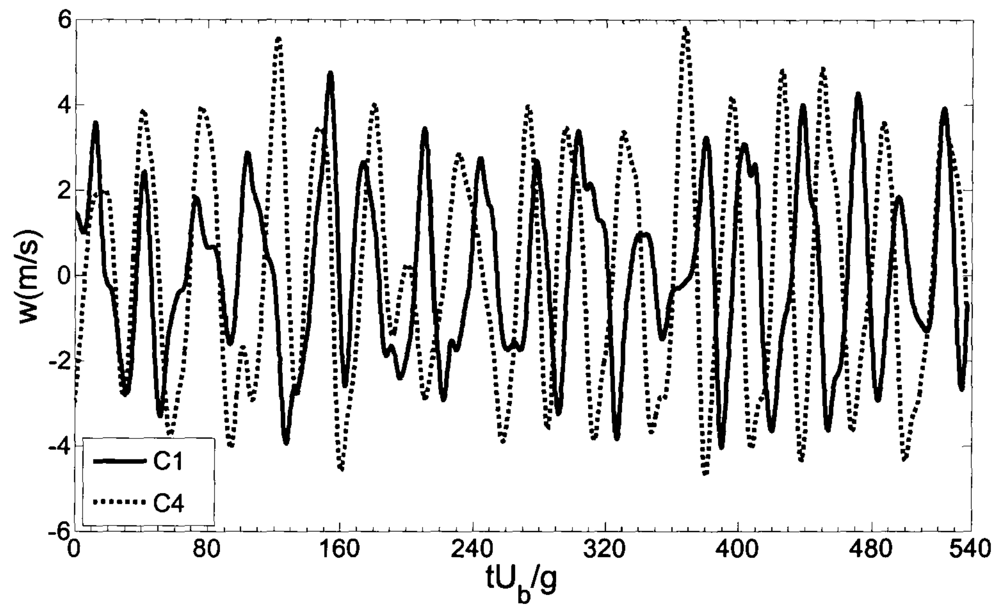

Figure 6.106 Time trace of the span-wise velocity at the gap centre for cases C1 and C4.

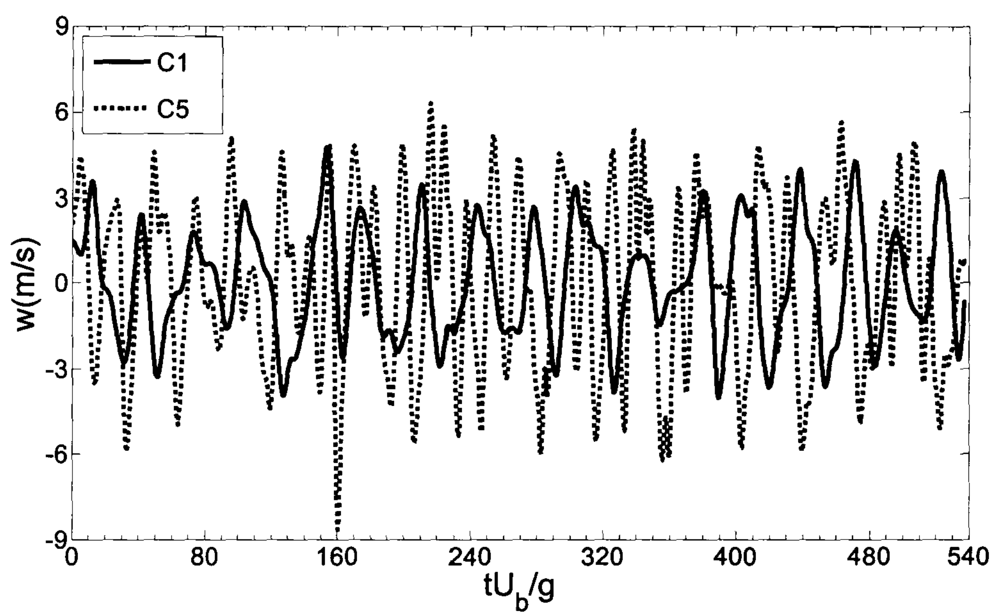

Figure 6.107 Time trace of the span-wise velocity at the gap centre for cases C1 and C5.

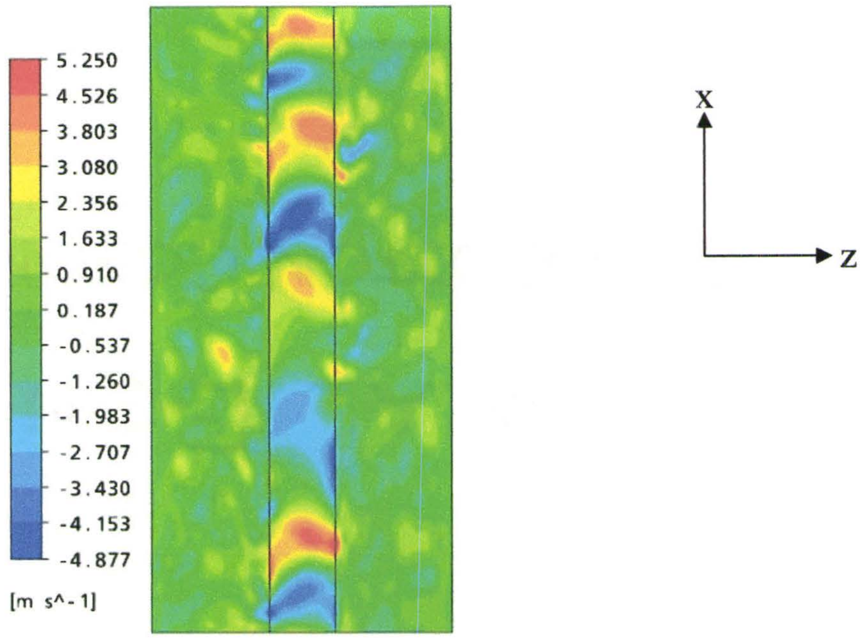

Figure 6.108 Snapshot of the span-wise velocity contour at the symmetry plane for case C4.

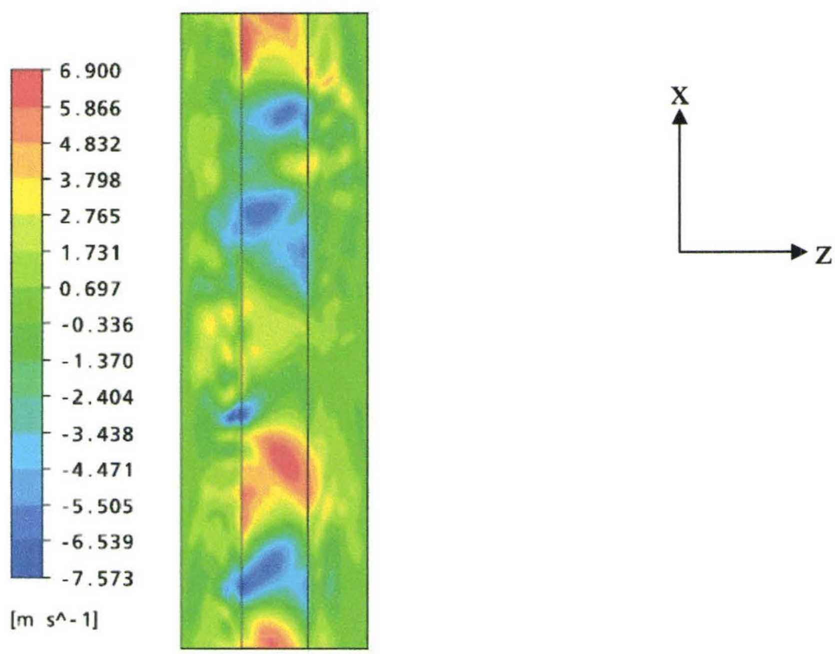

Figure 6.109 Snapshot of the span-wise velocity contour at the symmetry plane for case C5.

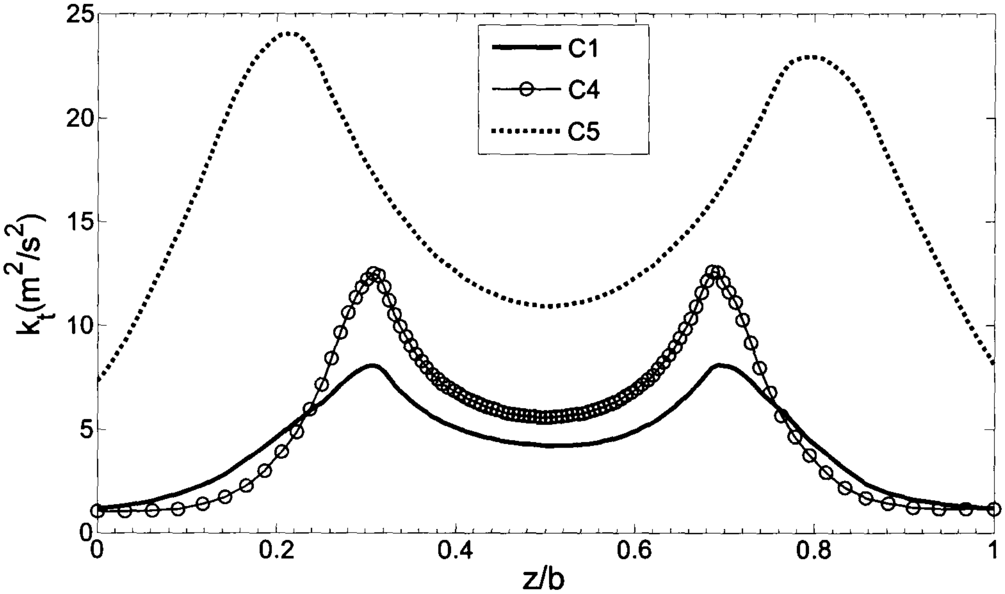

Figure 6.110 Comparison of the variation of the turbulent kinetic energy along the span-wise direction for cases C1, C4 and C5 (z/b: normalized span-wise length, b: distance between centre of sub-channels).

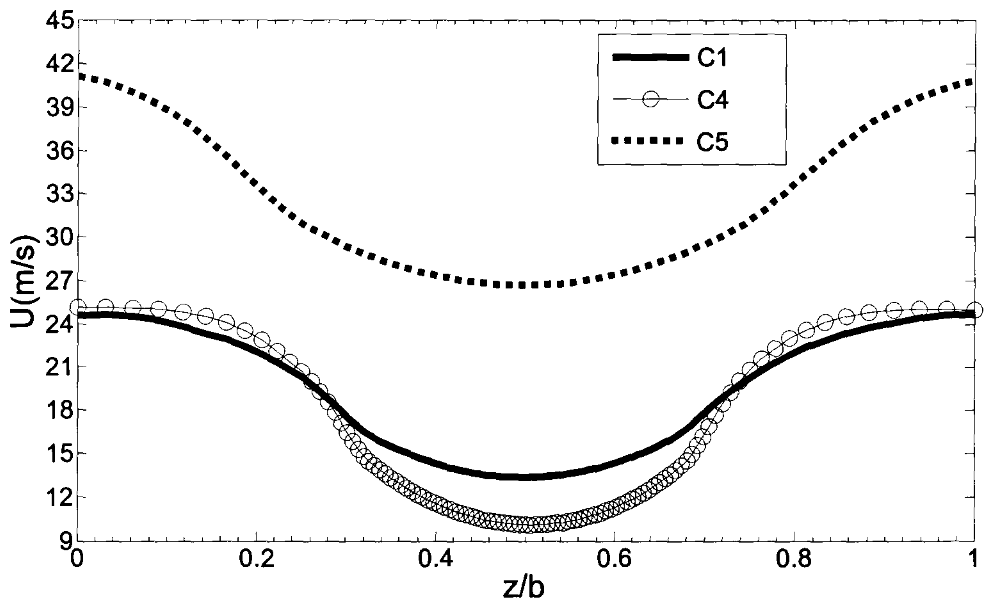

Figure 6.111 Comparison of the span-wise variation of the time averaged axial velocity for cases C1, C4 and C5 (z/b: normalized span-wise length, b: distance between centre of sub-channels).

velocity transferred through the gap increases. The variation of the turbulent kinetic energy along the span-wise direction for the three cases is shown in Figure 6.110. In the figure, z/b = 0 and z/b = 1, represent the centre of the sub-channels. The turbulent kinetic energy for case C4 is larger than case C1 throughout the gap region. The peak turbulent kinetic energy for case C4 was found to be higher than case C1, by a factor of 1.5, around the vicinity of the gap edge. It can thus be concluded that reducing the gap height, slightly increased the intensity of the flow pulsations and the cross flow velocity (mixing) through the gap. For case C4, the dominant frequency of the flow pulsations was found to be 68.4 Hz, whereas that reported in the experiment was 64.7 Hz (Meyer and Rehme, 1994).The turbulent kinetic energy for case C5 is significantly larger than case C1. The peak turbulent kinetic energy at the gap edge region, for case C5 was higher than case C1 by a factor of 3.0. On an average, from Figure 6.110 the turbulent kinetic energy for case C5 is higher than case C1 by a factor of 3.0. The Reynolds number for case C5 was larger than case C1 by approximately 9%. The hydraulic diameter of the sub-channel for case C5 is smaller than case C1 by approximately 58%. The sub-channel bulk velocity for case C5 is larger than case C1 by approximately 72%. The span-wise variation of the time averaged axial velocity for the three cases is shown in Figure 6.111. Case C5 has larger mean flow velocities in comparison to both the cases C1 and C4. On an average, from Figure 6.111 the mean velocity for case C5 is larger than case C1 by approximately 88%. The larger turbulent kinetic energy (Figure 6.110) and cross flow velocities (Figure 6.107) for case C5 in comparison to case C1 can be possibly associated to a combination of larger mean flow velocities for case C5 and reduction of the sub-channel sizes (geometry effect).

When the sub-channel sizes are reduced, the transverse path length is shortened and hence, the fluid flow encounters a lower resistance. This possibly results in increase in the intensity of the flow pulsations and thus, higher cross flow velocity (mixing) through the gap.

6.8 Effect of Reynolds number

The larger Reynolds number case in relation to the reference case C1 is represented by case C6 (see Tables 6.2, 6.3, 6.4). Cases C1 and C6 had the same geometry, only the Reynolds number was changed from 2.2×10^5 for case C1 to 3.1×10^5 for case C6. About 40% increase in Reynolds number. Figures 6.112 and 6.113 show the comparison in the span-wise velocity time traces between cases C1 and C6 at the gap centre and gap edge respectively. The velocity time traces for case C6 have similar quasi-periodic characteristics as case C1. The peak amplitude of the velocity at the gap centre is slightly higher for case C6 as compared to case C1. For case C6, the peak amplitude of the velocity at the gap edge is appreciably higher than case C1. Case C6 has similar negative skewness like case C1 in the span-wise velocity at the gap edge. Figure 6.114 shows the comparison of the instantaneous span-wise velocity contours at the symmetry plane between cases C1 and C6 for different simulation times. The higher cross flow velocity through the gap for case C6 in comparison to case C1 can be associated to the higher Reynolds number for case C6. The variation of the turbulent kinetic energy along the span-wise direction for cases C1 and C6 is shown in Figure 6.115. In the figure, $z/b = 0$ and $z/b = 1$, represent the centre of the sub-channels. The turbulent kinetic energy for

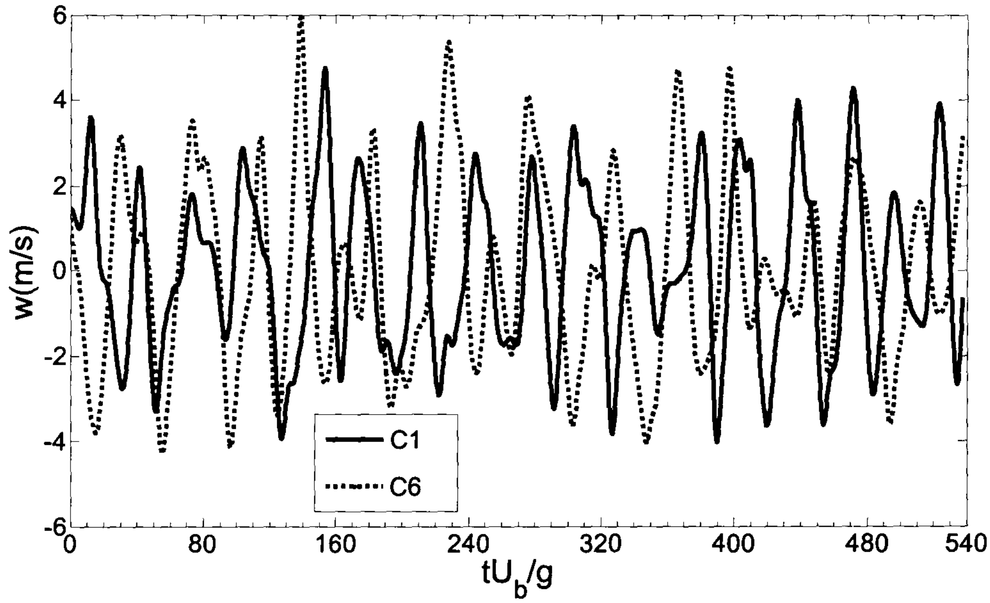

Figure 6.112 Time trace of the span-wise velocity at the gap centre for cases C1 and C6.

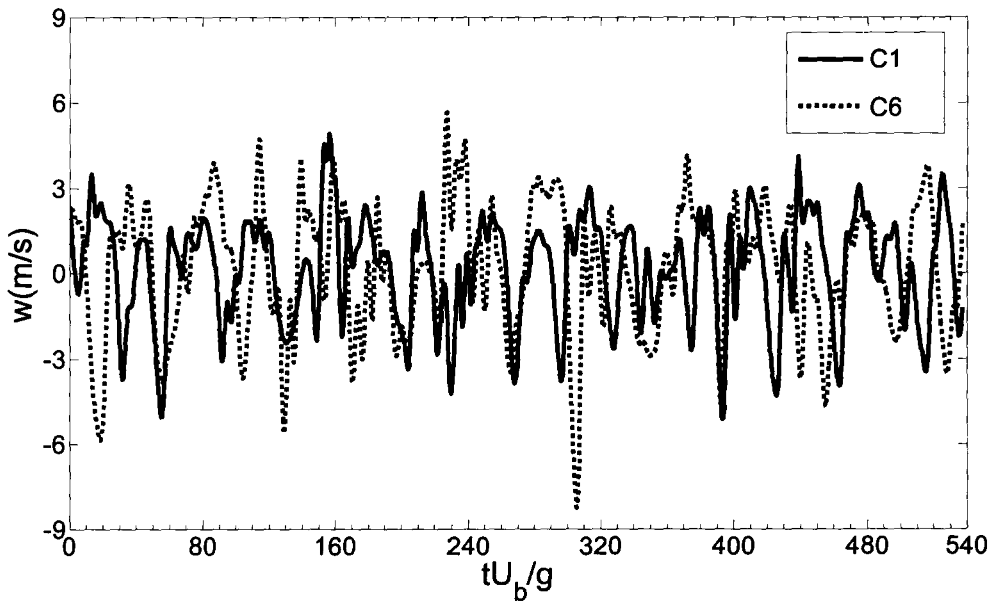

Figure 6.113 Time trace of the span-wise velocity at the gap edge for cases C1 and C6.

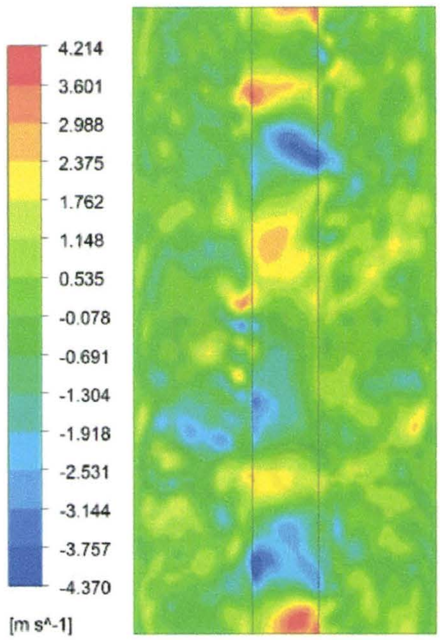

t = 0.76 sec, Case C1

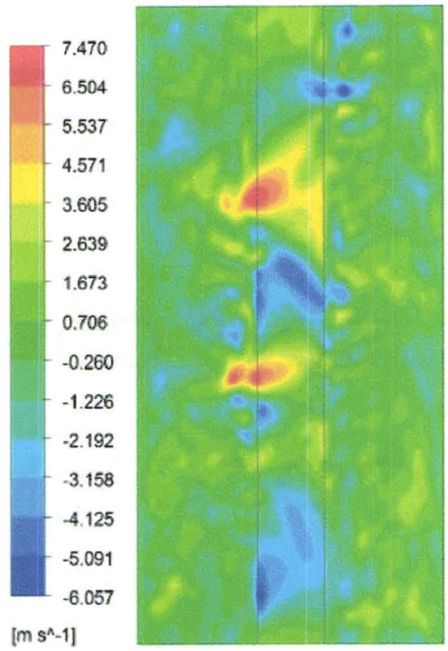

t = 0.76 sec, Case C6

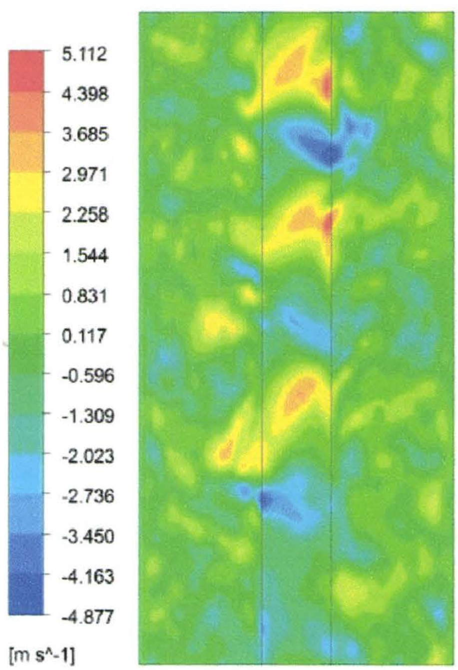

t = 1.28 sec, Case C1

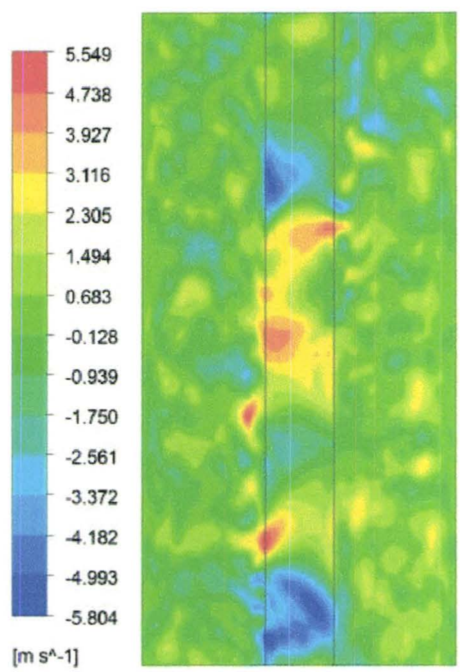

t = 1.28 sec, Case C6

Figure 6.114 Comparison of the span-wise velocities between cases C1 and C6 at the symmetry plane.

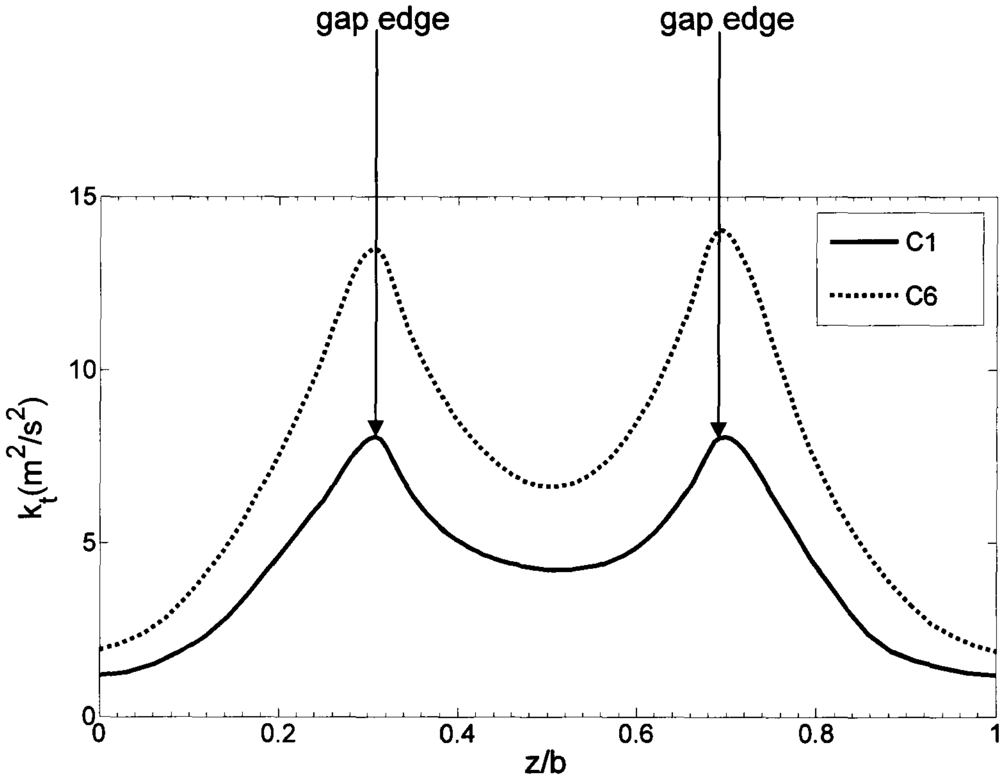

Figure 6.115 Comparison of the variation of the turbulent kinetic energy along the span-wise direction for cases C1 and C6 (z/b: normalized span-wise length, b: distance between centre of sub-channels).

case C6 is larger than case C1 throughout the gap region, which is consistent with its higher Reynolds number. The peak turbulent kinetic energy for case C6 is higher than case C1 by approximately a factor of 1.7, which is consistent in terms of the factor by which the Reynolds number is higher for case C6 with reference to case C1. Thus, with the increase in Reynolds number the intensity of the flow pulsations through the gap increases.

CHAPTER 7

CONCLUSIONS AND RECOMMENDATIONS FOR FUTURE WORK

7.1 Conclusions

This thesis was concerned with the numerical investigation of the flow pulsation phenomena for an isothermal turbulent flow in a twin rectangular sub-channel geometry. The central objective of this thesis work was to assess the applicability of the hybrid URANS-LES approach, specifically the DES-SST model in predicting the dynamics associated with the flow pulsation phenomena. It was of interest to see the capability of the DES-SST model to shed light into the important physics of the flow pulsation phenomena. This was perhaps the first time (to the author's knowledge) that the hybrid URANS-LES methodology was used to study this phenomena. The research work conducted in this thesis was divided into two phases.

In phase one of the research work, a review of the literature indicated that a hybrid URANS-LES approach could be a suitable choice to resolve the dynamics of sub-channel flow pulsations. This choice was made based on both computational considerations and the requirement that the model be able to resolve the effects of the large-scale quasi-periodic structures responsible for fluid flow pulsations. The Strelets (2001) DES model had been previously validated for flow with boundary layer separation such as those occurring in aerodynamics applications. As such, the first step in the research work was to assess the suitability of the model to predict non-separating boundary layer flows. Thus, the model was used to simulate the benchmark channel flow problem considered in the DNS study of Moser et al. (1999). It was found that the DES-SST model is suitable for turbulent flow problems without boundary layer separation and the results from this validation study were published in Home et al. (2009).

The second phase of the research work pertained to the simulation of the large-scale flow pulsation phenomena in compound rectangular channels using the DES-SST model. Predictions were compared to the results from the experiments conducted by Meyer and Rehme (1994). A reference case (case C1) was chosen (see Tables 6.1 and 6.2) for the numerical study for which detailed results were provided by Meyer and Rehme (1994). It was found that the simulation had sufficient spatial and temporal resolution to capture the dynamics of the flow pulsations around the vicinity of the gap region. The URANS zones were limited to near-wall regions and the LES mode was operational in regions of interest. Approximately, 73% of the turbulent kinetic energy in the LES zone around the gap region was provided by the resolved scales of motion. The following points summarize the findings of the numerical study in relation to the experiments:

1. The quantitative comparisons between the DES-SST model and the experimental results for the turbulence variables were in the same ballpark region for the different monitor points.
2. The DES-SST model was able to correctly predict the qualitative aspects (physics) of the flow field associated with the flow pulsation phenomena. The turbulent kinetic

energy, the Reynolds shear stress, and the axial and normal turbulent intensities had characteristic peaks near the gap edge region. The gap parallel Reynolds shear stress and the span-wise turbulent intensity was found to be large (compared to other regions in the flow field) throughout the entire length of the gap region.

3. The time traces of the span-wise velocity showed the expected quasi-periodic behavior. The instantaneous velocity components were found to be within the experimental range. The DES-SST model was able to correctly reproduce the negative skewness associated with the span-wise velocity at the gap edge which was shown in the experimental data as well.
4. The spatial-temporal correlation functions and the frequency analysis from the power spectra showed the expected quasi-periodic nature of the fluid flow. The cross flow mixing from one sub-channel to the other is due to the large-scale quasi-periodic oscillations in the gap region. The predicted peak frequency associated with the flow pulsations exactly matched the fundamental frequency reported by Meyer and Rehme (1994). The predicted wavelength from the spatial cross-correlation function was found to be larger by a factor of 1.3 as compared to the experimental result.

The following points summarize the most significant findings from the numerical study of the DES-SST model and the essential contributions from this thesis work:

1. The instantaneous momentum transfer from one sub-channel to the other is associated with a pressure difference pulse, which possibly arises from an instability near the gap edge region. The transverse pressure difference is a response to the instability mechanism.

2. The analysis from the numerical results has identified three different mixing patterns. The dominating (major) mixing pattern at an instant in time occurs when the fluid streams coming from either of the sub-channels flushes into the other sub-channel. In a sub-channel geometry, the flow is transported from the region of high momentum (sub-channels) to the narrow gap along the walls and it is transported back to the region of low shear. The other two mixing patterns are viz., when fluid streams travel from the respective sub-channels and converge near the gap, and when low velocity fluid diverges out from the gap to the respective sub-channels.
3. The Q-criterion identified the flow field to be comprised of eddies, shear zones and high speed streams. The fluid streams appear to bring high momentum fluid from the core of the sub-channel towards the gap region. It is the combination of high speed streams and the instantaneous pressure difference across the sub-channels that causes the fluid to pulsate. It appears that the coherent vortical structures formed near the vicinity of the gap edge region are responsible for altering the pressure difference across the sub-channels.
4. The origin of the flow pulsations or the instability arises from the near gap region, where there is an interaction of the low and high speed fluids. The span-wise variation of the time averaged stream-wise velocity profile was found to be inflectional in nature and is similar to a wake like velocity profile for cross flow over bluff bodies. The instability causing the fluid flow pulsations was associated with this inflectional velocity profile.

Following are the additional findings from the channel length and parametric studies:

1. The shorter (case C2) and longer (case C3) channel length simulations gave similar statistical and dynamical description of the flow field as compared to the reference case. However, frequency independent results could not be obtained.
2. The study on the sub-channel geometry with reduced gap height (case C4) suggested that by reducing the gap height the intensity of the flow pulsations and the cross flow velocity (mixing) through the gap increases, as compared to the reference case. From the study on the reduced sub-channel size (case C5) the larger cross flow velocity as compared to the reference case was attributed to a combination of larger mean flow velocity (for case C5) and geometry effect. It was eluded, that when the sub-channel sizes are reduced, the fluid flow perhaps encounters a lower flow path resistance and higher intensity in the fluid flow pulsations are observed.
3. With the increase in the Reynolds number the intensity of the flow pulsations through the gap increased, which is an expected result.

The DES-SST model was thus, successful in capturing the dynamics of the sub-channel flow pulsations. The quantitative and qualitative findings from the model are in accordance with the physics of the problem.

7.2 Future work

The DES-SST model shows promise for simulation of flows in more realistic sub-channel geometries formed by rod bundle arrangements. The next step is to extend this modeling methodology to non-isothermal sub-channel flow problems. It will be of great interest to see how the DES-SST model performs when heat transfer is involved. Seale's (1979) experimental study on rod bundle geometry arrangement inside a rectangular duct would be the perfect test case to assess the modeling capability of the DES-SST model for a non-isothermal sub-channel flow. After this, the DES-SST model can be used to simulate the non-isothermal flow in a 37-rod bundle hexagonal geometry arrangement for which detailed experiments were performed by Meyer (1994) and, Krauss and Meyer (1996) respectively. Once, the aforementioned studies are complete, then the DES-SST model can potentially be used to develop the simplified physical model for sub-channel mixing that could be used in broader safety analysis codes.

It is recommended that the sensitivity of the results be tested by changing the model constants of the DES-SST model, which include the constants of the SST model and the constants associated with the numerical blending function. The sensitivity of the results should also be tested by changing the turbulence model.

It is recommended that study be performed to find out how frequency influences the cross-flow mixing and the effects of frequency on total mixing.

BIBLIOGRAPHY

Aly, A. M. M, Trupp, A. C., and Gerrard, A. D., Measurements and prediction of fully developed turbulent flow in an equilateral triangular duct. *Journal of Fluid Mechanics*, Vol. 85, pp. 57-83, 1978.

Asai, M., Minagawa, M., and Nishioka, M., The instability and breakdown of a near-wall low-speed streak. *Journal of Fluid Mechanics*, Vol. 455, pp. 289-314, 2002.

Baggett, J. S., On the feasibility of merging LES with RANS for the near-wall region of attached turbulent flows. *Annual Research Briefs*, Center for Turbulence Research (Stanford University), 1998.

Balaras, E., Benocci, C., and Piomelli, U., Two-layer approximate boundary conditions for large-eddy simulations, *AIAA Journal*, Vol. 34, pp. 1111-1119, 1996.

Bartzis, J. G., and Todreas, N. E., Turbulence modelling of axial flow in a bare rod bundle. *ASME Journal of Heat Transfer*, Vol. 101, pp. 628-634, 1979.

Biemuller, M., Meyer, L., and Rehme, K., Large eddy simulation and measurement of the structure of turbulence in two rectangular channels connected by a gap. *Engineering Turbulence Modelling and Experiments*, Rodi, W., Bergeles, G. (Ed), Elsevier, Amsterdam, Vol. 3, pp. 249-258, 1996.

Brundrett, E., and Baines, W.D., The production and diffusion of vorticity in duct flow. *Journal of Fluid Mechanics*, Vol. 19, pp. 375-394, 1964.

Cabot, W., and Moin, P., Approximate wall boundary conditions in the large eddy simulation of high Reynolds number flow. *Flow, Turbulence and Combustion*, Vol. 63, pp. 269-291, 1999.

Caraghiaur, D., and Anglart, H., Measurements and CFD predictions of velocity, turbulence intensity and pressure development in BWR fuel rod assembly with spacers. *In: Proceedings of the 12th International Topical Meeting on Nuclear Reactor Thermal Hydraulics (NURETH-12)*, Pittsburgh, Pennsylvania, U.S.A., September 30-October 4, 2007.

Carajilescov, P., and Todreas, N.E., Experimental and analytical study of axial turbulent flows in an interior subchannel of a bare rod bundle. *ASME Journal of Heat Transfer*, Vol. 98, pp. 262-268, 1976.

Castellana, F.S., Adams, W.T., and Casterline, J.E., Single-phase subchannel mixing in a simulated nuclear fuel assembly. *Nuclear Engineering and Design*, Vol. 26, pp. 242-249, 1974.

Chang, D., and Tavoularis, S., Unsteady numerical simulations of turbulence and coherent structures in axial flow near a narrow gap. Journal of Fluids Engineering, Vol. 127, pp. 458-466, 2005.

Chang, D., and Tavoularis, S., Numerical simulation of turbulent flow in a 37-rod bundle. *Nuclear Engineering and Design*, Vol. 237, pp. 575-590, 2007.

Chapman, D., Computational aerodynamics, development and outlook. *AIAA Journal*, Vol. 17, pp. 1293-1313, 1979.

Constantinescu, G., and Squires, K. D., LES and DES investigations of turbulent flow over a sphere. *AIAA Paper 2000-0540*, 2000.

Constantinescu, G., Chapelet, M., and Squires, K. D., Turbulence modelling applied to flow over a sphere. *AIAA Journal*, Vol. 41, No. 9, pp. 1733-1742, 2003.

Davidson, L. and Billson, M., Hybrid LES-RANS using synthesized turbulent fluctuations for forcing in the interface region. *International Journal of Heat and Fluid Flow*, Vol. 27, pp. 1028-1042, 2006.

Davidson, L. and Dahlstöm, S., Hybrid LES-RANS: An approach to make LES applicable at high Reynolds number. *International Journal of Computational Fluid Dynamics*, Vol. 19, no. 6, pp. 415-427, 2005.

Davidson, L. and Peng, S. H., Hybrid LES-RANS: A one-equation SGS model combined with a $k-\omega$ model for predicting recirculating flows. *International Journal of Numerical Methods in Fluids*, Vol. 43, pp. 1003-1018, 2003.

Deardorff, J., A numerical study of three-dimensional turbulent channel flow at large Reynolds number. *Journal of Fluid Mechanics*, Vol. 61, pp. 481-507, 1970.

Durbin, P. A., Separated flow computations with the $k-\varepsilon-\upsilon^2$ model. *AIAA Journal*, Vol. 33, pp. 659-664, 1995.

Eiff, O.S., and Lightstone, M.F., On the modelling of single-phase turbulent energy transport in subchannels. *Proceedings of the Annual Conference-Canadian Nuclear Society CNA/CNS annual conference*, Toronto, ON, June, 1997.

Gosset, A., and Tavoularis, S., Laminar flow instability in a rectangular channel with a cylindrical core. *Physics of Fluids*, Vol. 18, 044108, 2006.

Grotjans, H., and Menter, F.R., Wall functions for general application CFD codes. In K.D.Papailiou et al., editor, *ECCOMAS 98 Proceedings of the Fourth European Computational Fluid Dynamics Conference*, pp. 1112-1117, John Wiley & Sons, 1998.

Guellouz, M. S., and Tavoularis, S., The structure of turbulent flow in a rectangular channel containing a cylindrical rod - Part 1: Reynolds-averaged measurements. *Experimental Thermal and Fluid Science*, Vol. 23, pp. 59-73, 2000.

Guellouz, M. S., and Tavoularis, S., The structure of turbulent flow in a rectangular channel containing a cylindrical rod - Part 2: Phase-averaged measurements. *Experimental Thermal and Fluid Science*, Vol. 23, pp. 75-91, 2000.

Hamba, F., An attempt to combine large eddy simulation with the $k-\varepsilon$ model in a channel flow calculation. *Theoretical Computational Fluid Dynamics*, Vol. 14, pp. 323-336, 2001.

Hamba, F., A hybrid RANS/LES simulation of turbulent channel flow. *Theoretical Computational Fluid Dynamics*, Vol. 16, pp. 387-403, 2003.

Hamed, A., Basu, D., and Das, K., Assessment of hybrid turbulence models for unsteady high speed separated flow predictions. *AIAA-2004-0684*, 42nd AIAA Aerospace Sciences Meeting and Exhibit, Reno, NV, 2004.

Home, D., Lightstone, M. F., and Hamed, M. S., Validation of DES-SST based turbulence model for a fully developed turbulent channel flow problem. *Numerical Heat Transfer, Part A*, Vol. 55, pp. 337-361, 2009.

Home, D., Arvanitis, G., Lightstone, M.F., and Hamed, M.S., Simulation of flow pulsations in a twin rectangular sub-channel geometry using unsteady Reynolds averaged

Navier-Stokes modelling. *Journal of Nuclear Engineering and Design*, Vol. 239, Issue 12, pp. 2964-2980, 2009.

Hooper, J.D., Developed single phase turbulent flow through a square-pitch rod cluster. *Nuclear Engineering and Design*, Vol. 60, pp. 365-379, 1980.

Hooper, J.D., and Rehme, K., Large-scale structural effects in developed turbulent flows through closely-spaced rod arrays. *Journal of Fluid Mechanics*, Vol. 145, pp. 305-337, 1984.

Hunt, J. C. R., Wray, A. A., and Moin, P., Eddies, streams, and convergence zones in turbulent flows. *Centre for Turbulence Research Proceedings of the Summer Program*, pp. 193-208, 1988.

Hussain, A., Coherent structures-reality and myth. *Physics of Fluids*, Vol. 26, No. 10, 2816-2850, 1983.

Ikeno, T., and Kajishima, T., Analysis of dynamical flow structure in a square arrayed rod bundle. *In: Proceedings of the 12th International Topical Meeting on Nuclear Reactor Thermal Hydraulics (NURETH-12)*, Pittsburgh, Pennsylvania, U.S.A., September 30-October 4, 2007.

Ingesson, L., and Kjellstrom, B., On gas mixing in rod bundles. *International Journal of Heat and Mass Transfer*, Vol. 13, pp. 429-431, 1970.

Jeong, H-Y., Ha, K-S., Kwon, Y-M., Lee, Y-B., and Hahn, D., A dominant geometrical parameter affecting the turbulent mixing rate in rod bundles. *International Journal of Heat and Mass Transfer*, Vol. 50, pp. 908-918, 2007.

Kapadia, S. and Roy, S., Detached eddy simulation over a reference Ahmed car model. *AIAA-2003-0857*, 41st AIAA Aerospace Sciences Meeting and Exhibit, Reno, NV, 2003.

Kim, S., and Chung, B.J, A scale analysis of the turbulent mixing rate for various Prandtl number flow fields in rod bundles. *Nuclear Engineering and Design*, Vol. 205, pp. 281-294, 2001.

Kim, S., and Park, G.C., Estimation of anisotropic factor and turbulent mixing rate in rod bundles based on the flow pulsation phenomenon. *Nuclear Technology*, Vol. 117, pp. 340-352, 1997.

Kim, S., and Park, G.C., Analysis of turbulent mixing in rod bundles with an anisotropic turbulent diffusion model based on the flow pulsation phenomenon. *Nuclear Technology*, Vol. 122, pp. 284-294, 1998.

Krauss, T., and Meyer, L., Characteristics of turbulent velocity and temperature in a wall channel of a heated rod bundle. *Experimental Thermal and Fluid Science*, Vol. 12, pp. 75-86, 1996.

Krauss, T., and Meyer, L., Experimental investigation of turbulent transport of momentum and energy in a heated rod bundle. *Nuclear Engineering and Design*, Vol. 180, pp. 185-206, 1998.

Lexmond, A. S., Mudde, R. F., Van der Haagen, T. H. J. J., Visualization of the vortex street and characterization of the cross flow in the gap between two subchannels. *In: Proceedings of the 11th International Topical Meeting on Nuclear Reactor Thermal Hydraulics (NURETH-11)*, Avignon, France, 2005.

Launder, B.E., Reece G.J., and Rodi, W., Progress in the development of a Reynolds-stress turbulence closure. *Journal of Fluid Mechanics*, Vol. 68, pp. 537-566, 1975.

Launder, B.E., and Ying, W.M., Prediction of flow and heat in ducts of square cross-section. *The Institution of Mechanical Engineering Proceedings*, Vol. 187, pp. 455-461, 1973.

Mathieu, J., and Scott, J., An introduction to turbulent flow. *Cambridge University Press*, Cambridge, 1999.

Menter, F.R., Improved two-equation $k-\omega$ turbulence models for aerodynamic flows. *NASA Technical Memorandum 103975*, 1992.

Merzari, E., Ninokata, H., and Baglietto, E., Numerical simulation of flows in tight-lattice fuel bundles. *Nuclear Engineering and Design*, Vol. 238, pp. 1703-1719, 2008.

Merzari, E., and Ninokata, H., Proper orthogonal decomposition of the flow in a tight lattice rod bundle. *In: Proceedings of the 13th International Topical Meeting on Nuclear Reactor Thermal Hydraulics (NURETH-13)*, Kanazawa City, Ishikawa Prefecture, Japan, September 27-October 2, 2009.

Meyer, L., Measurements of turbulent velocity and temperature in axial flow through a heated rod bundle. *Nuclear Engineering and Design*, Vol. 146, pp. 71-82, 1994.

Meyer, L., and Rehme, K., Large-scale turbulence phenomena in compound rectangular channels. *Experimental Thermal and Fluid Science*, Vol. 8, pp. 286-304, 1994.

Moin, P., Numerical and physical issues in large eddy simulation of turbulent flows. *International Journal of Japan Society of Mechanical Engineers*, Vol. 41, No. 2, Series B, pp. 454-463, 1998.

Moller, S.V., On phenomena of turbulent flow through rod bundles. *Experimental Thermal and Fluid Science*, Vol. 4, pp. 25-35, 1991.

Moller, S.V., Single-phase turbulent mixing in rod bundles. *Experimental Thermal and Fluid Science*, Vol. 5, pp. 26-33, 1992.

Moser, R.D., Kim, J., and Mansour, N.N., Direct numerical simulation of turbulent channel flow up to $\mathrm{Re}_\tau = 590$. *Physics of Fluids*, Vol. 11, No. 4, pp. 943-945, 1999.

Nikitin, N. V., Nicoud, F., Wasistho, B., Squires, K. D., and Spalart, P. R., An approach to wall modeling in large-eddy simulations. *Physics of Fluids*, Vol. 12, no. 7, pp. 1629-1632, 2000.

Patankar, S. V., Numerical heat transfer and fluid flow. *Hemisphere Publishing Corp.*, 1980.

Piomelli, U., and Balaras, E., Wall-layer models for large-eddy simulations. *Annual Review of Fluid Mechanics*, Vol. 34, pp. 349-374, 2002.

Piomelli, U., Balaras, E., Pasinato, H., Squires, K. D., and Spalart, P. R., The inner-outer layer interface in large-eddy simulations with wall-layer models. *International Journal of Heat and Fluid Flow*, Vol. 24, pp. 538-550, 2003.

Pope, S. B., Turbulent flows. *Cambridge University Press*, Cambridge, 1999.

Rapley, C.W., and Gosman, A.D., The prediction of fully developed axial turbulent flow in rod bundles. *Nuclear Engineering and Design*, Vol. 97, pp. 313-325, 1986.

Rehme, K., The structure of turbulent flow through a wall subchannel of a rod bundle. *Nuclear Engineering and Design*, Vol. 45, pp. 311-323, 1978.

Rehme, K., Turbulent momentum transport in rod bundles. *Nuclear Engineering and Design*, Vol. 62, pp. 137-146, 1980.

Rehme, K., Distributions of velocity and turbulence in a parallel flow along an asymmetric rod bundle. *Nuclear Technology*, Vol. 59, pp. 148-159, 1982.

Rehme, K., The structure of turbulent flow through rod bundles. *Nuclear Engineering and Design*, Vol. 99, pp. 141-154, 1987.

Rehme, K., Experimental observations of turbulent flow through subchannels of rod bundles. *Experimental Thermal and Fluid Science*, Vol. 2, pp. 341-349, 1989.

Rehme, K., The structure of turbulence in rod bundles and the implications on natural mixing between the subchannels. *International Journal of Heat and Mass Transfer*, Vol. 35, No. 2, pp. 567-581, 1992.

Renksizbulut, M., and Hadaller, G., An experimental study of turbulent flow through a square-array rod bundle. *Nuclear Engineering and Design*, Vol. 91, pp. 41-55, 1986.

Robinson, S. R., Coherent motions in the turbulent boundary layer. *Annual Review of Fluid Mechanics*, Vol. 23, pp. 601-639, 1991.

Rowe, D.S., Johnson, B.M., and Knudsen, J.G., Implications concerning rod bundle crossflow mixing based on measurements of turbulent flow structure. *International Journal of Heat and Mass Transfer*, Vol. 17, pp. 407-419, 1974.

Rock, R.C.K., and M.F. Lightstone, A numerical investigation of turbulent interchange mixing of axial coolant flow in rod bundle geometries. *Numerical Heat Transfer*, Vol. 40, pp. 221-237, 2001.

Schumann, U., Subgrid scale model for finite difference simulations of turbulent flows in plane channels and annuli. *Journal of Computational Physics*, Vol. 18, pp. 376-404, 1975.

Seale, W.J., Turbulent diffusion of heat between connected flow passages, Part 1: Outline of problem and experimental investigation. *Nuclear Engineering and Design*, Vol. 54, pp. 183-195, 1979.

Seale, W.J., Turbulent diffusion of heat between connected flow passages, Part 2: Predictions using the k-ε turbulence model. *Nuclear Engineering and Design*, Vol. 54, pp.197-209, 1979.

Seale, W.J., The effect of subchannel shape on heat transfer in rod bundles with axial flow. *International Journal of Heat and Mass Transfer*, Vol. 24, pp. 768-770, 1981.

Seale, W.J., Measurements and predictions of fully developed turbulent flow in a simulated rod bundle. *Journal of Fluid Mechanics*, Vol. 123, pp. 399-423, 1982.

Shur, M., Spalart, P., Strelets, M., and Travin, A., Detached-eddy simulation of an airfoil at high angle of attack. In W. Rodi and D. Laurence (eds.), *Engineering Turbulence Modelling and Experiments-4*, Elsevier Science, pp. 669-678, 1999.

Silin, N., and Juanicó, L., Experimental study on the Reynolds number dependence of turbulent mixing in a rod bundle. *Nuclear Engineering and Design*, Vol. 236, pp. 1860-1866, 2006.

Skinner, V.R., Freeman, A.R., and Lyall, H.G., Gas mixing in rod bundles. *International Journal of Heat and Mass Transfer*, Vol. 12, pp. 265-278, 1969.

Spalart, P. R., and Allmaras, S. R., A one-equation turbulence model for aerodynamic flows. *In: 30th Aerospace Sciences Meeting and Exhibit*, Reno, Nevada, January 6-9, 1992.

Spalart, P. R., Jou, W. H., Strelets, M., and Allmaras, S. R., Comments on the feasibility of LES for wings, and on a hybrid RANS/LES approach. *First AFOSR International Conference on DNS/LES*, Ruston, LA, in C. Liu and Z. Liu (eds.), *Advances in DNS/LES*, Greyden Press, 1997.

Spalart, P. R., Strategies for turbulence modelling and simulations. *International Journal of Heat and Fluid Flow*, Vol. 21, pp. 252-263, 2000.

Strelets, M., Detached eddy simulation of massively separated flows. *AIAA Paper*, 2001-0879, Reno, NV, 2001.

Suh, Y. K., and Lightstone, M. F., Numerical simulation of turbulent flow and mixing in a rod bundle geometry. *Nuclear Energy*, Vol. 43, No. 1, pp. 1-11, 2004.

Tavoularis, S., Madrane, A., and Vaillancourt, R., Numerical simulation of coherent structures in axial flows through a rectangular channel containing a cylindrical rod, *In: Proceedings of the CFD Society of Canada*, Windsor, ON, June, 2002.

Temmerman, L., Leschziner, M., and Hanjalić, K., A priori studies of near-wall RANS model within a hybrid LES/RANS scheme. In W. Rodi and N. Fueyo (eds.), *Engineering Turbulence Modelling and Experiments-5*, Elsevier Science, pp. 317-326, 2002.

Temmerman, L., Leschziner, M., Mellen, C., and Fröhlich, J., Investigation of subgrid-scale models and wall-function approximations in large eddy simulation of separated flow in a channel with streamwise periodic constrictions. *International Journal of Heat and Fluid Flow*, Vol. 24, pp. 157-180, 2003.

Temmerman, L., Hadžiabdić, M., Leschziner, M. A., and Hanjalić, K., A hybrid two-layer URANS-LES approach for large eddy simulation at high Reynolds numbers. *International Journal of Heat and Fluid Flow*, Vol. 26, pp. 173-190, 2005.

Tóth, S., and Aszódi, A., CFD analysis of flow field in a triangular rod bundle. *In: Proceedings of the 12th International Topical Meeting on Nuclear Reactor Thermal Hydraulics (NURETH-12)*, Pittsburgh, Pennsylvania, U.S.A., September 30-October 4, 2007.

Travin, A., Shur, M., Strelets, M., and Spalart, P. R., Detached-eddy simulations past a circular cylinder. *Flow, Turbulence and Combustion*, Vol. 63, pp. 293-313, 2000.

Trupp, A. C., and Aly, A. M. M., Predicted secondary flows in triangular array rod bundles. *ASME Journal of Heat Transfer*, Vol. 101, pp. 354-363, 1979.

Trupp, A. C., and Azad, R. S., The structure of turbulent flow in triangular array rod bundles. *Nuclear Engineering and Design*, Vol. 32, pp. 47-84, 1975.

Tucker, P., and Davidson, L., Zonal $k-l$ based large eddy simulation. *Computers and Fluids*, Vol. 33, no. 2, pp. 267-287, 2004.

Van Der Ros, T., and Bogaardt, M., Mass and heat exchange between adjacent channels in liquid-cooled rod bundles. *Nuclear Engineering and Design*, Vol. 12, pp. 259-268, 1970.

Vonka, V., Measurement of secondary flow vortices in a rod bundle. *Nuclear Engineering and Design*, Vol. 106, pp. 191-207, 1988.

Werner, H., and Wengle, H., Large eddy simulation of turbulent flow over and around a cube in a plate channel. *In: 8th Symposium on Turbulent Shear Flows*, pp. 155-168, 1991.

Wu, X., On the transport mechanisms in simulated heterogeneous rod bundle subchannels. *Nuclear Engineering and Design*, Vol. 158, pp. 125-134, 1995.

Wu, S. R., and Rehme, K., An experimental investigation on turbulent flow through symmetric wall subchannels of two rod bundles. *Nuclear Technology*, Vol. 89, pp. 103-115, 1990.

Wu, X., and Trupp, A.C., Experimental study on the unusual turbulence intensity distributions in rod-to-wall gap regions. *Experimental Thermal and Fluid Science*, Vol. 6, pp. 360-370, 1993.

Wu, X., and Trupp, A.C., Spectral measurements and mixing correlation in simulated rod bundle subchannels. *International Journal of Heat and Mass Transfer*, Vol. 37, pp. 1277-1281, 1994.

Yang, A. C., and Chieng, C. C., Turbulent heat and momentum transports in an infinite rod array. *Journal of Heat Transfer*, Vol. 109, pp. 599-605, 1987.